

Copyright © 2005, by the author(s).
All rights reserved.

Permission to make digital or hard copies of all or part of this work for personal or classroom use is granted without fee provided that copies are not made or distributed for profit or commercial advantage and that copies bear this notice and the full citation on the first page. To copy otherwise, to republish, to post on servers or to redistribute to lists, requires prior specific permission.

**INTERFEROMETRIC PATTERN AND
PROBE-BASED ABERRATION MONITORS**

by

Garth Charles Robins

Memorandum No. UCB/ERL M05/20

20 May 2005

Over

**INTERFEROMETRIC PATTERN AND
PROBE-BASED ABERRATION MONITORS**

by

Garth Charles Robins

Memorandum No. UCB/ERL M05/20

20 May 2005

ELECTRONICS RESEARCH LABORATORY

College of Engineering
University of California, Berkeley
94720

Interferometric Pattern and Probe-Based Aberration Monitors

by

Garth Charles Robins

B.S. (The Ohio State University) 1997

M.Phil. (University of Cambridge) 1999

M.S. (University of Cambridge) 2000

A dissertation submitted in partial satisfaction of the

requirements for the degree of

**Doctor of Philosophy
in**

Applied Science and Technology

in the

GRADUATE DIVISION

of the

UNIVERSITY OF CALIFORNIA, BERKELEY

Committee in charge:

Professor Andrew R. Neureuther, Chair

Professor Nathan W. Cheung

Professor Stanley A. Klein

Spring 2005

Interferometric Pattern and Probe-Based Aberration Monitors

© 2005

by

Garth Charles Robins

Abstract

Interferometric Pattern and Probe-Based Aberration Monitors

by

Garth Charles Robins

Doctor of Philosophy in Applied Science and Technology

University of California, Berkeley

Professor Andrew R. Neureuther, Chair

This thesis introduces a new class of interferometric pattern and probe-based aberration monitors based upon the principle of coherent electromagnetic spillover among transmitting phase-shifting regions and assesses their implementation on the currently installed base of photolithographic exposure tools. The mathematical theory developed is based upon the diffraction integral for coherent imaging and shows that the optimum patterns for measuring aberrations are the two-dimensional inverse Fourier transforms of the original aberration functions, expressed as Zernike polynomials. As a result, each aberration monitoring target consists of a sub-resolution probe surrounded by a number of pattern rings which are near the resolution limit of the exposure tool. The positions and phasing of the rings are determined by the original aberration function. The rings act to spill electric-field over onto the central probe position in an amount which varies linearly with the amount of the given aberration.

Through simulation the monitors show an intensity response at the central probe position of 20 to 30% of the clear field per 0.01λ rms of aberration. This is over 50 \times stronger than the Strehl ratio response. Using the defocus target, it has been possible to measure the defocus aberration down to 0.01λ rms. Simulation results also show that the

targets are, at most, 1/6 as sensitive to other, similar aberrations that they are not designed to detect.

The targets were fabricated in multi-phase masks for a maximum numerical aperture of 0.80 and wavelengths of 248 nm and 193 nm, and their experimental performance has been characterized using AIMS and photoresist exposures. In practice, the performance of the targets is limited by a number of second order effects. Analysis shows that misalignment, biasing, and phase etch error all affect the defocus target to less than 5% in electric-field. The most influential factor is the impact of the illumination partial coherence, as it weights the spillover fields from the ring elements differently depending upon their radii. While this causes a 28% change in the electric-field for $\sigma = 0.30$, the effect can be reduced to less than 4% by lowering σ to 0.15. The second most important effect is that of the electromagnetic mask transmission for etched features, which reduces the field from the probe by 20%. This effect can be eliminated however by biasing the feature edges by $0.044 \frac{\lambda}{NA}$. Finally, while it does not impact the probes, high-numerical aperture polarization effects at $NA = 0.80$ change the desired aerial image fields from the rings by 20%. This is reduced to less than 6% however when the image is transferred into photoresist.

Professor Andrew R. Neureuther
Committee Chairman

To Mom and Stephanie.

I think I thought I would feel smarter.

TABLE OF CONTENTS

ACKNOWLEDGEMENTS	V
1. INTRODUCTION	1
1.1. <i>Imaging Effects</i>	3
1.1.1. Loss of Image Fidelity due to the Diffraction Limit	4
1.1.2. The Effect of Aberrations	5
1.1.3. Electric-Field Spillover and Perturbation from Aberration	6
1.1.4. Foundation for the Work in this Thesis	8
1.1.5. Research Context	10
1.2. <i>Thesis Organization and Goals</i>	10
2. BACKGROUND	14
2.1. <i>Optical Imaging Theory</i>	14
2.1.1. Imaging System	15
2.1.2. Resolution, Depth of Focus, and Partial Coherence	17
2.1.3. Diffraction Integral	20
2.1.4. Point and Line Spread Functions	24
2.2. <i>Masks</i>	26
2.2.1. Phase-Shifting Masks and Opportunities	27
2.2.2. PSM Realization Issues	27
2.3. <i>Aberrations</i>	28
2.3.1. The Circle Polynomials of Zernike	28
2.3.2. Aberration Levels and Impact in Imaging Systems	31
2.3.3. Aberrated Point Spread Electric-Field	33
2.3.4. Survey of Methods for Measuring Aberrations	38
3. ELECTRIC-FIELD SPILLOVER METHODS	45
3.1. <i>Knife Edge</i>	45
3.2. <i>Pattern and Probe-Based Aberration Monitors</i>	48
4. THEORY	54
4.1. <i>Formal Mathematical Justification</i>	54
4.1.1. Utilizing the Electromagnetic Diffraction Integral	55
4.1.2. Benefits of the Zernike Polynomial Basis	58
4.2. <i>Optimum Test Targets as IFT's of Zernikes</i>	59
4.3. <i>Mathematical Target Characteristics</i>	65
4.3.1. One-Dimensional Treatment	66
4.3.2. Location of Maximum Radiation for Each Order	69

4.3.3.	Constant Square Wave Drive and Finite Target Size	71
4.3.4.	Implications for the Two-Dimensional Case	73
4.4.	<i>Examples of Discretized Test Targets</i>	75
4.4.1.	Summary	79
5.	SIMULATION CHARACTERIZATION	81
5.1.	<i>Lithography Demons</i>	81
5.2.	<i>Summary of Test Target Performance</i>	83
5.2.1.	Typical Target Response	84
5.2.2.	Phasor Electric-Field Model	88
5.3.	<i>Mask, Illumination, and Tool Effects</i>	95
5.3.1.	Mask Making Tolerances	96
5.3.2.	Illumination – Partial Coherence Factor (σ)	97
5.3.3.	The Effect of Adding More Rings	99
5.3.4.	Resizing the Chrome Isolating Region	102
5.3.5.	Phase Shifting Mask Intensity Imbalance	105
6.	INITIAL EXPERIMENTAL RESULTS	108
6.1.	<i>Preliminary Aerial Image Measurement System™ Results</i>	109
6.1.1.	AIMS Modification for Initial Experiment	110
6.1.2.	AIMS Calibration	111
6.1.3.	Target CCD Images	116
6.1.4.	Analysis of Focus	117
6.2.	<i>Preliminary Photoresist Exposure Results</i>	119
6.2.1.	Focus Monitor Performance	121
6.2.2.	Coma Monitor Performance	128
6.3.	<i>Performance in the Production Environment</i>	131
6.3.1.	Focus Monitor	132
6.3.2.	Coma Monitor	140
6.3.3.	Spherical Monitor	142
6.3.4.	Summary	144
7.	ADVANCED EXPERIMENTS	146
7.1.	<i>Strategy of Factorization and Mask Fabrication</i>	146
7.2.	<i>In-Depth Analysis of the Mask</i>	149
7.2.1.	Phase Layer Alignment	149
7.2.2.	Phase Etch Depth	154
7.3.	<i>Advanced AIMS Results for the Defocus Target</i>	155
7.3.1.	Test Target Modifications and Results	156
7.4.	<i>Experimental Characterization of Target Elements</i>	158
7.4.1.	Imaging Phase-Shifted Dots	159
7.4.2.	Imaging Phase-Shifted Lines	163

7.4.3.	Imaging Phase-Shifted Rings	165
7.5.	<i>Analysis of Full Target Response</i>	167
7.5.1.	Target Response at $\sigma = 0.30$ and 0.17	168
7.6.	<i>General Trends in the Data</i>	170
7.6.1.	Changes with Probes	170
7.6.2.	Changes with σ	171
7.6.3.	Summary	171
8.	QUANTITATIVE ANALYSIS	173
8.1.	<i>Estimated Influences of Non-Idealities</i>	173
8.1.1.	Alignment	173
8.1.2.	Bias	175
8.1.3.	Phase Etch Error	176
8.1.4.	Topography Effects	177
8.1.5.	High-NA	178
8.2.	<i>Partial Coherence</i>	179
8.2.1.	Ring Self-Influence	179
8.2.2.	Searching for an Imaginary Component	182
8.3.	<i>Conclusions and Outlook for the Future</i>	183
9.	ABERROMETRY FOR THE HUMAN EYE	187
9.1.	<i>Background</i>	187
9.2.	<i>Potential of Pattern and Probe Monitors</i>	189
9.2.1.	Benefits and Drawbacks	194
9.2.2.	Conclusions	196
	APPENDIX A – ZERNIKE CIRCLE POLYNOMIALS	198
	APPENDIX B – THE TAYLOR EXPANSION	199
	APPENDIX C – STREHL BEHAVIOR	202
	APPENDIX D – IFT TARGET LAYOUT	204
10.	REFERENCES	206

Acknowledgements

This work represents the combined efforts and knowledge gained by the opportunities that I have had to work with many people. I would like my advisor, Professor Andrew R. Neureuther for sharing his expertise and advice during countless hours of meetings, as well as for providing excellent contacts to industrial collaborators, without whom this work would have been impossible. They include ASMLithography, Advanced Microdevices, Photronics, and DuPont Photomask. The individuals at these companies to whom I owe thanks include Mircea Dusa, Bruce Griffing, Brian Kasproicz, Jongwook Kye, and Alden Acheta. I would also like to thank my coworkers in the TCAD group: Kostas Adam, Tom Pistor, Mike Williamson, Lei Yuan, Mike Lam, Dan Ceperly, Frank Gennari, and Greg McIntyre. They have always been excellent sounding boards for ideas and problems. I would also like to express my thanks to the Applied Science and Technology Graduate Program as well as the University itself for providing me with this opportunity. Finally, none of this would have been possible, or fun, without the continuing support of my family and friends.

This work was funded by the Lithography Network SRC 96-LC-460 and DARPA MDA972-97-1-0010, by the State of California and Industry in the SMART (Semiconductor Manufacturing Alliance for Research and Training) program SM97-01, SMART99-10051, and the Feature Level Compensation and Control Award.

1. Introduction

Aberrations are important in image formation. In the eye, aberrations can play a significant role in visual performance. Anyone who has visited the eye doctor and come away with a prescription for glasses or contact lenses is familiar with how aberrations affect the optical performance of one of the world's most common imaging systems, their eyes. They are also familiar with some of the ways in which aberrations are measured, ranging from the observation of sets of lines in various configurations to the seemingly ubiquitous "E" eye chart. These tests tell the doctor the amount of focus error and astigmatism in their patients' eyes, giving them a prescription for how to grind a lens to compensate for these optical effects.

The ability to make good lines is important in fabricating semiconductor chips. Chips are made by essentially taking a "picture" of a template called a mask, photomask, or reticle, containing the image of the circuit design using a process called "lithography". The "camera", called a stepper or a scanner, is actually a multi-million dollar tool which has been highly-engineered to try to eliminate aberrations and yield the optimum image quality possible across a large field. It contains a light source that illuminates the template and a lens that collects the light, focusing it onto the "film" plane. A silicon wafer covered with a thin layer of photosensitive material, called photoresist, takes the place of the photographic film.

An exposure generally covers a field of about $2\text{ cm} \times 2\text{ cm}$ on the wafer and takes approximately one second. After the exposure a shutter blocks the light and the wafer is stepped to the next exposure field where the process is repeated. Using this "step and repeat", or a similar "scan, step and repeat" technique, 400 to 1,000 chips can be exposed

on a single 300 mm diameter wafer. The wafer is then placed into a chemical solution and those areas exposed by light are developed away, leaving some areas of the wafer exposed. From this point, further processing steps such as materials deposition, etching, or ion implantation can be performed to control the electrical properties of the underlying semiconductor material.

Garza has shown [1] that the effects of residual aberrations in lithographic exposure tools are important in image formation at the wafer plane. Small amounts of aberrations do not distort a point image very much but they can cause significant interactions between nearby features, ruining all or part of the image by causing features to image larger or smaller than intended or by causing them to shift from their desired positions. The use of phase-shifting masks and off-axis illumination can exacerbate these problems [2] and the feature shifts due to aberrations can be up to half as big as those being applied in optical proximity correction techniques [3].

While a great deal of time and effort goes into reducing the amount of aberrations in a lithographic exposure tool, small amounts of residual aberrations do remain. Defocus and astigmatism are just two examples of aberrations which can affect both the eye and lithography tools. There is actually an infinite number of aberrations, each of which affects the quality of the image in a slightly different manner. While the levels of aberration under consideration for the human eye are relatively large and easily measured by sets of lines and eye charts, the levels of aberration in lithography tools are tiny in comparison. It is important to be able to measure these aberrations in order to either fix the tool or to modify the circuit layout or fabrication process to achieve the yield

necessary for volume manufacturing of the chips. This is accomplished by using specially designed structures which are sensitive to the various aberrations.

The goal of this thesis is to determine the optimum patterns to detect extremely small amounts of individual aberrations and to quantify their sensitivity. The principle that is used is the perturbation to the lateral spillover of electric-field from features onto one another that is caused by the presence of aberrations. Through simulation and theory a new class of structures has been discovered based upon a reference probe and an optimal surrounding pattern for a given type or set of aberrations.

A key enabling technology for this approach is the use of phase-shifting masks. Phase-shifting masks allow the unique opportunity to engineer the phase of the wavefront leaving the mask object, rather than just the binary amplitude afforded by standard masks. The increasing availability of such masks to the semiconductor industry helped greatly in the realization of the aberration monitoring patterns.

The ability to implement this approach of course depends upon the detailed performance in practice that can be obtained through design, fabrication, and test of the structures. Much of this thesis consists of determining how factors such as the finite partial coherence of the illumination, electromagnetic transmission effects through the mask, high-numerical aperture polarization effects, resist effects, and mask geometry errors affect their performance and how engineering design can be applied to obtain a satisfactory embodiment.

1.1. *Imaging Effects*

To understand why they are important and how they might be measured, it is important to look at the effect that aberrations have upon images. In this section the effect

of the diffraction limit and the effects of the imperfect optical path caused by aberrations upon image formation are investigated.

1.1.1. Loss of Image Fidelity due to the Diffraction Limit

At each point in the lithographic process, some of the fidelity of the printed pattern to the original design can be, and often is, lost. Perhaps the most evident of these fidelity losses occurs during the imaging of the pattern onto the wafer. As feature sizes are pushed lower and lower in order to increase the speed and number of devices on a single chip, they become smaller and smaller compared to the available resolution of the exposure tool, resulting in the spillover of electric-field between nearby features. Thus the influence of mask openings on their neighbors becomes stronger and stronger. As a result, sharp features such as inside and outside corners print less and less like they are designed. Common optical effects such as (a) line end shortening, (b) corner rounding, and (c) proximity spillover resulting in feature bulging are illustrated in Figure 1-1, where the left side shows the pattern design on the mask and the right side indicates how the pattern images after passing through the optical system.

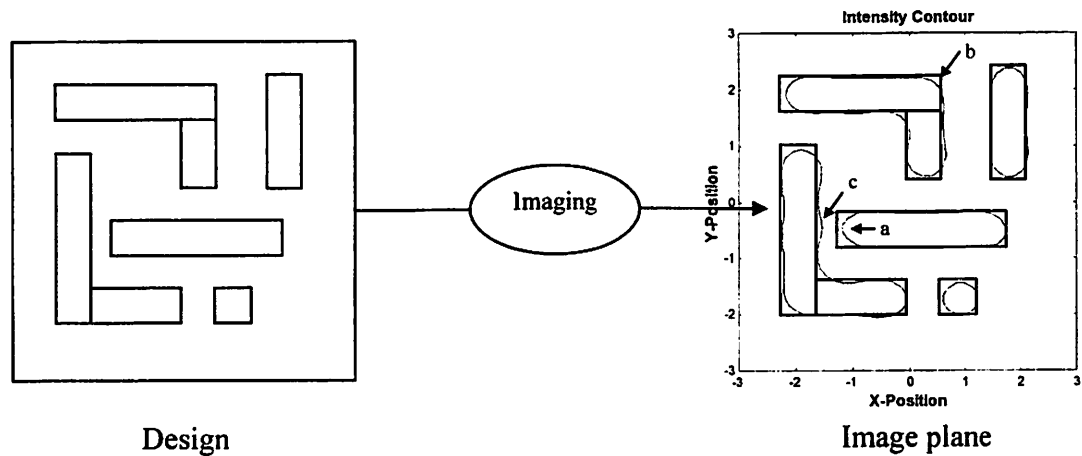


Figure 1-1. (Left) Mask pattern as designed. (Right) Resulting image overlaid with original mask pattern.

1.1.2. The Effect of Aberrations

Given a perfect, or “diffraction-limited”, lens, the image generally differs from the object only in size (due to magnification) and fine detail because of the low ray angle filtering which occurs due to the finite size of the imaging lens. Aberrations in the imaging lens however, cause image shifts and additional spillover of light, redirected from mask openings to other areas in the image plane. Figure 1-2 shows the image of the pattern design for a good lens with much less aberration than a typical human eye. It is seen that even small amounts of aberrations can significantly affect (a) the interaction between features as well as (b) the placement of printed features. The effects of an imperfect optical path as well as interactions between adjacent features are difficult to predict but are of critical importance in creating a manufacturable design with good yield. It is thus very important to be able to measure the aberrations in a lithographic tool to very high precision.

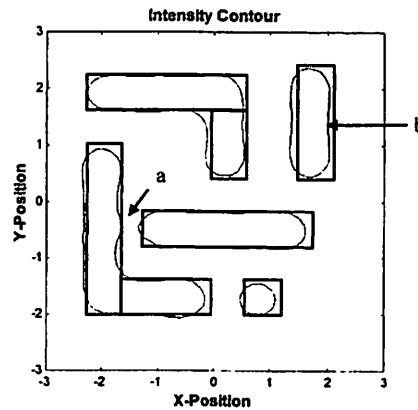


Figure 1-2. Printed result of mask layout seen in Figure 1-1 with a small amount of aberration.

1.1.3. Electric-Field Spillover and Perturbation from Aberration

The additional lateral spillover due to aberration can be illustrated by examining the image of an opaque knife edge with defocus. The top part of Figure 1-3 shows a large clear opening abutting a large dark area along a long straight edge. The lower part of Figure 1-3 shows a cut-line through the intensity just inside the dark region beyond the knife edge for different amounts of defocus. With defocus aberration only there is no image shift and only spillover. All of the intensity values are normalized by the “clear field” (CF) value by dividing them by the intensity that would come through a large clear opening in the mask.

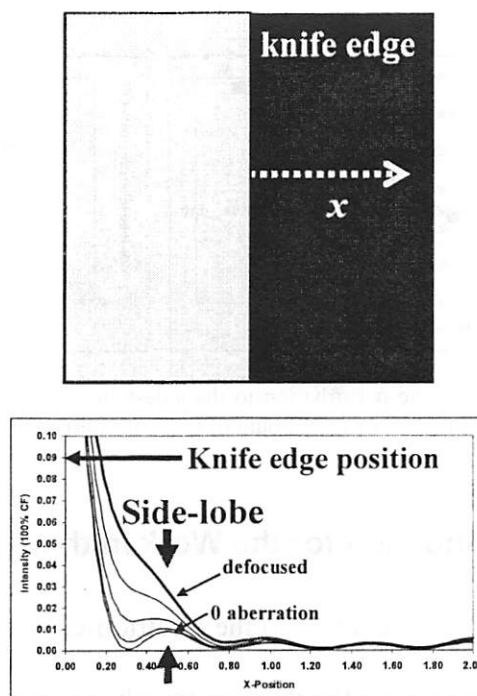


Figure 1-3. Image of a knife edge mask pattern in a binary mask with no aberration and with increasing amounts of defocus aberration.

When no defocus is present a small intensity side-lobe of 0.92% CF is found at a characteristic distance from the knife edge. The intensity at a given point is the time average square of the electric-fields at that position so this intensity gives an unaberrated electric-field reference value of magnitude $\sqrt{0.92\%CF} = 0.096$ at the side-lobe position. When defocus is added to the simulation, the electric-field arriving at the side-lobe position is perturbed and the side-lobe clearly rises. Using the techniques presented in this thesis, the side-lobe electric-field contributions are broken into both a regular image component and an aberration-induced component. The key point is that the aberration-induced component varies linearly with the amount of aberration. This can be seen in the plot on the left of Figure 1-4. This results in a parabolic behavior of the side-lobe intensity with aberration. This parabola may or may not go to zero, depending on the nature of the aberration.

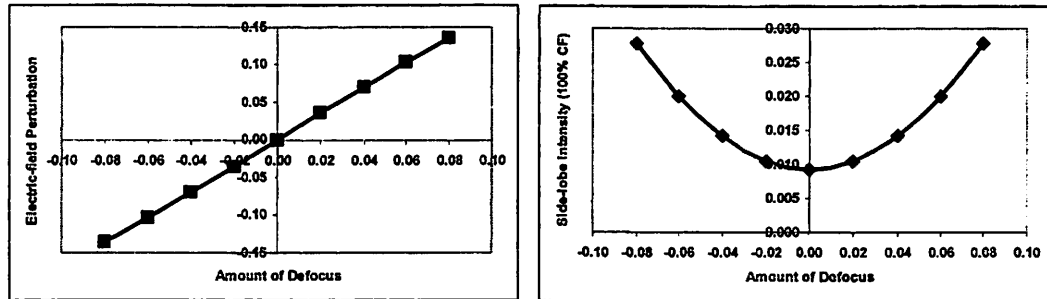


Figure 1-4. (Left) Plot of the perturbation to the side-lobe spillover electric-field and (Right) plot of the side-lobe intensity as a function of the amount of defocus aberration.

1.1.4. Foundation for the Work in this Thesis

The fact that the perturbation to the electric-field spillover is linear with the amount of aberration has stimulated the work in this thesis to generate very sensitive aberration monitors as ‘canaries’ to be used in any form of projection printing or imaging. Figure 1-5 shows two examples of this new class of aberration targets, designed to measure defocus and astigmatism. The targets are implemented in dark-field phase-shifting masks. Each consists of a phase-shifted probe, surrounded by a ring of chrome, to monitor the change in electric-field spilled over from a set of fully transmitting pattern rings whose position and phase are determined by the form of the aberration of interest.

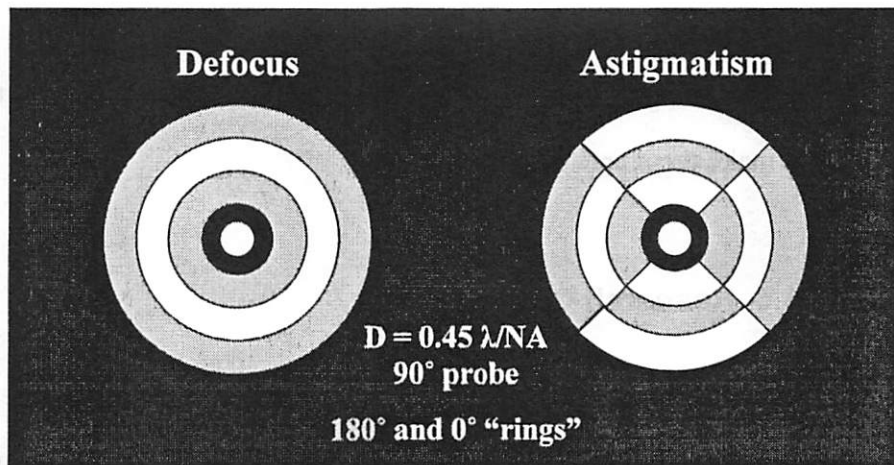


Figure 1-5. Example of an optimized patterns for measuring small amounts of the defocus and astigmatism aberrations.

Clearly, these patterns are likely to be more sensitive to aberrations than dense features and there are four major improvements in these designs over the simple knife edge. The first improvement is the use of the probe to raise the reference electric-field from that of a weak side-lobe (0.096) to 0.45 to 0.55 (corresponding to 20% to 30% CF in intensity), depending upon the size of the probe. The second is that the spillover source is wrapped around the point of measurement. The third is that a unique pattern can be generated to measure any individual aberration. And finally, using a phase-shifting mask allows both 0° and 180° rings to be used simultaneously, roughly doubling the sensitivity to aberration from a binary pattern.

The key goals of this thesis are to:

- 1) Present a rigorous theoretical foundation for the aberration monitors.
- 2) Design, fabricate, and test the first experimental embodiments of the aberration monitors.
- 3) Rank order the influence of potential limiting factors on aberration monitor performance.

and

- 4) Seek design improvements to extend the limits of aberration monitor performance and make them practical to use.

1.1.5. Research Context

Also important are other related research themes. Having established the linearity of the perturbation to the electric-field spillover with aberration, the aberration monitor patterns lend themselves to techniques of pattern matching developed by Frank Gennari [4], wherein a test pattern is scanned over a circuit layout in order to determine which points in the layout are most similar to the aberration-sensitive pattern and therefore most susceptible to a given aberration. Success with aberration test patterns in the author's work has helped to stimulate more general work on the use of phase-shifting masks as precision instruments for the characterization of imaging systems. They are part of a toolbox of highly-experimental photomask structures which include illumination monitors [5, 6, 7], and monitors for other phenomena such as flare [8,9] and thermal processing [4].

1.2. *Thesis Organization and Goals*

This thesis begins by introducing the basic concepts of optical imaging theory, including resolution, depth of focus, coherence, the diffraction integral, and electric-field spillover at the beginning of Chapter 2. The Zernike representation of optical aberrations is then given, along with the effects of individual aberrations on images and a survey of competing methods for measuring aberrations. This is followed by an introduction to photomask technology and a discussion of the physical phenomenon underlying the

operation of the pattern and probe-based aberration monitors. Finally, the main iterations of pattern and probe photomask designs are presented.

Chapter 3 investigates electric-field spillover methods for aberration detection, beginning with the traditional knife edge geometry. Electric-field spillover onto an interferometric probe is the underlying physical principle upon which the pattern and probe-based aberration monitors work. The second half of this Chapter explains how the geometry can be arranged so as to maximize the effect of spillover due to aberrations into a central probe in the design.

One goal is to make a rigorous determination that the optimum pattern for detecting an aberration is the inverse Fourier transform (IFT) of the aberration function itself. Chapter 4 uses the electromagnetic diffraction integral presented in Chapter 2 to establish a formal mathematical justification for the aberration monitor pattern layout. It shows that the optimum target for detecting any Zernike aberration using this scheme is as the inverse Fourier transform of the aberration function itself. This chapter goes on to discuss the predictive mathematical characteristics of the targets, as well as to show simulated results from the first generation of target design.

In Chapter 5, a divide and conquer framework is presented as a strategy for unraveling the complexities of target operation. The main thrust of this chapter is to use rigorous electromagnetic simulation to predict and explain the behavior of the targets. The results lead to a phasor model of the electric-field contributions to target intensity which is used throughout the rest of the thesis to explain differences between experimentally observed and ideal target performance. The important issues of as pattern

geometry, illumination conditions, mask making tolerances, and mask electromagnetic effects are also studied in this chapter.

The first systematic experimental evidence showing that the aberration monitors work in practice is presented in Chapter 6. Both Aerial Image Measurement System (AIMS™) results and photoresist exposures are used. In these initial experiments the major issues which limit the performance of the aberration monitors come to light. These “demons”, which include thick mask electromagnetic effects, high-numerical aperture polarization effects, the mitigation of high-numerical aperture effects by the photoresist, and mask error effects, were initially presented as dominant second-order effects in Chapter 5.

The experimental observations made in Chapter 6 help to guide redesigning of the targets for the more advanced experiments presented in Chapter 7. In this chapter the targets are not only redesigned but they are also decomposed into their constituent parts to characterize the performance-limiting factors found in the initial experiments. An in-depth study of the imaging of phase etched lines and dots is given, indicating a slight disagreement between simulation and experiment.

Chapter 8 gives the engineering assessment of the experimental results and quantitative analysis of the non-ideal second-order factors that dominate target performance. The effects of the individual physical phenomena, described in Chapters 6 and 7, upon the various components which constitute the aberration monitors are studied and it is found that, the dominant ones are the partial coherence of the illumination, mask edge electromagnetic effects, and high-numerical aperture polarization effects.

It is important to note throughout this thesis that, while the main developmental thrust has been for the conditions required by and offered for semiconductor photolithography,

the science herein is broadly applicable to any type of wave phenomena. Chapter 9 investigates how this technology might be applied in new and novel ways in measuring aberrations in human eyes.

2. Background

This chapter introduces the basic tool and concepts of image formation for projection printing, as well as the more advanced concepts of the point spread function and the effects of specific aberrations. Section 2.1 shows a simplified imaging system and explains the associated fundamental quantities of resolution, depth of focus, and partial coherence that influence image formation and pattern interaction. Section 2.2 introduces phase-shifting masks and discusses the challenges and opportunities inherent in their fabrication and use. Section 2.3 introduces the Zernike polynomials as the orthonormal basis used for the decomposition of circular lens aberration functions and shows how small aberrations perturb the fields arriving at the image plane. Section 2.3.3 establishes that perturbations due to aberrations change the side-lobe spillover fields from pinhole and line openings on the mask in a specific manner, depending upon the nature of the aberration. The effect of an aberration upon a printed pattern is highly dependant upon the exact positions and phases of all of the mask openings in a given neighborhood. It is this very effect which will be leveraged in order to create a new class of interferometric aberrometers based upon the pattern and probe method. This chapter concludes with a survey of common methods used to measure aberrations in imaging systems.

2.1. *Optical Imaging Theory*

The physics of optics was well established prior to 1900 and is applicable today. References to optics particularly relevant to projection printing include the texts of Hecht [10], Sheats and Smith [11], Goodman [12, 13], Mahajan [14], and Born and Wolf [15]. The author found the wave-optics and Fourier analyses of imaging systems in Goodman,

the discussion of the effect of wavefront variance upon imaging in Mahajan, and the use of the Zernike circle polynomials in Born and Wolf to describe aberrations particularly useful, and the linear electric-field perturbation model introduced in Born and Wolf and employed by Dirksen [16] is followed herein. The effects of small amounts of aberrations upon images are theoretically predicted by Born and Wolf and in [2] Brunner examines the impact of these different types of aberrations via simulation. In this thesis the theoretical considerations of Born and Wolf are used, complemented by the aberration notation of Mahajan in order to establish optimum patterns for detecting aberrations.

Experimentally, the behavior of the photoresist is an issue, along with the process context. The behavior of resist in general is discussed in [17, 18] and more extensive models are available in [19, 20, 21, 22]. While the photoresist has many interesting properties that influence how the final printed pattern looks on the wafer, these can be ignored for the most part as it is the aerial image which is of primary concern in this work. In this thesis photoresist is treated simply as a threshold detector, fully exposing and developing in a given area above a certain exposure dose.

2.1.1. Imaging System

A typical photolithographic imaging system is seen in Figure 2-1. The system consists of a narrowband light source radiating at a wavelength λ , an illumination condenser lens (L_1), an object (photomask) with the circuit pattern on it, projection optics (L_2 and L_3), and a substrate where the image is created.

In the illumination system, the source is placed at the focal length of the condenser lens and imaged into the pupil of the objective lens via L_2 . An aperture is placed in front

of the condenser lens to limit the lateral size of the source. The points in the source radiate incoherently, and in this special type of illumination setup, known as Köhler illumination, each of the source points produces a plane wave illumination of the mask. The benefit of Köhler illumination is that irregularities in the brightness distribution on the source do not cause irregularities in the intensity of the mask illumination. The ratio of the lateral size of the source image a to the entrance pupil size b (i.e., the pupil fill factor) is known as the partial coherence factor and is denoted by the symbol σ .

$$\sigma = \frac{a}{b}$$

Equation 2-1. The partial coherence factor.

The mask, which lies at the focal length of L_2 , diffracts the illumination fields into scattered orders, some of which are collected by L_2 , and relayed to the imaging lens. The fields incident upon the pupil plane are the Fourier transform of the mask geometry. The imaging lens then creates an image at the wafer by inverse Fourier transforming the orders that it collects. Because the pupil is finite in size, it low-pass filters the incident Fourier components, blocking those that carry the high spatial frequency information from the mask. The net result of this is that the orders carrying the information about sharp edges and corners on the mask fall outside of the pupil, causing corner rounding and possible interaction between nearby mask openings. Those orders which are just collected by the edge of the lens carry the highest spatial frequency information that can be used in image formation. The *sine* of the maximum angle of light incident upon the image plane from the imaging lens is commonly known as the system's numerical aperture.

$$NA = \sin(\theta_{i_max})$$

Equation 2-2. Numerical aperture of the imaging system at the image plane.

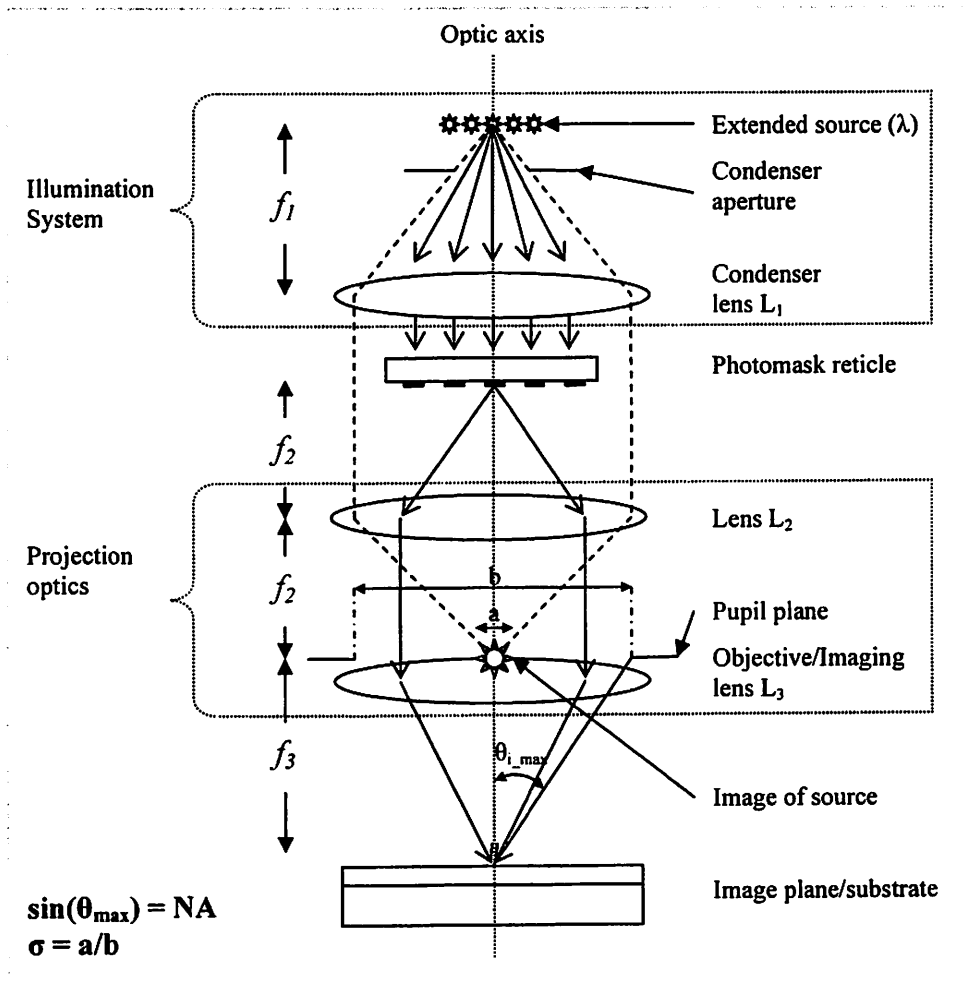


Figure 2-1. Schematic diagram of a projection optical lithography system.

2.1.2. Resolution, Depth of Focus, and Partial Coherence

The photolithographic imaging system is governed by two fundamental quantities: the resolution and the depth of focus. The system's resolution limit, given in Equation 2-3, indicates the smallest feature separation which can be achieved while still maintaining sufficient contrast to give distinguishable features when imaged [11, p. 199].

$$R = k_1 \frac{\lambda}{NA}$$

Equation 2-3. Resolution limit for photolithography.

Here k_1 is a scale factor which indicates the ease of a given lithographic process and $\frac{\lambda}{NA}$ is a commonly used unit of measure for features. The depth of focus is the amount by which the image plane may be moved and rays from the center and edge of the lens remain essentially in-phase. This value was calculated by Lord Rayleigh and is given in Equation 2-4.

$$DOF = \frac{\lambda}{2NA^2}$$

Equation 2-4. Depth of focus for photolithography

The third key parameter affecting the performance of an imaging system is the partial coherence of the illumination for the Köhler setup. The degree of coherence μ_{12} , describes the correlation of the electric-field disturbances at two points, P_1 and P_2 , in the image plane. The mutual coherence function μ is the Fourier transform of the source and in the case of circular or “top hat” illumination is

$$\mu_{12} = \frac{2J_1(2\pi r)}{(2\pi r)\sigma}$$

Equation 2-5. The degree of coherence of the electric-field disturbances at points P_1 and P_2 in the image plane [15, p. 575].

Because J_1 is the first-order Bessel function of the first kind, μ_{12} is seen only to be a function of the distance r between P_1 and P_2 , measured in units of $\frac{\lambda}{NA}$. The expression in Equation 2-5 is plotted in Figure 2-2 as a function of r for four different values of the

pupil fill factor σ . It is seen that for each, μ_{12} decreases steadily from a value of unity at $r = 0$. Thus, as P_1 and P_2 get further and further apart, the degree of coherence between the two steadily decreases, falling to zero when $r = 0.61 \frac{\lambda}{NA\sigma}$. While Born and Wolf use the (arbitrary) criteria that the maximum permissible departure from $\mu_{12} = 1$ is 12% in order to consider a circular area to be “almost coherently” illuminated, a less restrictive criteria is used in this work. For the discussion herein, a “coherence radius” is defined coinciding with the distance from the center to the first null of the μ_{12} function.

$$r_c = 0.61 \frac{\lambda}{NA\sigma}$$

Equation 2-6. The coherence radius is the distance from the center to the first null of the mutual coherence function.

As σ is decreased by stopping down the condenser aperture the coherence radius increases steadily, as indicated in the figure.

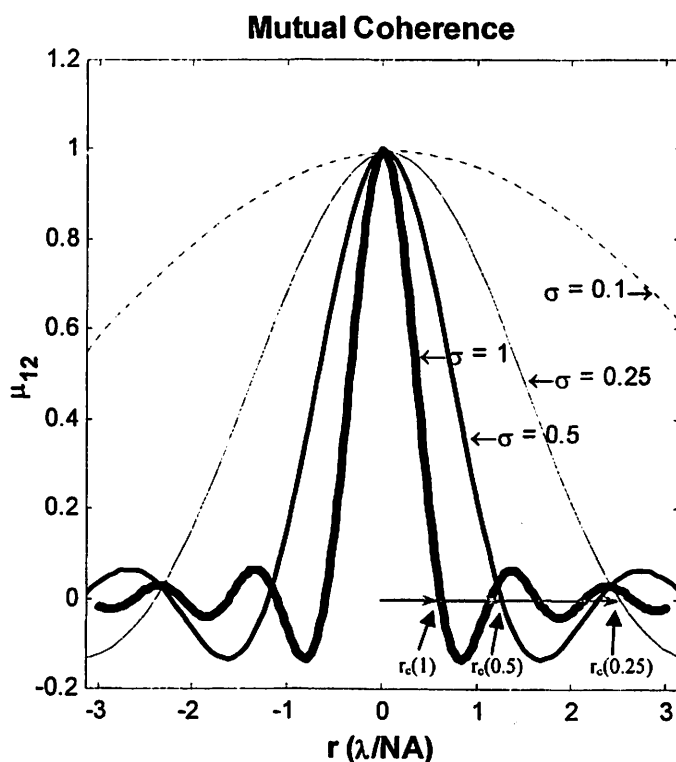


Figure 2-2. The mutual coherence between to points separated by a distance r in the image plane.

2.1.3. Diffraction Integral

The key relationship needed for the development of this thesis is the Fourier transform in electric-field between the mask and pupil planes. The theory of Fourier optics and imaging has been well established and a number of excellent references are available on the subject [11, 12, 15]. The Huygens Principle and the Fraunhofer (far-field) approximation allow the coherent image of any pattern to be calculated in the presence of aberrations using the diffraction integral introduced in [15] and shown in Equation 2-7 for a simple imaging system.

$$E_{Image}(x', y') = \frac{1}{\pi} \iint_{pupil} E_{Diff}(\rho, \theta) e^{\frac{jk}{z} [\rho \cos(\theta)x' + \rho \sin(\theta)y']} e^{jk\Phi(\rho, \theta)} \rho d\rho d\theta$$

Equation 2-7. Electromagnetic diffraction integral for a simple imaging system.

Here, (x', y') are image plane coordinates and (ρ, θ) are lens pupil coordinates with the pupil radius normalized to one. The parameter k is $\frac{2\pi}{\lambda}$. The limits of integration extend over the circular pupil with $0 \leq \theta < 2\pi$ and $0 \leq \rho \leq 1$. $E_{Diff}(\rho, \theta)$, represents the fields generated by the object and incident upon the lens aperture. More specifically, $E_{Diff}(\rho, \theta)$ is the diffraction spectrum of the object normalized to unity [12, p. 145, 15, p. 428] $e^{\frac{jk}{f_3}[\rho \cos(\theta)x' + \rho \sin(\theta)y']}$ indicates a phase difference induced across the aperture giving the lensing action. Finally, $e^{jk\Phi(\rho, \theta)}$ represents the effects of aberrations in the lens aperture, where $\Phi(\rho, \theta)$ is the optical path difference (OPD) across the pupil arising from the presence of aberrations. This formulation of the electric-field distribution at the image plane from the waves in the pupil is of fundamental importance in the development of this research.

It is straightforward to see that if $E_{Diff}(\rho, \theta) = 1$, as is the case when imaging a sub-resolution pinhole opening, and $e^{jk\Phi(\rho, \theta)} = 1$ in Equation 2-7, that the point spread function is actually the two-dimensional Fourier transform of the unaberrated circular pupil, given by

$$E_{Image}(x', y') = e^{jkf_3} e^{jk\left(\frac{x'^2 + y'^2}{2f_3}\right)} \frac{\pi NA^2 f_3}{j\lambda} \left[2 \frac{J_1(kNA\sqrt{x'^2 + y'^2})}{kNA\sqrt{x'^2 + y'^2}} \right].$$

Equation 2-8. The point spread electric-field function of an unaberrated pupil.

The intensity distribution is simply the time average squared of the electric-field distribution, given by

$$I_{Image}(x', y') = \langle E_{Image}(x', y') E_{Image}^*(x', y') \rangle = \left(\frac{\pi NA^2 f_3}{\lambda} \right)^2 \left[2 \frac{J_1(kNA\sqrt{x'^2 + y'^2})}{kNA\sqrt{x'^2 + y'^2}} \right]^2.$$

Equation 2-9. Intensity distribution at the image plane for an unaberrated pupil.

Again, J_1 is the first-order Bessel function of the first kind, order 1. The form of the Fourier transform used herein is given by

$$\mathfrak{F}\{g\} = \int_{-\infty}^{\infty} \int g(x, y) e^{-j2\pi(f_x x + f_y y)} dx dy$$

Equation 2-10. Form of the two-dimensional Fourier transform used herein.

where $g(x, y)$ is the original function and $\mathfrak{F}\{g\}$ is the Fourier spectrum of that function.

When aberrations are present $\Phi(\rho, \theta)$ is non-constant and the electric-fields arriving at the image plane are perturbed from their original values. Defocus is an excellent pedagogical example of how an aberration can affect imaging. Defocus is particularly interesting because it can be treated as a system or experimental parameter that can be changed simply by moving the object or the image plane along the optic axis. Aberrations are best understood by taking a wavefront analysis approach.

For an unaberrated lens, a true point source in object space results in a perfect converging spherical wavefront at the exit pupil of the lens, creating a diffraction-limited spot in the image plane. Aberrations are simply deviations of this wavefront from perfect sphericity. As seen in Figure 2-3, the difference between the real and ideal wavefronts can be measured in terms of the OPD. For a point source, the ideal spherical wavefront leaving the lens is shown as a dashed line. This wavefront comes into focus at the original image plane. If the image plane is moved away from the lens by an amount δ ,

then this wave no longer comes into focus, but rather a defocused wavefront (one with a larger radius of curvature) does. This introduces an error in the optical path distance to the image plane with respect to the original reference wavefront. This error increases with pupil radius and has the overall effect of blurring the image of the point.

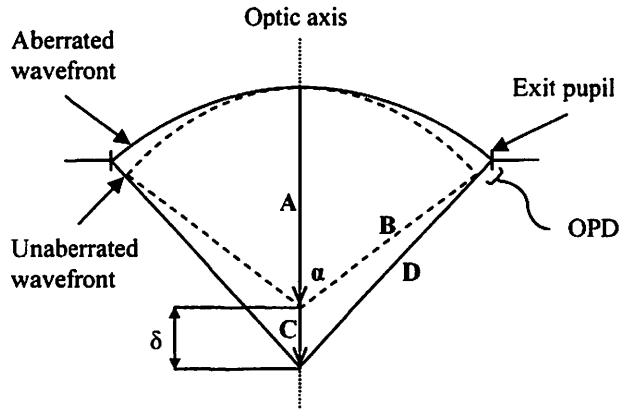


Figure 2-3 The effect of defocus.

Describing the position in the exit pupil by an angle α , the OPD between the real and ideal wavefronts can be related to the amount of defocus (δ) as $OPD = \delta(1 - \cos \alpha)$. After a little bit of geometry, this can be converted to the $\Phi(\rho, \theta)$ form used in the diffraction integral (Equation 2-7)

$$\Phi(\rho, \theta) \approx \delta \left(1 - \sqrt{1 - (\rho NA)^2} \right)$$

Equation 2-11. Lens pupil OPD function for defocus.

where the \approx symbol is used because the paraxial approximation is invoked. The diffraction integral then becomes

$$E_{Image}(x', y') \approx \frac{1}{\pi} \iint_{pupil} E_{Diff}(\rho, \theta) e^{\frac{jk}{f_3} [\rho \cos(\theta)x' + \rho \sin(\theta)y']} e^{jk\delta(1 - \sqrt{1 - (\rho NA)^2})} \rho d\rho d\theta.$$

Equation 2-12. Diffraction integral with defocus aberration.

2.1.4. Point and Line Spread Functions

The fundamental characteristic of a linear imaging system is its impulse response, or point spread function. The electric-field point spread function generated by an ideal diffraction-limited imaging system is the well-known Airy function, given in Equation 2-8, which is simply the Fourier Transform of the unaberrated pupil. The upper right part of Figure 2-4 shows the SPLAT [23] simulated electric-field profile of a sub-resolution $0.4 \frac{\lambda}{NA} \times 0.4 \frac{\lambda}{NA}$ square pattern in an ideal diffraction-limited imaging system with highly coherent illumination. Because SPLAT gives the intensity profile at the image plane and because any side-lobes are relatively small with respect to the central peak, the square root of the intensity is plotted in order to show the fine detail in the magnitude electric-field distribution. The lower two plots are cut-lines through the actual electric-field and intensity distributions at the image plane.

The most striking feature in the plot is that the square opening in the object actually images as a circle. This is because the feature is sub-resolution and those scattered orders carrying the high-spatial frequency information from the mask are filtered out by the spatially-limited pupil in the imaging system. Observing the plot of the electric-field incident upon the image plane, it is seen that the first zero-crossing of the electric-field occurs at $0.61 \frac{\lambda}{NA}$, which corresponds to the first null in the Airy intensity pattern. The

first side-lobe occurs at a radius $0.82 \frac{\lambda}{NA}$. While it appears as a minimum in the electric-field, this side-lobe is a small peak in intensity in the lower right hand plot.

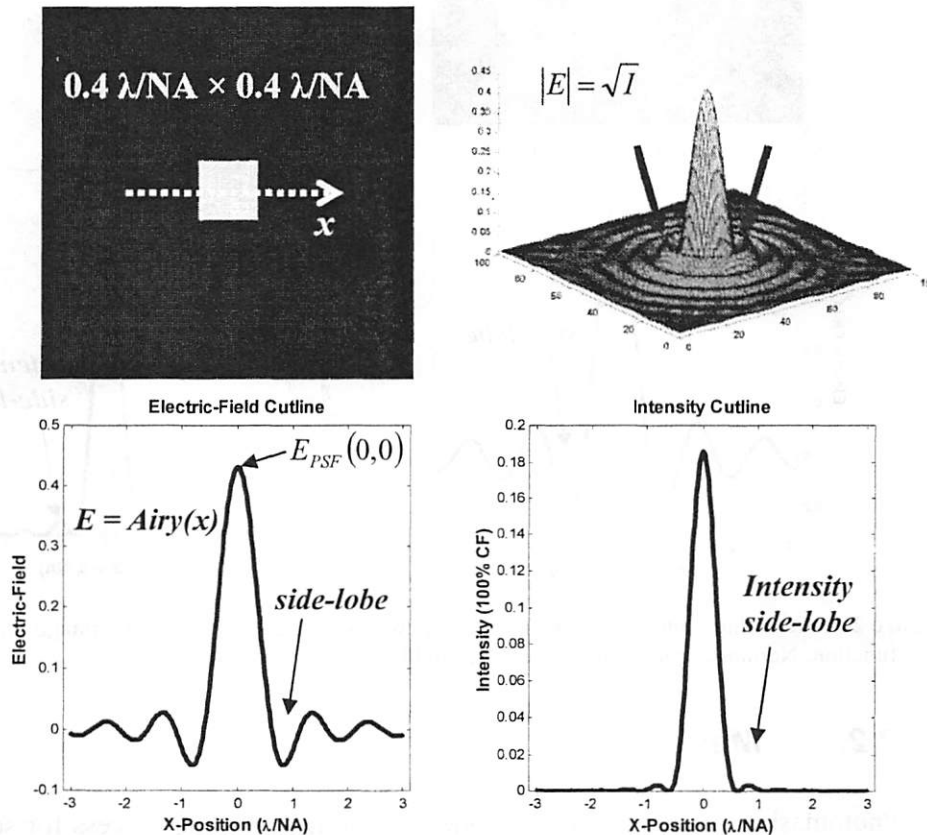


Figure 2-4. The magnitude of the diffraction-limited electric-field point spread function for an unaberrated imaging system is the Airy function. The first side-lobe ring is indicated by the arrows. Normalized intensity and electric-field.

Figure 2-5 shows the simulated electric-field profile of a line which is $0.6 \frac{\lambda}{NA}$ in width. The mask pattern is shown in the upper left and cut-lines through the electric-field and intensity distributions at the image plane are shown below. While the electric-field from the small probe behaves as the Airy distribution, that of the line behaves as the *sinc* function.

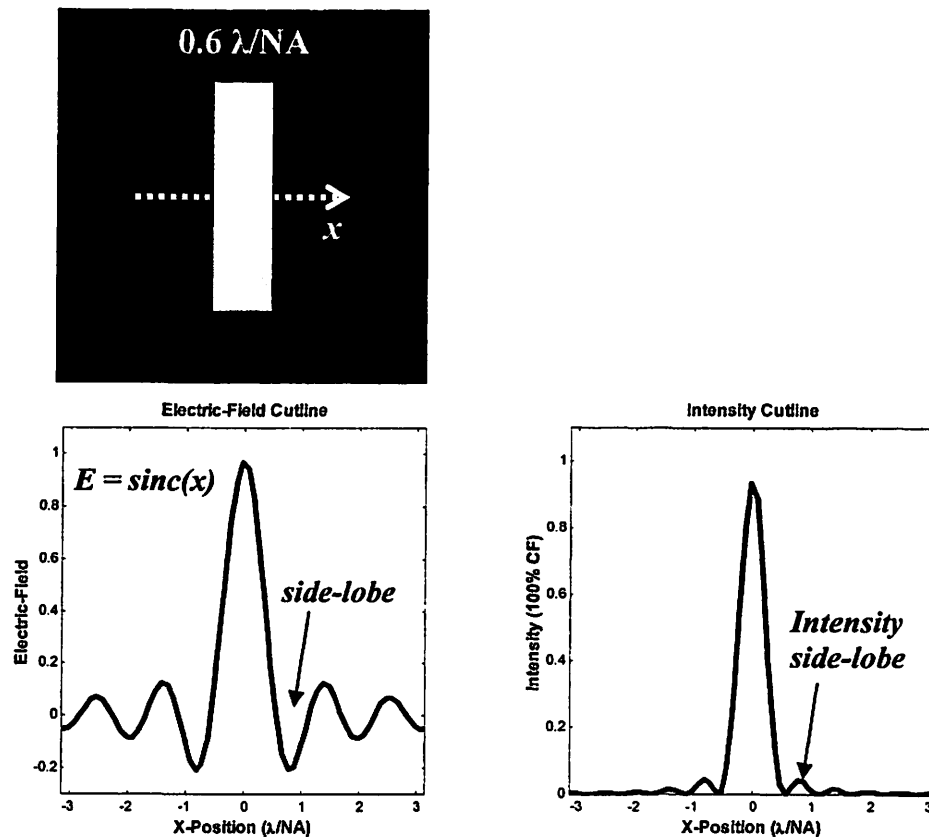


Figure 2-5. An isolated line in a dark field object creates an electric-field at the image plane given by the *sinc* function. Normalized intensity and electric-field.

2.2. Masks

Photomasks are an integral component of the lithographic process for semiconductor manufacturing. A mask generally consists of a thin layer of chrome (~ 100 nm) atop a thick glass substrate. Feature openings are etched into the chrome, allowing light to pass through in certain areas. This yields an electric-field profile just after the mask which is a cookie cutter cutout of the mask pattern. These fields scatter from the mask openings and undergo Fourier transforms and filtering as they pass through the imaging system. One of the key issues in this thesis is to determine whether or not it is possible to make the mask precisely enough to use it as a precision instrument to characterize the imaging system.

2.2.1. Phase-Shifting Masks and Opportunities

In the effort to improve the resolution of lithographic imaging systems, all three of the factors in Equation 2-3, k_1 , λ , and NA, have been pushed to their limits. While λ has decreased and NA's have increased steadily over the years, k_1 has been reduced by the use of off-axis illumination, sub-resolution assist features, post-exposure ashing and etching, and perhaps most importantly, phase-shifting masks. A phase-shifted mask opening is achieved by first removing the chrome in a given region and then digging a trench in the glass via wet and/or dry etching. The fields which exit the mask via an etched opening are phase-shifted with respect to light exiting through a simple opening in the chrome because of the difference in refractive index between the glass and the surrounding medium (generally air). The amount of the phase shift, measured in wavelengths is given by

$$\text{Phase shift } [\lambda] = d \left(\frac{n_1}{n_2} - 1 \right)$$

Equation 2-13. Equation for determining the phase shift of the fields exiting an etched trench.

where d is the etch depth, n_1 is the refractive index of the glass, and n_2 is that of the surrounding medium.

2.2.2. PSM Realization Issues

While the use of phase-shifting masks has come increasingly into vogue, there are many drawbacks to their use. The most obvious hurdle is the complexity of their fabrication and their resultant great cost. While the industry has historically been dominated by the use of binary masks, which require only a single processing cycle to

create the circuit patterns in the chrome, phase-shifting masks require multiple processing cycles to create the chrome openings and then to selectively phase etch certain of these regions. As a result, it is not uncommon for a phase shift mask to cost at least twice as much as a binary mask.

Secondary to the financial concerns is the significant intensity difference seen at the image plane between phase-shifted and non phase-shifted openings of the same size. This “intensity imbalance” is due to the inherent topography of phase-shifted regions and was first observed by Pierrat, Wong, and Vaidya via rigorous electromagnetic simulation using the time-domain finite-difference algorithm TEMPEST [24]. Intensity imbalance can be very important in lithography because phase-shifted regions tend to print as if they were smaller than they truly are.

2.3. *Aberrations*

2.3.1. The Circle Polynomials of Zernike

The OPD between the real and ideal wavefronts over a two-dimensional circular pupil is measured in μm , λ , or phase and can be a complicated function of both ρ and θ . It is extremely useful for analysis to break the wavefront up into an orthogonal set of basis functions. The circle polynomials introduced by Fritz Zernike in the early 1900s [25] are commonly used to describe optical wavefront aberrations. Excellent references are available for learning about Zernike circle polynomials and wavefront aberrations in the previously mentioned references, as well as in [26]. Zernike polynomials are expressed in terms of polar coordinates within the pupil and are of the form

$$Z_{n,m}(\rho \sin \theta, \rho \cos \theta) = R_{n,m}(\rho) e^{im\theta},$$

Equation 2-14. Form of the Zernike circle polynomials.

where $R_{n,m}(\rho)$ is a polynomial dependant only upon the normalized pupil aperture radius, ρ , and $e^{im\theta}$ depends only upon the angle, θ , within the pupil plane. The Zernike polynomials form an orthonormal set over the unit circle so, just as any well-behaved function in one dimension can be decomposed into *sines* and *cosines* via a simple Fourier transform, any well-behaved function over the unit circle can be decomposed into Zernike polynomial terms. Generally, 30 to 60 Zernike terms are used to describe wavefront aberrations in photolithographic tools. A list of the mathematical equations describing the first 36 Zernike terms is found in Appendix A. The first nine Zernike terms of interest for lithography are plotted in Figure 2-6 and their mathematical equations are inset. Here the subscript pairs adhere to the convention of Born and Wolf. These terms represent those aberrations which tend to dominate image degradation in lithography. The plots show that some of the Zernike polynomials vary both radially and angularly while some of the terms, such as defocus and spherical, are rotationally-symmetric. Some of the terms, including all of the rotationally-symmetric terms and astigmatism, are even functions within the pupil, while terms such as coma and trefoil are odd functions.

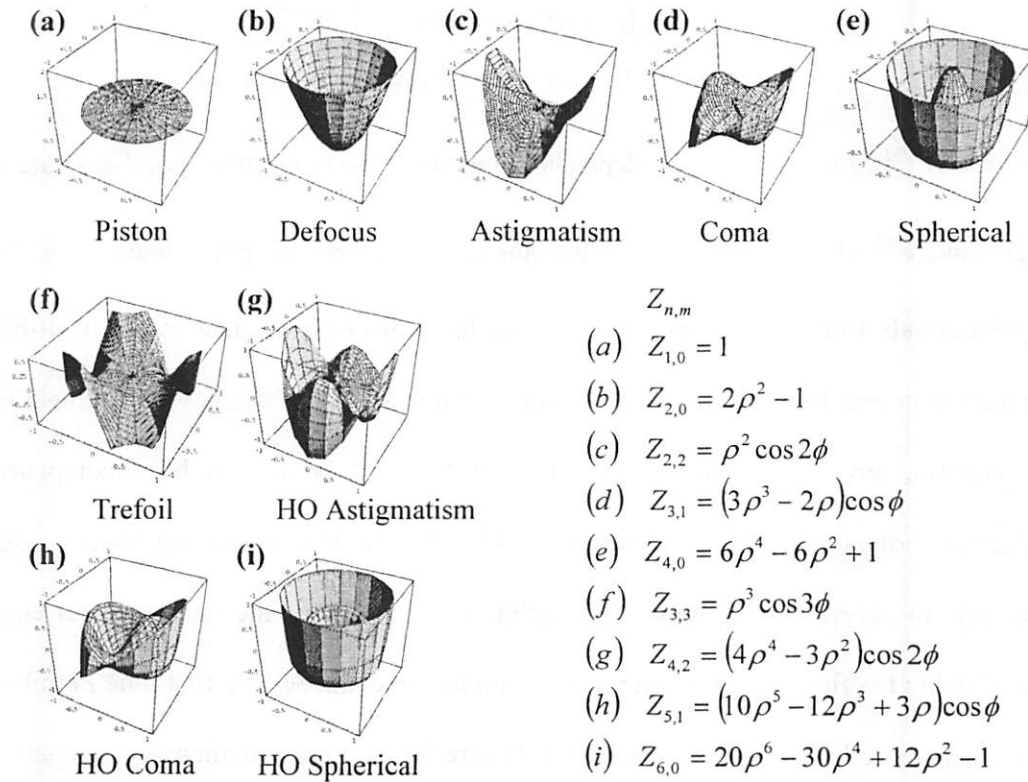


Figure 2-6. Graphical representation of first nine Zernike terms of interest for lithography. Inset is the mathematical equation for each.

In general, any well-behaved complex function on the unit circle, can be decomposed into a linear combination of Zernike polynomials. Following the labeling convention of Born and Wolf the expansion is

$$f(\rho, \theta) = \sum_{n=1}^{\infty} \sum_{m=0}^n C_{n,m} Z_{n,m}(\rho, \theta),$$

Equation 2-15. Zernike expansion of any well-behaved real-valued function on the unit circle.

where $C_{n,m}$ is the complex coefficient of the term $Z_{n,m}$ in the expansion. The OPD function of a lens is a real function and therefore has coefficients which are real.

2.3.2. Aberration Levels and Impact in Imaging Systems

Following Equations 2-8 and 2-9 for the unaberrated pupil, and using the fact that

$$\lim_{\rho \rightarrow 0} \frac{J_1(\rho)}{\rho} = \frac{1}{2} \quad [27],$$

in the limit that the distance from the optic axis approaches zero,

the electric-field and intensity at the origin in the image plane are

$$E_{Image}(0,0) = e^{jkf_3} \frac{\pi NA^2 f_3}{j\lambda} \quad \text{and} \quad I_{Image}(0,0) = \left(\frac{\pi NA^2 f_3}{\lambda} \right)^2.$$

Because the Bessel function of the first kind, order one decreases regularly from its maximum value of unity at the origin, this is the peak of the intensity spread function for an unaberrated lens. A common metric of lens quality, known as the Strehl ratio [11, p. 225], is the peak intensity of the aberrated spread function divided by that of an equivalent, but unaberrated lens. A perfect diffraction-limited lens has a Strehl ratio of one while that of an aberrated lens is less than one.

For small mask openings of lateral size $l \leq 0.4 \frac{\lambda}{NA}$, the peak intensity is well-approximated in [28] by

$$I_{peak} = 8.5l^4.$$

Equation 2-16. Peak point spread intensity for a small mask opening.

Aberrations cause the peak intensity value to decrease, yielding a Strehl ratio of less than one. The peak intensity of the aberrated lens can be determined either experimentally or via simulation. It can also be calculated for small amounts of aberration, if the aberration

function $\Phi(\rho, \theta)$ is known, as in Equation 2-12. In general, the Strehl ratio decreases quadratically with the amount of defocus aberration present in the system [15, ch. 8].

A high-quality microlithography lens may have a Strehl ratio of up to 97.5%. Mahajan shows that for small aberrations the Strehl ratio is independent of the specific nature of the aberration and, for values greater than 10%, is well-approximated by the empirical formula

$$SR \approx \exp\left[-4\pi^2 \sum_{n=1}^{\infty} \sum_{m=0}^n A_{n,m}^2\right],$$

Equation 2-17. Equation for determining Strehl ratio in the presence of small amounts of aberration.

where $A_{n,m}$ is the coefficient of each individual Zernike aberration term in the wavefront

expansion and $\sum_{n=1}^{\infty} \sum_{m=0}^n A_{n,m}^2$ is the total wavefront variance. The Strehl ratio is plotted as a

function of total rms wavefront variance in Figure 2-7.

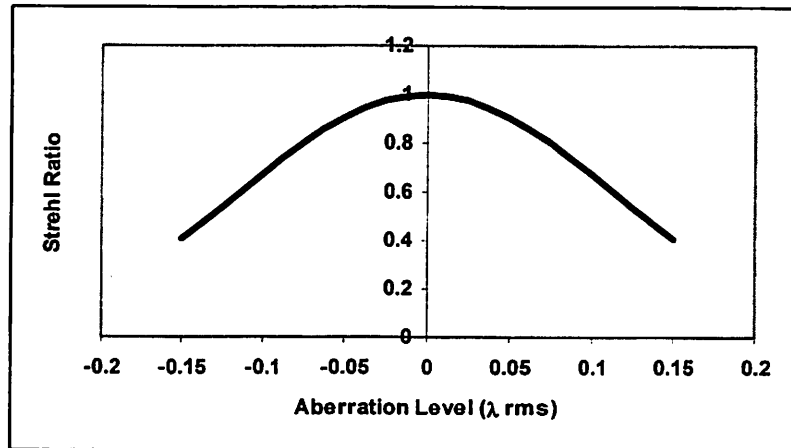


Figure 2-7. Plot of the Strehl ratio as a function of the rms wavefront error.

If, for a lens with a Strehl ratio of 97.5%, all of the variance results from a single Zernike term, $Z_{n,m}$, then the coefficient of that term, $A_{n,m}$, is 0.025λ rms. It is thus necessary to measure aberrations to an accuracy of 0.01λ rms in order to reliably and usefully characterize such good lenses.

2.3.3. Aberrated Point Spread Electric-Field

Following Born and Wolf, for small amounts of aberration, $\Phi(\rho, \theta)$ is small and the $e^{jk\Phi(\rho, \theta)}$ term in the diffraction integral (Equation 2-7) can be expanded in a Taylor series to yield $1 + jk\Phi(\rho, \theta)$. (See Appendix B for the limits of validity of this expansion). Substituting this back into the integral it is seen that the electric-field at the image plane is simply the superposition of the ideal, diffraction-limited, fields and a set of perturbation fields which derive directly from the form of the $\Phi(\rho, \theta)$ aberration term.

$$E_{\text{image}}(x', y') = \frac{1}{\pi} \left[\iint_{\text{pupil}} E_{\text{ideal}}(\rho, \theta) e^{jk[\rho \cos(\theta)x' + \rho \sin(\theta)y']} \rho d\rho d\theta + jk \iint_{\text{pupil}} E_{\text{ideal}}(\rho, \theta) e^{jk[\rho \cos(\theta)x' + \rho \sin(\theta)y']} \Phi(\rho, \theta) \rho d\rho d\theta \right]$$

Equation 2-18. Equation showing that the aberrated electric-field at the image plane is a linear superposition of the ideal fields and a set of perturbation fields.

Analysis by Fukuda, *et al.* [29] indicates that odd aberrations produce electric-field perturbations that are real while even aberrations produce perturbations that are imaginary.

The effects of different aberrations on the electric-field spread function are seen in the plots in Figure 2-8. A typical wavefront variance for a good projection lens is about 0.02λ rms and these plots show the magnitude of the point spread electric-field distribution for 0.02λ rms of (a) spherical, (b) coma, (c) astigmatism and (d) trefoil aberration. The

results show that each aberration has a unique effect upon the side-lobe spillover. Spherical aberration causes a focus shift that depends upon the specific feature being imaged. Coma is associated with image asymmetry and pattern-dependent image shift. Astigmatism, which is a familiar ophthalmological aberration, causes orientation-dependent focus shifts. Finally, trefoil aberration causes imaging anomalies which are associated with threefold symmetry. There are an infinite number of Zernike aberration terms, but these few indicate the richness in variation and pattern sensitivity of even just a small set.

The plots for coma and trefoil aberration show pronounced side-lobes with first and third order rotational symmetry associated with their $\cos(1\theta)$ and $\cos(3\theta)$ variations, respectively. Astigmatism has two pairs of symmetrical side-lobes due to its $\cos(2\theta)$ variation with these side-lobes being only of moderate size. Spherical aberration has a broad, rotationally invariant side-lobe associated with its constant angular behavior. Table 2-1 shows quantitative values for the peak electric-field and the change in side-lobe electric-field for the unaberrated case and for each of these aberrations, plus defocus.

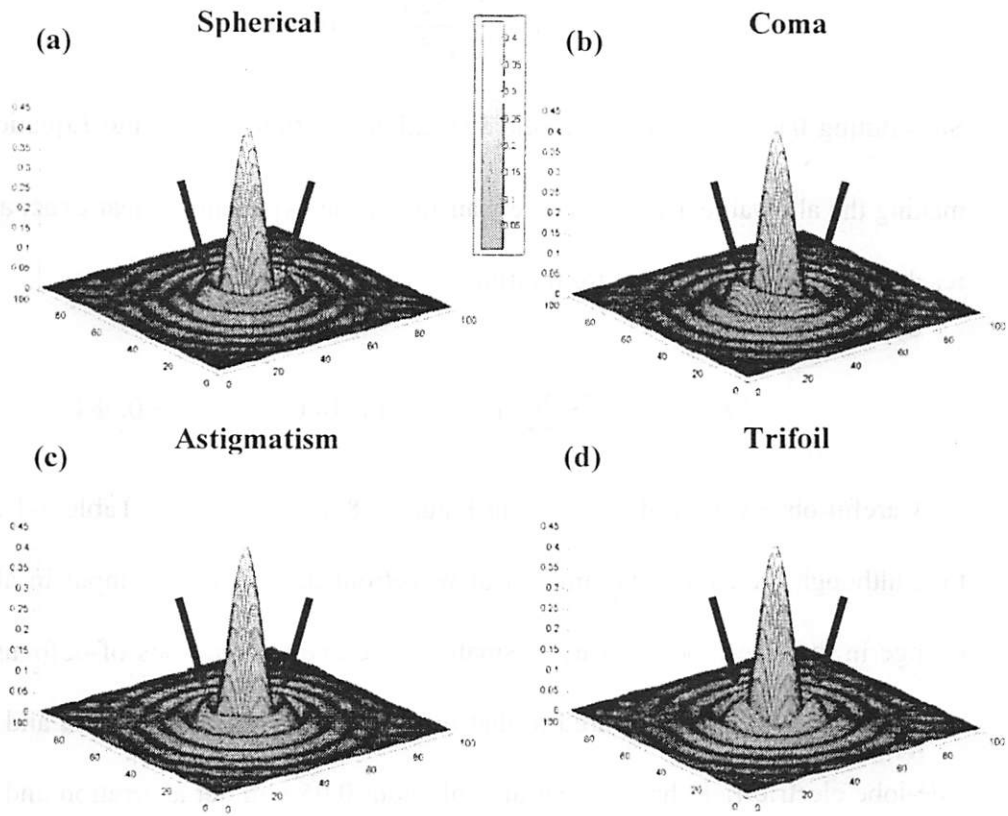


Figure 2-8. Simulated intensity spread functions given 0.02λ rms of (a) spherical, (b) coma, (c) astigmatism, and (d) trefoil aberration. The arrows indicate the first side-lobe.

Zernike aberration	Left side-lobe	Center	Strehl ratio	Right side-lobe
None	-0.0502 (reference)	0.4357	1.000	-0.0502 (reference)
Defocus	+0.0017 (change)	0.4322	0.984	+0.0017 (change)
Spherical	+0.0039 (change)	0.4323	0.984	+0.0039 (change)
Coma	+0.0226 (change)	0.4324	0.985	-0.0248 (change)
Astigmatism	-0.0019 (change)	0.4325	0.985	-0.0019 (change)
Trefoil	+0.0208 (change)	0.4325	0.985	-0.0229 (change)

Table 2-1. Change in the magnitude point spread electric-field levels at the left side-lobe ($0.84 \frac{\lambda}{NA}$ from the center), the center, and the right-side-lobe ($0.84 \frac{\lambda}{NA}$ from the center) for 0.02λ rms of the given Zernike terms.

It is noted that the central peak field drops to almost the same value (0.4324), regardless of the aberration used in the simulation. The Strehl ratio is thus given by

$$SR = \left(\frac{0.4324}{0.4357} \right)^2 = 0.985.$$

Substituting 0.02λ rms as the single aberration coefficient $A_{n,m}$ into Equation 2-12 and making the allowable Taylor series expansion of the exponential, near exact agreement is reached for the value of the Strehl ratio.

$$SR \approx 1 - 4\pi^2 \sum_{n=1}^{\infty} \sum_{m=0}^n A_{n,m}^2 = 1 - 4\pi^2 (0.02 \lambda \text{ rms})^2 = 0.984$$

Careful observation of the plots in Figure 2-8 and the data in Table 2-1 also reveals that, although the same total amount of wavefront deformation is input in all cases, the change in the side-lobe intensity is small for the even aberrations of defocus, spherical, and astigmatism when compared to that for the odd aberrations of coma and trefoil. The side-lobe electric-field has a magnitude of about 0.05 without aberration and changes by about 0.02 for coma (0.0226) and trefoil (0.0208), but only by about 0.002 for defocus (0.0017), spherical (0.0039), and astigmatism (0.0019).

Because the fields incident upon the image plane in the unaberrated case are purely real and the perturbations to these fields due to odd aberrations are also purely real, the two fields add collinearly in the complex plane, as seen in the left side of Figure 2-9. In the case of even aberrations however, seen in the right side of the figure, the perturbation field is purely imaginary and the electric-field contributions add in quadrature. It is this type of diagram and analysis that was used to determine that the perturbation to the spillover fields for the knife edge varies linearly with the amount of aberration in Figure 1-4.

The electric-field plots for Figure 2-8 and the numbers for Table 2-1 were obtained by taking the square root of the intensity distributions generated by SPLAT. Therefore, the effect of the perturbation on the side-lobes for even aberrations appears to be much less than that for odd aberrations. In reality however, the magnitude of the electric-field perturbation is approximately the same whether the aberration is odd or even. The total electric-field arriving at the side-lobe position can be represented mathematically. Following the form of Equation 2-18 the total electric-field is given by

$$E_{tot} = E_i + jE_{pert}$$

Equation 2-19. The total electric-field contribution at the first side-lobe position with aberration present.

where E_i is real and -0.0502. For odd aberrations, $E_{pert} \approx 0.021$ is exactly equal to the change in electric-field ΔE . For even aberrations, however, the same amount of perturbation must be added in quadrature to the unaberrated fields, predicting $\Delta E \approx 0.0038$, which is nearly equal to that calculated in Table 2-1 for spherical aberration, and only a factor of two different than the values calculated for defocus and astigmatism. Thus, while the change of the side-lobe peak is linear for odd aberrations, the central peak and the side-lobe peak for even aberrations have a quadratic dependency on the amount of aberration.

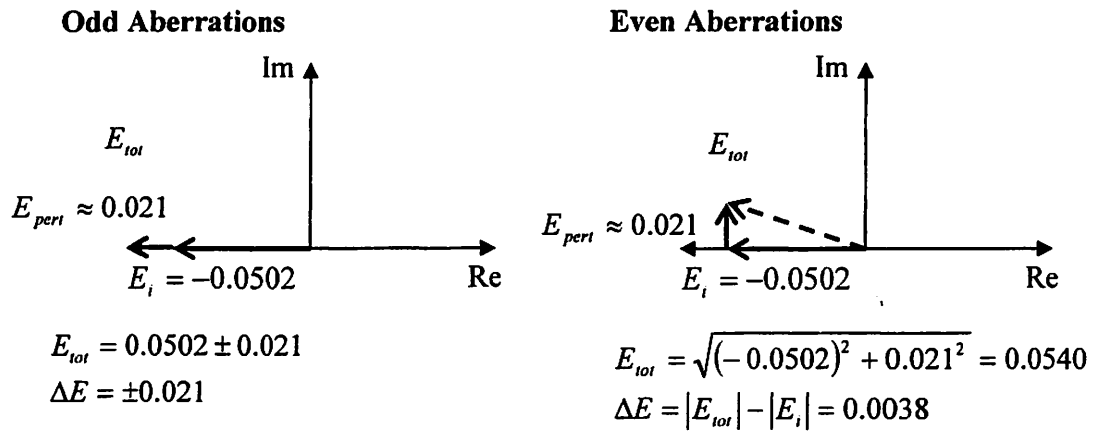


Figure 2-9. Argand diagrams showing the real and imaginary electric-field contributions at the first side-lobe position of the point spread function given an even or an odd aberration.

This kind of field perturbation model is used in this thesis to develop a new pattern and probe-based approach for measuring aberrations. With the basic properties of the Zernike aberration terms established, patterns will begin to be generated using the concepts of electric-field spillover and reciprocity. After beginning to build the patterns in this manner, a unified theory of pattern design with formal mathematical justification will be presented. This is followed by a discussion of experimental results and observations which have lead to improvement of target design.

2.3.4. Survey of Methods for Measuring Aberrations

The field of aberrometry and aberration correction has a rich history in the field of traditional optics and astronomy. Semiconductor projection printing presents unique challenges, as the resolution and across chip linewidth variation requirements are so great that aberrations must be measured to levels below 0.01λ rms. Garza notes that, for the typical level of aberration in a microlithographic exposure tool, the sensitivity to layer overlay error and deleterious effects such as “pinch off” of line features, increase with

respect to the unaberrated case. An excellent overview of effects of aberrations in projection printing has been given by Brunner [2]. In an effort to meet this challenge, a number of techniques for measuring aberrations have been invented. A large number of photoresist-based techniques were recently classified by Kirk [30]. Common methods are classified herein according to the physical principle upon which they operate. These principles are:

- 1) Sub-pupil image shift
 - 2) Wavefront splitting (Shack-Hartmann)
 - 3) Image distortion
 - 4) Wave phase interferometry (fringe interferometry)
- and
- 5) Spillover interferometry

Aberrometry of the Human Eye

Aside from lithographic exposure tools, there are a number of other imaging systems that are of great interest. Among the most common of these is the human eye. While everyone who has prescription glasses or contact lenses is familiar with the tests used to determine the imaging quality of their eyes, ophthalmological aberrations are significantly greater than those found in lithography, resulting in significantly lower Strehl ratios. Aberrometry of eyes is difficult because the natural processes of accommodation, dilation, and tear film production, as well as the simple passage of time, all change the amount and distribution of the aberrations in the eye. Furthermore, because the image plane (retina) is essentially inaccessible, significant effort must be expended to

obtain quantitative data on the level of aberrations. Nonetheless, a great deal of research [31, 32, 33, 34] has been done in the field of adaptive optics in order to image the retinal plane and systems have been built which can obtain aberration data on living subjects. Despite the presence of significant amounts of other aberrations, only defocus and astigmatism are traditionally corrected in order to yield 20/20 vision. Today however, commercial tools are available from Wavefront Sciences, Inc. and Visx, Inc., based upon the Shack-Hartmann interferometer, which can be used to measure the higher-order aberrations of the eye and provide the information needed for correction via wavefront-guided laser ablation of the cornea.

Phase shift focus monitor

The phase-shift focus monitor [35, 36, 37, 38, 39, 40, 41, 42], developed by Brunner at IBM and currently sold by Benchmark Technologies, works on the principle that non-180° phase shifted regions can cause image asymmetries through focus. By placing a 90° phase shifter next to a chrome line on the photomask, the imaginary component of the electric-field from the opening is maximized. This purely imaginary field interacts strongly with the purely imaginary perturbation to the field due to the defocus aberration, causing the image of the line edge to shift. This feature shift on the wafer can be measured in a SEM and the technique yields an accuracy of better than 0.004λ rms in measuring focus. However, defocus is only one of the many even aberrations which cause an imaginary perturbation to the electric-field. This technique therefore is most likely plagued by the issue of measurement contamination by even aberrations other than defocus.

“InspecStep™ Interferometer”

The “InspecStep™ Interferometer” from Litel Instruments, is a commercialized tool for measuring aberrations in lithographic exposure tools [43, 44]. It is based upon the Shack-Hartmann interferometer for measuring local wavefront tilt and works by splitting the image from a special test mask into a “reference” image and an “encoded” image. The light which is used to image the pieces of the reference pattern fills the entire pupil, thereby averaging out most of the effects of aberrations. Specially designed aperture restrictions cause the light used to image the pieces of the encoded pattern to pass through and sample individual points within the pupil. In doing so, these rays are strongly influenced by the local wavefront slope (aberration) at given points within the pupil. This translates to a shift of the encoded image with respect to the reference image that is directly proportional to the local wavefront slope. The shift, which can be measured in a SEM, indicates the wavefront slope at that position in the lens and can be integrated to give the actual wavefront. While this method can report the first 28 Zernike terms for the lens with better than 0.016λ rms accuracy and good repeatability, it is extremely expensive as each test mask must be individually characterized and calibrated for the software analysis package.

ARTEMIS®

The ARTEMIS® (Aberration Ring Test Exposed at Multiple Illumination Settings) technique, developed at ASML and based upon work done by Dirksen, *et al.* [16, 45], consists of imaging a circular 180° phase object in a clear field, roughly $\frac{\lambda}{NA}$ in diameter at multiple NA and σ settings. When no aberrations are present, SEM images of exposed

photoresist show that the feature prints as a perfect donut of resist due to the phase edge created by the 180° circular edge on the mask. When aberrations are present however, the resist image gets distorted. Fourier analysis of the shape is used to extract Zernike aberration coefficients. While this technique shows a sensitivity of 0.007 λ rms in the measured wavefront aberrations, it gives only the weighted sum of aberrations with same θ dependence in the lens. This technique is related to the interferometric pattern and probe-based aberration monitors in that, in their theoretical analysis, small aberrations add a linear term to the final aerial image intensity.

Phase Grating

A three-beam interferometer based upon use of a photomask with equal lines of 0° and 90° phase has been used to measure both focus and spherical aberrations [46]. The interferometer works by imaging the phase structure into a highly absorbing photoresist and measuring the resulting relief grating with a dark-field optical microscope and a CCD array. The gratings are placed at regular angular intervals in order to sample the lens in many different locations. By measuring the brightness of the gratings, the focus and spherical aberrations can be measured to approximately 0.0005 λ rms and 0.0001 λ rms, respectively. Because this is a multi-beam interference technique, it is more like photoresist characterization techniques [47] than like other techniques used for aberrometry.

Other Techniques

There are many more schemes used to measure various aberrations. Other techniques of aberrometry include phase-shifting point diffraction interferometry [48], direct printing

of the point spread function into photoresist [49], and a technique which measures focus using line-end metrology [50].

Half tone octagonal knife edge

Work particularly relevant to understanding the operation of the pattern and probe-based aberration monitors is the use of an octagonal knife edge feature to measure aberrations [51, 52]. In this method, developed at Hitachi, Ltd., a 180° phase-shifted octagonal opening is made in a 6% transmitting mask and measurements of the exposure sensitivity of side-lobe artifacts of the knife edges are made. By comparing the imbalances in exposure energy between sets of side-lobes from the feature edges to results from simulation, the coma and trefoil aberrations have been measured to 0.01 λ rms. This work is of particular interest herein because the 6% transmitting region around the opening provides an interferometric reference electric-field upon which the electric-field side-lobes add coherently. This will be discussed in greater detail in Section 3.1.

Pattern and probe-based

Neureuther, Hotta, and Adam [53] studied the interaction between mask features and nearby defects in the presence of aberrations. They established that for small amounts of aberration, the side-lobes of small features in a dark field tend to grow linearly with the amount of aberration, while the peak intensity of a dark field feature or the minimum intensity of a clear field feature varies as the square of the amount of aberration. Further reference material on this subject is available in [54, 55, 56]. They noted that by placing a programmed “defect” or a probe at the location of the side-lobe spillover of a feature, the

intensity change at the side-lobe position due to aberration can be greatly enhanced due to the interferometric nature of the electric-field provided by the probe.

Building upon the concept of side-lobe printability, the effect of electric-field spillover can be magnified by wrapping the feature edge around a small opening (probe) in a dark field. In this setup it is the probe which provides the reference field rather than the attenuating region, as will be shown in this thesis. By creating a surrounding pattern which is equivalent to the inverse Fourier transform (IFT) of the individual Zernike aberration of interest, and by phasing the central probe appropriately at 0° for odd aberrations and at 90° for even aberrations, a sensitivity of approximately 0.01λ rms in all Zernike terms is possible.

Pattern and probe-based aberration monitors are very closely related to the “interference mapping” structures recently introduced for the optimization of contact hole printing under various illumination conditions by Socha, *et. al* of ASML [57]. They are also similar to the theoretical considerations of Levinson and Schellenberg [58] and Rosenbluth [59] in that they attempt to answer the question of what constitutes optimum patterns for a given purpose.

The rest of this thesis will focus on the development and characterization of these interferometric pattern and probe-based aberration monitors both theoretically and in the context of mask fabrication technology and the installed base of lithographic exposure tools and experimental apparatus. Simulation will be used to aid in target design and in the analysis of experimental data. These are highly-advanced structures requiring many complex interactions to occur at the same time in order to operate properly. Therefore, extensive theory, data collection, and analysis must be undertaken.

3. Electric-Field Spillover Methods

This chapter begins with a discussion of the side-lobe spillover effect present in a knife edge implemented in an attenuating phase-shifting mask, also known as an attenuating phase shifting mask, in Section 3.1. Section 3.1 ends with an explanation of how a small probe can be used to provide an interferometric background reference electric-field to enhance aberration sensitivity of patterns in a purely dark-field mask. Finally, the development of the pattern and probe-based aberration monitors is introduced in Section 3.2, using the concept of inverse mapping of electric-field spillover.

3.1. Knife Edge

In this thesis the coherent electric-field spillover method is the most interesting and relevant. Returning to the concept of the knife edge, the left side of Figure 3-1 shows the image of a large 180° phase-shifted area (the basic component of the half-tone octagonal knife edge used by Fukuda, *et al.* [52]) against a 6% transmitting area with no aberration and with 0.035 rms waves of balanced (Zernike) coma oriented toward and away from the mask edge. In contrast to the binary knife edge discussed in Section 1.1.3, there is a large background field provided by the attenuating region of $\sqrt{6\%CF} = 0.245$, upon which the spillover and perturbation can coherently add. Simulation shows that at a distance of about 0.5 to 0.6 $\frac{\lambda}{NA}$ from the nominal line edge, the intensity level of the side-lobe changes by a factor of four as the aberration is rotated. The intensity goes from a value of 12.0% CF with no aberration to a minimum of 5.0% CF and a maximum of 21.2% CF. These large changes are facilitated by use of the attenuating phase-shifting mask.

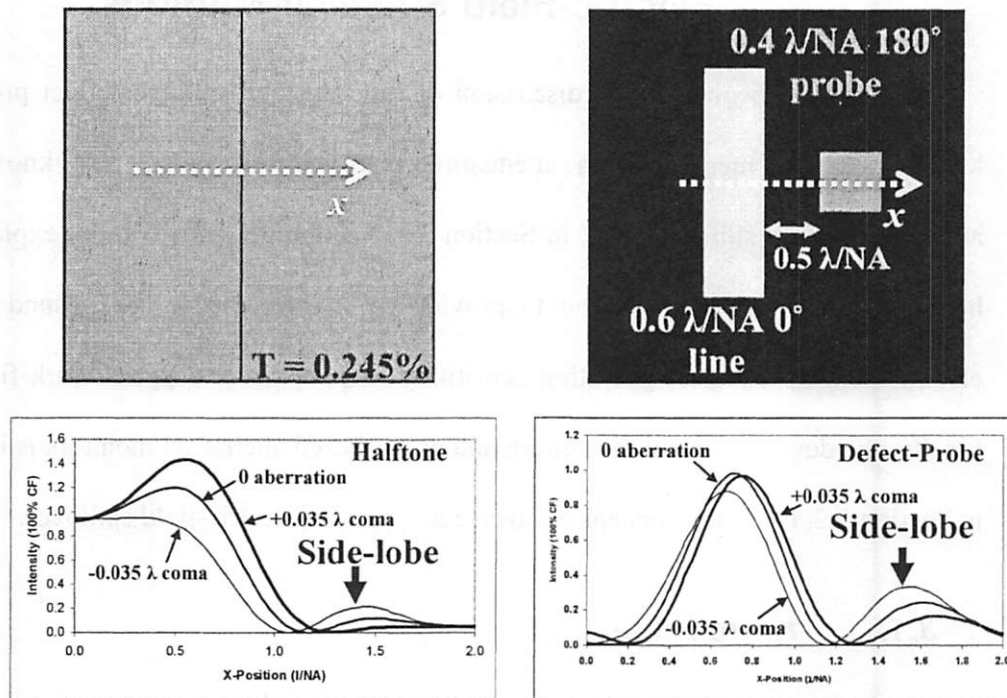


Figure 3-1. (Left) Image of a 180° knife edge mask pattern in a 6% transmitting mask with no aberration and $\pm 0.035 \lambda$ of balanced x-coma. (Right) Image of a 0° $0.6 \frac{\lambda}{NA}$ line with a 180° $0.4 \frac{\lambda}{NA} \times 0.4 \frac{\lambda}{NA}$ defect with no aberration and $\pm 0.035 \lambda$ of balanced x-coma.

The benefit of using a phase-shifting mask is that the designer can control both the magnitude and phase of the reference field upon which the spillover falls. This is seen at the right side of Figure 3-1 where the mask is not attenuating, but rather dark-field. In this case the electric-field, which had been provided by the constant 6% background transmission in the case of the attenuating phase-shift mask, is provided instead by a $0.4 \frac{\lambda}{NA} \times 0.4 \frac{\lambda}{NA}$, 180° phase-shifted probe placed $0.5 \frac{\lambda}{NA}$ to the right of a line near the resolution limit, $0.6 \frac{\lambda}{NA}$. Simulation shows that, as the amount of x-coma aberration is changed, the intensity at the probe position changes noticeably more than the peak intensity of the line. With no aberration the intensity at the probe position is 24.5% CF.

When -0.1 and $+0.1 \lambda$ (peak-to-peak) of x-coma are added to the simulation, the side-lobe intensity changes to 33.5% and 16.6% CF, respectively. Just as the 6% transmitting portion of the halftone mask provides an interferometric reference electric-field for the knife edge spillover to add to, the probe provides a reference field with magnitude 0.43 and phase 180° .

Figure 3-2 shows the normalized intensities of three features of interest as a function of the amount of coma present, each implemented in a different type of mask. The bottom curve is for the first side-lobe of a knife edge in a binary mask, the middle curve is for the same type of feature in an attenuating phase-shifting mask with 6% transmission, and the top curve is for the probe placed next to a line. The knife edge in the binary mask has the weakest response to the coma aberration, while the other two features have virtually the same response, aside from an offset which is unimportant. The binary knife edge has a weak response because it has no reference electric-field and therefore the spillover and perturbation fields are the only contributions to the final intensity. Meanwhile, the attenuating phase-shift mask knife edge and the line and probe in the phase-shift mask have considerable reference fields, provided by the attenuating region and the probe, respectively.

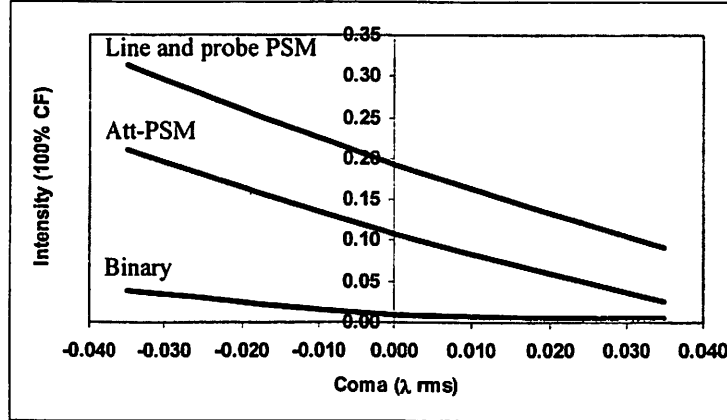


Figure 3-2. Normalized side-lobe intensity as a function of the amount of coma for (bottom curve) binary knife edge, (middle curve) attenuating phase-shift knife edge, and (top curve) phase-shift mask line and probe ($0.5 \frac{\lambda}{NA}$ from line edge).

3.2. Pattern and Probe-Based Aberration Monitors

The implementation of the programmed probe-based strategy to measure aberrations begins by using a small ($\sim 2/3$ minimum feature size) square which interacts with the side-lobe electric-field spillover from a surrounding target pattern [60, 61]. The process of target design is based upon the concept of reciprocity of the electric-field spillover. If a given aberration, such as coma, has the tendency to spread energy about a point source in a certain manner, as seen in Figure 2-8 (b), then placing an appropriately phased point source at the location of the spillover will, in turn, spill electric-field back onto the original point source. So, for a given aberration, the point spread electric-field distribution is first characterized, then a pattern that is sensitive to that aberration is generated by inverse-mapping this electric-field to give the location and phase of the target pattern components surrounding the probe.

The coma aberration, for example, takes energy from one side of a pattern and throws it to the other side. Looking at only at the perturbation to the spillover rings on the right

side of the pattern, a pattern similar to that seen in Figure 3-3 (a) is found. Filling in the regions where these perturbations occur with appropriately phased point sources in a dark field, as seen in Figure 3-3 (b), causes the total field and final intensity at the probe position to be highly sensitive to the aberration. Only the first spillover ring is used in this example but the sensitivity can be even further improved by adding additional rings to the target pattern. Finally, additional components with a rotational ordering and phasing consistent with that of the aberration under test are added. This not only serves to enhance sensitivity to the aberration of interest but it decreases the probe's sensitivity (or increases its orthogonality) to all other aberrations (Figure 3-3 (c)).

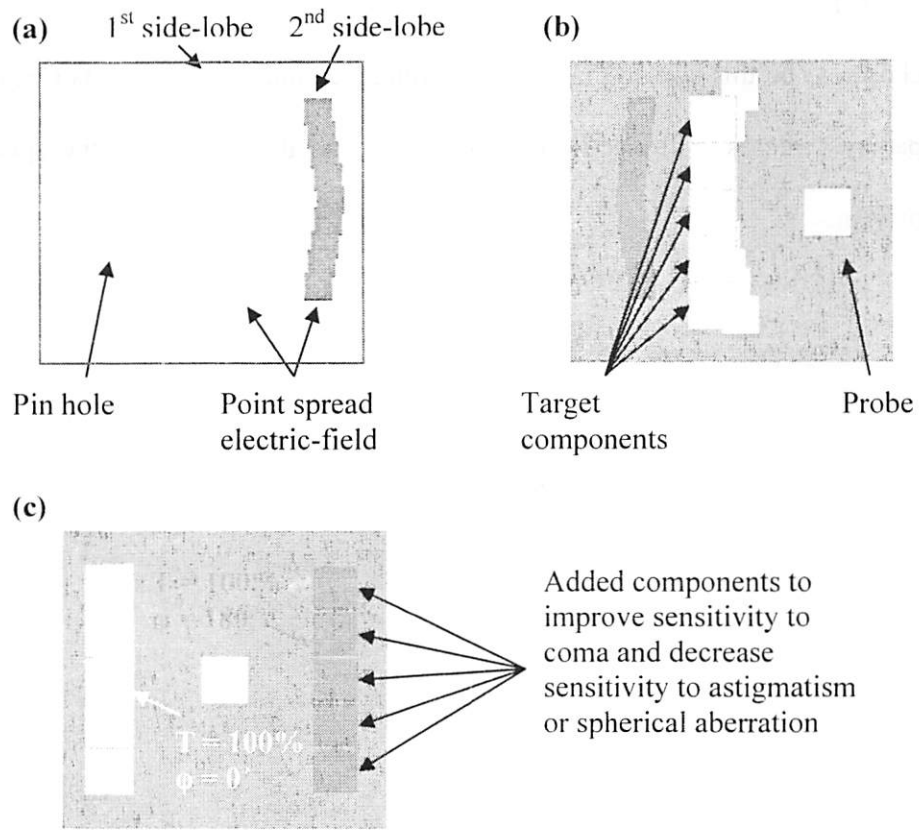


Figure 3-3. Strategy for building aberration target geometry.

As this research has progressed and more knowledge has been gained about design, layout, and mask fabrication capabilities, these patterns have developed through an iterative process. Patterns very similar to the first iteration of interferometric pattern and probe-based aberration monitors, created in 2000, are shown in Figure 3-4. These targets, which are referred to in this thesis as “Target Set 1”, are available for aerial image simulation using SPLAT through the UC Berkeley TCAD “Lithography Analysis using Virtual Access” (LAVA) website, located at <http://cuervo.eecs.berkeley.edu/Volcano/> under “Applications” → “Probe-Based Aberration Targets” → “Test Your Aberrations” → “BACUS Targets”. Each target lies in a dark chrome field and consists of a $0.4 \frac{\lambda}{NA} \times 0.4 \frac{\lambda}{NA}$ square probe surrounded by phase-shifted pattern features. The probe is chosen to be this size so that it gives a reference intensity of 19.2% CF, upon which the pattern features spill electric-field in relation to the amount of the specific aberration present.

Target Set 1 (“BACUS targets”)

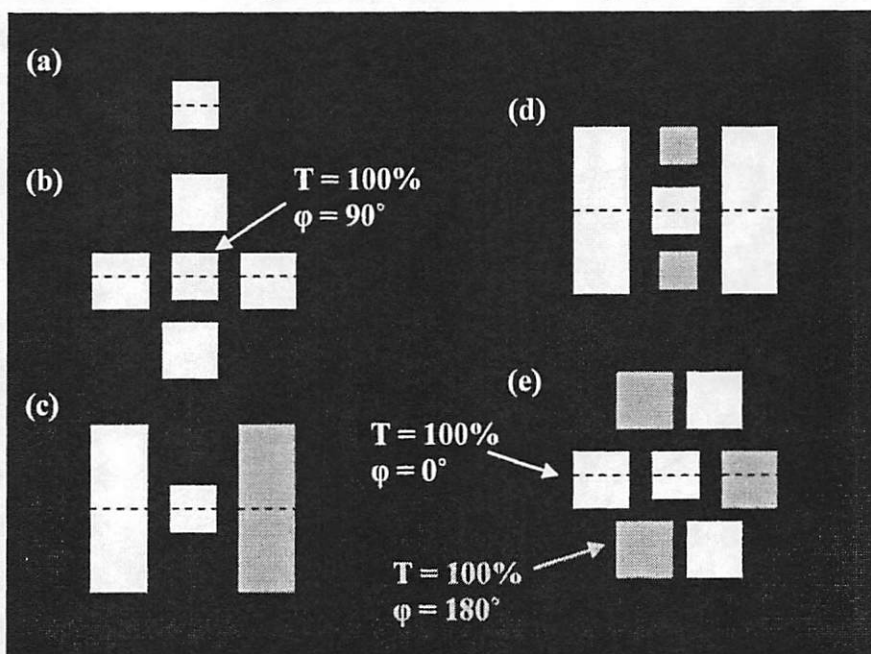


Figure 3-4. The first iteration of interferometric pattern and probe-based aberration monitors. (a) isolated probe, (b) spherical, (c) coma, (d) astigmatism, and (e) trefoil targets.

The second iteration of targets, herein referred to as “Target Set 2”, can be found on the website under the heading “EIPBN Targets”. These were laid out by hand, which resulted in their relative “chunkiness” with respect to later versions of the targets. As in Target Set 1, the probes are $0.4 \frac{\lambda}{NA} \times 0.4 \frac{\lambda}{NA}$, but in this case it is easier to see the symmetries due to the more complete rings. For reference, the top row is all even—specifically, rotationally-symmetric, targets, which have 90° probes. The bottom row is all odd targets, which have 0° probes.

Target Set 2 (“EIPBN Targets”)

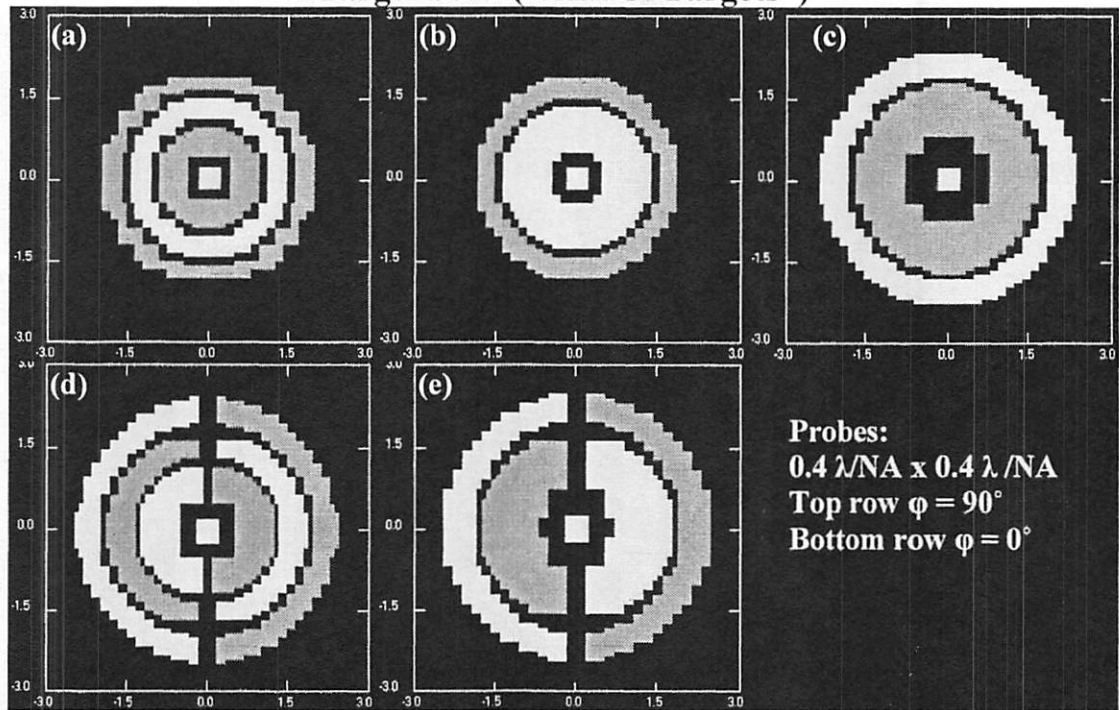


Figure 3-5. The second iteration of the targets, laid out by hand. (a) defocus, (b) spherical, (c) higher-order spherical, (d) coma, and (e) higher-order coma targets. The top row, which has all even aberration targets, has 90° probes and the bottom row, which has all odd targets has 0° probes. The inner ring of the defocus target is 180° and the second ring is 0° .

The third iteration of the targets, “Target Set 3”, represents the finest pixilation which has been used in target layout. These targets each have a small circular probe of appropriate phase along with a large number of extremely smooth rings. Also seen to the side of each target is a small isolated probe for experimental characterization of mask effects and focus position. The top two rows contain targets for even aberrations, while the bottom row has targets for odd aberrations. The probes have diameter $0.45 \frac{\lambda}{NA}$ and are equivalent in area to the square probes in Target Sets 1 and 2. Smaller, two-ring versions of these targets are available on the website under the heading “Smooth Targets”.

Target Set 3 ("Smooth Targets")

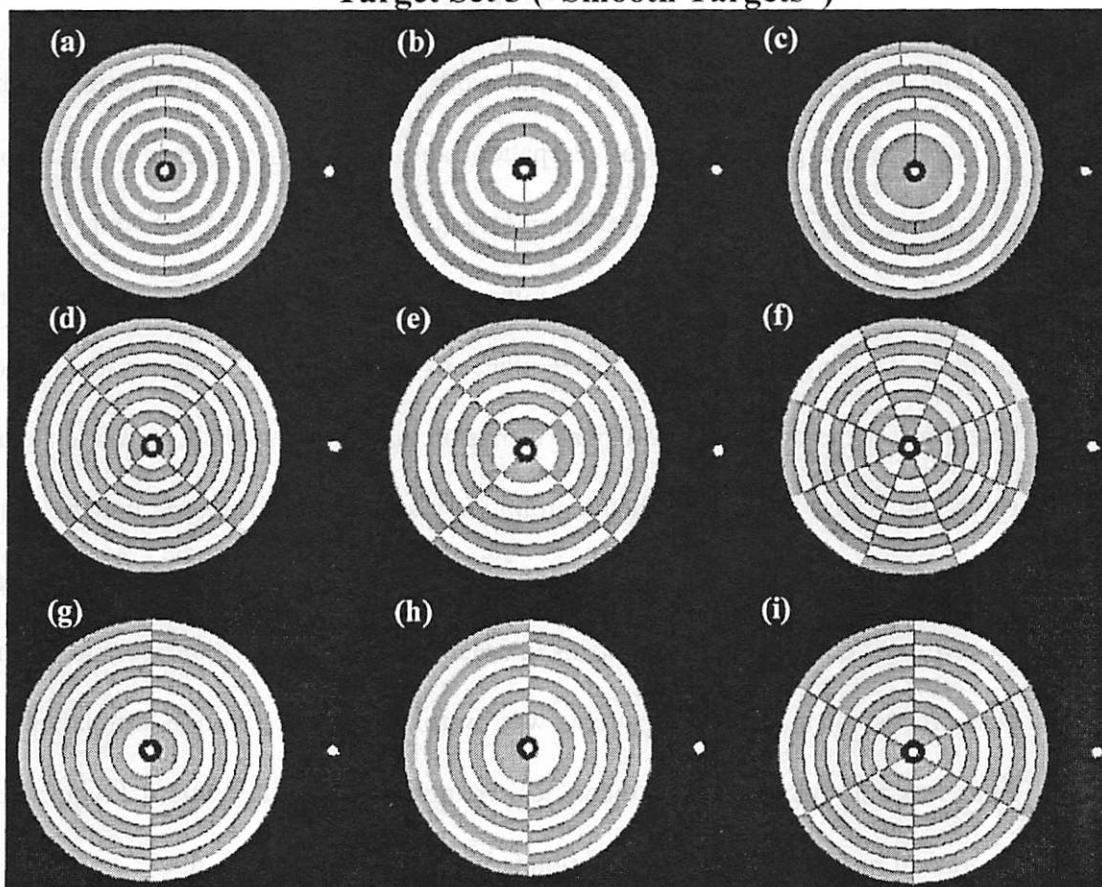


Figure 3-6. The third iteration of the targets, laid out with the assistance of CAD software. (Top row) Even aberration targets: (a) defocus, (b) spherical, and (c) higher-order spherical. (Middle row) Even aberration targets: (d) astigmatism, (e) higher-order astigmatism, and (f) 4-foil. (Bottom row) Odd aberration targets: (g) coma, (h) higher-order coma, and (i) 3-foil. The inner ring of the defocus target is 180° and the second ring is 0° .

4. Theory

One of the major contributions of this work is a systematic mathematical formulation of the expected performance of the pattern and probe-based aberration monitors. The foundation begins with the electromagnetic diffraction integral that shows how aberrations can interact with unique mask patterns to produce significant intensity changes at a given point in the image plane. In developing the mathematical theory, the blueprint for the design of individual aberration targets is established. While Neureuther, Hotta and Adam [60] established a preliminary set of interferometric pattern and probe-based targets that were designed to take advantage of the electric-field spillover properties of coherent optical systems in order to measure individual Zernike aberrations, their process of building the patterns was by trial and error through simulation. That is, there was no specific formal theoretical framework to guide pattern layout. Here, the theoretical model for optimal aberration target design is established.

4.1. *Formal Mathematical Justification*

The main goal of the pattern and probe-based aberration monitors is to use a mask pattern to engineer or “aberration-compensate” a wavefront, which will resonate with aberrations in the lens. The foundation of this section is the manipulation of the electromagnetic diffraction integral. In general, this is done by making a Taylor series expansion of the phase term in the complex pupil function and by making Zernike polynomial expansions of both the fields incident upon the lens and the lens aberrations themselves. The favorable properties of the Zernikes are then employed to simplify the

mathematics on the path to establishing the optimum mask patterns. Finally, the probe phase is chosen so as to maximize the target's sensitivity to a given aberration.

4.1.1. Utilizing the Electromagnetic Diffraction Integral

The diffraction integral presented in Equation 2-7 defines the electric-field distribution at image plane coordinates (x', y') in terms of pupil plane coordinates (ρ, θ) as

$$E_{Image}(x', y') = \frac{1}{\pi} \iint_{pupil} E_{Diff}(\rho, \theta) e^{\frac{jkNA}{w} [\rho \cos(\theta)x' + \rho \sin(\theta)y']} e^{jk\Phi(\rho, \theta)} \rho d\rho d\theta,$$

Equation 4-1. Electromagnetic diffraction integral.

where $\frac{1}{f_3}$ in Equation 2-7 has been replaced by the numerical aperture divided by the

lens radius, $\frac{NA}{w}$. The diffraction spectrum incident upon the pupil, $E_{Diff}(\rho, \theta)$, contains

two non-interacting wavefronts: $E_{Ideal_p}(\rho, \theta)$, scattered by the probe and the “aberration

compensated” wave, $E_{Diff_Pattern}(\rho, \theta)$, from the surrounding pattern. Because the probe is

sub-resolution its scattered fields uniformly fill the pupil and there is only one Zernike

term, $Z_{1,0}$ (piston), in its expansion. The amount of energy in this wave is directly related

to the square of the area of the small opening. $E_{Diff_Pattern}(\rho, \theta)$, on the other hand, must

be described by the full expansion $\sum_{n=1}^{\infty} \sum_{m=0}^n D_{Pattern_n,m} Z_{n,m}(\rho, \theta)$, where $D_{Pattern_n,m}$ are the

complex amplitude coefficients of the Zernike expansion of the wavefront.

$E_{Diff}(\rho, \theta)$ is the sum of these two waves, and is given by

$$E_{Diff}(\rho, \theta) = |E_{Ideal_P}| e^{j\phi_p} Z_{1,0} + \sum_{n=1}^{\infty} \sum_{m=0}^n D_{Pattern_n,m} Z_{n,m}(\rho, \theta),$$

Equation 4-2. Expansion of the electric-fields incident upon the pupil in Zernike polynomials.

where the phase of the field from the probe has been explicitly factored from its complex amplitude coefficient, E_{Ideal_P} , in the term $e^{j\phi_p}$. This emphasizes that ϕ_p is a parameter that can be chosen so as to maximize the target's sensitivity to aberration.

Substituting the expression in Equation 4-2 into the diffraction integral and looking only at the central position where the probe is placed in the image plane, $(x', y') = (0, 0)$, the expression

$$E_{Image}(0,0) \approx \frac{1}{\pi} \iint_{pupil} \left(|E_{Ideal_P}| e^{j\phi_p} Z_{1,0} + \sum_{n=1}^{\infty} \sum_{m=0}^n D_{Pattern_n,m} Z_{n,m}(\rho, \theta) \right) e^{jk\Phi(\rho, \theta)} \rho d\rho d\theta$$

is obtained. Performing a Taylor series expansion on $e^{jk\Phi(\rho, \theta)}$ to linearize the aberration term and expanding the aberration function in Zernikes, this becomes

$$E_{Image}(0,0) \approx \frac{1}{\pi} \iint_{pupil} \left(|E_{Ideal_P}| e^{j\phi_p} Z_{1,0} + \sum_{n=1}^{\infty} \sum_{m=0}^n D_{Pattern_n,m} Z_{n,m}(\rho, \theta) \right) \left(1 + jk \sum_{n=1}^{\infty} \sum_{m=0}^n A_{n,m} Z_{n,m}(\rho, \theta) \right) \rho d\rho d\theta.$$

Invoking the orthonormality of the Zernike polynomials over the pupil, the diffraction integral can be greatly simplified. Using the property that the pupil-weighted area of any Zernike is zero, two of the terms are eliminated, and the resulting normalization is

$$E_{Image}(0,0) \approx |E_{Ideal_P}| e^{j\phi_p} + jk \frac{D_{Pattern_n,m} A_{n,m}}{\pi(n+1)},$$

Equation 4-3. Electric-field at the central probe position in the image plane.

where the coefficients $A_{n,m}$ are real. As discussed in Section 2.1, the fields scattered from the pattern surrounding the probe are the Fourier transform of the mask pattern. Hence, for surrounding test patterns with even symmetry, $D_{Pattern_{n,m}}$ is real, and for patterns with odd symmetry, $D_{Pattern_{n,m}}$ is imaginary [62]. This makes it easy to see that, in order for the two electric-field contributions to add collinearly, the probe phase must be 90° for targets with even symmetry and 0° for targets with odd symmetry.

The extremes of the intensity normalized to a clear field value of unity and the diffraction-limited probe intensity I_{Ideal_p} are found if the probe phase is chosen such that the vector describing its electric-field contribution is collinear with the perturbation fields from the pattern spillover onto the probe.

$$I_{TotalMax_or_Min}(0,0) = \left[|E_{Ideal_p}| e^{j\phi_p} + jk \frac{D_{Pattern_{n,m}} A_{n,m}}{\pi(n+1)} \right]^2 \approx I_{Ideal_p} \pm 2k \sqrt{I_{Ideal_p}} \frac{|D_{Pattern_{n,m}}| A_{n,m}}{(n+1)}$$

Equation 4-4. The extremes in intensity are found when the probe and spillover perturbation fields are collinear.

In summary, it is evident that the target response depends mainly on four factors. They are: the phase and magnitude of the probe fields, the amount of the given Zernike aberration in the lens, and how well the test pattern on the mask can generate the Fourier transform of that Zernike at the pupil plane. If the probe phase is chosen properly so that the electric-field contributions are collinear then the change in intensity at the center of the target is directly proportional to the product of the last three of these terms.

The obvious question is: what is the sensitivity of the ideal pattern to a given amount of aberration? That is, how much does the observable intensity at the probe position of, say, the defocus target change for $A_{2,0} = 0.01 \lambda$ rms. If the ideal defocus target electric-

fields were generated at the mask plane, then $D_{Pattern_{2,0}} = 1$ and $n = 2$. The magnitude of the change in intensity is

$$|\Delta I_{Total Max_or_Min}(0,0)| \approx 2k \sqrt{I_{Ideal_P}} \frac{|D_{Pattern_{n,m}}| A_{n,m}}{(n+1)} = 2 \frac{2\pi}{\lambda} \sqrt{0.192} \frac{0.01\lambda}{3} = 1.84\%CF.$$

Thus, the ideal target sensitivity is

$$Sensitivity_{2,0} = \frac{1.84\%CF}{0.01 \lambda rms}$$

Equation 4-5. Theoretical sensitivity of the defocus target.

In terms of Rayleigh units of defocus, this equates to a sensitivity of $\frac{13.7\%CF}{1RU}$.

4.1.2. Benefits of the Zernike Polynomial Basis

The physical characteristics of the ring patterns surrounding the probes on the mask can now be determined from their required behavior in the pupil in order to react with individual Zernike terms. The Zernike polynomials make an ideal basis for decomposing the aberration functions. Given the completeness and orthogonality of the Zernikes, the best target for detecting the $Z_{n,m}(\rho, \theta)$ aberration is a pattern $E_{T,n,m}(x, y)$, where (x, y) are the coordinates in the mask plane, whose far field Fourier transform behavior at the pupil is proportional to $Z_{n,m}(\rho, \theta)$. Taking the inverse of this Fourier transform, the physical field produced by the surrounding mask pattern $E_{T,n,m}(x, y)$ is thus the inverse Fourier transform of the assumed pupil distribution $Z_{n,m}(\rho, \theta)$. While the resulting function is continuous and takes on both positive and negative values (and is thus difficult to realize) it can be said to be an optimum mask pattern. This is because it

produces far fields in the pupil that are perfectly orthogonal to other Zernike aberrations while at the same time giving the maximum on-axis electric-field contribution per unit of energy diffracted into the pupil.

The Zernike polynomials have zero pupil-weighted area, a number of zero crossings that grows with the radial order, and a bandwidth limit due to the finite pupil size. These well-known mathematical properties of the Zernike polynomials allow many of the general properties of the test patterns to be deduced in advance. For example, the test patterns will all have a zero on axis, grow in radius with the radial order, and have ripples at a period $\frac{\lambda}{2NA}$ with finite slopes. These properties also indicate that these patterns are suitable for implementation. Only positive and negative real and positive imaginary electric-fields are required. Thus, only three phases are needed on the mask. Also, the on-axis null in the Fourier transforms provides an optimum place to put the interferometric probe.

4.2. Optimum Test Targets as IFT's of Zernikes

An efficient way of developing test targets that address the problem of separating radial aberration effects is to examine the inverse Fourier transforms of the different radial orders of Zernike aberrations. A MATLAB integration routine was written by Kostantinos Adam for this purpose. Closed-form solutions for the Fourier transforms of Zernike polynomials are also available in [63]. Figure 4-1 shows $E_{Pattern_n,m}(x,y)$ on the mask for the cases of: no aberration ($Z_{1,0}$), defocus ($Z_{2,0} \equiv Z_3$), spherical ($Z_{4,0} \equiv Z_8$), and higher-order spherical ($Z_{6,0} \equiv Z_{15}$). Here the subscript pairs use the convention of Born and Wolf. The normalization is such that the aberration is one at the pupil edge and

either magnitude one (even aberrations) or zero (odd aberrations) at the pupil center. A plot on a radial cut line along the x-axis for each of these is shown in Figure 4-2.

The examples of optimum mask test target electric-fields $E_{pattern_{n,m}}(x, y)$ in Figures 4-1 and 4-2 clearly show the fundamental properties inherited from the Zernike polynomials. All but the uniformly-filled pupil have a zero on axis surrounded by a sizeable dark area, thus providing a natural location for a probe. As a point of reference, the first null in the case of the uniformly filled pupil is at a radius of $0.61 \frac{\lambda}{NA}$. The electric-field is real and requires both negative (180° phase-shifted) and positive (un-shifted) target rings. The bright areas of the targets grow in radial size as the order increases. They are located at 0.57 , 0.93 and $1.31 \frac{\lambda}{NA}$, respectively. The ripple distance is similar in all of the figures and is on the order of $\frac{\lambda}{2NA}$ corresponding to the interference of waves from the edges of the pupil.

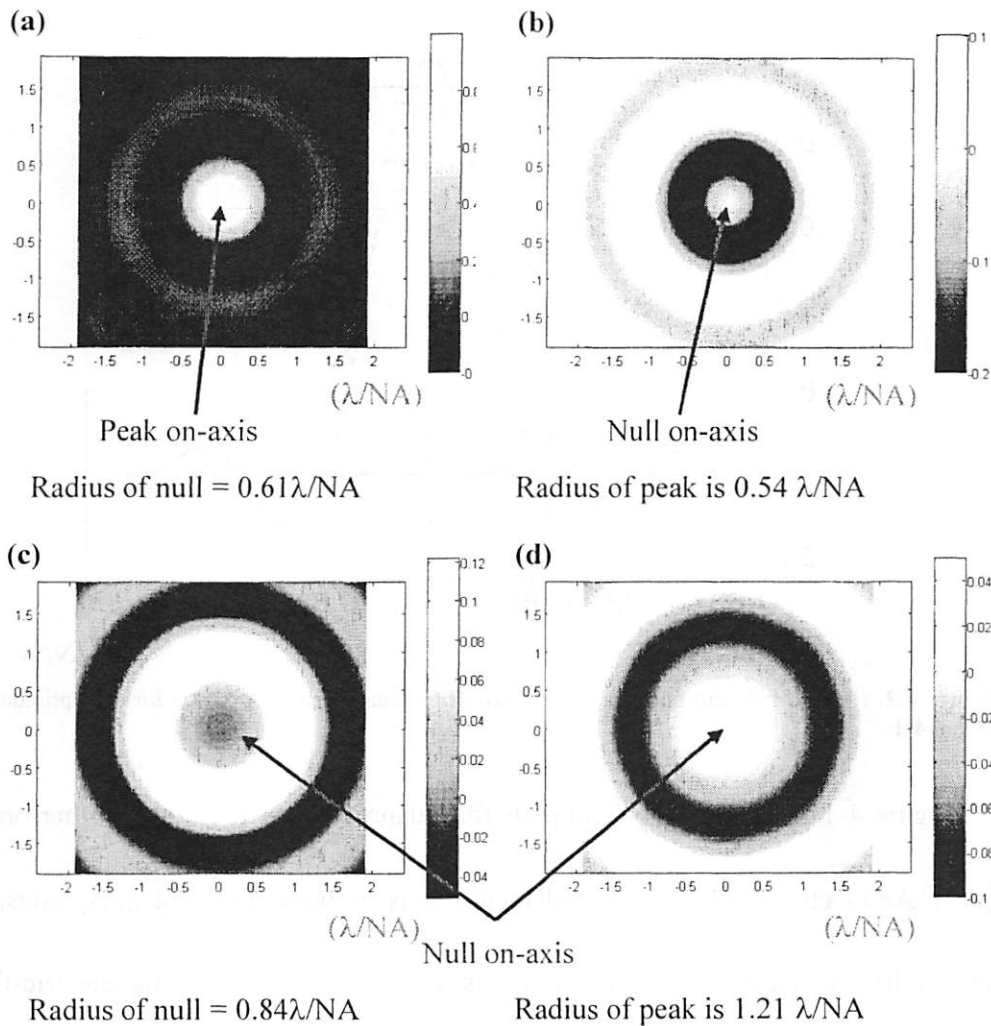


Figure 4-1. Two-dimensional inverse Fourier transforms of pupil distributions for (a) a uniformly filled pupil (no aberration), (b) defocus ($Z_{2,0}$), (c) spherical ($Z_{4,0}$), and (d) higher-order spherical ($Z_{6,0}$) aberrations.

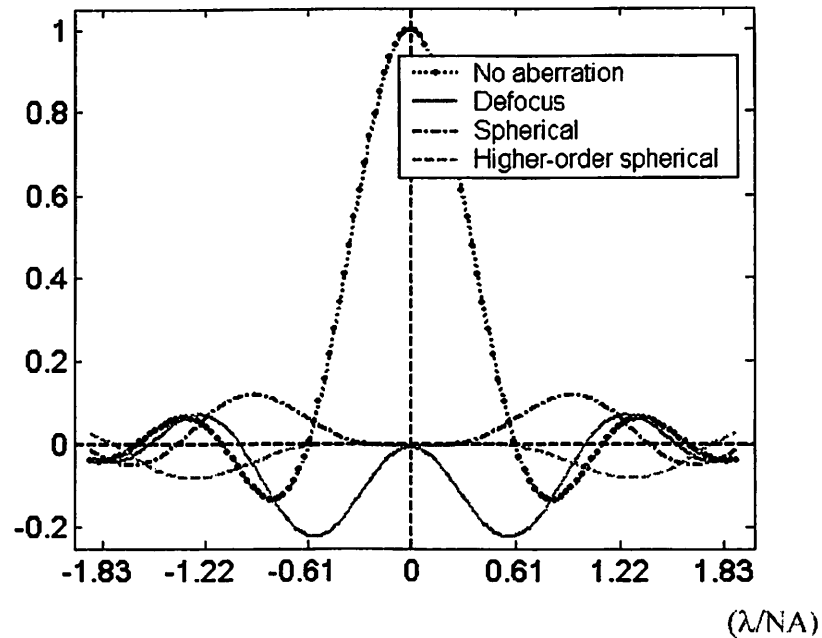


Figure 4-2. Electric-field cut-line along the x-axis at the mask along the x-axis for the optimum targets in Figure 4-1.

Figure 4-1 shows electric-field plots for balanced coma ($Z_{3,1}$) and higher-order coma ($Z_{5,1}$). An electric-field plot on a radial cut line is shown in Figure 4-2. Again each of the targets has a sizeable dark region at its center. In this case the electric-fields are imaginary and anti-symmetric about the pattern center on the mask. The radius of the bright area increases with the radial order and the interference ripple is again on the order of $\frac{\lambda}{2NA}$, occurring at 0.76 , and $1.14 \frac{\lambda}{NA}$, respectively.

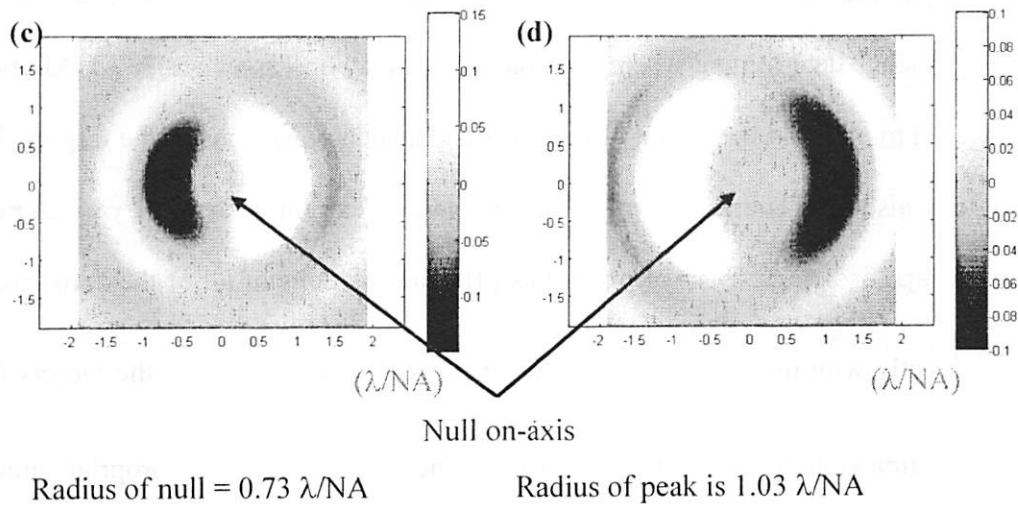


Figure 4-3. Two-dimensional inverse Fourier transforms of pupil distributions for the cases of a) coma ($Z_{3,1}$) and b) higher-order coma ($Z_{5,1}$) aberrations.

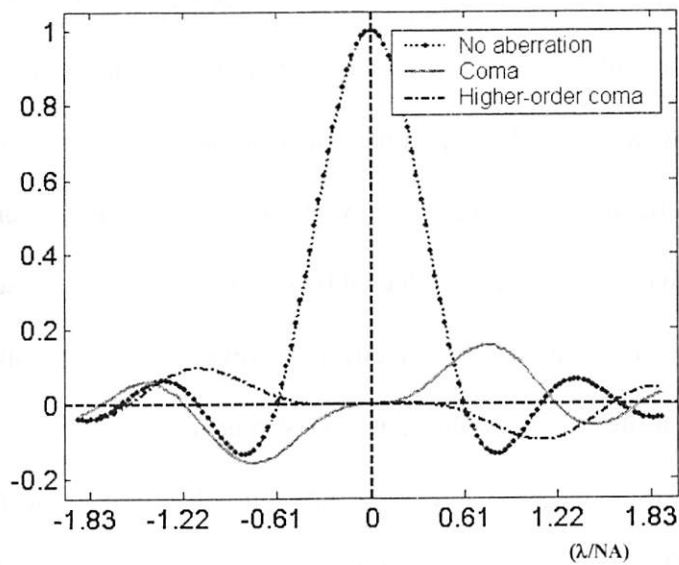


Figure 4-4. The electric-field at the mask along the x-axis for the optimum targets in Figure 4-3.

The key to laying out the targets to go on the mask, for Target Sets 2 and 3, is to use the zero-crossings of the electric-field functions seen in Figures 4-1 through 4-4 to guide the design. For Target Set 2 this was done by hand using a piece of graph paper. The

bright regions were made 0° and the dark regions were made 180° with the zero-crossings determining where the phase changes. For Target Set 3, a CAD program was used to program the layout of the rings and angular variations of the targets. Target Set 3 can also be generated using Frank Gennari's extremely helpful `pattern_gen` and `display3d_drawmask` programs [4]. The positions of all of the zero-crossings scale directly with the imaging system parameters $\frac{\lambda}{NA}$, so laying out the targets for different imaging systems merely requires magnifying the targets by an appropriate amount.

For the purposes of discussion, the imaging system shown in Figure 2-1 can be collapsed into a single lens system such as that seen in Figure 4-5. To illustrate the operation of the pattern and probe-based aberration monitors, an aberration is assumed in the lens. In the case pictured the aberration is defocus, with its OPD represented by the mesh pattern within the lens. Light is scattered from the probe and the target and the resultant wavefront incident upon the lens consists of two components: a spherical wave from the probe and an engineered wave from the target rings. For small aberrations, the spherical wave is only slightly affected by the aberration as it passes through the lens (see Section 2.3). The engineered wavefront however, which contains the majority of the energy transmitted through the mask, is shaped in such a way so that it is advanced anywhere in the lens where the OPD function will retard it and it is retarded anywhere that the OPD function will advance it. In the ideal case this cancels out the effect of the aberration on this wavefront component and adds an amount of electric-field to the center of the target, where the probe resides, which increases linearly with the amount of aberration.

While an ideal aberration target would have to be infinite in extent and produce a smoothly varying electric-field, mask making currently constricts their implementation to three or four phases usually with binary transmission. Because they are spatially-limited and approximate the ideal smoothly varying sinusoidal electric-field transmission with a square wave (Figure 3-6), the targets show higher-order effects, such as crosstalk between targets designed to measure similar aberrations, which require investigation.

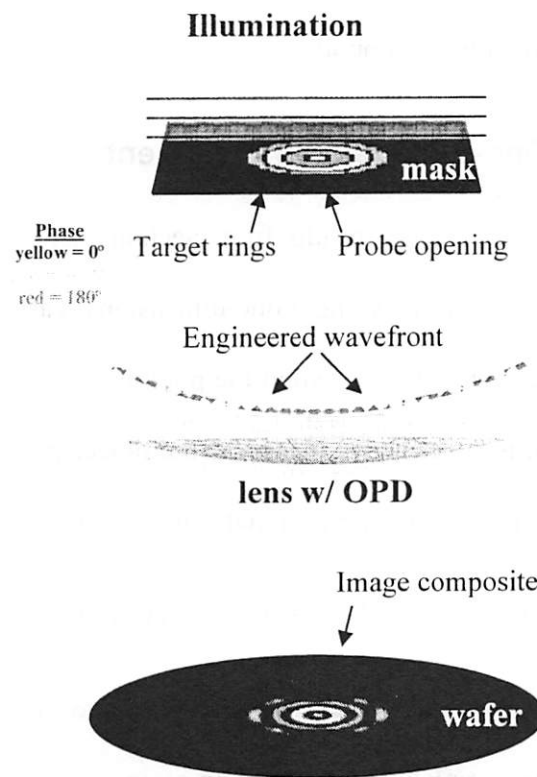


Figure 4-5. Implementation of a pattern and probe-based aberration monitor in an aberrated imaging system. Notice that the wavefront incident upon the lens consists of two non-interacting components.

4.3. Mathematical Target Characteristics

In principle it is always possible to create a diffraction-limited image of a δ -function in the image (wafer) plane, regardless of how badly aberrated the lens is. By time reversal and reciprocity for coherent imaging systems, if a δ -function in intensity is present at the

image (wafer) plane and passes backwards through the lens, the resultant electric-field at the object plane is the scaled Fourier transform of the generalized pupil function, or the aberrated point spread function (PSF) of the system. Thus, if an electric-field equivalent to the (non spatially-limited) aberrated PSF of the system is generated at the object (mask) plane, an Airy pattern will be observed in the image plane. It is thus always possible, in principle at least, to create the aberration-compensated wavefront at the entrance pupil which interacts appropriately with the aberrations in the lens to create an unaberrated wave at the exit pupil.

4.3.1. One-Dimensional Treatment

Insight into the complex results from Sections 4.1 and 4.2 for the two-dimensional case can be attained by analyzing a one-dimensional case. The approach is analogous to that in two-dimensions: the aberration the pupil is simply expanded using the orthogonal basis and then this spectrum is placed at the object plane. In this discussion, both the object and the pupil are one-dimensional. The object plane lies in physical (x) space and the pupil extends from $-k_0NA$ to $+k_0NA$ in frequency (k_x) space, where $k_0 = \frac{2\pi}{\lambda}$.

Instead of the Zernikes that are used as the orthonormal basis over a two-dimensional circular pupil, the complete set of *sines* and *cosines* is used over a one-dimensional pupil.

The expansion of the aberration function in one dimension is a simple Fourier transform.

The generalized Fourier series is given by

$$f(x) = \frac{1}{2}a_0 + \sum_{n=1}^{\infty} a_n \cos(nx) + \sum_{n=1}^{\infty} b_n \sin(nx),$$

where

$$a_0 = \frac{1}{\pi} \int_{-\pi}^{\pi} f(x) \delta x, \quad a_n = \frac{1}{\pi} \int_{-\pi}^{\pi} f(x) \cos(nx) \delta x, \quad b_n = \frac{1}{\pi} \int_{-\pi}^{\pi} f(x) \sin(nx) \delta x, \quad \text{and } n = 1, 2, 3, \dots$$

Equation 4-6. Generalized one-dimensional Fourier series of a function in one-dimension.

Consider for example the case as seen in Figure 4-6 (a) where the aberration is simply a single *cosine* term over the finite lens, represented by a *rect*-function. Invoking the convolution theorem, the Fourier transform of the aberration times the finite support function of the lens is simply the convolution of the Fourier transforms of each factor. The *cosine*-function can be expressed as the sum of two complex exponentials and its Fourier transform is merely the sum of two δ -functions, each shifted equally from the origin. The Fourier transform of the *rect*-function is the well-known *sinc*-function.

The optimum fields from a target in the object plane for this one-dimensional aberration are given by

$$Ideal\ Target = FT \left\{ \cos \left(\pi n \frac{k_x}{r_{p,k}} \right) \times rect \left(\frac{k_x}{2r_{p,k}} \right) \right\} = FT \left\{ \frac{1}{2} \left(\exp \left(j \pi n \frac{k_x}{r_{p,k}} \right) + \exp \left(-j \pi n \frac{k_x}{r_{p,k}} \right) \right) \right\} \otimes FT \left\{ rect \left(\frac{k_x}{2r_{p,k}} \right) \right\},$$

where $r_{p,k} = k_0 NA = \frac{2\pi}{\lambda} NA$ is the half-length of the pupil and n is the order of radial variation of the aberration in the pupil. This yields a target which is the sum of two shifted *sinc*-functions.

$$Ideal\ Target = \left[\frac{1}{2} \delta \left(x - \frac{n}{2r_{p,k}} \right) + \frac{1}{2} \delta \left(x + \frac{n}{2r_{p,k}} \right) \right] \otimes 2r_{p,k} \text{sinc}(2r_{p,k}x) = r_{p,k} \left[\text{sinc} \left(2r_{p,k}x - \frac{n}{2r_{p,k}} \right) + \text{sinc} \left(2r_{p,k}x + \frac{n}{2r_{p,k}} \right) \right]$$

Equation 4-7. Representation of an ideal one-dimensional Fourier transform aberration target as the sum of two shifted *sinc*-functions.

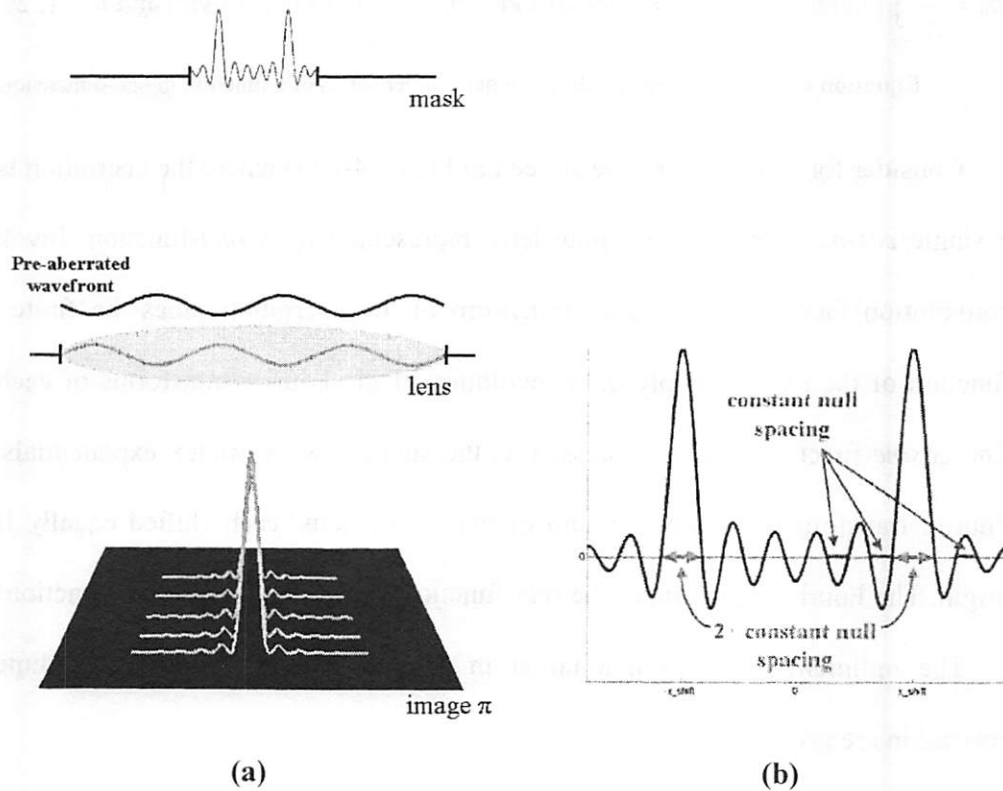


Figure 4-6. (a) Simplified one-dimensional aberration model. (b) Fourier transform of a single *cosine* aberration over a spatially limited one-dimensional pupil.

Being the sum of two shifted *sinc*-functions, the ideal one-dimensional aberration target reflects many of the general properties of the *sinc*-function. Firstly, a “fat” feature is present, nearly double the width of all of the other features in the object plane. This originates from the *sinc*’s central lobe, which is two times as wide as its side-lobes. Secondly, there is an infinite number of side-lobe features which originate from those of the *sinc* itself. Because the side-lobes of the *sinc*-function decrease in height as $\frac{1}{\pi x}$, their contribution to the ideal one-dimensional target at the central position of the conjoined *sinc*-function is small.

Finally, another property of the ideal target is not a property of the *sinc*-function, but rather a property of the aberration’s frequency. That is, the more rapidly the aberration

oscillates inside the lens (i.e., the larger the value of n), the larger the characteristic size of the target. This is reflected in the separation of the two peaks of the *sinc*-functions being directly proportional to n . Intuitively it can be argued that the two wide central lobes are similar to Young's double slits, with their diffracted fields interfering at the pupil. If a given aberration oscillates rapidly over the lens then the "slits" must be placed wide apart to sample the lens at appropriately short intervals. If the aberration varies less rapidly then the slits must be brought closer together to increase the separation of the interference fringes.

4.3.2. Location of Maximum Radiation for Each Order

As seen in Figure 4-7 (a), the dominant electric-field contribution comes from the two strong central peaks separated by a distance Δx in the object plane. In an imaging system, for a structure of period Δx , the Fourier components of the scattered light are separated by

$$\Delta k_x = \frac{2\pi}{\Delta x},$$

Equation 4-8. Separation of diffracted orders in k-space.

which reflects the constant space-bandwidth product in the Fourier transform relationship between the object and pupil planes. The peak-to-peak spacing of the aberration in the lens, Δk_x , as seen in Figure 4-7 (b) can be given by

$$\Delta k_x \approx 2 \frac{r_{p,k}}{n}.$$

Equation 4-9. Peak-to-peak spacing of the aberration function in the lens. (Bragg condition between the mask and lens.)

This indicates that the characteristic target size increases linearly with the frequency of oscillation of the aberration in the lens in the form

$$\Delta x \approx \frac{n\pi}{r_{p,k}} = n \left(0.5 \frac{\lambda}{NA} \right).$$

Equation 4-10. Equation showing that the characteristic target size increases linearly with n .

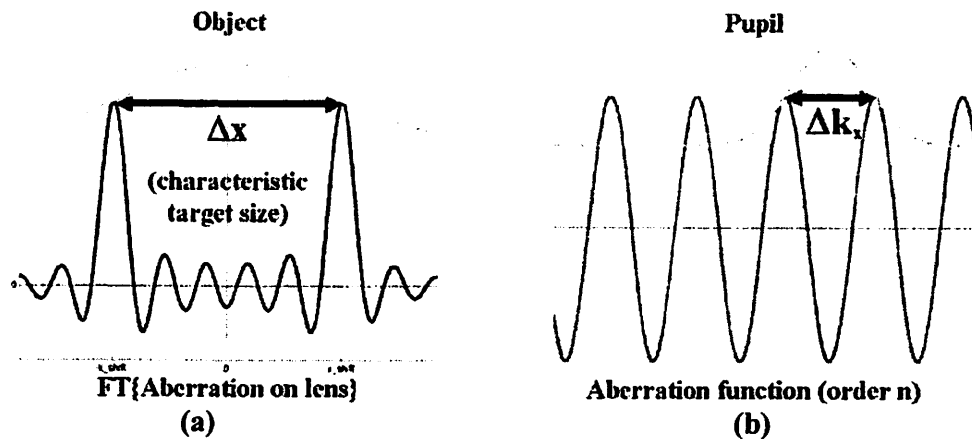


Figure 4-7. (a) A one-dimensional aberration function in the pupil with peak-to-peak spacing, Δk_x . (b) Spacing, Δx , of the central peaks of two laterally shifted *sinc*-functions representing the ideal fields at the object plane to detect a given sinusoidal aberration in the lens.

Equation 4-9 is directly related to the Bragg condition for the system, which is the stationary phase condition for the integral over the pupil of the product of the phase of the wave incident on the pupil and the phase of the aberration. When the wavefronts scattered from the target and incident upon the lens oscillate much more or much less rapidly in the pupil plane than the aberration then the signal is small. When the wavefronts match with the Bragg condition then the aberration acts to rectify the signal from the incident wavefront, thereby maximizing the value of the integral. When the equation is satisfied the Bragg condition for two-dimensional aberration targets is achieved.

4.3.3. Constant Square Wave Drive and Finite Target Size

The smoothly varying, sinusoidal function in Figure 4-8 (a) shows the ideal electric-field desired at the object plane to detect a given aberration, along with an approximation to this function with a train of *rect*-functions of constant amplitude. If the *rect*-train approximation of the fields is generated at the object plane then it is the Fourier transform of these fields which is incident upon the pupil. The first few terms in the Fourier series of a square wave of amplitude $k = 1$ (corresponding to a unity transmission coefficient in the open areas of the mask) are given by

$$f(x) = \frac{4k}{\pi} \left(\sin(x) + \frac{1}{3} \sin(3x) + \frac{1}{5} \sin(5x) + \dots \right).$$

Equation 4-11. Fourier components of a square wave train.

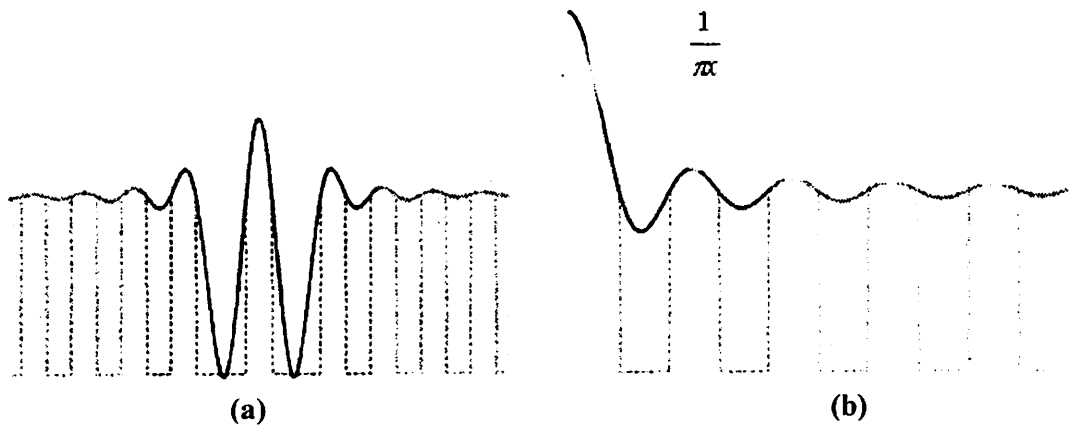


Figure 4-8. (a) Cut-line of the ideal smoothly varying electric-field desired at the object plane to detect a given aberration. The darkened areas indicate that the real targets are spatially-limited and the square wave indicates the approximation of the ideal field desired at the object plane with a mask having binary transmission with 0° (positive or yellow) and 180° (negative or red) phase shift. (b) Modulation of the *sine*-function by a hyperbola, indicating that the outer portion of the aberration targets is significantly overdriven by the square wave implementation. The darkened areas indicate that the real targets are spatially-limited and the square wave shows the approximation of the ideal field desired at the object plane with a mask having binary transmission with 0° (positive or yellow) and 180° (negative or red) phase shift.

Three main second-order effects arise in the substitution of these sharply defined electric-fields for the ideal fields. Firstly, it is seen that the fundamental frequency, for even a sinusoidal function of constant amplitude, is overdriven by a factor of $\frac{4}{\pi}$. This is beneficial to target operation because it indicates that the approximate fields are more sensitive to the aberration under test than the ideal fields.

Secondly, while the side-lobes of the ideal fields decrease rapidly in magnitude moving away from the center, the *rect*-train approximation is of constant amplitude. The result is that the side-lobe positions are significantly overdriven with respect to the innermost fat peaks. In fact, the further away from the center the side-lobe position is, the more relatively overdriven it is. The net result of this is that the spillover into the center from the outer side-lobe is too large.

Thirdly, the expansion in Equation 4-11 shows that, because of the sharp corners in the approximate fields, an infinite number of scattered orders are incident upon the pupil plane. Each of these produces a field at the pupil plane which is a convolution of a *sinc*-function (from the Fourier transform of the finite support function of the target on the mask) convolved with two δ -functions (arising from the sinusoid itself), each shifted laterally by an amount proportional to the order number. While these higher order peaks tend to fall outside of the collection angle of the imaging lens, the *sinc*-function extends to infinity with an asymptotic spectral tail and a number of its side-lobes are collected by the pupil. The more periodic the structure of the fields in the object plane the more the fields from the spectral tails add coherently inside the pupil, disrupting the interaction of the desired fields with the lens aberration.

When the fields from the side-lobes interact to change the magnitude of the field at the position of the δ -functions in k -space of the fundamental frequency, cross-talk results between the target and higher order aberrations. The cross-talk factor can be estimated in one dimension by noting that the n^{th} order in the expansion of a square wave has $\frac{1}{n}$ times the magnitude of the fundamental frequency and that the *sinc*-function decreases as the $\frac{1}{x}$ distance from its central peak, as it is shifted from the pupil center by a distance proportional to n . Thus the $n = \pm 3$ order drives the third-order aberration in the lens, resulting in excess fields contributing to the measured signal in the amount of $2 \times \frac{1}{3} \times \frac{1}{3}$. This phenomenon helps to explain the results observed in two dimensions where aerial image simulation shows that cross talk between the lower order targets is a maximum of approximately 1/6. While the square wave drive is a significant non-ideality, it is unavoidable given today's mask making capabilities.

4.3.4. Implications for the Two-Dimensional Case

The challenges in fabrication for the highly experimental masks required for this work can be seen in the SEM in Figure 4-9. This SEM is from an experiment designed for $\lambda = 193$ nm and NA = 0.55, and shows the various phase etches required as well as the abrupt height changes at the phase transitions for a 4-foil aberration target. While it is impossible to achieve the true inverse Fourier transform electric-fields shown in Figures 4-1 and 4-3, this mask pattern represents the most accurate approximation to those fields which can be achieved using today's mask fabrication technology.

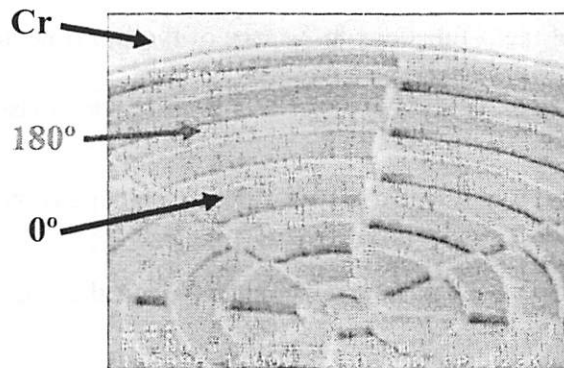


Figure 4-9. SEM image of a 4-foil target on a phase edge mask for $\lambda = 193$ nm (SEM courtesy Ebo Croffie, LSI Logic.).

Analysis of the properties of the ideal electric-fields for aberration detection in one-dimension yields great insight into the more complex two-dimensional case. In the early, empirical development of Target Set 1, the underlying nature of the targets was not fully understood. Here it is revealed that, for a given Zernike aberration, the ideal target consists of a single “fat” ring concentric with an infinite number of thinner rings of thickness $\sim 0.5 \frac{\lambda}{NA}$. The rings are a direct artifact of the Bessel function, which is analogous to the *sinc*-function in that it has a central peak that is wider than its side-lobes. The fat ring comes from the wide central peak of the Bessel function with the thin rings arising from its side-lobes. It is approximately double the width of the other rings, with its exact thickness being determined by the separation of the Bessel functions. This separation results directly from the order, n , of the aberration in the pupil.

Furthermore, all of the target rings alternate in phase and decrease in magnitude with increasing radius from the target center. In Figure 4-10 the radial positions of the first few zero crossings in electric-field are plotted as a function of n for a handful of the lower-order Zernikes (see Figures 4-1 through 4-4). It is evident that the predictions concerning

the size and positioning of the target rings for the optimum two-dimensional targets were accurate. Averaging the slopes of the plotted data, the characteristic target size is given by

$$R \approx (0.186n + r_0) \frac{\lambda}{NA}$$

Equation 4-12. Characteristic target size as a function of n , the order of radial variation of the Zernike aberration of interest.

where r_0 is the position of a given ring in the Airy pattern.

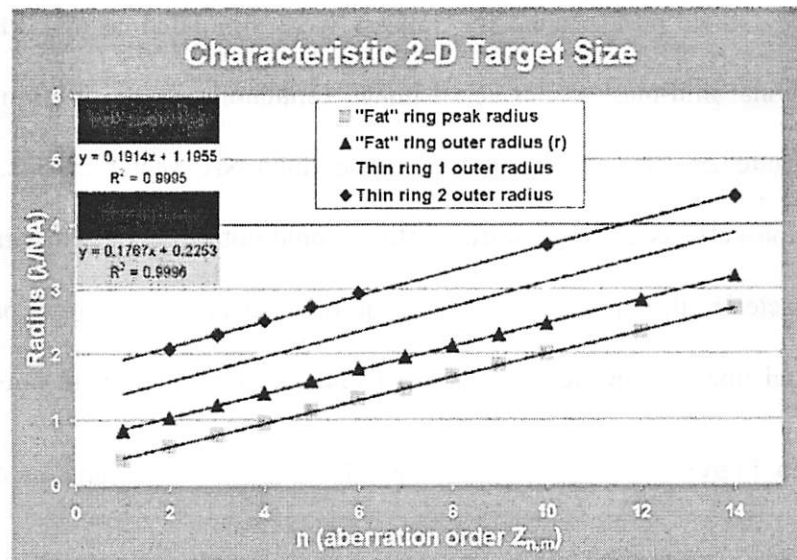


Figure 4-10. Dependence of characteristic target radius upon the order of the radial variation, n , of the aberration function.

4.4. Examples of Discretized Test Targets

While the theory of operation of the pattern and probe-based aberration monitors lies upon a detailed mathematical foundation established in Section 4.1, many approximations are necessary to adapt the ideal detection fields calculated in Section 4.2 to patterns on a photomask. The patterns are implemented on binary transmission photomasks with up to four phases, which is uncommon as most phase-shifting reticles contain only two phases.

Each approximation to the ideal fields affects the performance of the target and therefore must be characterized. The major issues of concern are the spatial truncation of the patterns, the use of binary transmitting regions to approximate the smoothly-varying electric-fields, mask making errors, the effects of mask topography, the effects of partial coherence, and the effects of imaging at high numerical apertures. To make the patterns work in practice, initial simulations and experiments were performed to screen for the influence of each of these effects upon target behavior.

The first group of targets to undergo extensive simulation studies was Target Set 2. To assess their performance the images were simulated using SPLAT [23], a two-dimensional thin-mask scalar aerial image simulator capable of taking resist film stack effects into account, but unable to model high-NA vector effects. Therefore, mask topography effects and polarization effects could not be seen. (Other methods were used to characterize the impact of these second-order effects upon target performance.) Only the aerial image is needed so the resist options in SPLAT were not used. The target fields in Figures 4-1 through 4-4 scale laterally with $\frac{\lambda}{NA}$ and in all of the SPLAT simulations presented herein $\lambda = 0.5 \mu\text{m}$ and $NA = 0.5$ is used so that $1 \mu\text{m}$ in the layouts always equals $1 \frac{\lambda}{NA}$. The SPLAT inputs in the following examples were normalized such that the Zernike aberration corresponded to a peak optical path difference of 0.05λ at the edge of the pupil. A small but finite partial coherence factor of $\sigma = 0.1$ was also used.

The targets in Target Set 2 have a maximum of three rings because, while the theory in Section 4.1.1 calls for fully-coherent on-axis illumination, lithography tools generally have a minimum σ value of around 0.30. The number of target rings that can be

effectively used is limited by the coherence radius, defined in Section 2.1.2. In general the constraints of the coherence of the illumination limits the maximum useable target size to a lateral dimension of $\sim 6 \frac{\lambda}{NA}$, corresponding to about three rings for the lower order Zernikes.

The detailed image response in the vicinity of the center of the target in the wafer plane for the spherical target, for various aberrations at the 0.05λ peak level is shown in Figure 4-11. The local image is similar to the image of an isolated pinhole and has a lateral dimension comparable to that of a contact hole. This fundamental shape is magnified or de-magnified by various aberrations. Without any aberrations the peak is at an intensity of 24.2% CF. When defocus is used the intensity at the probe position decreases to 16.8% CF. Third order spherical shows a decrease to 13.5% CF. When spherical aberration is included this peak rises to 95.5% CF, or by over 70% of the clear field intensity. When normalized to rms, this is a sensitivity of 32% CF per 0.01λ rms of spherical aberration. The cross contamination of this target by 0.05λ of defocus and higher-order spherical are, in the worst case, only about 1/6th of this value. To the author's knowledge this is the first test target that is both highly sensitive to spherical aberration as well as nearly independent of focus.

Figure 4-11 shows images at the wafer plane of the defocus and spherical targets for three lens quality conditions. The spherical target clearly shows that it is dark at the center with no aberration and remains dark in the presence of defocus. However, when spherical aberration is present a bright dot appears at the center. The defocus target behaves in a similar manner but the change is a little more difficult to observe due to the high starting peak level at the center of the target.

Figure 4-12 shows images at the wafer plane of the coma and higher-order coma targets for three lens quality conditions. The higher-order coma target clearly shows that it is dark at the center with no aberration and remains dark in the presence of coma. When higher-order coma is present a bright dot appears at the center. The coma target behaves in a similar manner but the change is slightly more difficult to see due to the moderate level of the central peak with no aberration. The results of the simulations shown in Figures 4-11 and 4-12 are important because they show that, despite the truncation of the infinite inverse Fourier transform patterns, and the binary transmission of the object, the patterns demonstrate sensitivity to their individual aberrations and orthogonality to other, even similar aberrations.

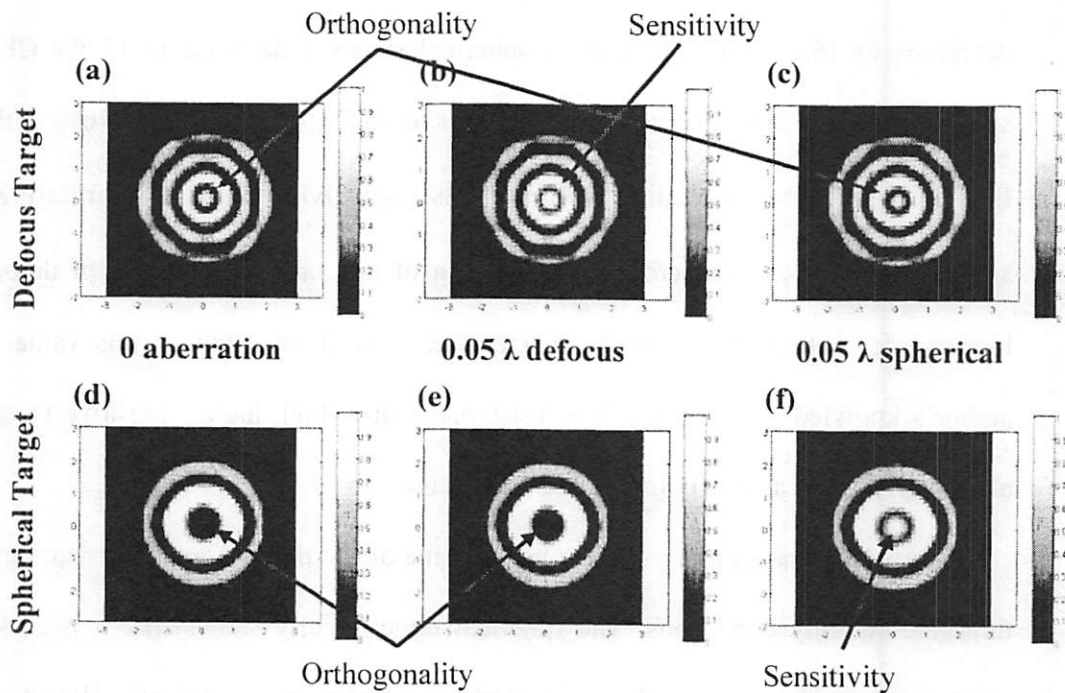


Figure 4-11. Images at the wafer plane for the defocus and spherical targets from Target Set 2 for no aberration (a and d), and 0.05λ peak of defocus (b and e) and spherical (c and f). Note the change in appearance of the central spot.

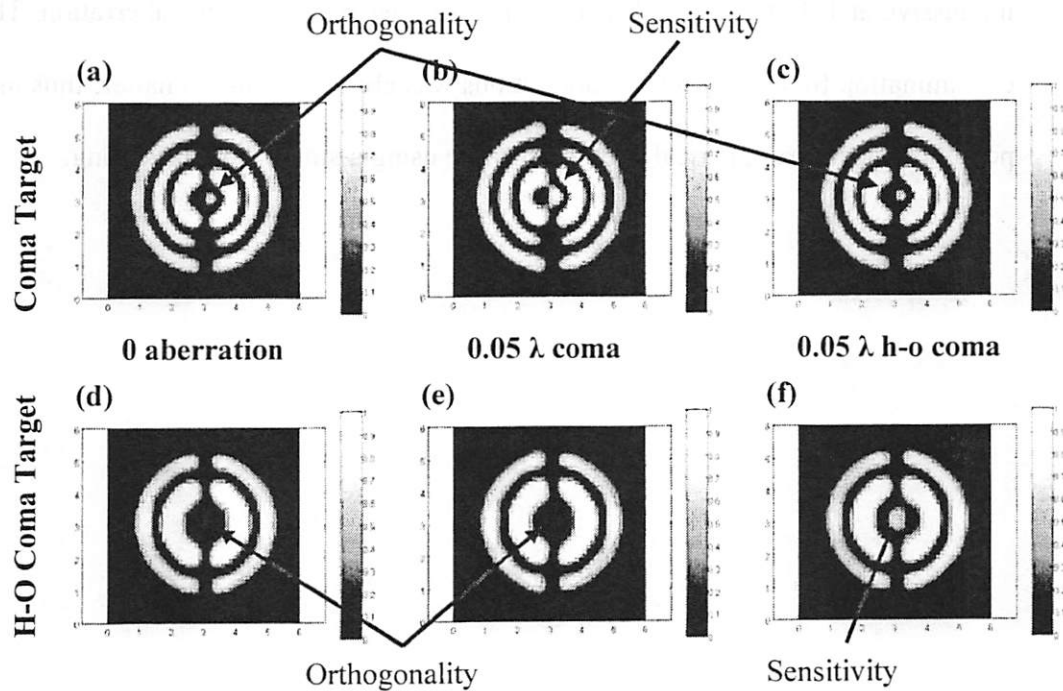


Figure 4-12. Images at the wafer plane of the coma and higher-order coma targets from Target Set 2 for no aberration, and for 0.05λ peak of coma and higher-order coma.

4.4.1. Summary

In this chapter a theoretical foundation has been developed for assessing the performance of programmed probe-based aberration targets. For small aberrations the reference probe alone is, to first order, unaffected by the aberrations and the perturbation of the signal at the probe position by a surrounding pattern rings is linearly proportional to the aberration level. The optimum targets are the inverse Fourier transforms of the individual terms in the Zernike representation. Many of the properties such as the on-axis null, phase oscillation, and increase in diameter with order follow directly from the transforms of the Zernike polynomials. Implementation of these targets as openings with 100% transmission and phases of 0° , 90° and 180° were tested by simulating their images at the wafer. The intensity variation of the central node for the five targets studied was

impressive at 1/3 of the full clear field intensity per 0.01λ of rms aberration. The cross contamination by closely related aberrations was about six times smaller, thus making it possible to measure spherical aberration while using a single defocus setting.

5. Simulation Characterization

The main focus of this chapter is on extensive ideal thin-mask, scalar imaging SPLAT simulations which predict target behavior. In the continuing downward march to achieve smaller and smaller feature sizes at the wafer, numerical apertures have been increased to values approaching, and in some cases surpassing, unity and resolution enhancement techniques such as strong phase-shifting have come increasingly into vogue. These approaches bring with them their own unique problems, which were previously insignificant, as scalar imaging formation and simple thin-mask approximations become invalid. The physical effects which cause the experimental behavior of phase-shifting masks imaged at high-NA to deviate from their theoretical behavior are also discussed and a framework for isolating and characterizing them via simulation and experiment is presented. These effects, herein called lithography “demons”, include thick-mask electromagnetic effects, polarization vector effects, photoresist effects, and mask error effects. This basic framework is developed using simulation and experimental investigations will follow in subsequent chapters.

5.1. *Lithography Demons*

Consider a classification of the lithography demons into four types. Mask electromagnetic effects are caused by the absorption of electric-field by the steep sidewalls of phase etched features and they manifest themselves as intensity imbalance in the image. That is, simple chrome openings on the mask tend to be noticeably brighter than phase-shifted regions of the same lateral size. This effect was originally discovered via simulation by Pierrat, Wong, and Vaidya [24]. The standard methods to compensate

for this include biasing the layout of phase shifted features with respect to 0° openings or creating an undercut etch along the chrome edges of the phase shifted features to physically move the sidewalls away from the openings.

High-NA polarization effects occur because the steep angles of incidence of the imaging rays upon the photoresist cause reduced coupling of the TE mode of the electric-field while causing reduced contrast in the TM mode [64]. Resist effects mainly refer to the photoresist's ability mitigate some of the high-NA effect by bringing the rays closer to normal due to its index of refraction (~ 1.7). Finally, mask errors effects result from mask geometry, pixilation, and layer registration. Observing these demons in the simulation/experimental space, as shown in Figure 5-1, it is seen that the problem of unbundling these effects to gain insight into possible ways to improve the design of the mask patterns lends itself to a divide and conquer strategy.

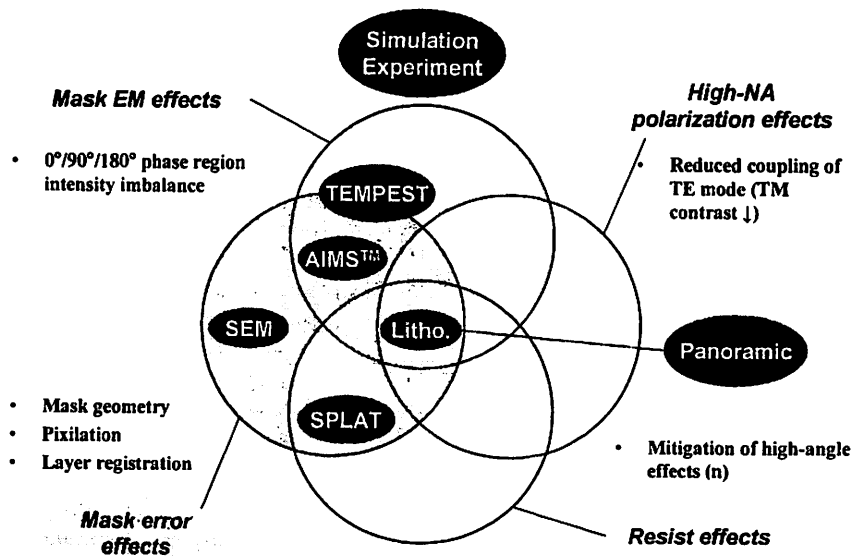


Figure 5-1. Framework for unraveling the lithography demons affecting the imaging of phase-shifting masks in high-NA systems.

Various methods are used to characterize the parameters and effects of each demon. Top-down SEM images of the photomask can be utilized to determine the mask geometry, including alignment errors and some processing non-idealities. AIMS™ allows for the rapid prototyping of the optical performance of the mask without having to do full photoresist exposures. AIMS results show experimentally the effects of mask errors and the influence of thick-mask electromagnetic effects. While the AIMS tool is designed to provide “stepper equivalent optical conditions” [65], it actually magnifies an image of the photomask pattern onto a CCD to achieve the desired resolution. Thus neither high-NA polarization effects nor no resist effects are present in the AIMS measurements. As described in Section 4.4, SPLAT 5.0 is used to simulate the thin-mask aerial image behavior of a given geometry with a scalar imaging model. A flag can be set in the program to account for the effect of photoresist if desired. TEMPEST [66] is a finite difference time domain (FDTD) simulator which iteratively solves Maxwell’s equations for a given three-dimensional mask geometry. Full optical lithography falls at the union of all of these effects. Finally, Panoramic Technology’s EM-Suite™ is a powerful suite of design and simulation tools, including a FDTD solver, which can be used to model each of these effects.

5.2. Summary of Test Target Performance

The simulation results presented in Section 4.4 demonstrate that the defocus, spherical, coma, and higher-order coma targets from Target Set 2 have a strong response to their individual aberrations and reasonably low cross-talk with other aberrations. In this section, an in-depth simulation study of target behavior is presented, along with an

electric-field phasor model to help explain target non-idealities. The key characteristics of the pattern and probe-based aberration monitors are each target's:

- 1) zero-aberration reference intensity level at the center
 - 2) sensitivity to the aberration under test
- and
- 3) orthogonality or insensitivity to other aberrations.

Each of these factors is important and it is necessary to understand how they are interrelated for subsequent design iterations.

5.2.1. Typical Target Response

Figure 5-2 shows cut-lines from left to right through the intensity profiles seen in Figures 4-11 and 4-12, generated by the two-ring spherical target and the three-ring defocus target, given various aberration conditions. A number of features are immediately evident from these plots. First, the position and relative size of the rings is easily discernable. Second, the intensity goes fully to zero midway between 0° and 180° lines. Third, the probe intensity is found to change greatly for the specific aberration that each target is designed to look for while changing very little for other, even similar, aberrations. The specific intensity values for the spherical target have been presented previously in Section 4.4, and indicate that the target shows a large intensity change at the center for small amounts of spherical aberration, while maintaining relatively good orthogonality to the very similar defocus aberration.

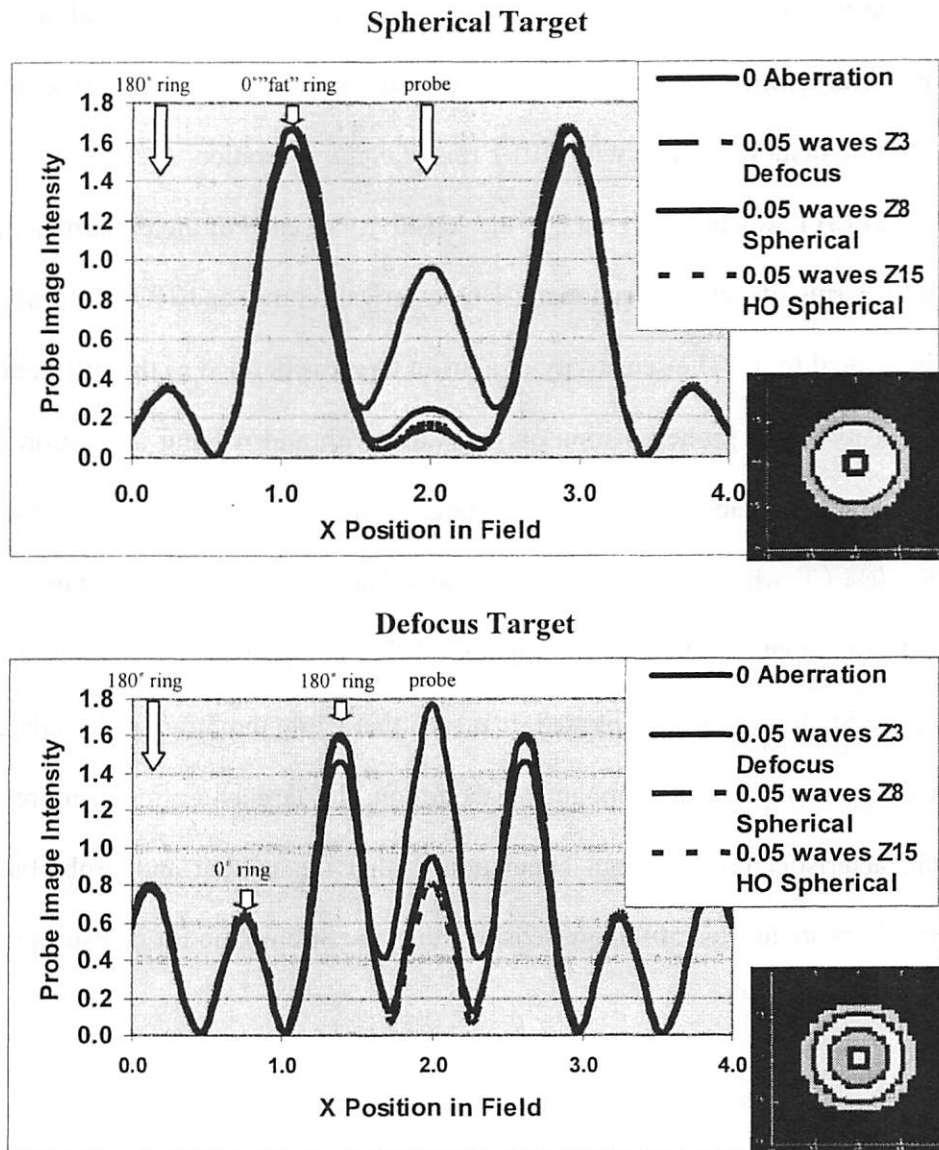


Figure 5-2. Intensity cut-lines through the images of the two-ring spherical target (top) and the three-ring defocus target (bottom) for 0.05λ (peak-to-peak) of various rotationally symmetric aberrations. The horizontal axis is in units of $\frac{\lambda}{NA}$. (Data from Figures 4-11 and 4-12.)

Rather than using peak-to-peak values for the aberrations in the simulations, it is best to compare target responses using rms values. This is because rms is a measure of the wavefront variance, which is the total integrated “volumetric” difference between the real and the ideal wavefronts. In other words, the Strehl ratios for two imaging systems are

the same, provided that the total wavefront variance of each is small and equal [67]. In practical terms, this means that the Strehl ratio for a system with 0.01λ rms of defocus is equal to that of a system with 0.01λ rms of coma aberration.

SPLAT was used to simulate the sensitivity of each of the patterns in Target Set 2 to 0.01λ rms of defocus, spherical, HO spherical, coma, and HO coma aberration, on an individual basis. The sensitivity of a given target is defined as the difference between the intensity at the probe position on the wafer with and without aberration divided by the rms amount of aberration. For these targets, the probe image intensity increases by 22% to 30% CF when 0.01λ rms of the individual aberration that the target is designed to detect is input, as illustrated in Figure 5-3. For comparison, the magnitude of the change of the Strehl ratio is also plotted. It is seen that while the Strehl ratio only drops by 0.4% CF from unity for this amount of aberration, the targets are much more sensitive. The characteristic trend through simulation is that the pattern and probe-based aberration monitors are at least $50\times$ more sensitive than the Strehl ratio for measuring aberrations.

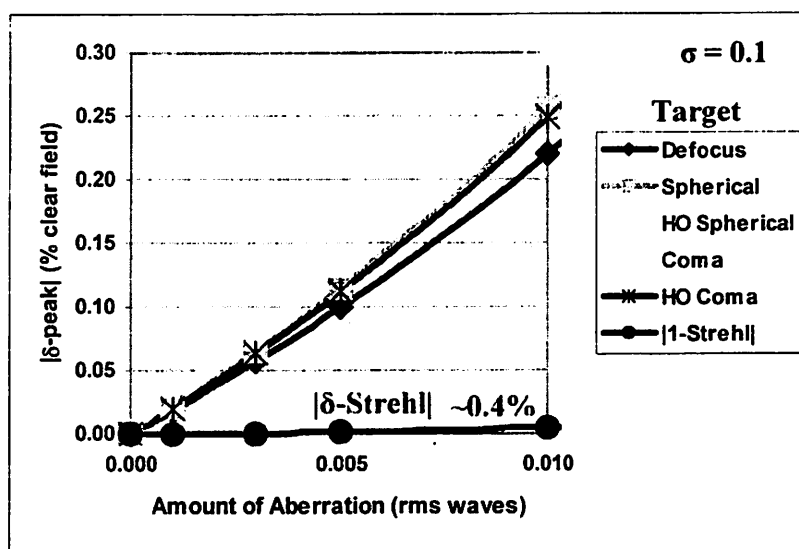


Figure 5-3. Change in probe image intensity with aberration for the layouts in Target Set 2. Note that all of the targets show a sensitivity of 22 – 30% of the clear field with 0.01λ rms of their individual aberration while the change in the Strehl ratio is less than 0.4% for that same amount of aberration. 0.30 on the vertical axis corresponds to an intensity change of 30% CF.

The complete set of results, including the sensitivity of each target to aberrations that it should be insensitive to, is tabulated in Table 5-1. Here each column corresponds to one of the test targets and each row corresponds to an aberration condition. The entries for the “No Aberration” row are the reference levels of the peak value at the center of the target normalized to a clear field intensity of one. The entries for the aberration rows show the change in this peak value as a fraction of the clear field value due to the introduction of 0.01λ rms of that aberration. The results are grouped by rotational symmetry of the aberrations to emphasize the radial effects within each symmetry class. The diagonal of the matrix shows the sensitivity of each target to the aberration for which it was designed. In all cases the phases of the rings and the probes have been chosen such that the addition of the aberration increases the intensity at the probe position. Most of the off-diagonal terms are negligible with the maximum crosstalk (noise/confounding) found to be about 40% between the defocus target and the HO spherical aberration target.

$\sigma = 0.10$	Target Set 2				
δ -peak (%CF) with 0.01λ rms of	Defocus	Spherical	HO Spherical	Coma	HO Coma
No Aberration	0.933	0.242	0.207	0.555	0.222
Defocus	+0.220	-0.034	-0.021	<+0.01	< -0.01
Spherical	<+0.01	+0.256	-0.056	<+0.01	<+0.01
HO Spherical	-0.084	-0.063	+0.299	<+0.01	<+0.01
Coma	+0.020	<+0.01	<+0.01	+0.299	-0.038
HO Coma	<+0.01	<+0.01	<+0.01	< -0.01	+0.249

Table 5-1. Summary of the target sensitivity and orthogonality. Each pattern in Target Set 2 is shown in a column and each row is for a 0.01λ rms of a given aberration.

Ideally, the center intensity with no aberration would be just that of the isolated probe ($\sim 19\%$ CF). This is because, if the mask pattern generates electric-fields which are the inverse Fourier transform of any Zernike aberration term, except $Z_{1,0} = 1$, then the fields incident upon the pupil plane are orthogonal to the unaberrated pupil function and the mathematical theory developed in Chapter 4 shows that the spillover contribution to the center is zero. However, there are many non-idealities in the target design and it is evident from the top row of the table, when no aberration is present, that the central intensity is too high for the defocus, spherical, and coma target designs. The question is: How much do each of the non-idealities, such as the use of a finite σ and mask openings with unity transmission, the spatial truncation of the target, and the chunkiness of the targets, affect their behavior?

5.2.2. Phasor Electric-Field Model

Given the complex interactions between all of the factors contributing to target behavior, it is particularly helpful to begin to split up target into its components to characterize the properties of each. This leads to a relatively simple to understand

electric-field phasor model of target operation, indicating the difficulty of deconvolving the effects. A phasor is simply a vector representation of an electric-field, wherein the magnitude of the field is given by the phasor length and the phase angle is given by its angle from the abscissa. Electric-fields with 0° or 180° phase lie along the positive and negative real-axes, respectively. Those with 90° or 270° phase lie along the positive and negative imaginary-axes, respectively. Fields with any other phase angle are represented by phasors which can be decomposed into both real and imaginary components.

Using a two-ring defocus target from Target Set 3, a full simulation of the target response in the presence of its implementation shortcomings is studied in detail. Figure 5-4 shows cut-lines through the simulated intensities generated by the probe alone (upper left) and by the rings alone (upper right) with $\sigma = 0.313$, for the zero aberration case, 0 RU, and for the case where $\frac{1}{2}$ RU of defocus is introduced into the system. The combination of rings and the probe, shown at the bottom of the figure, is far more sensitive to defocus than either the probe itself or the rings themselves. With no aberration the probe reaches an intensity of $\sim 19\%$ of the clear field. Taking the square root of the intensity at any given position gives the magnitude of the electric-field. Thus, E_p , the normalized electric-field at the probe position, is 0.43. With no aberration, the intensity at the center of the rings alone is due to the well-known proximity effect. Its value is 31% CF, giving an electric-field at the center, E_R , of 0.56.

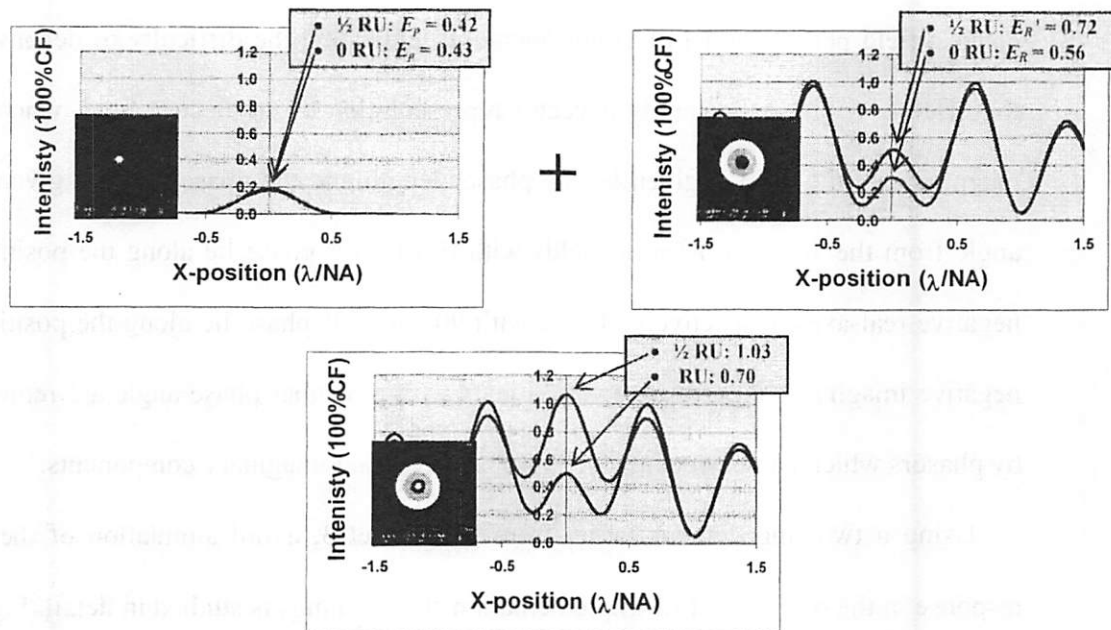


Figure 5-4. Electric-fields generated at the center of the defocus target by (top) the probe and the rings individually and (bottom) the complete target ($\sigma = 0.313$). The electric-fields are calculated with no aberration and with $\frac{1}{2}$ RU of defocus. Only the isolated probe has a lower intensity and electric-field at the central position when the defocus aberration is present.

On the left side of Figure 5-5 an electric-field phasor diagram is shown, indicating the real and imaginary contributions at the center of the target in the image plane when there is no aberration. Because the probe is 90° phase-shifted, E_p is purely imaginary. E_R , on the other hand, is purely real. Coherent addition of these vectors calls for taking the square root of the sum of the squares of their magnitudes to predict the electric-field which results from simulating the full target (probe and rings together) with zero defocus. Adding the field contributions in quadrature predicts that the full target should have an electric-field of 0.706 at the center. Simulation of the full target in SPLAT (Figure 5-4, bottom) gives 0.70, which is in excellent agreement with the predicted value. The prediction of this value from the individual field contributions is important because it is the magnitude of the square of this vector that is finally observed in the image plane.

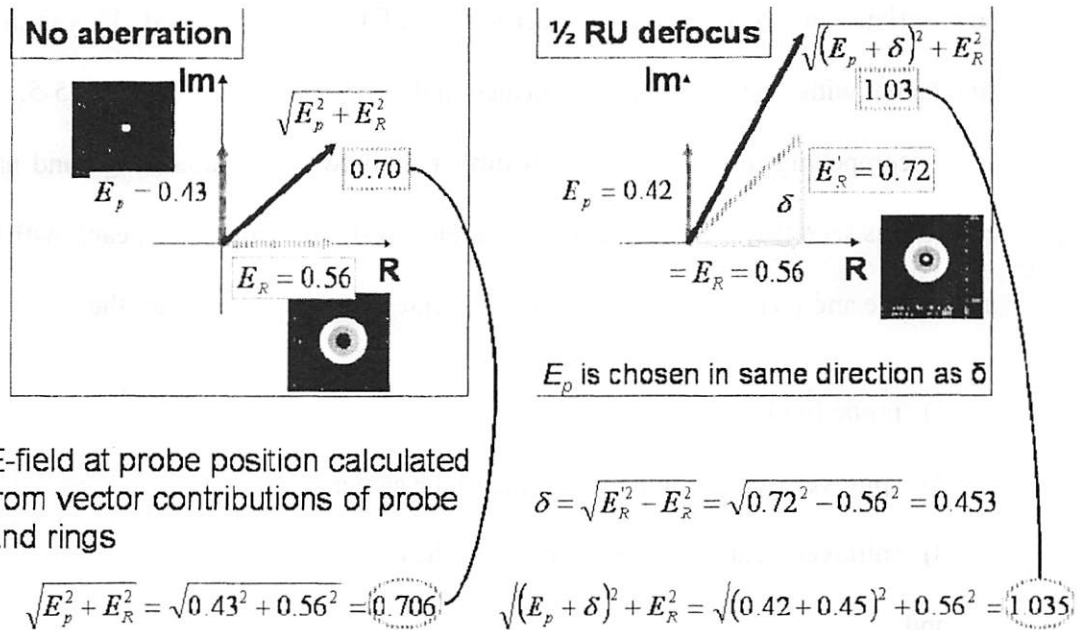


Figure 5-5. (Left) Coherent addition of electric-field contributions from probe and surrounding target rings when no aberration is present. This scenario consists of two vectors which compose the final electric-field at the center of the pattern. (Right) Coherent addition of the probe field, the spillover field from the surrounding rings (proximity effect), and the perturbation to this spillover due to the presence of defocus aberration.

Adding $\frac{1}{2}$ RU of defocus to the simulation decreases the peak intensity of the isolated probe to $\sim 17\%$ CF, but the electric-field decreases only slightly to 0.42. In fact, for small amounts of defocus, the fields from the probe can be considered constant. The field at the center of the rings alone however is perturbed significantly, increasing to 51% CF, corresponding to an electric-field, E_R' , of 0.72. Assuming that the purely real part of the proximity effect spillover component of the field, E_R , does not change with small amounts of aberration, the total perturbed spillover vector $E_R' = 0.72$, can simply be decomposed into its real and imaginary components. It is seen that the perturbation to the spillover, δ , is 0.45. Squaring the sum of E_p and δ and adding that to the square of E_R predicts the final perturbed intensity at the center of the target. Substituting the

appropriate numerical values, an electric-field of 1.035 is predicted. This is in excellent agreement with the value of 1.03 indicated in the right hand side of Figure 5-5.

Decomposing the target one step further, into two individual rings and an isolated probe, it is seen that there are actually four electric-field components, each with their own magnitude and phase angle, that contribute center intensity. These are the:

- 1) probe field
 - 2) spillover field from the inner ring to the center
 - 3) spillover field from the outer ring to the center
- and
- 4) perturbation to the spillover fields with aberration.

These contributions are illustrated in the ideal phasor diagram in Figure 5-6.

The magnitude of the field from the probe, indicated by the length of the vector, E_p , is determined by the size of the probe and also somewhat by the phase etch depth. The phase angle of the probe field is determined by the phase etch depth and ideally lies along the imaginary axis. Because surrounding pattern rings are ideally 0° and 180° , the spillover vectors that they produce at the center lie along the real axis, with magnitudes E_{outer_ring} and E_{inner_ring} , respectively. In Figure 5-6, the contribution from the 180° inner ring is drawn as if its spillover were 180° phase-shifted and the contribution of the 0° outer ring is drawn as if its spillover were 0° merely for illustrative purposes. In reality, whether the spillover vectors from these rings lies along the positive or negative real axis depends not only upon the phase of the ring but also upon the distances of the inner and outer edges of the ring from the target center and the partial coherence of the

illumination. Finally, when defocus aberration is added into the optical system, the spillover vectors are perturbed, yielding a fourth electric-field vector, with magnitude δ directed along the imaginary axis. For small aberrations, δ is directly-proportional to the amount of aberration.

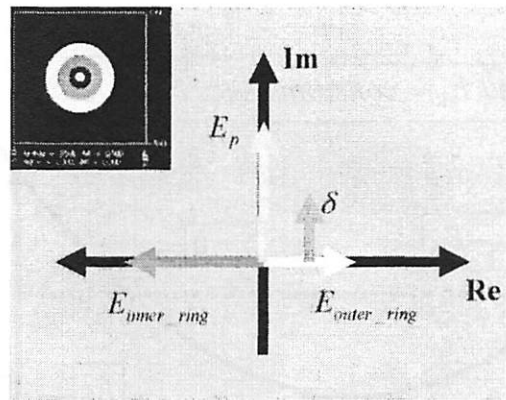


Figure 5-6. Electric-field phasor diagram of the contributions from the probe, ring spillover, and perturbation to the ring spillover due to defocus.

The influence of each of these components upon the intensity at the probe position as a function of the amount of defocus is illustrated in Figure 5-7. In the diagram, the bottom, downward-opening parabola indicates the Strehl behavior of an isolated probe. The isolated probe intensity, E_p^2 , is relatively insensitive to defocus, with the peak of the parabola occurring as expected at best focus. The intensity from the combined spillover of the rings is given by E_R^2 . This value is independent of the amount of defocus. Because coherent addition of the phasor contributions can be assumed and because the total combined spillover of the rings is orthogonal to the fields from the probe, the intensity at the center of the target at best focus ($\delta = 0$) is simply $I_{center} = E_p^2 + E_R^2$. When defocus is added to the system δ is no longer zero. The plot indicates that for positive amounts of defocus, the perturbation vector points in the same direction as that generated by the

probe and for negative amounts of defocus it points opposite to that of the probe. Accounting for the aberration-independent term and an aberration-dependent term, the intensity at the center of the target in the image plane is given by $I_{center} = (E_p + \delta)^2 + E_R^2$, which is illustrated by the upward-opening parabola in the figure.

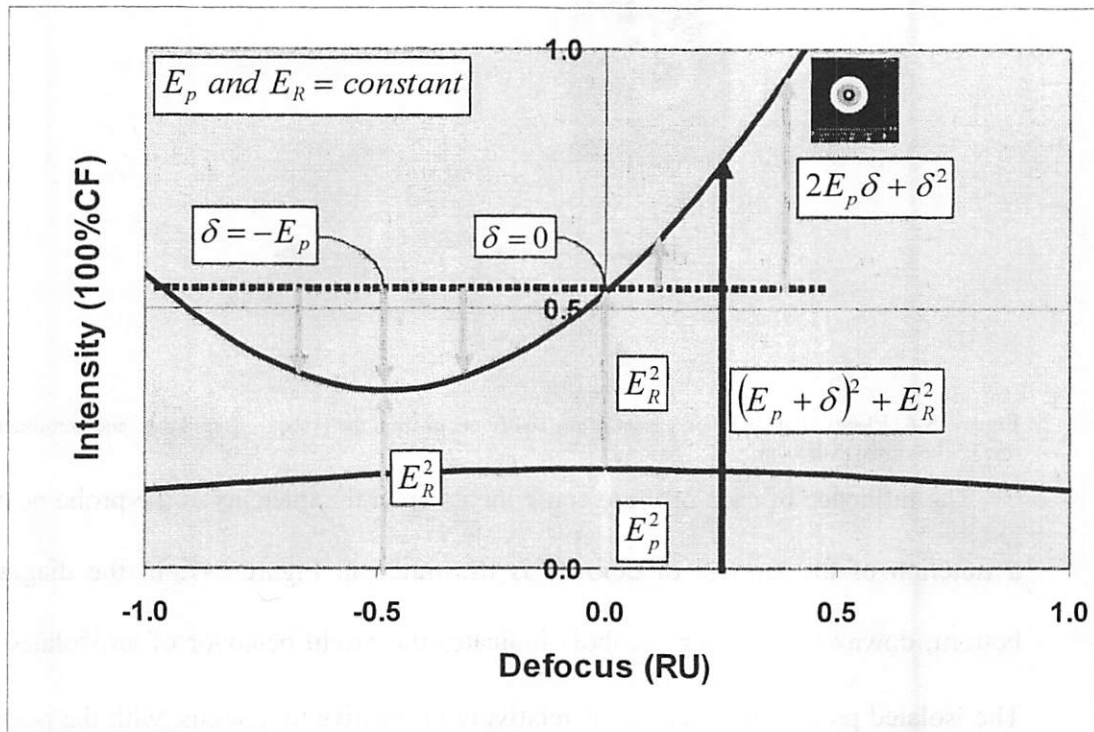


Figure 5-7. Electric-field contributions at the center of the 2-ring defocus target for varying defocus. The magnitude and phase of the electric-field from the probe (E_p), as well as that from the proximity-effect (E_R), are constant while the perturbation to the spillover (δ) varies with the amount of the given aberration.

A couple of things are obvious from the simulated target response in Figure 5-7. First, the intensity at the probe position is parabolic with the amount of defocus. Second, the minimum of the parabola does not occur at best focus, but rather it is shifted by about $-\frac{1}{2}$ RU. The amount of lateral shift is directly related to the magnitude of the field generated by the probe. This is because, a certain amount of defocus is needed to make $\delta = -E_p$. This lateral shift makes it so that there is a relatively steep slope of target response for

small amounts of defocus around best focus. This slope is the sensitivity of the target and for this target is 70% CF/RU or nearly 1% CF/0.01 λ rms of defocus.

The keen observer may note that the goal of reducing the central intensity in the unaberrated case to just that of the isolated probe, δ^2 , is achieved if the total ring spillover vector $E_R = 0$. In other words, if E_{outer_ring} and E_{inner_ring} are equal and opposite then the pattern is orthogonal to the $Z_{1,0} = 1$ “aberration”. In Figure 5-7 however, the non-idealities of finite partial coherence, target truncation, and unity transmission cause E_{outer_ring} and E_{inner_ring} not to cancel each other, resulting in a center intensity of about 55% CF at best focus. Careful observation reveals that this is actually only an issue in the rotationally-symmetric targets because any target with azimuthal variation has equal amounts of 0° and 180° area weighted at equal distance from the center. The reason that the unaberrated intensities in Table 4-1 for the coma and HO coma targets do not exactly match that of isolated probes is because the maximum intensity in the central probe region was reported rather than the intensity exactly at the center of the target. The lack of orthogonality to the unaberrated case is just one of a number of second-order effects inherent in the rotationally-symmetric targets.

5.3. Mask, Illumination, and Tool Effects

Of key importance is the ability to predict the performance of pattern and probe-based aberration monitors in a realistic production environment in the context of tool constraints, mask making, and the mask’s electromagnetic performance. The issues having to do with illumination, include the effects of the partial coherence factor (σ), the effect of off-axis illumination, and the effect of obscuration due to alignment optics.

These factors, as well as mask performance issues such as fabrication tolerances and the effects of intensity imbalance, are the focus of this section.

5.3.1. Mask Making Tolerances

Mask making tolerances are a major concern for the implementation of pattern and probe-based aberration monitors because both the minimum grid size and the ability to produce the required phases are important. The targets pictured in Figure 5-8 decrease in complexity and increase in pixel size from left to right. The target on the far left is the HO spherical target from Target Set 2, containing 117 rectangles on the mask, with a minimum pixel size of $0.076 \frac{\lambda}{NA}$. This corresponds to a pixel size on the mask of >100 nm for a 4× lithographic stepper tool with $\lambda = 193$ nm and $NA = 0.55$. The remaining targets consist of 53, 21, and 9 mask openings, respectively. The rings for all of the targets are at least a minimum feature size ($\sim 0.5 \frac{\lambda}{NA}$). As can be seen from the plot, the aberration sensitivity is greatest for the target with the largest number of rectangles at about 30% CF/0.01 λ rms. The sensitivity decreases monotonically as the targets become less and less ideal, with a noticeably sharp drop between the targets made of 53 and 21 rectangles. Thus, while the orthogonality of all of these targets to other rotationally symmetric aberrations remains relatively good, the targets made with 21 and 9 rectangles trade simplicity for a decreased orthogonality (increased sensitivity) to aberrations with four-fold symmetry, such as astigmatism.

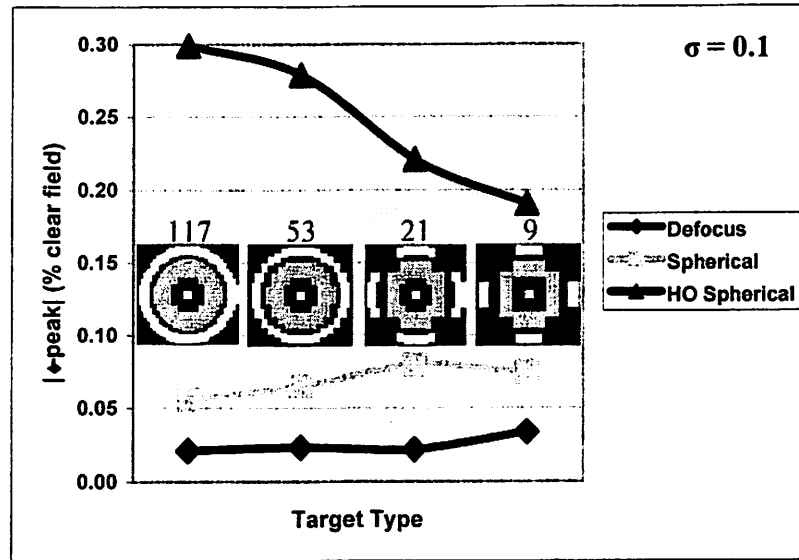


Figure 5-8. High-order spherical aberration target response to 0.01λ rms of given rotationally symmetric aberrations ($\sigma = 0.10$). The probe is phase shifted at 90° , the inner ring is phase shifted at 180° , and the outer ring is un-phase shifted.

5.3.2. Illumination – Partial Coherence Factor (σ)

As previously mentioned, lithography tools have minimum σ values of about 0.30. As σ increases, it is reasonable to expect a loss in target sensitivity and perhaps an increase in cross-contamination from other aberrations. The question of how to mitigate these effects given larger σ values is important in understanding the operation of the targets. Understanding the mutual coherence function for a given illumination condition can be used to guide redesign the targets to partially compensate for these effects.

To study the effects of partial coherence, the spherical aberration target from Target Set 2 was chosen as a typical example and tested with rotationally symmetric aberrations. Its behavior at different values of σ was investigated and the results for the change in intensity at the probe position in the image plane are plotted in Figure 5-9. The inset in the figure shows the target layout and the coherence radius of $3.05 \frac{\lambda}{NA}$ for $\sigma = 0.20$ and

$1.22 \frac{\lambda}{NA}$ for $\sigma = 0.5$. At small σ (< 0.33) the light is considered to be coherent over the entire target. From the plot, for $\sigma = 0.10$, it is seen that the intensity at the probe position on the wafer increases from the unaberrated value by 26% CF when 0.01λ rms of spherical aberration is added. The cross-contamination (noise) from the same amount of other similar aberrations is at most 1/4 this value, or 6.5% CF. As σ is increased to 0.5, corresponding to a coherence radius smaller than the target size, the sensitivity decreases to a level nearly equal to the noise. Thus, σ is quite important in determining the signal-to-noise ratio for the target. Despite the sensitivity loss, it may be possible to use this type of target at a σ of about 0.30 given that the cross-contamination from other aberrations is less than 40% of the sensitivity. Other factors however, such as polarization effects, electromagnetic edge effects, and phase etch errors may significantly degrade target performance.

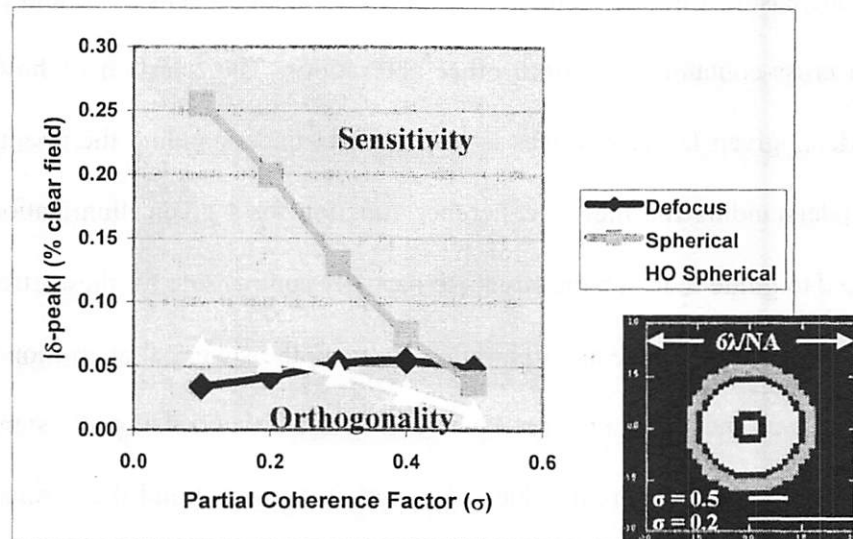


Figure 5-9. Change in intensity at the probe position as a function of the partial coherence factor (σ) on the spherical aberration target response to 0.01λ rms of various rotationally symmetric aberrations. Note the high sensitivity of the target to spherical aberration and good orthogonality to similar aberrations at low σ .

5.3.3. The Effect of Adding More Rings

Every modification to the target layouts is an attempt to optimize their zero-aberration reference level, their sensitivity, and their orthogonality. In order to address some of the first-order effects such as the effect of the chunkiness and the limited number of rings in the targets in Target Set 2, the logical step was to create high-quality smooth patterns with many rings, as seen in Target Set 3. While σ does set a practical limit on the target size, it is important to understand the effect of adding more rings.

Using a σ value of 0.30 in SPLAT, the responses of one-, two-, three-, and four-ring versions of defocus targets from Target Set 3 have been studied. The intensity at the center of each target, as well as the Strehl behavior of an isolated probe, is shown as a function of the amount of defocus programmed into SPLAT in Figure 5-10. In general, the sensitivity is indicated by the slope of the parabola in the operating region around best focus, where many processing steps occur. At best focus the general trend is for the slope of the parabola to increase with the number of rings. The maximum slope is observed for the target with three rings, with the four-ring target showing only the second largest slope. This is most likely because, with the larger radius of the outer ring in the four-ring target, the coherence of the perturbation to the spillover fields from the outer ring is degraded.

A number of other interesting features are highlighted in Figure 5-10. Firstly, a larger number of rings gives a greater minimum intensity for the target. This is simply because the total proximity-effect spillover into the middle of the target is directly related to the total amount of (properly phased) open area around the probe [68]. Secondly, the zero-defocus intensity for each target increases with the number of rings. This is simply an

extension of the previous observation in that the unaberrated target intensity is equal to the minimum target intensity plus the probe intensity. Thirdly, the defocus value at which each parabola reaches its minimum moves towards the right as the number of target rings increases. Following the previous discussion, this implies that if more rings are present then less defocus is required to perturb the spillover fields sufficiently to fully counterbalance the field from the probe, E_p . A target with more rings has somewhat greater sensitivity to the given aberration than one with fewer rings.

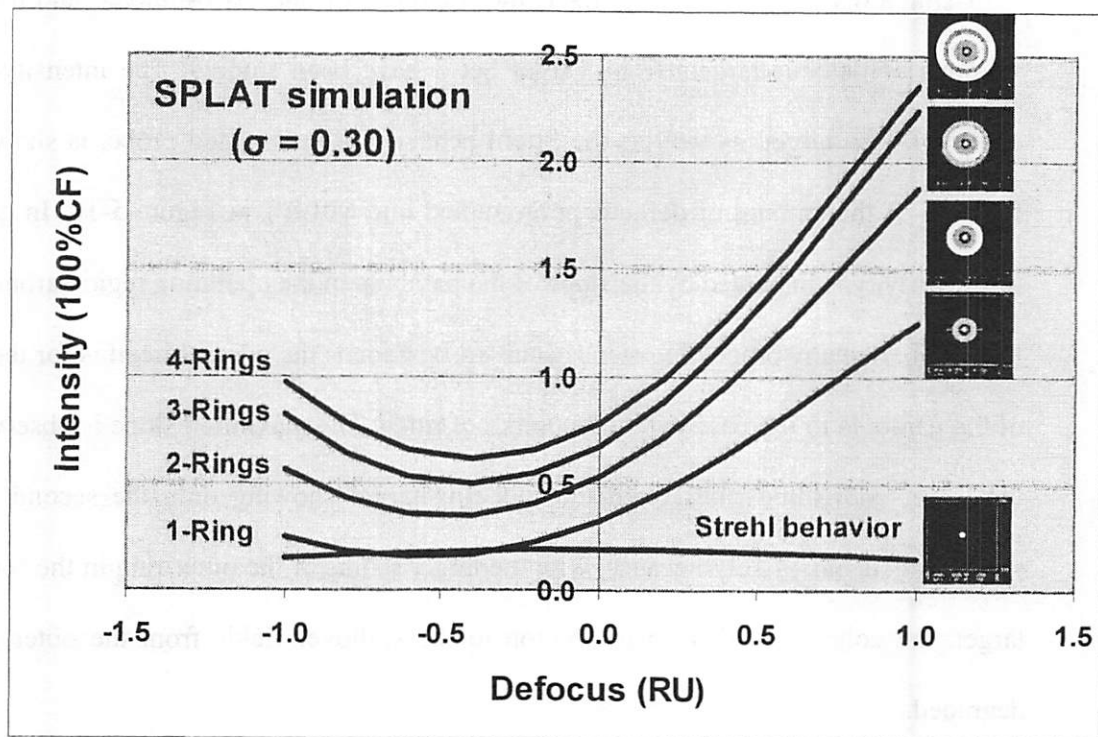


Figure 5-10. Simulated intensity at the center of 1-, 2-, 3-, and 4-ring defocus targets (mask patterns inset) for varying values of defocus. The through-focus peak intensity of a sub-resolution mask opening shows the parabolic Strehl behavior, reaching a peak of 19% CF at best focus.

Despite the greater sensitivity, a problem which arises when more rings are added to the target is that the target radius can grow larger than the coherence length of the illumination. To study what happens when additional target rings begin to fall outside of

the coherence radius, a spherical aberration target consisting of seven concentric rings from Target Set 3 was chosen as a typical example. This target is shown on the left side of Figure 5-11.

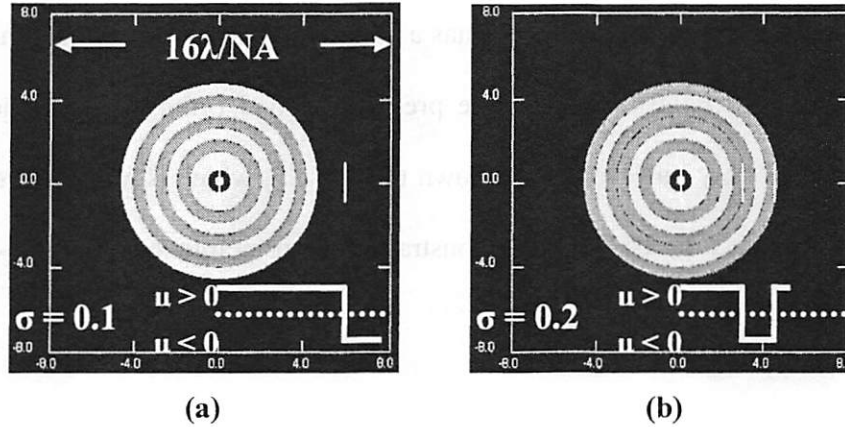


Figure 5-11. Mask layouts of large seven ring spherical aberration target. The black area is $16 \frac{\lambda}{NA} \times 16 \frac{\lambda}{NA}$. The target on the right is optimized for $\sigma = 0.20$ by modulating the phases of the rings by the sign of the mutual coherence function.

Inset in Figure 5-11 is the sign of the mutual coherence function as a function of distance from the probe center for (a) $\sigma = 0.1$ and (b) $\sigma = 0.20$. For $\sigma = 0.10$ the light is coherent over the entire large seven-ring target area. A sensitivity of 50% CF/0.01 λ rms of spherical aberration results; which is nearly twice the sensitivity of the two ring target. However, the zero-aberration value of the probe is 77% CF, which is much higher than the 24% for the two-ring version of the target from Target Set 2. When σ is increased to 0.20, the coherence radius shrinks by a factor of two and the mutual coherence function has positive sign from the probe center to the boundary between the fourth and fifth pattern rings and negative sign for the remaining outer portion of the pattern. When $\sigma = 0.20$, and the original ring phases, as seen in Figure 5-11 (a), are used, the sensitivity to

spherical aberration drops to 24% CF/0.01 λ rms, the orthogonality remains quite good, and the zero-aberration probe intensity is 64% CF.

Modulating the ring phases by the sign of the mutual coherence function as a function of radius to compensate for coherence effects yields the target seen in Figure 5-11 (b). For $\sigma = 0.20$, this modified target has a sensitivity slightly better than the uncompensated target, 26% CF/0.01 λ rms, while preserving good orthogonality. The zero-aberration central intensity however, drops down to 23% CF, which is much nearer to the 19% CF of an isolated probe. This demonstrates the principle of target re-optimization for different illumination conditions.

5.3.4. Resizing the Chrome Isolating Region

Another feature of the targets, which has not been discussed to this point, is the size of the chrome isolating region, or “donut”, which separates the probe from the innermost target ring. The size of this region, r_{cr} , is measured from the center of the target to the inner edge of the first ring and is shown in Figure 5-12 for the two-ring defocus and coma targets from Target Set 3. For reference, the circular probes have a radius given by $k_1 = 0.2257$. Simulations were performed using SPLAT, varying r_{cr} from $k_1 = 0.5$ to $k_1 > 1$, and the results plotted in Figure 5-13. They show that the target response of is highly dependant upon r_{cr} .

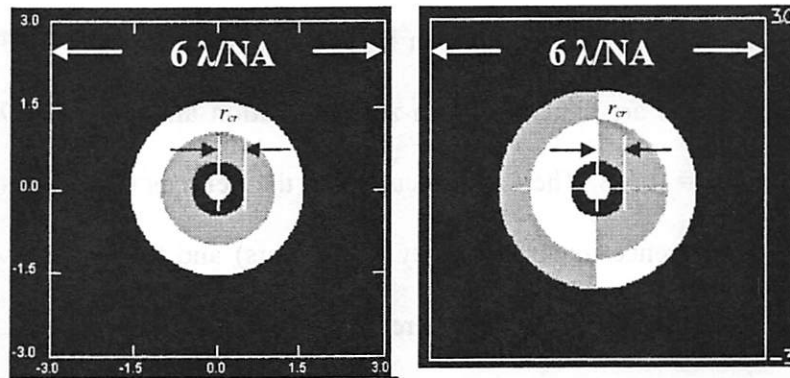


Figure 5-12. Mask layout of the two-ring defocus Zernike target (left) and the two-ring coma Zernike target (right) indicating the radius of the chrome region isolating the probe from the surrounding target pattern.

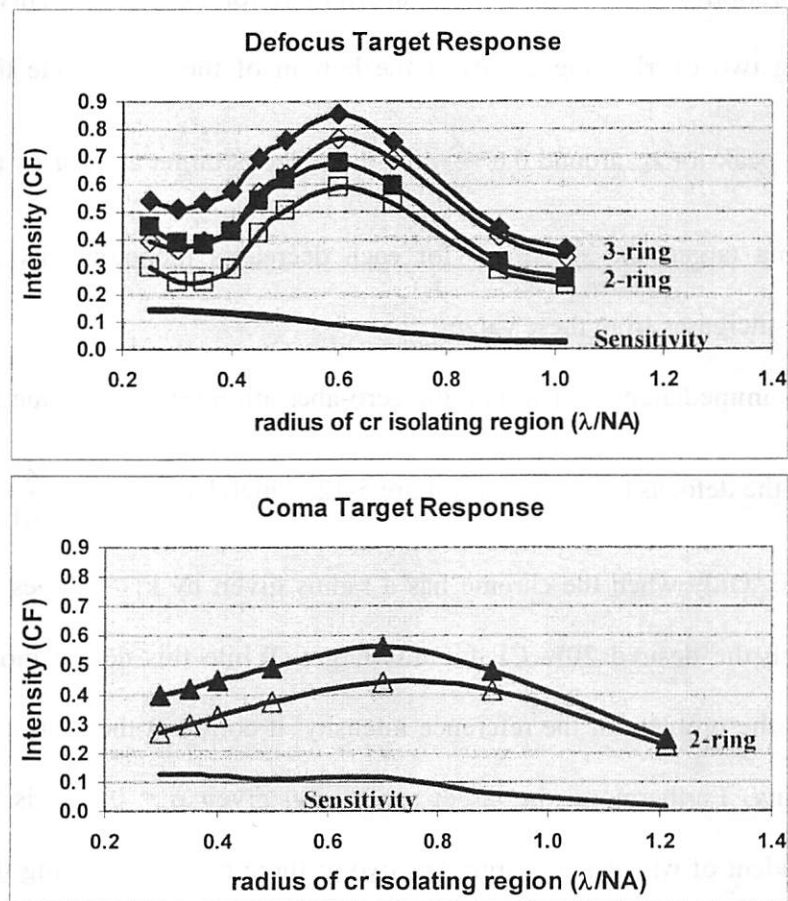


Figure 5-13. Sensitivity of defocus and coma target responses to the size of the chrome isolating region separating the probe from the surrounding target pattern rings ($\sigma = 0.313$). In the top plot, squares are for the two-ring and diamonds are for the three-ring defocus target from Target Set 3. Empty data points are with zero aberration. Solid data points are with 0.01λ rms of the associated aberration. Their difference is plotted as the target's sensitivity.

A great deal of information can be gleaned from the plots in Figure 5-13. In each case, the targets are simulated with zero aberration and with 0.01λ rms of defocus or coma with $\sigma = 0.313$. The top two curves in the defocus target response show the zero-aberration reference intensity (empty data points) and the intensity with 0.01λ rms of defocus (solid data points) for a three-ring target. The middle two curves on this plot show the same information for a two-ring version of the target. The difference between the aberrated and unaberrated intensity values (i.e., the sensitivity of each target configuration to 0.01λ rms of the aberration) for each set of curves is also plotted, yielding two overlapping curves at the bottom of the plot. While the intensity values show a peak for r_{cr} around $0.6 \frac{\lambda}{NA}$ for the defocus target and for r_{cr} around $0.7 \frac{\lambda}{NA}$ for the coma target, the sensitivity for each decreases monotonically as the size of the chrome increases from these values.

It is immediately evident that the zero-aberration reference value is very sensitive to r_{cr} . For the defocus target seen in Figure 5-12, which has $r_{cr} = 0.5 \frac{\lambda}{NA}$, this value is about 50% CF. Only when the chrome has a radius given by $k_1 > 1$ does the intensity value approach the desired 20% CF for this target. While this design modification helps to address the problem of the reference intensity, it comes at the cost of about a $4\times$ loss in sensitivity. Furthermore, the target sensitivity, given $\sigma = 0.313$, is almost completely independent of whether the target has two or three rings. This being the case, sensitivity can be maintained and the desired zero-aberration reference intensity can be more readily approached by using a two-ring target and by shrinking r_{cr} to around $0.35 \frac{\lambda}{NA}$. At this

point on the plot, the sensitivity is about 14% CF/0.01 λ rms and the zero-aberration reference value is about 23% CF.

5.3.5. Phase Shifting Mask Intensity Imbalance

Until now, all of the investigation and analysis has been to characterize how changes in the planar geometry of the mask openings affect the ideal thin-mask behavior of the image. In practice, a significant intensity imbalance is observed between the phase shifted and un-phase shifted elements when the targets are printed. That is, mask openings that are phase shifted by 180° are found to require a higher exposure dose than regions of equal size that are un-phase shifted mask openings to print equally.

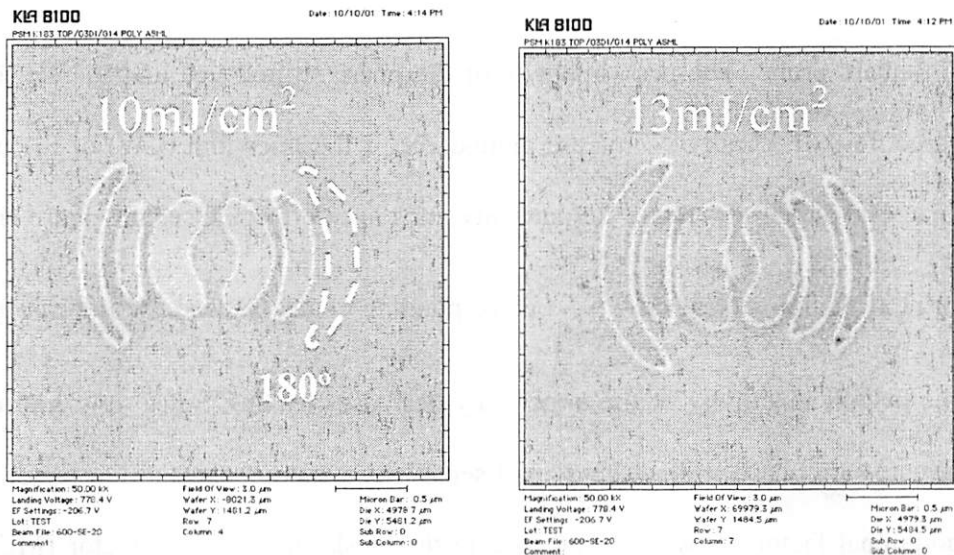


Figure 5-14. SEM's of coma aberration target exposure at two different exposure doses. There is a noticeable intensity imbalance between the phase shifted and non-phase shifted rings. (Curtosey Nick Eib & Ebo Croffie, LSI Logic.)

For example, Figure 5-14 shows two photoresist exposures of the coma target from Target Set 2 in a very preliminary experiment carried out by Ebo Croffie of LSI Logic.

Noting the phases of this target from Figure 3-5, it is found that, at an exposure dose of 10 mJ/cm^2 all of the 0° regions print while the regions phase shifted at 180° print significantly smaller or not at all. The 180° phase shifted region shown to be missing in (a) prints, at 13 mJ/cm^2 as its 0° twin prints at 10 mJ/cm^2 . Thus, the intensity imbalance is about a 30% effect for this target. In essence, the phase shifted region acts smaller than it actually is. Normally a designer would compensate for this by finding an equivalent bias and laying out the phase shifted region larger so that it prints as its correct size.

To investigate the effect of intensity imbalance on the ability of the pattern and probe-based aberration monitors to measure aberrations, a highly modified coma target was simulated. Figure 5-15 shows the layout of the target, consisting of a single 0° mask opening of width of $0.69 \frac{\lambda}{NA}$, a single 180° phase shifted mask opening, and a standard 0° square probe. The peak intensity of the phase shifted line and the sensitivity of the target to 0.01λ rms of coma are plotted versus the linewidth (LW) of the phase shifted line. The plot shows that if the intensity imbalance effect causes the phase shifted line to print as though it were $0.50 \frac{\lambda}{NA}$, corresponding to a 31% decrease in peak line intensity, the overall sensitivity of the target only decreases by 8%. Since only half of the target features are phase shifted the overall sensitivity would decrease by a factor of two. The additional factor of two is likely due to the mask enhancement factor (MEF) in image formation. Because the probe spillover is directly proportional to electric-field spillover, this additional MEF contribution does not occur in the interferometric probe response. Thus, it is concluded that biasing the phase shifted region in a simple pattern such as this is not a dominant factor in determining target sensitivity.

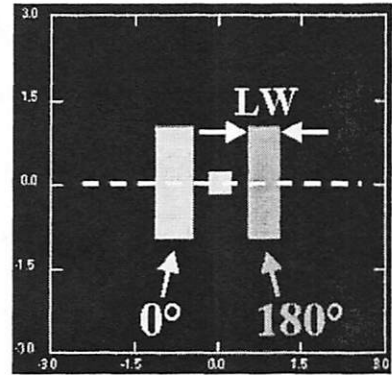
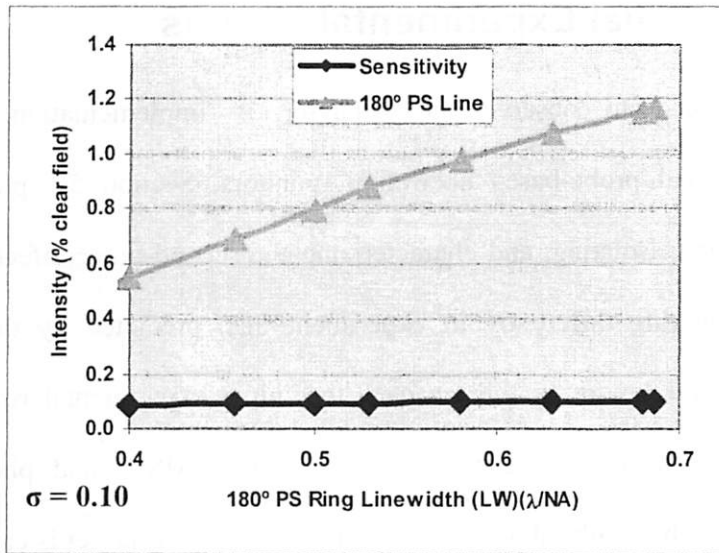


Figure 5-15. Plot of the intensity of the 180° phase shifted line and target sensitivity (aberrated probe peak intensity minus unaberrated probe peak intensity) as a function of 180° phase shifted line line width. Note that the target sensitivity remains relatively constant while the intensity of the line decreases dramatically with line width ($\sigma = 0.10$).

6. Initial Experimental Results

Experiment is needed to observe the behavior in implementation of the interferometric pattern and probe-based aberration monitors. Section 5.1 presents a framework for identifying, isolating, and characterizing the second-order effects which lead to the targets operating differently in experiment than predicted by thin-mask simulation at low-NA and low- σ . In this chapter, the initial experimental results for aberration targets designed for $\lambda = 248$ nm, using both AIMSTTM and photoresist exposures are presented. The results show in general that the defocus target is capable of measuring focus to the required level of about 0.01λ rms but that this and the other targets tested from Target Set 3 have significant second-order effects which influence target response and readability.

The multi-phase photomasks used throughout this work were generously donated by DuPont Photomask, Inc. and Photronics, Inc. as part of what has become the UC-SMART (Semiconductor Manufacturing Alliance for Research and Training) Program's Feature Level Compensation and Control Award. A total of four masks have been fabricated to date, three designed for $\lambda = 248$ nm and one for $\lambda = 193$ nm. The masks designed for use at 248 nm are referred to as 248A, 248B, and 248C. These masks are highly-experimental, requiring expensive fabrication processes. They contain experimental structures for several students, and compromises had to be made regarding design and fabrication to achieve the minimum cost/scientific benefit ratio. Effort was taken to keep costs down by minimizing write time and by accepting the masks from the manufacturers on a first-write basis with no error checking.

6.1. Preliminary Aerial Image Measurement System™

Results

As mentioned briefly in Section 5.1, the AIMS™ tool, first invented at IBM and now manufactured and marketed by Zeiss, is designed to provide, “stepper equivalent optical conditions”, which can generate the real intensity distributions that mask patterns will produce on the wafer. There are a number of versions of the AIMS tool: the MSM 100 ($\lambda = 248$ nm), originally invented in 1993, the AIMS™ fab for wavelengths down to 248 nm, and the AIMS™ fab 193 for the 193 nm wavelength. Each of these models represents advances in ease of use, tool stability, aberration control, and lithographic resolution.

At its heart an AIMS tool is simply a DUV microscope with two operating modes: a reflected light optical mode (not available for the AIMS™ fab 193), in which it is possible to locate the target of interest in a larger field at a relatively low magnification (10× and 50×), and a transmitted light imaging mode where 193, 248, or 365 nm light is be passed through the mask in order to obtain the aerial image given the illumination and imaging parameters. The optics of the AIMS tool are small compared to those of a lithographic exposure tool and the imaging field is correspondingly small. In the tool, two separate apertures are used to control the partial coherence of the illumination and the other to set the numerical aperture of the collection lens.

The aerial image is captured by passing light through the photomask, mounted on a computer-controlled X-, Y-, Z-positioning stage, and then collecting the scattered fields with the microscope objective. The fields are brought to focus inside the microscope tube but because the resolution of CCD arrays is insufficient to capture many interesting

features resulting from the typical 4× reduction of the mask openings, it is not this plane which is imaged. Instead, a second set of optics is used to magnify this “image” onto the CCD. While the latest AIMS systems can simulate exposure tools with NA’s surpassing 0.80, it is in this final step that high-NA polarization effects are lost in the tool. In general, a data set consists of a through-focus series of images, using the computer control to move the stage along the optic (Z-) axis by a pre-determined amount in between exposures. Though it was originally conceived of and marketed as a tool to measure mask quality and defect printability, AIMS has proven a powerful technique for investigating the pattern and probe-based aberration monitors discussed herein.

6.1.1. AIMS Modification for Initial Experiment

Unfortunately, the features on the first photomask fabricated for this experiment, mask 248A, were oversized by an extra factor of 4×. The key enabling factor in using the AIMS technique on this mask was the modification by Bruce Griffing of the MSM 100 DUV & i-Line system in the Round Rock, Texas facility of DuPont Photomask, Inc. to image at an NA of 0.2. With this model of the tool, special apertures of 150 nm and 300 nm could be inserted manually into the imaging and illumination paths. This required first making pinholes to replace the apertures provided with the tool to test the feasibility of the approach and then mounting and inserting commercially available pin holes. A critical step was aligning the pin holes and the lenses. Finally, the operation set-up was also modified to extend the CCD camera capture time from its typical value of a few hundred milliseconds to approximately eight seconds. Good signal to noise was observed although no special effort was made to optimize image quality during the modified

operation. Fortunately, the setup modification could be introduced or removed in about one hour through the efforts of technicians Jason Hickethier and Rahim Momin.

Given the uncertainty of the actual optical parameters that would result, the investigation was limited to the two-ring versions of the targets in Target Set 3. The experiment took place over the course of two days. On each day the apertures had to be inserted into the system and aligned separately to optimize the quality of both the illumination and the captured light. Alignment of a field stop was also required. Before the exposures were taken on each day, and at regular intervals during a measurement session, a clear field reference was measured through a large area mask opening. Subsequent scans were normalized by these clear field reference scans and image plane intensity values are given as a percentage thereof. The data was taken over the course of two days and one significant difference between the data taken on the first and second days is that the optics of the system were adjusted on the second day to center the focus reference around the highest Strehl ratio.

6.1.2. AIMS Calibration

In order to utilize the modified AIMS tool to quantitatively analyze the response of the aberration targets the horizontal scale factor, focus scale factor, numerical aperture, and partial coherence of the system must be calibrated. In addition, the reference level of an isolated interferometric probe and noise levels in the measurements must also be determined. Determining these factors can be confusing and were accomplished as follows.

The AIMS output pixel size was first calibrated by measuring the location of the printed phase edge for the two-ring defocus target. Figure 6-1 shows the target layout and the AIMS tool CCD image normalized to the clear field reference. The intensity minimum caused by the phase edge is clearly evident and, as will be seen in the intensity cut-lines in Figure 6-6, has a null-to-null spacing (diameter) of 116 pixels. Using the knowledge that the location of the printing of phase edges tends to be very insensitive to the NA of the system ($NA_{measured}$), combined with the fact that the innermost phase edge of the defocus target is designed to have a diameter of $2.04 \frac{\lambda}{NA_{design}}$, a useful horizontal scale for AIMS data is extracted. One pixel on the AIMS tool is calculated to be $0.01759 \frac{\lambda}{NA_{design}}$.

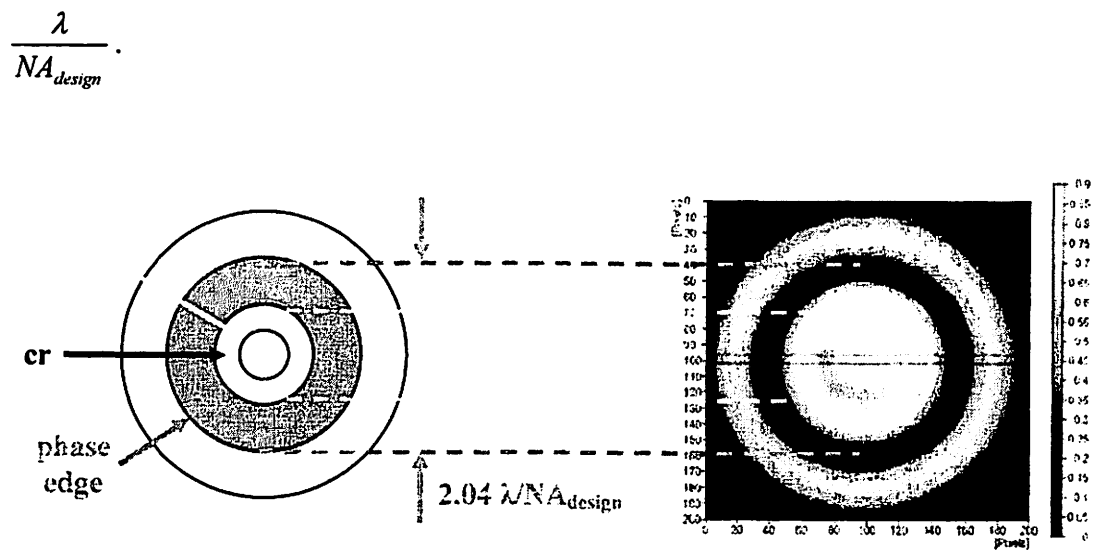


Figure 6-1. (Left) GDS layout of the two-ring defocus target. (Right) AIMS CCD image of the defocus target at maximum defocus.

The working NA of the AIMS tool, $NA_{measured}$, was then determined from the point spread function (PSF) of the system, which was obtained by imaging an isolated probe. The intensity versus field position in pixels is shown in Figure 6-2 for 11 focal planes.

The spacing between the first nulls of the PSF is 75 pixels, or $1.319 \frac{\lambda}{NA_{design}}$. This distance is $1.22 \frac{\lambda}{NA_{measured}}$, which implies that one pixel is $0.01627 \frac{\lambda}{NA_{measured}}$. Hence

$NA_{measured}$ is estimated to be $(1.22/1.319) \times NA_{design} = 0.18$.

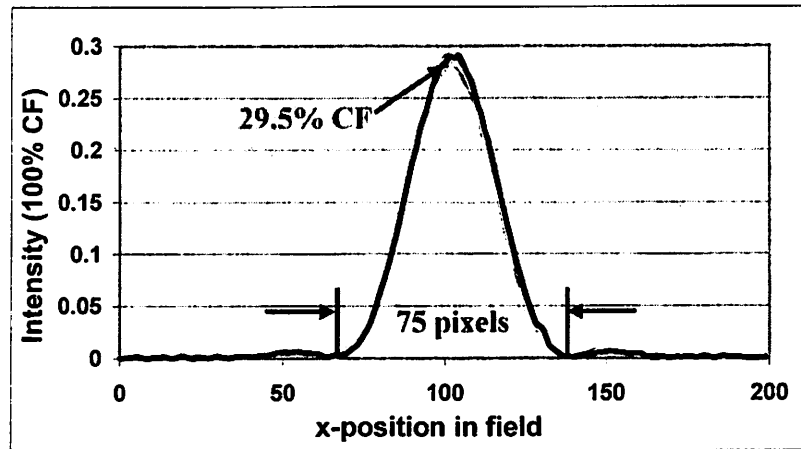


Figure 6-2. Point spread function of the AIMS tool for an isolated probe (nominally $0.45 \frac{\lambda}{NA}$ in diameter) through 11 focal positions. $NA_{design} = 0.2$, $NA_{measured} = 1.8$.

The focus scale factor can be determined from the change in peak intensity of the PSF with focus. Figure 6-3 shows the intensity versus focal position for 11 focal planes around the best focus. Although there is some noise in the data, a parabola fit to the points indicates a peak value of 29.3% CF at 7.6 focal units. Referring to Appendix C, 1 RU of defocus aberration alone results in a Strehl ratio of 79%. From this, the size of a focal unit in μm or λ can be determined. The focal position at which the parabola is 79% of its maximum represents 1 RU of defocus. This occurs 15.8 focal units on either side of best focus. Using Equation 2-4, 1 RU of defocus in this system is $3.83 \mu\text{m}$. This gives a horizontal calibration of 1 focus unit = $0.24 \mu\text{m}$ or 0.063 RU. In hindsight, it would have

been more appropriate to run this experiment with the focal steps a factor of $M^2 = 16$ larger in order to sample more of the parabolic behavior of the probe intensity through focus.

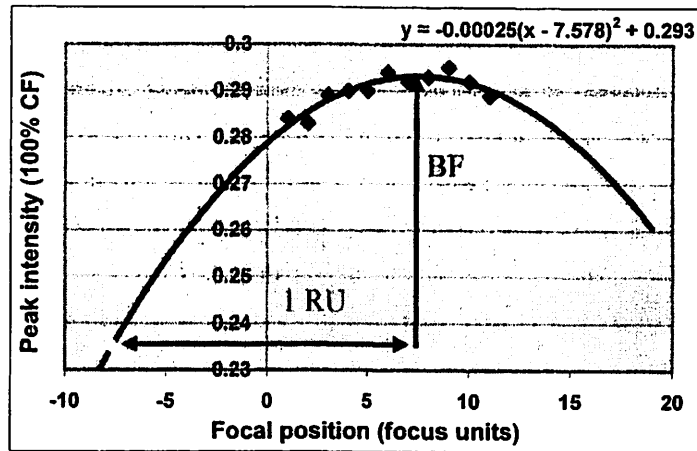


Figure 6-3. Peak intensity of isolated probe as a function of focal position. A parabola is fitted to demonstrate the Strehl ratio behavior and to find best focus.

The noise in the intensity measurements on the AIMS tool with the modification was quite low. The multiple intensity measurements for the isolated probe in Figure 6-2 roughly indicate that the noise level is less than 1% CF. Figure 6-3, the peak value extracted versus focus, shows this in greater detail.

The radius of the isolated probe can also be calibrated from Figure 6-2. The peak intensity of the PSF along with NA_{measured} , yields the actual size of the probe. A probe of diameter $k_1 = 0.45 \frac{\lambda}{NA}$ has a simulated peak intensity of 18.8% CF while the maximum intensity of the actual probe investigated was 29.5%. The higher intensity at a lower NA indicates that the probe-opening radius was oversized by two factors in radius. The first factor increasing the radius compensates for NA_{measured} being only 92% of NA_{design} to bring the intensity up to the nominal 18.8%. The second factor accounts for the fact that

the peak intensity measured is significantly higher than this nominal 18.8%. It was determined via simulation that, assuming that the aberrations in the tool are small, the isolated sub-imagable probe was oversized by 23.5% in diameter.

To complete the baseline calibration of the AIMS tool the coherence of the illumination needs to be understood, as well as the presence of other important aberrations. This is investigated by studying how a large feature, a line of width $\sim 2.35 \frac{\lambda}{NA} = 13 \mu\text{m}$, prints. Figure 6-4 shows a cut-line through the AIMS intensity data as well as three simulation results for a line of the same size with various illumination and aberration conditions. An attempt is made first to match the magnitude of the peaks at the edges of the line and then to match the left-to-right imbalance by introducing an appropriate amount of x-coma aberration. Simulations were performed using SPLAT and the lowest curve in at x-position $= 3 \frac{\lambda}{NA}$ is the AIMS data. With no aberrations, simulation results for $\sigma = 0.50$ and 0.30 are symmetric and they overlap in the middle. The $\sigma = 0.30$ result reaches a higher peak value, more closely matching the AIMS data. It is therefore concluded that σ is at least as small as 0.30 , meeting the operational constraints of the experiment. Adding 0.01λ rms of balanced coma in the x-direction causes an asymmetry in the simulated peak heights, approximating the peak height asymmetry in the measured data. This shows the probable presence of coma in the AIMS system.

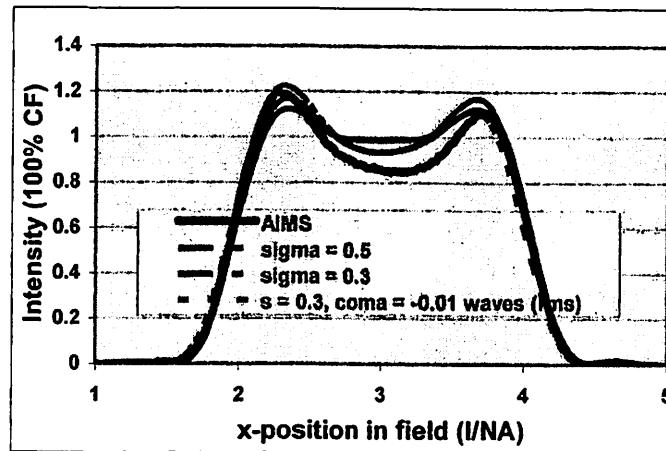


Figure 6-4. Intensity cut-lines through AIMS data and SPLAT simulations of a 13 μm line. The simulation approximates the measured data when σ is small and a small amount of x -coma is present in the system.

6.1.3. Target CCD Images

To the observer not familiar with these targets, it is very easy to recognize each target by its intensity pattern at the image plane. Figure 6-5 shows the AIMS CCD images of two-ring aberration targets from Target Set 3. The three targets with rotational symmetry, which are the defocus, spherical, and higher-order spherical targets, are readily identifiable while the two-fold symmetry of the coma and HO coma targets makes them obvious. The higher-order symmetries of the other images indicate the individual aberrations that they are designed to detect. Observation of the images also indicates second-order effects in target printing. In the non-rotationally-symmetric targets it can be seen that, while the layout may have certain symmetries, the intensity patterns show some differences. For example, the image intensity of the 4-foil target shows that the open areas in the inner ring of the target have alternating high and low intensities every 45° . While this may be due to the intensity imbalance effect commonly found in phase shifted mask areas it could also be a property of the lens. Large amounts of aberrations may be

present in the modified AIMS tool, which could result in such asymmetries. Finally, it is seen that, for certain targets, the image of the probe tends to "bleed" into the phase shifted regions of the inner target rings. This is especially evident in the coma and higher-order coma targets and suggests that increasing the size of the chrome region surrounding the probe might benefit target operation.

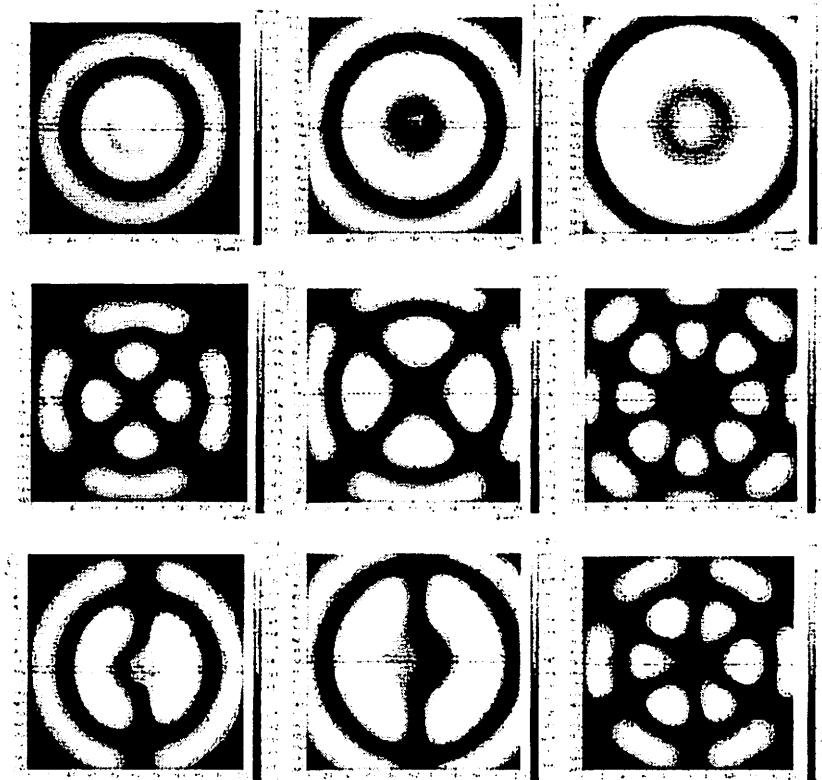


Figure 6-5. AIMS CCD images of two-ring IFT aberration targets (in same order as Figure 3-6). For $\sigma = 0.30$, the illumination is coherent over the radius of two-ring targets.

6.1.4. Analysis of Focus

Because the object plane position can be computer controlled in the system, the defocus target is the obvious candidate for in-depth investigation. The simulation results in Section 5.2 indicate that the probes at the center of the aberration monitors are far more sensitive to aberrations than ordinary features. The first experimental confirmation

of this was achieved by observing the response of a two-ring defocus target from Target Set 3 using AIMS. Figure 6-6 shows intensity cut-lines through the AIMS data for a two-ring defocus target. The 11 focal positions are the same as those in Figure 6-3, with each step being $0.24 \mu\text{m}$.

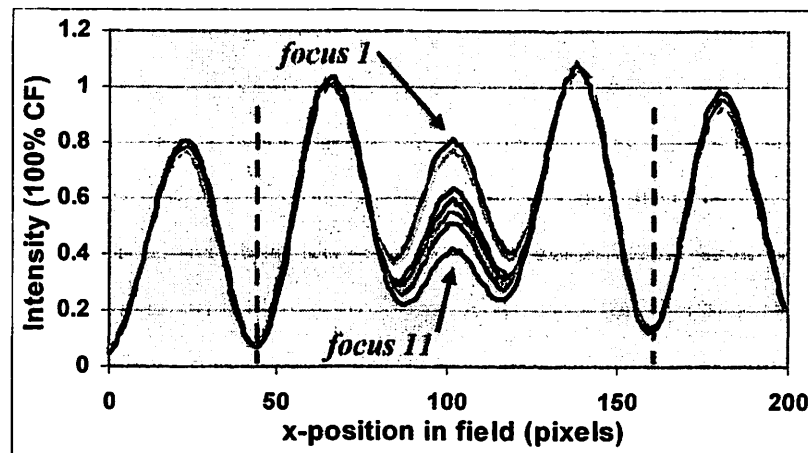


Figure 6-6. Measured AIMS intensity cut-lines showing target response to focal position.

Figure 6-7 shows the center intensity of the target measured in Figure 6-6 as a function of the programmed defocus along with the Strehl behavior of the isolated probe (the PSF). On the horizontal axis, 15.8 focal units equals 1 RU of defocus. While the Strehl ratio changes quadratically, with very little variation in small steps about best focus, the linear response of the defocus target makes it very attractive for highly accurate focus measurements. The isolated probe intensity changes little over the focal range ($= 3.2 \mu\text{m}$). The target probe intensity varies by 39% CF, giving a 12.2% intensity change per μm of defocus. Given that 1 RU of defocus in this system is $3.83 \mu\text{m}$, $1 \mu\text{m}$ of defocus $= 0.26 \text{ RU}$. Thus, the defocus changes linearly by 47% CF/RU when measured in a $\pm 1/2 \text{ RU}$ interval about best focus. With a measurement error of 1 - 2% CF, the focal

position can be determined to within 1/40 RU. This is the first experimental evidence of the high sensitivity and linearity of these aberration monitors. Furthermore, the absolute determination of best focus agrees with that of the Strehl ratio behavior to within 1/35 of a RU. If the target probe were oversized by 23.5% (given the NA_{measured} of the system) however, the accuracy is reduced to only 1/5 of a RU.

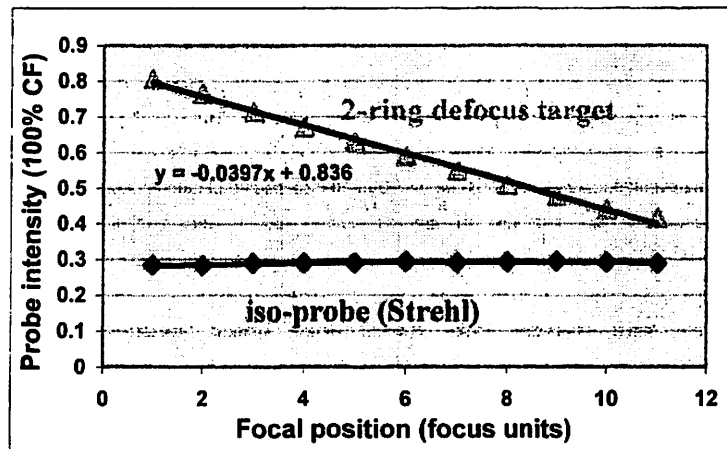


Figure 6-7. Intensity of isolated probe and two-ring defocus target probe v. focal position. Note that the peak intensity of the isolated probe remains relatively constant while the defocus target probe intensity changes significantly over the same range of focus values. 12 focal units = 1 RU.

6.2. Preliminary Photoresist Exposure Results

As mentioned in the introduction, the aberration targets require a difficult-to-fabricate multi-phase mask. For this experiment, a new reticle, 248B, with correctly sized openings, was made for measuring nine different Zernike terms at multiple locations in the field on five different exposure tools operating at a wavelength of 248 nm. The designs include a 5× tool with $NA = 0.5$ and two 4× ASML scanners (/750 and /850) with $NA = 0.70$ and 0.80 , respectively. In anticipation of using partially-coherent illumination with σ about 0.30 one, two, three, and four ring patterns that are contained fully within the mutual coherence distance of the probe were included. A relative bias of the 180°

features was included to help offset the intensity imbalance effect. Figure 6-8 shows the aberration module which was instantiated at 13 positions across the field, separated by a horizontal distance of 1800 μm each at the wafer plane. There were four rows of these 13 sets of targets for the 4 \times portion of the mask to measure the lens top to bottom as well.

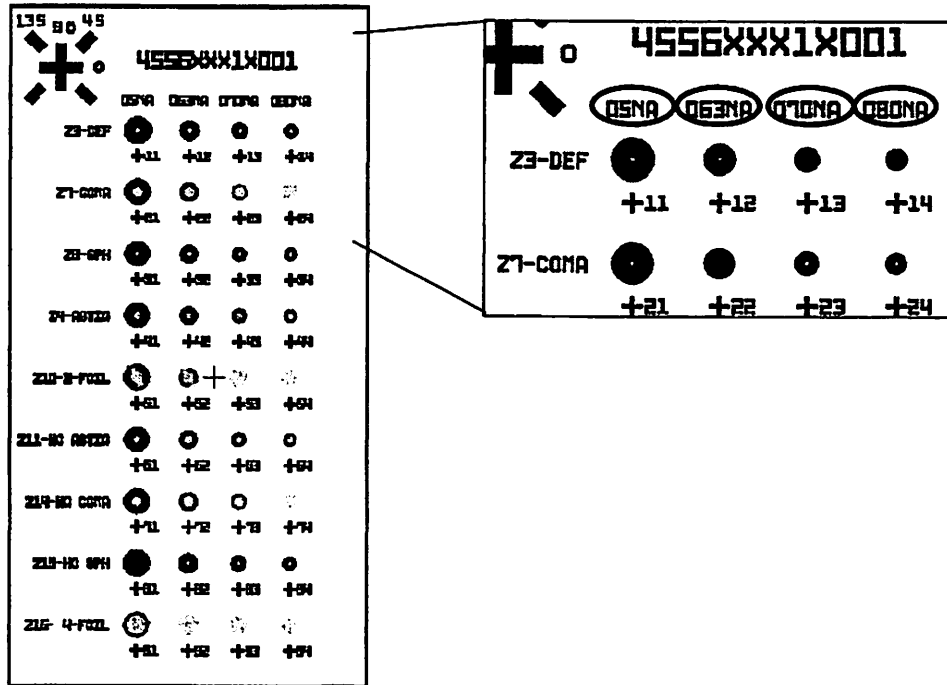


Figure 6-8. GDS layout of the aberration module containing targets for the first nine Zernike aberrations designed for exposure tools with NA = 0.50, 0.63, 0.70, and 0.80. Not shown are the targets with only one or two rings for small σ .

The exposures for this experiment were done on a /850 scanner with variable NA and σ at the ASML Demo Lab in Tempe, AZ. In all cases, the wavelength was 248 nm, NA = 0.80, and $\sigma = 0.313$, corresponding to a Rayleigh depth of focus unit of 194 nm. The resist stack and process was a standard 2975 \AA of UV III0 atop 600 \AA of AR2 BARC, yielding a uniformity of 25 \AA and a dose to clear $E_0 = 7 \text{ mJ/cm}^2$. A standard coat, exposure, bake, and development process was used. The experiment consisted of exposing focus-dose matrices of the targets and observing their printed images on the

wafers to detect the printing of the probe at the center. For this experiment, a CD-SEM was used to determine the exposure tool's best focus in either the nominal or the aberrated state by observing Bossung plots generated by line-space patterns in the resist. The /850 scanner was operated in two states. One was the "nominal" state in which the aberrations were minimized to achieve the maximum Strehl ratio. The other was the "coma" state in which machine parameters were adjusted to induce a tilt in coma across the field. Experiments were performed by first exposing wafers in the nominal state and then switching over to the aberrated state and repeating the exposures with the same focus and dose settings.

6.2.1. Focus Monitor Performance

An independent measurement of best focus was made using the Strehl technique for an isolated $k_1 = 0.722$ diameter probe on the mask (i.e., designed for $NA = 0.50$ but exposed with $NA = 0.80$). The results through focus and dose are shown in Figure 6-9. Here the focal steps are 100 nm (approximately $\frac{1}{2}$ RU) and the dose steps are 0.3 mJ/cm^2 . The resist image behavior is quite systematic through both energy and focus. Plotting the behavior of the Airy function along with the dose-to-clear as a threshold (see the bottom of the figure), best focus can be determined by finding the exposures where the dot prints with the largest diameter. Direct visual inspection can differentiate between two exposures laterally, corresponding to a 100 to 200 nm accuracy in determining focus with this method.

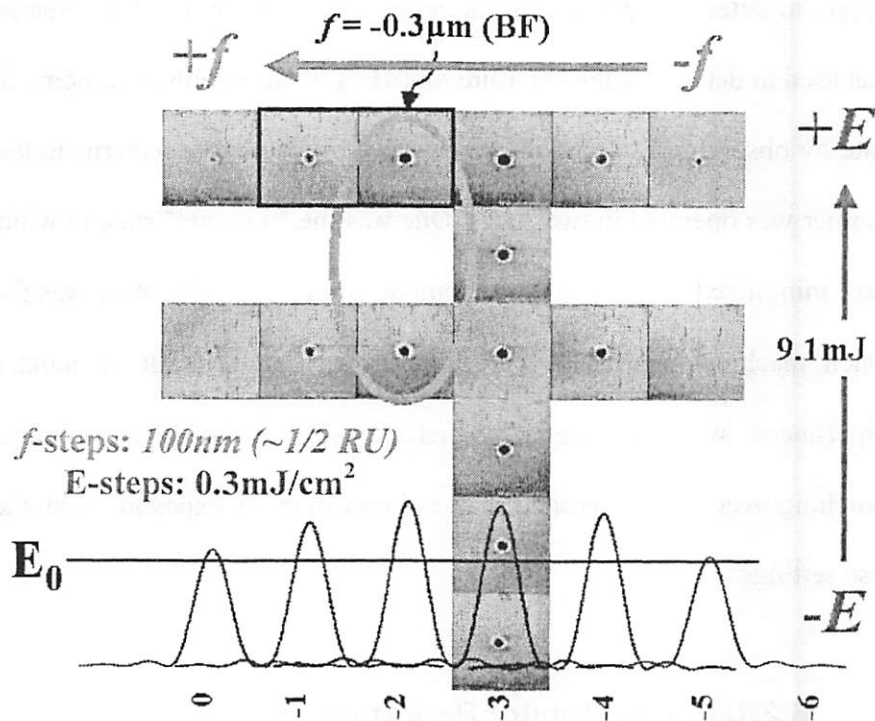


Figure 6-9. Through-focus exposures of the isolated probe designed for $NA = 0.50$ but printed with $NA = 0.80$. Best focus (BF) is determined by the point at which the PSF of the system reaches a maximum. At the bottom is a model of how the PSF prints in relation to the dose-to-clear.

Because the probe in the middle of each aberration target is nominally sub-printable and surrounded by a pattern which is designed to have a small amount of proximity-effect spillover, the center of a target should print as a $1 \frac{\lambda}{NA}$ diameter resist disk, due to the chrome donut around the probe, when the specific Zernike of interest is not present in the correct amount. For the defocus target, at a certain defocus value the intensity at the center breaks through the resist exposure threshold and the probe begins to print as a hole inside the resist disk. If there is enough defocus, then soon the energy in the middle becomes so large that the resist disk is consumed from the inside out, leaving nothing but the outer target features. This is important to understand because it is somewhat

counterintuitive that the probe prints stronger out of focus than at best focus. To summarize, there are three states that the target can be in:

- 1) the resist disk is present but the probe does not print
 - 2) the probe prints within the resist disk
- and
- 3) the probe prints so large so as to consume the entire central resist disk.

Figure 6-10 shows the results of one two-ring defocus target printed through focus (left to right) and dose (top to bottom). As in Figure 6-9, the focal steps are 100 nm and the dose steps are 0.3 mJ/cm^2 . Best focus was determined to be column -2 and the general trend is for the central probe to print when the tool is significantly out of focus. It is interesting and somewhat intuitive to note that the rings print most strongly at best focus. Thus, it is postulated that the energy passing through the target on the mask spills over into printing the probe when defocus is present and goes into printing the rings when there is little defocus. One observation is that the exposures show an overall diagonal trend through focus and dose. This is expected because increasing either defocus or dose can be used to make the dot print stronger. In the bottom row the printed dot response is easiest to read from column 1 to column 0. It would have been better experimentally to continue to higher doses so that the edge of the diagonal region that just prints moves over closer to best focus. That is, the dose should be increased to shift the smallest printed dot to best focus.

The second observation which can be made from this series of exposures is exemplified by the rate at which the printing of the target dot changes with a focus step of 100 nm. A single focus step causes a diameter change of the target dot that is larger than that seen for three focus steps with the isolated dot in Figure 6-9. The image generated by the defocus target is thus read to be about a factor of 4× better at measuring the focal position than the peak of the point spread function generated by a small opening.

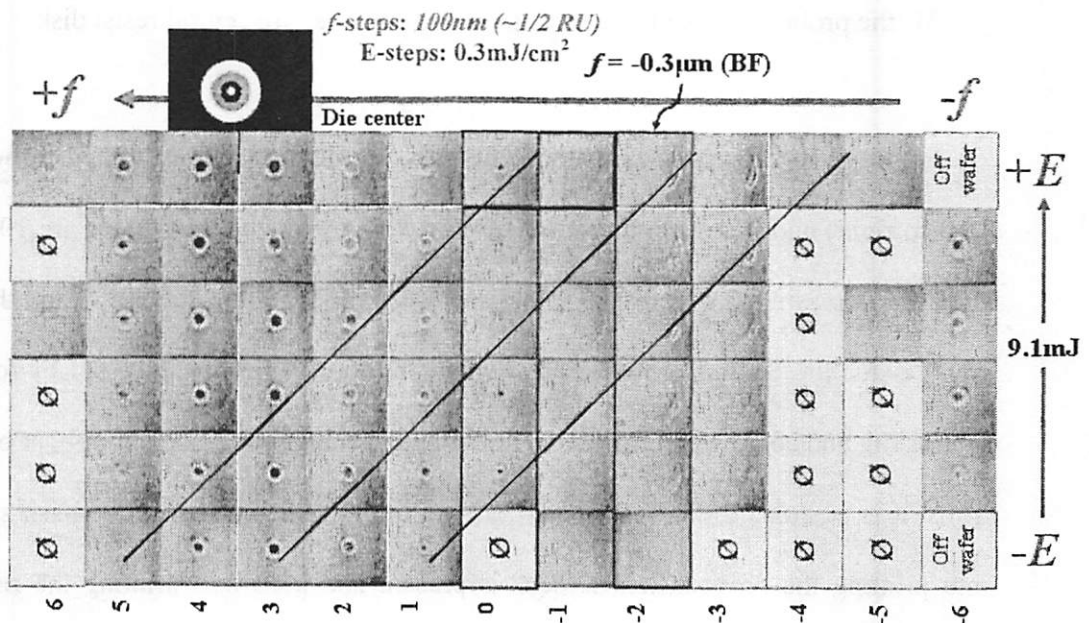


Figure 6-10. Images of two-ring focus target resist exposures through focus and dose.

Each of the images in Figure 6-10 was taken at the same position on many different die on a single wafer and taken together they establish the behavior of the target through dose and focus. Looking at how many copies of the target print across the field helps to determine across-field focus variation combined with wafer and chuck flatness. Figure 6-11 is used to investigate both the best method of reading the resist images and to determine the across-field focus variation. The top row of images is from 13 copies of the

defocus target across the die (field). The bottom row of images is from the same targets but taken with the focus changed by 200 nm (~1 RU) from the top row. Very little difference is seen in how the target prints across the die in the top row, revealing little information about the die topography. However, the bottom row shows a noticeable trend with the dot printing strongly on the left hand side of the die, then disappearing approximately 1/4 of the way across the field, then reappearing slightly in the middle, disappearing again 3/4 of the way across the die, and finally reappearing steadily as the right hand side of the lens is reached.

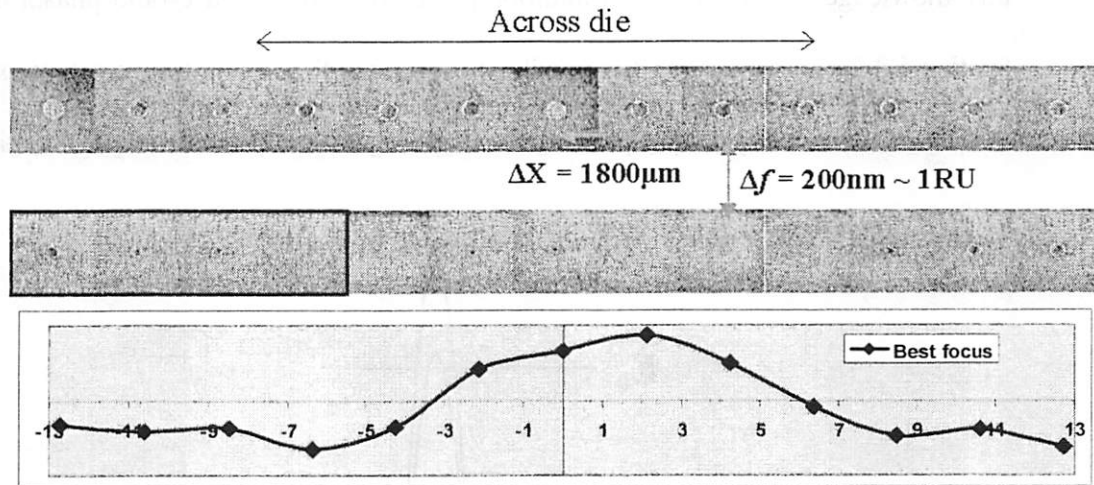


Figure 6-11. (Top) Exposures of 13 focus targets across a single die. (Middle) Exposures of the same targets with a 200 nm focus shift. (Bottom) ASML FOCAL measurement of best focus with field position.

To characterize focus it is better to read the lower row of exposures, which occurs when there is just enough dose and defocus present for the dot to begin to print, rather than reading the upper row of exposures where the dot always prints strongly. Figure 6-12 shows schematically why this is so. The two curves in the figure represent the target probe intensity under different amounts of defocus and the horizontal line E_0 is the resist exposure threshold. When the dot is printing strongly the probe intensity is given by the

top curve. In this case E_0 cuts the intensity profile further down along its wider part, printing a large dot. While the initial dot prints strongly in this case, small changes in defocus which causes the intensity profile to go up and down slightly yield very small changes in dot size, which is difficult to read. On the other hand, if the conditions are such that the probe is just at the printing threshold then E_0 cuts the curve at the tip. In this case, shown by the lower curve, small changes in defocus cause the dot to appear or disappear and to change lateral size rapidly. Thus, it is easier and more informative to read the peak of the intensity rather than the diameter to quantify aberrations. Combining this knowledge with the physical intuition gained from the electric-field phasor model in Section 5.2.2, it is noted that it is possible to make the focus monitor even more sensitive to focus differences by simply printing the target significantly out of focus to begin with.

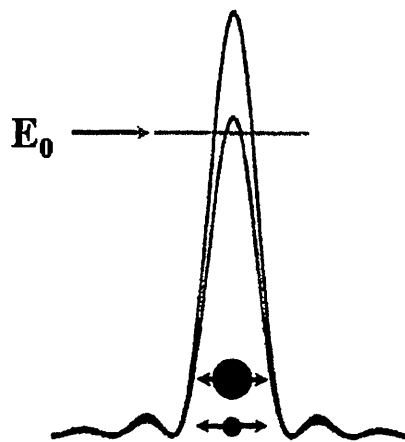


Figure 6-12. Breaking of the resist exposure threshold by the intensity at the center of the target showing that it is better to read the targets when they just break the threshold rather than when the probes are printing strongly. The upper dot corresponds to the upper curve where the dot is already printing strongly and indicates that the width of the dot does not change much as the aberration level changes. The bottom dot corresponds to the bottom curve and indicates that the presence or absence of the dot is highly dependant upon the amount of aberration.

If comparison is made between Figure 6-10 and the four exposures on the left hand side of the bottom row of Figure 6-11, where copies of the defocus target are imaged at

13 different locations across the slit, it can be determined that the defocus target can be read to an accuracy of 25 nm in focus. This is approximately 1/8 the Rayleigh depth of focus. In these four images there is a regular trend of decreasing dot size from left to right, with the leftmost dot printing like the dot in column 0 and the fourth dot from the left printing like the dot in column -1 of the top row of Figure 6-10. Thus the defocus target can be read to approximately 1/4 of the difference described in Figure 6-10, or 25 nm in focus. This represents about an 8× improvement in focus sensitivity to the point spread function. The defocus target may thus be sensitive enough to be able to measure the effects of both inter- and intra- die wafer shape.

A proposed application of the defocus target is as a wafer flatness monitor. This could be accomplished by imaging an array of defocus targets on a die, near the threshold energy at a give focal setting for the central target probe. Because the exposure energy and focal setting would be the same for every target in the exposure, any variation in the printability of the central probes would be a measurement of the combination of the exposure tool field curvature as well as any height variation within the die due to thickness variation and chucking of the substrate.

ASML's independent FOCAL test measurement of best focus across the scanner slit is shown at the bottom of the Figure 6-11. The same kind of general gradual trend in best focus is seen across the lens in this data as is seen in the bottom row of the defocus target exposure. However, the pattern and probe monitors also respond to wafer thickness variation across the die and, as such, this is probably the dominant effect in the images indicating the 100 to 200 nm focal trend. Thus, the defocus monitor may find application as a new kind of wafer flatness monitor. Further evidence for this is found in Figure 6-10

in the constant focus column 0. Here images of the same mask target taken in different fields are shown and a trend in dot size is observed from die-to-die. This dot size does not increase monotonically with the increasing exposure dose from the bottom to the top of the column. The exposure tool performs a leveling at each individual die, which indicates that variation in the printing of a given target is probably due to variations in wafer height at that position in each die.

6.2.2. Coma Monitor Performance

A two-ring version of the Target Set 3 coma target is shown with images of the pattern exposed in resist in Figure 6-13. The image on the left hand side has circles of diameter $1.00 \frac{\lambda}{NA}$ and $1.22 \frac{\lambda}{NA}$ to show scale and the size of the point spread function, while the image on the right hand side is overlaid with contours generated from SPLAT simulation at 5, 10, 15, and 20% CF.

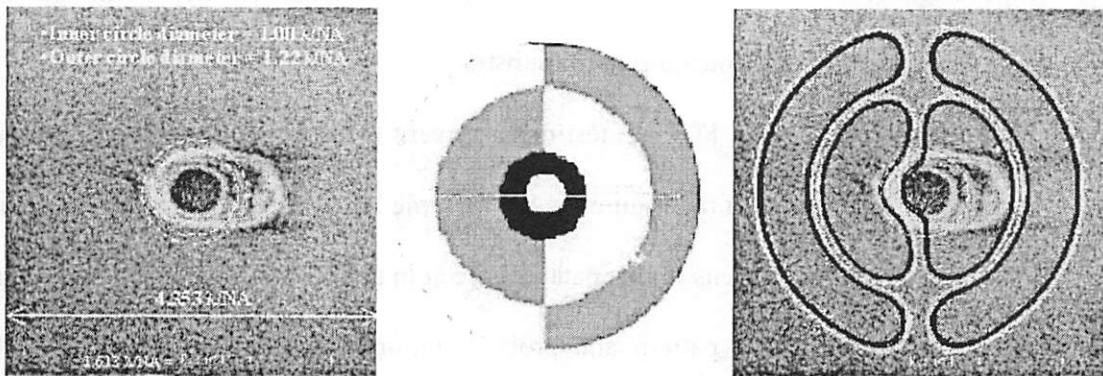


Figure 6-13. (Left) Resist exposure of two-ring coma target with circles drawn at $1.00 \frac{\lambda}{NA}$ and $1.22 \frac{\lambda}{NA}$ (the diameter of the point spread function). Note that the probe appears to be printing as a dot within the inner circle. (Center) Two-ring coma target used in simulation. (Right) The same resist exposure with 5, 10, 15, and 20% CF contours shown.

Three observations are immediately evident from these images. First, the probe, which does appear to fully expose the resist in a small dot pattern within the larger exposed region, appears to print at a size slightly smaller than the point spread function. This indicates that, given the amount of coma at this position in the lens and the energy and focus of the exposure, the peak of the probe intensity is only slightly higher than the exposure threshold for the resist. Secondly, the image on the right shows that the probe and the inner half-ring of the same phase are merging, or bleeding into each other. These two features print, at least partially, all the way up until the phase change between the 0° and 180° half rings on the right hand side of the target. The bleeding is probably due to a combination of factors. Firstly, because the probe and the inner half-ring on the right are of the same phase, the electric-field at the image plane does not change sign when going from one feature to the other. This natural tendency for the 0° ring and the 0° probe to bleed into each other may be combated by increasing the size of the chrome isolating region surrounding the probe. Secondly, the merging is exacerbated by the fact that all of the 0° regions, including this probe were slightly oversized due to a bias being added for mask fabrication purposes. Finally, the image also shows that, while the probe appears to print fully, there is very little evidence of any of the rings printing. This implies that there are significant differences between the simulated coma target performance and its actual behavior.

This final observation becomes even clearer when considering Figure 6-14. The top of this figure shows the results of the ASML FOCAL test for coma aberration on the left hand side of the lens after the introduction of the aberration by adjusting machine parameters. Below, a set of simulated intensity profiles of the target given an equivalent

amount of aberration across the slit is seen. Finally, the bottom of the figure shows images of the target performance in resist through different focus values. The simulated results indicate that the intensity of the central probe should vary linearly with small amounts of coma aberration, that the intensity of one of at least one of the inner half-rings is always greater than that of the probe, and that the inner half-rings vary significantly in intensity with varying amounts of coma. The simulated intensity cut-lines through the target are shown along with an arbitrary exposure threshold. On the far left hand side of the lens the amount of coma present should cause the probe to break through the exposure threshold and print. The probe in the next target to the right will just be at the exposure threshold. Continuing right towards the center of the lens, decreasing the amount of coma, the probe intensity decreases. While the theory for the quantitative interpretation of the amount of coma relies upon determining the intensity at the probe position, the maximum aberration sensitivity may be indicated by other features such as the intensities of the inner half-rings. The simulations clearly show that the intensities of the inner half-rings change significantly with respect to one another as the amount of aberration changes. The printing of these rings themselves might be used for an aberration monitoring methodology similar to that used with the half tone octagonal knife edge described in Section 2.3.4.

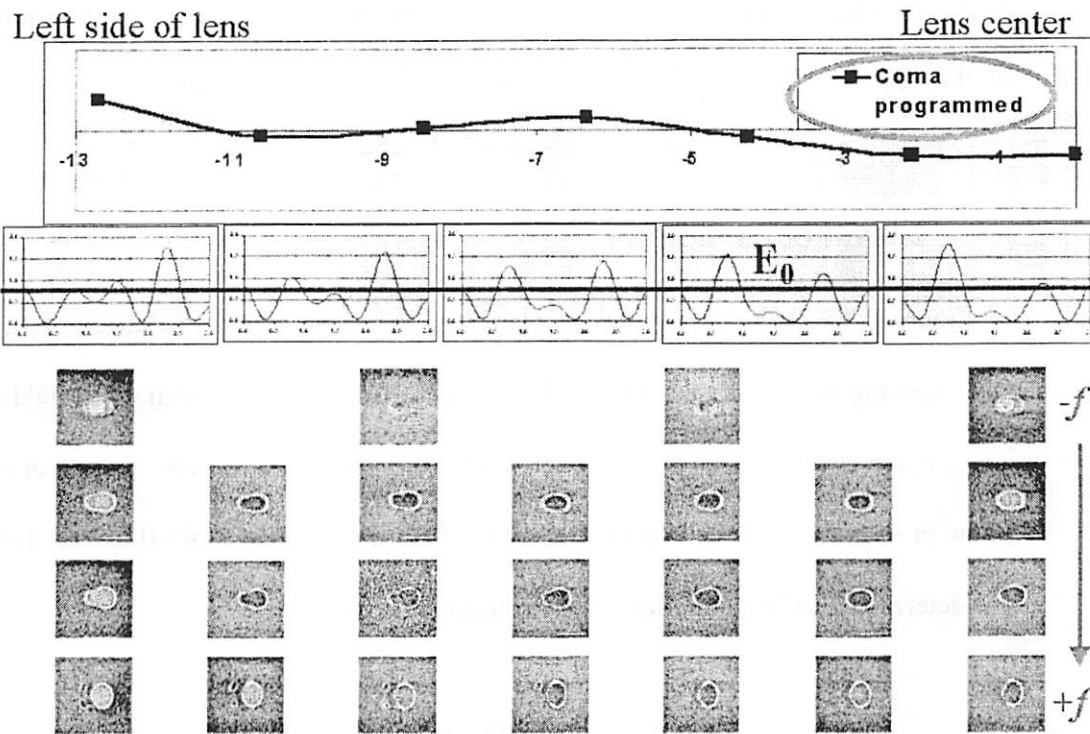


Figure 6-14. (Top) ASML FOCAL measurement of coma on the left hand side of the lens after coma has been induced. (Middle) Simulations of coma target response to coma. The arbitrary exposure threshold helps to visualize which areas of the resist should be fully exposed and which shouldn't. (Bottom) Resist exposures of two-ring coma target across the field and through focus.

6.3. Performance in the Production Environment

Using the same mask, a second set of photoresist exposures was performed at Advanced Microdevices in Santa Clara, CA on a Canon FPA-5000 ES4 scanner with variable NA and customizable illumination in order to determine the performance of the aberration monitors in the production environment. In all cases, the wavelength was 248 nm, NA = 0.80, and σ was chosen to be either 0.25 or 0.30, depending upon the exposure. These optical parameters correspond to a Rayleigh depth of focus unit of 194 nm. The resist stack and process was a standard 3000 Å of UV II10 atop 620 Å of AR3 BARC and the dose-to-clear was $E_0 = 98 \text{ J/m}^2$. Again, a standard coat, exposure, bake, and development process was used throughout, with the wafers being developed immediately

after exposure. The FPA-5000 scanner was operated in its nominal production-mode state at all times.

6.3.1. Focus Monitor

Figure 6-15 shows a focus-dose matrix of the same two-ring defocus target, with focus varying from left to right and dose varying from top to bottom. The field of view for each sub-image is $2.0\ \mu\text{m}$ and σ was set to 0.25 for the exposures. The focal steps are $50\ \text{nm}$ or $\sim 1/4\ \text{RU}$ and the minimum dose is $\sim 1.5 \times E_0$ with steps of $\sim 0.2 \times E_0$. Best focus was determined to be in the third column from the left.

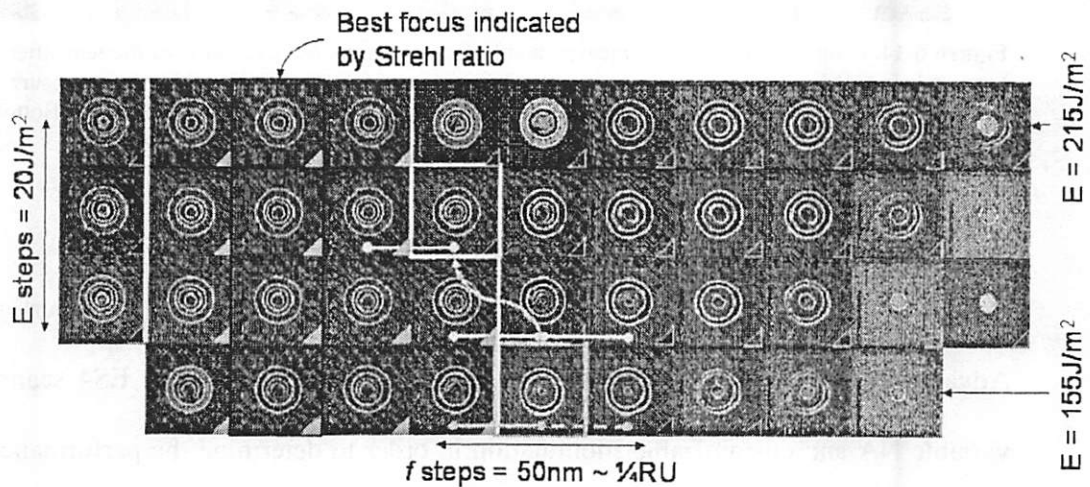


Figure 6-15. SEM images of the two-ring defocus target printed in resist through focus (left to right) and dose energy (top to bottom) at $\text{NA} = 0.80$ and $\sigma = 0.30$.

The probe does not print at any of the energies shown when the tool is at best focus. Moving from left to right, the data follows the same general trend as the exposures in Figure 6-10 with the probe printing within the resist disk at the far left hand side, not printing near best focus, and then reappearing when the exposures are sufficiently out of

focus on the other side of best focus. With sufficient defocus, the probe consumes the resist disk entirely, as seen on the far right hand side.

Two light lines have been added to the figure to indicate where the probe transitions between not printing and printing. Beginning at the far left, 100 nm out of focus, the probe prints within the resist disk at doses of 175, 195, and 215 J/m². The probe stops printing moving towards the right through best focus and begins to print again after passing the second light line. It is generally observed that more defocus is needed to get the probe to print for a lower exposure dose than for a higher dose. This is evident in that the probe begins to print two columns to the right of best focus (100 nm of defocus) for the 215 J/m² and 195 J/m² exposures but does not print until the third column to the right of best focus (150 nm of defocus) for the 175 J/m² and 155 J/m² exposures. The fact that the focal setting at which the probe prints for the 175 J/m² dose is asymmetric about best focus while the other doses appear to be symmetric may be an indication of differences of die topography or it may be a reflection of the asymmetry of the simulated probe intensity curves.

The sensitivity of the target is estimated by comparing the change with focus to the change with exposure dose. The fact that the probe goes from not printing at all to printing strongly in a single focus step indicates that, when the energy at the probe position is near the resist exposure threshold, this target can easily measure 50 nm in focus. This is equivalent to a focus sensitivity of 0.02 λ rms. Close examination shows that the size and behavior of the printed probe is the same for the image in the fifth column from the left at an energy of 195 J/m² and the that in the sixth column at an

energy of 155 J/m^2 . This means that a 50 nm step in focus is approximately equal to a 40 J/m^2 energy step under these conditions.

Figure 6-16 shows the resist images of the 13 copies of the two-ring defocus target across the die exposed at 155 J/m^2 (bottom) and 195 J/m^2 (top). The center image, which is outlined in each set, is the same exact outlined image seen in Figure 6-15 for the two respective energies. Zoom-in images of every other SEM with a field of view of $0.32 \mu\text{m}$ have been placed underneath these two sets of data to give an enhanced view of the image of the probe.

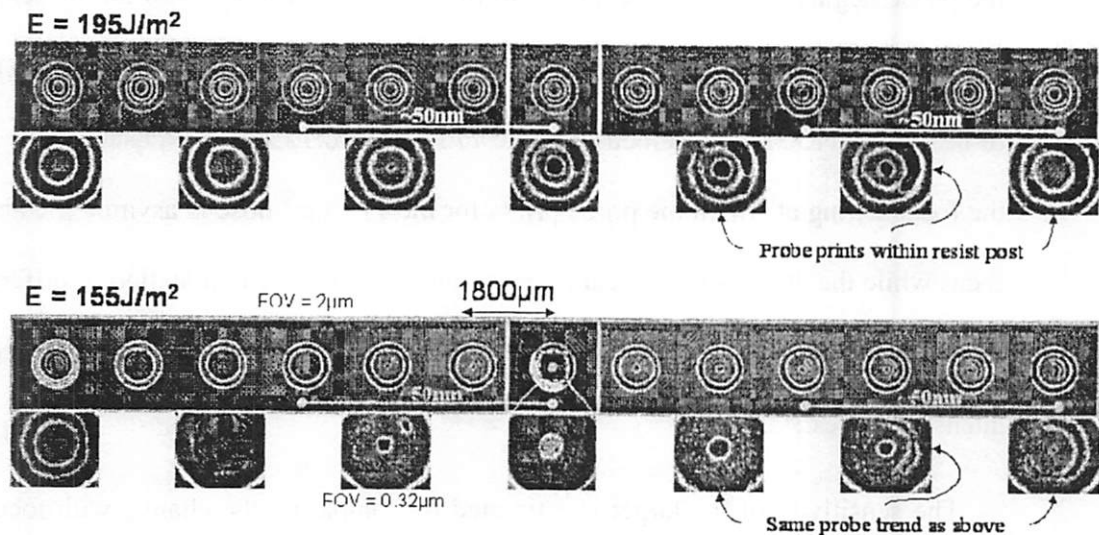


Figure 6-16. SEM images of 13 copies of the 2-ring defocus target across the scanner field exposed at 195 J/m^2 (Top) and 155 J/m^2 (bottom) The outlined middle image in each set is the same as the outlined image at the corresponding energy in Figure 6-15.

Both of these sets of across-field exposures show the same general trends. Starting from the leftmost images, the resist disk is present in the middle but no probe printing is observed until the fifth image to the right. Considering the simulated behavior of the center intensity shown in Figure 5-7 in Section 5.2.2, it can be said that the probes at wafer positions one through five are closer to the bottom of the parabolic intensity

profile. It is noted that the probe in the fifth image prints much stronger in the lower energy exposures than at the higher energy. Because both of these die were exposed with the same lens, this is probably due to chucking and differences in topography between the two die. Proceeding to the right, the probe appears to increase in size monotonically through the center of the die until the tenth image. This corresponds to climbing up the parabola in intensity. The probe then decreases in size monotonically from the tenth through the 13th images, at which point the probe disappears for the higher energy exposure and is only barely visible at the lower energy. Again, this may be due to differences in the die topography. The general decrease in energy at the probe position can be interpreted as sliding back down the parabola and ending at a focal value very close to that on the left side of the die.

To estimate the range of focus across the field the changes seen in Figure 6-16 are compared with those seen earlier in Figure 6-15 for focus. For both energies seen in Figure 6-16 the probe goes from not printing at the fourth position to printing at the strongly at the seventh position. A similar change is seen in Figure 6-15 for a focus step of 50 nm. It is thus concluded that the across-field variation is about 50 nm. If the 50 nm focal variations that both of these sets span are each divided into three focal steps, a minimum sensitivity of 17 nm, corresponding to, 1/10 RU or 0.01 λ rms in focus, is calculated.

This entire experiment was repeated on the same exposure tool but with a slightly different imaging condition of NA = 0.80 and $\sigma = 0.30$ to confirm the above results. Images from the focus-dose matrix and across the field are shown in Figures 6-17 and 6-18, respectively.

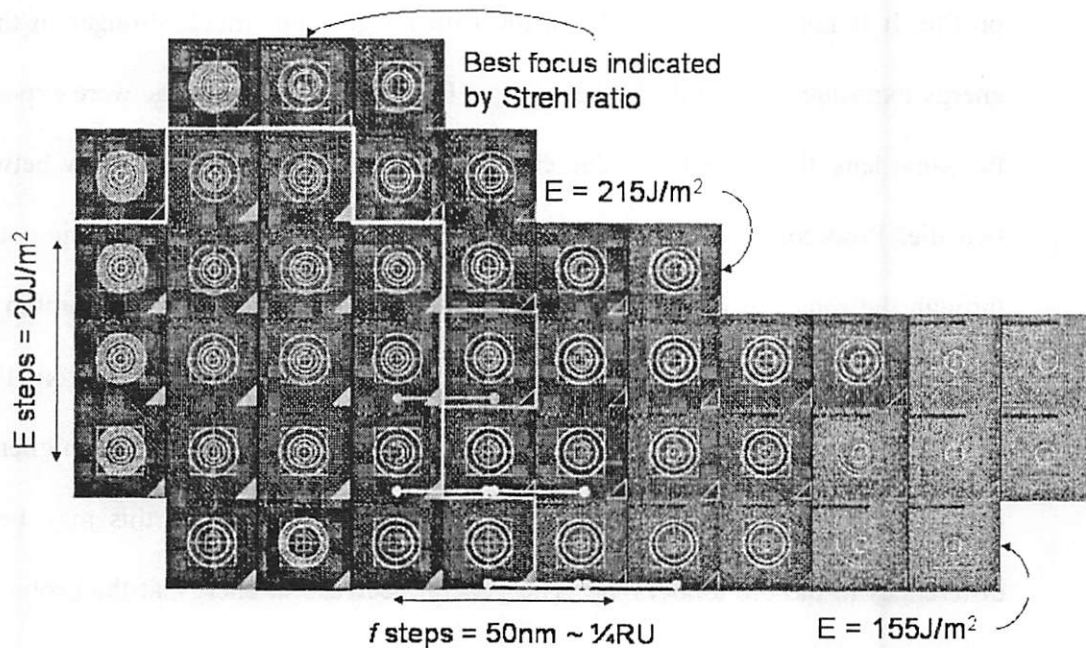


Figure 6-17. SEM images of the two-ring defocus target printed in resist through focus (left to right) and dose energy (top to bottom) at $NA = 0.80$ and $\sigma = 0.30$.

In Figure 6-17 the exposures below and to the left of the light line indicate where there is no discernable probe printing within the resist disk. There are some differences between this set of images and the set seen in Figure 6-15 in that the focal positions at which the probe begins to print for given energies do not always agree. The general trends of ring versus probe printing, energy-focus equivalence, and the three states of probe printing, however, do coincide with the previous set of exposures. It is again seen in these images that the probe shows a clear transition from not printing to printing within one focal step of 50 nm.

Figure 6-18 shows how the target prints in 13 positions across the field at 195 J/m^2 with 100 nm of defocus. The outlined image in the middle corresponds with the outlined image in Figure 6-17, two columns to the right of best focus. In agreement with the images in Figure 6-16, a 50 nm focus signature is found on the left hand side of the die.

The images in Figure 6-18 however, show that the 50 nm focus trend on the right hand side of the die seems to occur over a much shorter 1800 μm rather than the 5400 μm indicated by Figure 6-16. This may be an indication that the wafer or resist used for this exposure had significant topography issues.

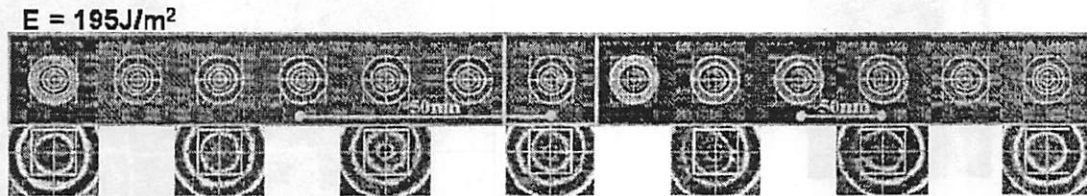


Figure 6-18. SEM images of 13 copies of the two-ring defocus target across the scanner field exposed at 195 J/m^2 . The outlined middle image is the same as the outlined image at the corresponding energy in Figure 6-17.

While the exposure results for mask 248B show the expected general trends of probe printing as predicted by simulation, a first-order improvement to the layout design, suggested by the plots in Figure 5-13 in Section 5.3.4. That is, to reduce the size of the chrome region surrounding the probe from $r_{cr} = 0.50$ to 0.35 to bring the zero-aberration reference intensity of the target down to just that of an isolated probe. In order to do so, the targets in Target Set 3 were fabricated in a new mask, mask 248C, with r_{cr} ranging from 0.35 up to 1.0 . The same lithographic exposure tool was used to again create a focus-exposure matrix, but in this case, because the chrome donut around the probe is so thin, the presence or absence of a small resist post is observed at the very center of the target. This is slightly different than looking for a hole inside a resist post which is slightly larger, but it conveys the same overall information about defocus. With the reduced size of the isolating chrome region, the point spread function from the probe causes the energy deposition to be spread in such a manner so as to consume the resist post from the outside in. If the resist post is present, as seen at the top left of Figure 6-19,

then the dose received at the center of the target must be less than the dose to clear. If the resist post is absent then the dose is somewhere above this value.

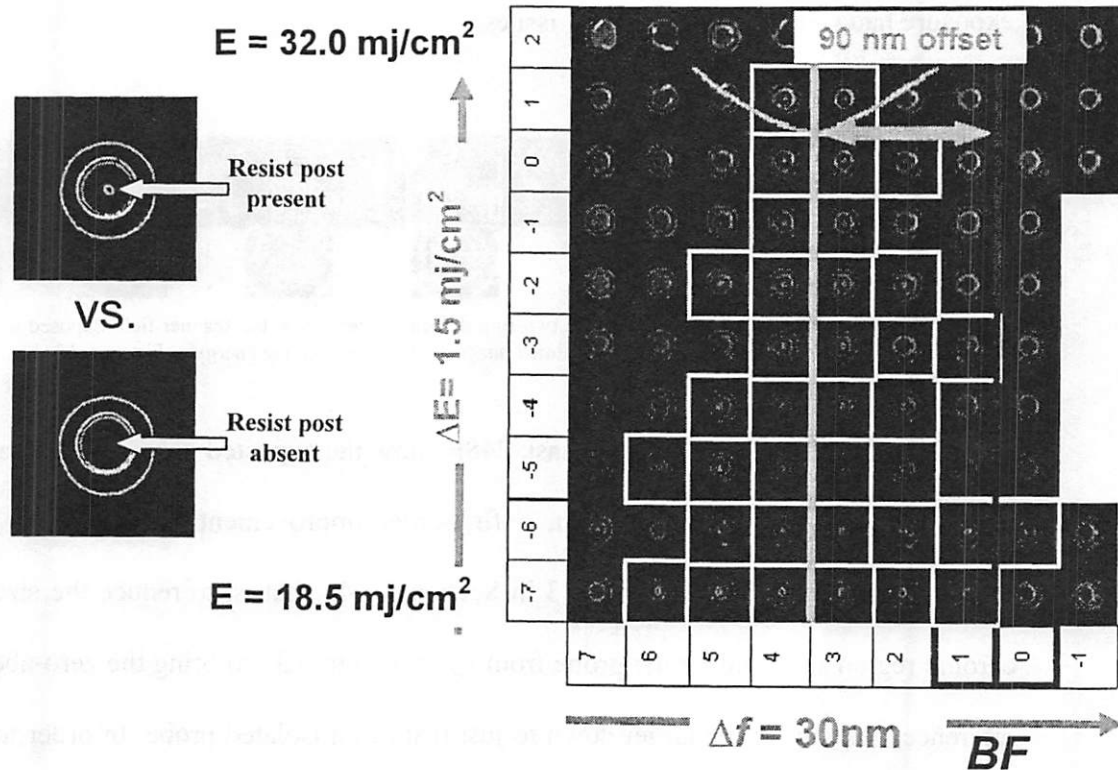


Figure 6-19. (Left) Target reading strategy for newly redesigned two-ring defocus targets. (Right) Focus-dose matrix of two-ring defocus targets showing the trend of target response.

The target was exposed through focus and dose at $NA = 0.80$ and the photoresist results are shown at the right side of Figure 6-19. The focus was commanded to change from left to right in steps of 30 nm while the dose was stepped from 18.5 mj/cm^2 to 32.0 mj/cm^2 from bottom to top. The machine's best focus, as determined by the Strehl behavior of an isolated probe, is indicated with a vertical line between the second and third columns from the right. The SEM images where the resist post is present have a light outline, while those where the post has been completely cleared have no marking.

The first observation from this data is that the focal setting at which the maximum exposure dose is needed to cause the resist post to disappear is approximately three columns to the left, or 90 nm away, from best focus. This agrees very well with the prediction of the SPLAT simulation results seen in Figure 5-7 in Section 5.2.2, where the 0.5 RU shift corresponds to 97 nm focus offset at $\lambda = 248$ nm and $NA = 0.80$. The exposures also show that the energy required to fully eliminate the resist post at this focus offset lies between 30.5 and 32.0 mj/cm^2 , corresponding to a brightness of 30 to 32% CF. This number is in very good agreement with the 34% CF minimum intensity indicated by the simulation. It is misleading however to conclude that the targets act as ideal thin-mask structures though since the simulated structure had an ideal 90° probe with no electromagnetic edge or mask geometry effects., while in reality the phase-shifted probes and rings are significantly more complicated.

Comparing the photoresist exposure data in Figure 6-19 with the AIMS fab data in Figure 6-20, it is seen that there is significant disagreement. The AIMS data indicates that there is little or no focus offset of the parabola describing target response to defocus, while theory, simulation, and photoresist exposures indicate that there should be an offset. Furthermore, the minimum intensity achieved at the center of the target via AIMS is 21.3% CF, which is notably lower than the 34% CF indicated by simulation and the 32% CF indicated by resist exposures. Because the AIMS and photoresist exposure data show such discrepancies, it is likely that high-NA polarization effects significantly impact image formation at the wafer. This is reasonable as the ring pattern acts somewhat like a radial grating, scattering light at relatively high angles, thereby overemphasizing the edges of the lens in comparison with the isolated probes. Finally, AIMS shows an

intensity of only 13.8% CF for a nominal-size 0° probe, which is well short of the 18.8% CF predicted by SPLAT. By splitting the targets up into their constituent components of isolated probes, ring patterns without probes, and other features, the physical effects in imaging strong phase-shift masks in high-NA systems are characterized in the following three chapters.

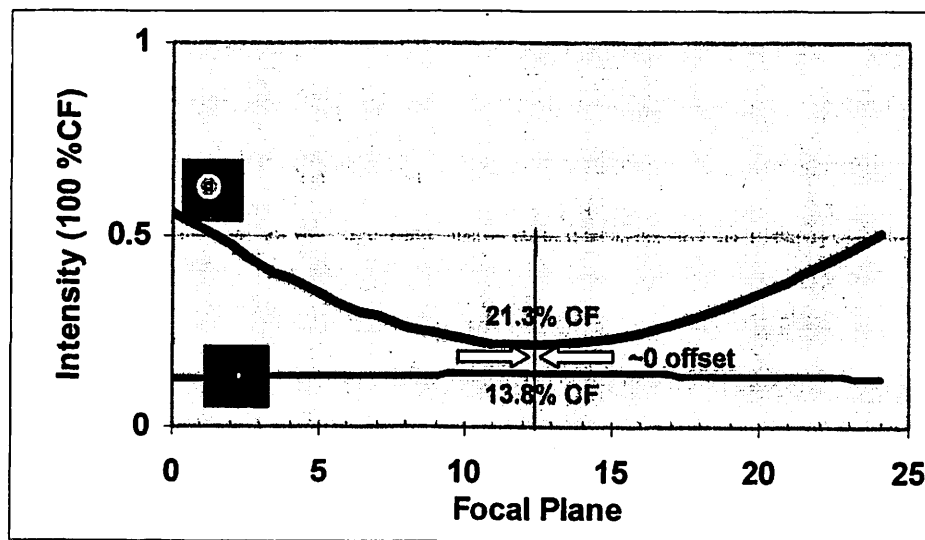


Figure 6-20. Mask 248C AIMS fab intensity response of isolated probe (bottom curve) and two-ring defocus target (top curve) through focus at $NA = 0.80$ and $\sigma = 0.30$.

6.3.2. Coma Monitor

Returning to mask 248B, SEM images of coma target exposures in the production environment are seen in Figure 6-21 and show that significant electromagnetic mask transmission effects are present. Simulation of the target shows that, given a low enough exposure dose, the probe should print as an isolated dot within a disk of resist. The top row of Figure 6-21 shows images of the target with dose increasing from left to right.

Unfortunately, there appears to be no energy in this range where the image of the probe separates from the inner portion of the target.

Simulation also indicates that the rings themselves may be useful in detecting coma aberration. While the quantitative theory for measuring aberrations with these targets has only been established for the very center position of the image, the rings of this target may provide an even greater response to coma. The bottom row of images in Figure 6-21 is of 13 copies of the two-ring coma target across the die, exposed at 95 J/m^2 . This energy was chosen for the across-field images because it appears to be the energy at which the resist at the center of the target just barely prints. There is very little variation in how the probe prints across the die, which may be an indication that there is very little change in coma across the field. Observing the 180° inner half-ring however, there is a noticeable difference in how this feature prints from left to the right. On the far left hand side, the feature prints as one continuous hole in the resist from top to bottom. Moving toward the right, the printed image of this feature begins to separate into two pieces. At the far right hand side there is a definite separation between the two pieces. This could be due to the coma changing from the left hand side to the right hand side of the lens. This behavior can probably not be attributed to focus variation across the die because, unlike the data shown in Figures 6-16 and 6-18, it is different on the far left and far right hand sides of the die.

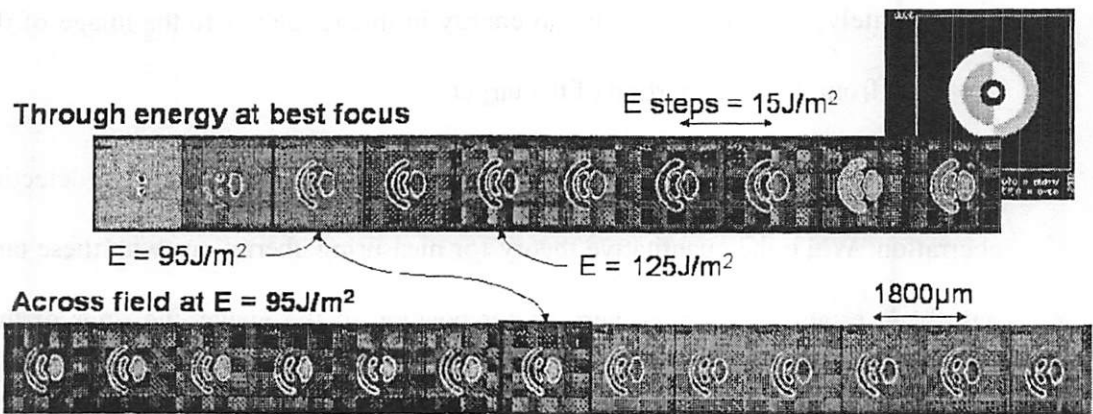


Figure 6-21. (Top) SEM images of resist exposures of two-ring coma target at best focus with increasing dose from left to right. (Bottom) SEM images of resist exposures of two-ring coma target at 13 positions across the field at best focus, exposed at 95 J/m^2 .

6.3.3. Spherical Monitor

In the case of the spherical aberration target, it is important to be able to avoid contamination of the measurement by defocus. While much effort has been spent on characterizing the performance of the defocus target, the spherical target is equally important. Unfortunately, as with coma, there is not a convenient and reliable way to control the amount of spherical aberration in the exposure tool in its production operation. Thus, the exposures were done with the machine's nominal amount of spherical aberration.

Figure 6-22 shows a two-ring spherical aberration target from Target Set 3, exposed through focus (top to bottom) and dose (left to right) at $\text{NA} = 0.80$ and $\sigma = 0.25$. Table 5-1 in Section 5.2.1 shows that with no aberration, this spherical target requires a higher exposure dose than the defocus target to print the probe, so this set of exposures was done with the energy beginning at 200 J/m^2 and stepping by 40 J/m^2 up to a maximum dose of 520 J/m^2 . The row at which the Strehl behavior indicates the tool is at best focus is found to be the second row from the top. In the best-focus row, the resist disk is present at the

middle of the target but no probe prints within it. It is found that the diameter of disk decreases as the dose is increased, probably due to increased flare exposure at higher dose. The exposures through focus at a given energy show that the diameter of the resist disk can also be significantly affected by defocus, disappearing completely in some cases. Thus, this data only shows two target states: either the resist disk is present or it is not present. Unfortunately, there is no dose or focus at which the probe prints as an isolated hole within a resist disk.

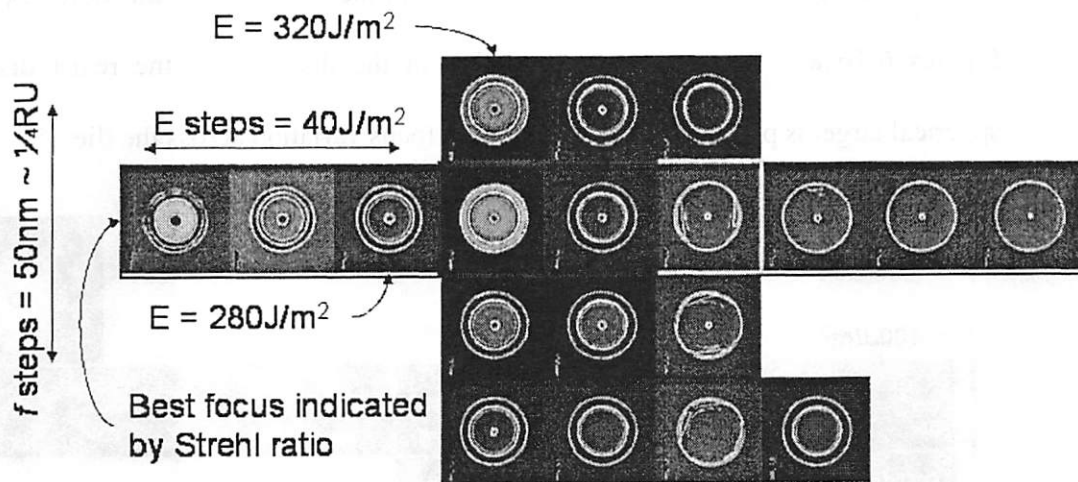


Figure 6-22. SEM images of the 2-ring spherical aberration target (layout inset) printed in resist through energy (left to right) and focus (top to bottom) at $NA = 0.80$ and $\sigma = 0.25$.

Again, the quantitative theory relating the energy at the probe position and probe printing to the amount of a given aberration only applies to the very center of the target. However, as with the coma aberration target, another feature besides the probe may be more sensitive to the aberration of interest. Figure 6-23 shows SEM images of 13 copies of the two-ring spherical aberration target exposed at best focus across a die at $360 J/m^2$ (top) and $400 J/m^2$ (bottom). The center image in the top set of data is the same as the center outlined image at $400 J/m^2$ in Figure 6-22 and the center image in the bottom set of

Figure 6-23 is the same as the center outlined image at 360 J/m^2 Figure 6-22. While the probe does not print in any of these images, the size of the resist disk varies noticeably in both cases. On the far left hand side of both die the disk is of a medium size. Moving towards the right, the disk increases in diameter until it reaches its maximum size around the center of the die. Continuing towards the right, the disk gets smaller and smaller until it is at its minimum diameter on the far right hand side of the die. While it is not possible to determine whether this variation is due to spherical aberration, the trend in the disk diameter is very similar to that seen for the probe diameter of the defocus target in Figures 6-16 and 6-18. Thus the variation in the diameter of the resist disk of the spherical target is probably a reflection of the focus variation across the die.

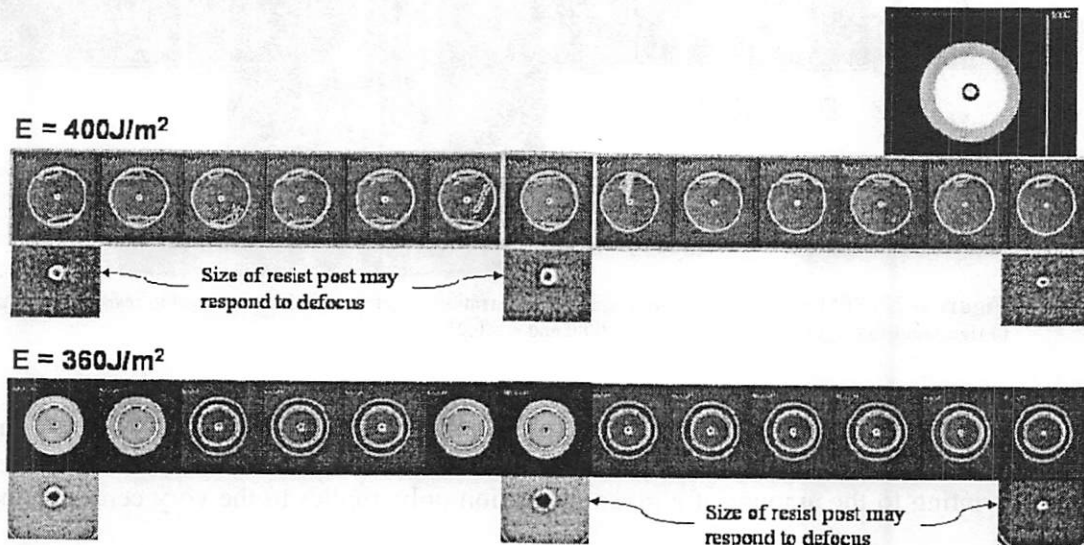


Figure 6-23. SEM images of the 2-ring spherical aberration target (layout inset) printed in resist through energy (left to right) and focus (top to bottom) at $\text{NA} = 0.80$ and $\sigma = 0.25$.

6.3.4. Summary

This chapter gives the first experimental evidence of the operation of interferometric pattern and probe-based aberration monitors for focus, coma, and spherical aberrations.

The patterns from Target Set 3 were used at 248 nm and, while the defocus targets show strong response to defocus, the influence of second-order effects such as mask electromagnetic transmission effects were plainly evident. AIMS measurements clearly showed the increased sensitivity of the probe to focus compared to the Strehl ratio. Exposures of the targets in photoresist on an exposure tool in production conditions show that the defocus target can be read visually to an accuracy of 17 nm, or better than 1/10 of the Rayleigh depth of focus, which is equivalent to 0.01λ rms, indicating that this is a viable technique compared to other aberration measurement techniques. The data indicate also that there is a systematic 50 nm focus variation across the field of the exposure tool. While the results for the focus target are promising, the coma and spherical aberration targets did not print as expected. The probe in the coma target is found to bleed into the inner half target ring of like-phase and there is a significant imbalance between the 0° and 180° regions indicating that the target should be redesigned to be insensitive to these effects. This echoes the main theme of this thesis, which is to find out how various factors limit the performance in practice and how these limits scale with feature size, with other forms of lithography, and other applications, such as ophthalmology. The following three chapters focus on how to improve the design of the targets and processing of the masks in order to achieve the highest aberration sensitivity while at the same time optimizing orthogonality and target readability.

7. Advanced Experiments

As this research has advanced, so have the experimental tools available. The main thrust of this chapter is the study of the imaging properties of isolated components of the aberration targets using the AIMS fab 193 to image a mask with patterns scaled for $\lambda = 193$ nm and $NA = 0.80$. SEMs are used to establish the lateral geometry of the features and, in some cases, provide information about the processing of the mask at given locations. SPLAT, with thin-mask approximation and no polarization effects, and Panoramic simulations, both with and without polarization, are used to predict the behavior of the individual target components and to help to assign causes to the discrepancies between theoretical and actual target performance.

7.1. *Strategy of Factorization and Mask Fabrication*

Because there are various factors which contribute to target performance, it is helpful to break up the problem up by splitting the two-ring defocus target, for example, into its constituent parts, as shown in Figure 7-1. First the full target is separated into an isolated probe and rings only. Then the probe is parameterized in size and phase, while the rings are further separated into isolated rings of various phases. Finally, the rings can be further simplified by unwrapping them into isolated lines of varying size and phase. The experimental results in this chapter were affected by residual aberrations in the AIMS optics and in some wafer areas by attempting to fabricate with a zero bias in the phase etch to preserve chromeless edges elsewhere on the mask.

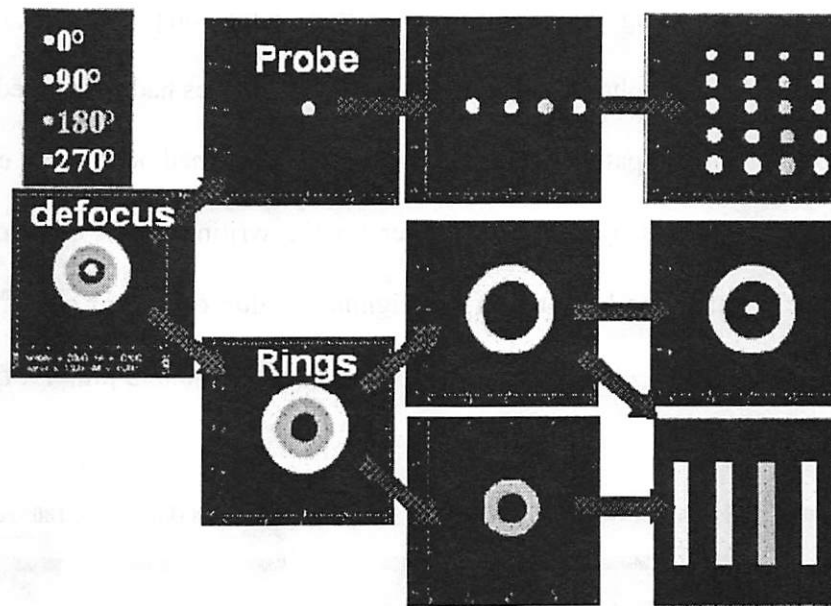


Figure 7-1 Schematic diagram of the factorization of a target into its elements.

Using the knowledge gained from SEMs, AIMS, and photoresist exposures from previous structures, feedback was provided to the mask process engineers to optimize the mask fabrication flow for the aberration monitors. A schematic outlining the fabrication process for the 193 mask is seen in Figure 7-2. First, all transmitting areas, regardless of phase, were opened by using an electron beam writer followed by a chrome etch. The reticle was then recoated with resist and an Alta laser tool was used to expose the regions which ultimately became 90° and 270° phase-shifted openings. This was followed by a 90° phase etch. Finally, the reticle was recoated and exposed, again using the Alta laser tool to open those areas designed to be 180° and 270°. This was followed by a 180° phase etch. A varying bias was used in each exposure step to ensure that the resist was fully cleared over the entire chrome opening. It is possible however that mis-sizing or misalignment of the exposures resulted in areas that were not properly phase etched, as illustrated in the figure. While this is the best approach for fabricating isolated phase-

shifted features using chrome as the etch stop, extra complications can arise when two regions of different phase abut each other. Several biases had to be used across the mask, as it contains many pattern-types and both chrome-defined no-chrome edge features. The alignments reported by the mask maker for the writing of the second and third levels were well within the laser tool's 3σ alignment value of 50 nm at: (2nd write) X-offset: 0.017 μm , Y-offset: -0.031 μm and (3rd write) X offset: -0.033 μm , Y-offset: 0.006 μm .

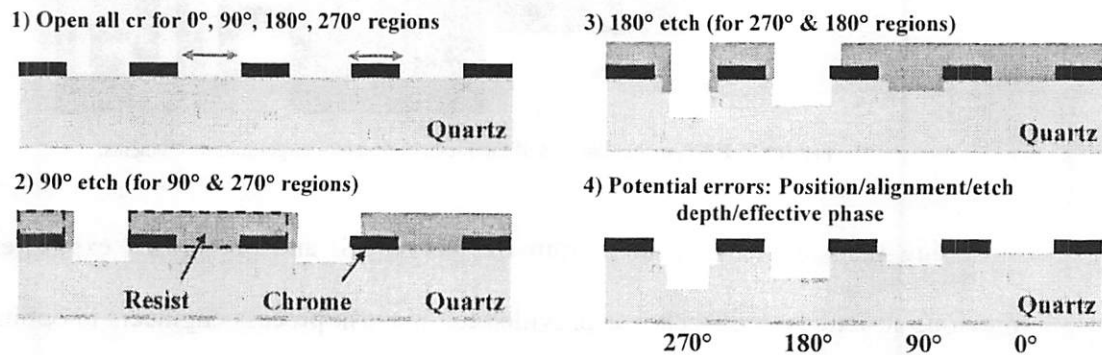


Figure 7-2. Process flow for the fabrication of the 4-phase mask designed for $\lambda = 193$ nm.

In order to study the imaging properties of the basic targets elements, isolated lines ranging in width from 50 nm to 250 nm, and isolated probes with diameters from 50 nm to 250 nm on the wafer were designed with 0°, 90°, 180°, and 270° phase. Figure 7-3 shows SEM images of eight isolated probes on the mask. The probes in the top row are all the same diameter ($k_1 = 0.4514$ or 109 nm on the wafer) as those contained in the full targets. Those on the bottom are 10% larger in diameter ($k_1 = 0.4965$).

If the fabrication alignment and biases were sufficient for a given probe then only a single circle is seen in its SEM, where the chrome cleanly defines the edges of the hole. The top row shows that, for this resist bias, the 90° probe appears to be properly exposed and etched, all the way to the chrome edge. The 180° and 270° probes however show that

alignment and process biasing have resulted in phase steps within the openings. This can cause decreased intensity at the image plane because, in the 180° probe, for example, two orthogonal contributions to the total electric-field are transmitted, one at 0° from the rim of the probe and one at 180° from the very center. The behavior of the 270° probe is even more complicated because there are three contributions to the total electric-field. Comparing the two rows, it is seen that the fabrication results can even be different for probes of the same phase, similar size, and close proximity on the mask. All of these factors impact the imaging performance of the probes and make analysis difficult.

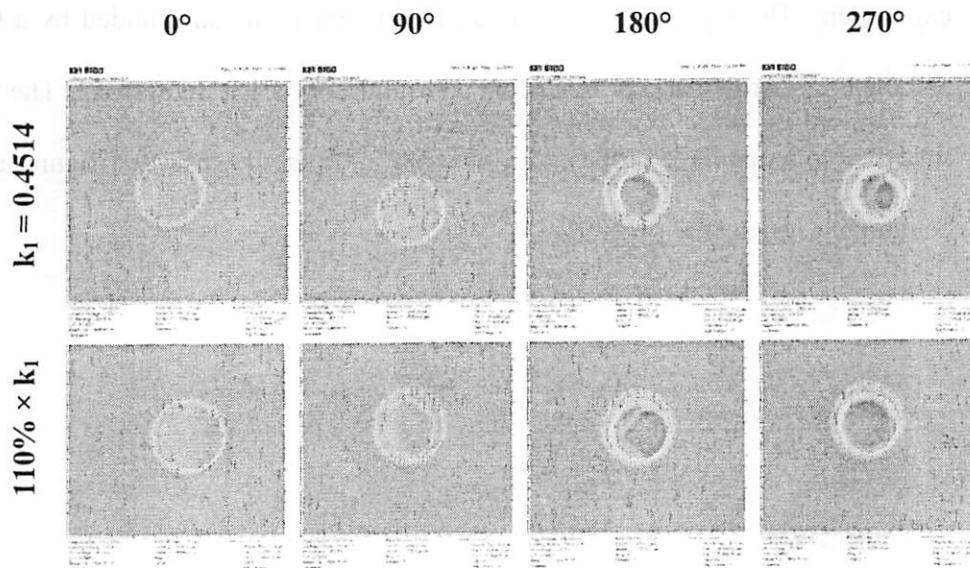


Figure 7-3. SEM images of 0°, 90°, 180°, and 270° phase etched nominal diameter ($k_1 = 0.4514$) (top row) and 110% diameter ($k_1 = 0.4965$) (bottom row) isolated probes on the mask.

7.2. In-Depth Analysis of the Mask

7.2.1. Phase Layer Alignment

Though a robust pattern, one which is relatively insensitive to processing effects, is desired, the alignment of the phase layers can be important for target performance.

Because they are so small, the target probes are especially vulnerable to alignment issues for multiple etches. They are also quite susceptible to electromagnetic edge transmission effects because they can have large sidewalls in comparison with their lateral size. Both of these factors act to shrink the length of the vector associated with the electric-field contribution of the probe. Furthermore, phase etch depth errors, which can be up to 10° in some places on the mask, can rotate the vector, decreasing the target's signal/noise ratio. Further complication arises because the biases and process flow required to fabricate all of the features affects chrome edges, glass edges, and abutting phases differently.

Figure 7-4 shows the multiple versions of the two-ring defocus target used in this experiment. The top row of targets has a 180° inner ring surrounded by a 0° outer ring and the bottom row has a 0° inner ring surrounded by a 180° outer ring. The targets in the first two columns have probes with 90° and 270° as shown in the figure, and the third column has no probes.

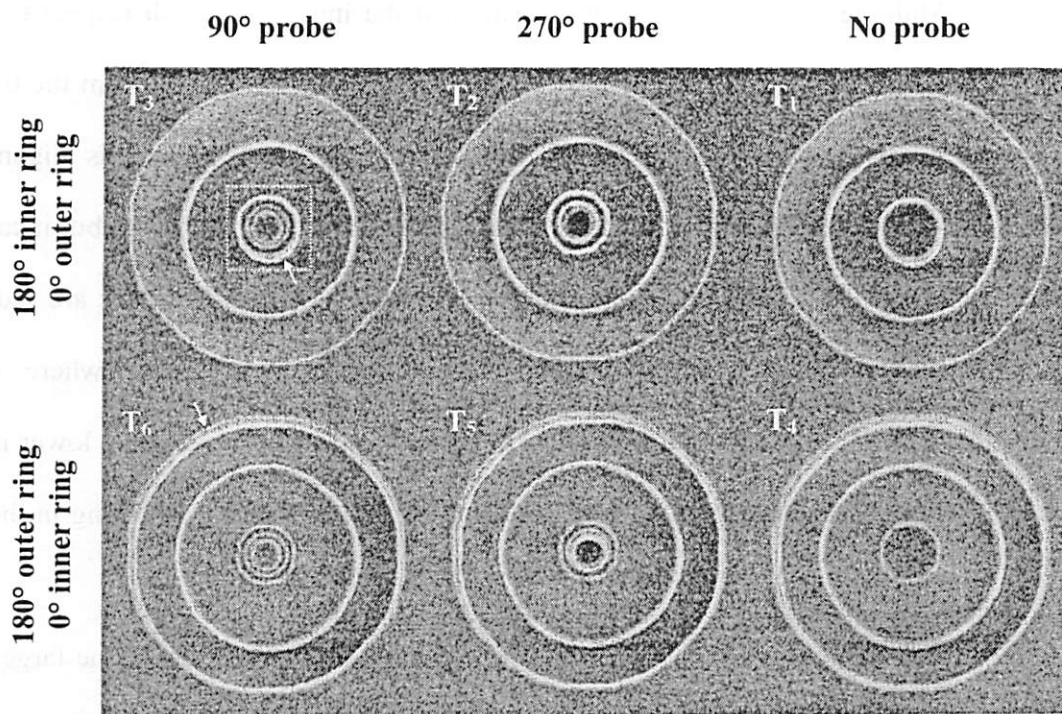


Figure 7-4. SEMs of multiple versions of the two-ring defocus targets designed for 193 nm. The field of view for each image is 3.6 μm . Detailed images of the probe regions are given in Figure 7-5.

The layout design diameter in mask dimensions is 1.97 μm for the inner ring and 3.00 μm for the outer ring. Careful analysis of the top row of targets reveals that the fabricated results for the inner and outer rings are 1.90 μm and 3.06 μm , respectively. This indicates an effective radial bias of +0.03 μm of the 0° layer for locations where it abuts chrome and a -0.035 μm bias of the 180° layer where it is adjacent to the 0° region. The measurements of the targets in the bottom row (with 0° inner rings) show that the fabricated results for the inner and outer rings are 2.03 μm and 3.05 μm . While this does not change the conclusions about the bias of the 0° layer where it abuts chrome, it fully supports the claim that the net result of the biases and fabrication process used is to enlarge the 0° region by about 0.03 μm so that it encroaches upon the 180° region at phase edges.

Multiple measurements of the position of the inner rings with respect to the outer rings also show that, after processing, the 180° layer is misaligned from the 0° layer by 0.036 μm in the X-direction and by -0.098 μm in the Y-direction. This alignment error cannot be seen by looking at the boundary of the inner and outer rings but it can be seen where the 180° region abuts the chrome. Examples of these locations are indicated by arrows in the upper left hand corner of the bottom row of targets, where a large 0° crescent shaped opening lies outside of the 180° outer ring, and at the lower right hand portion of the chrome region which isolates the probe from the 180° ring in the top row of targets.

Figure 7-5 shows zoom-in images of the probe region of each of the targets seen in Figure 7-4. Layer alignment, biasing, and processing effects have obviously significantly impacted the probes, as the ideal probe size is indicated by a dashed circle in each of the images with no probes. Given the mask process flow outlined in Figure 7-2, it is apparent that the 90° probes within the targets consist of a 0° ring surrounding a 90° dot of approximately the same area. This will significantly affect the performance of this target. It is difficult to tell what the actual phases of the pieces of the probe seen in the 270° probe column are from top-down SEM images. This is because the process flow may again result in a 0° ring, surrounding a 270° dot, or there might be a more complicated structure with some combination of 0°, 90°, 180°, and 270° phase regions in the probe area. Aside from these bias and alignment issues, the fact that the probes are so small may affect their phase etch depths because of the limitation of the transportation of etchants to and/or etch products away from the bottom of the probe.

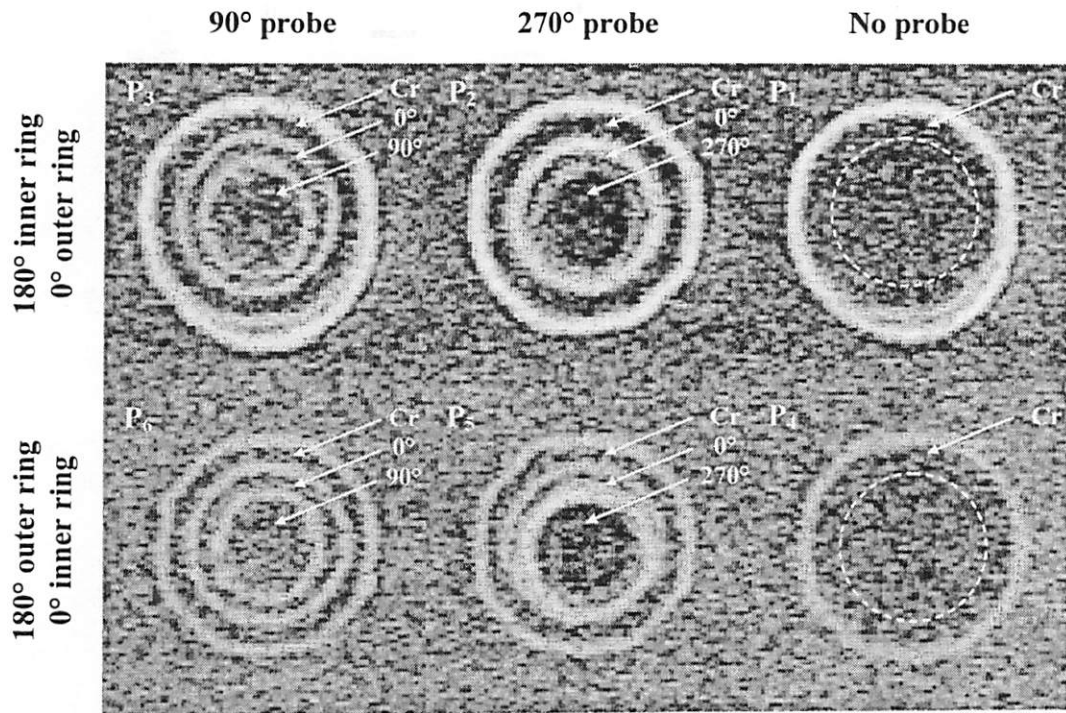


Figure 7-5. SEMs of the probes from the targets in Figure7-4. The field of view for each image is $0.95\ \mu\text{m}$. The ideal probe size is indicated by the dashed circle in each of the images in the third column.

Isolated defocus target rings (no probe) are seen in Figure 7-6. These rings were designed to be identical except for their phases. Because of the biases and phase layer misalignments during processing, the dimensions of the final fabricated structures depend upon their phase.

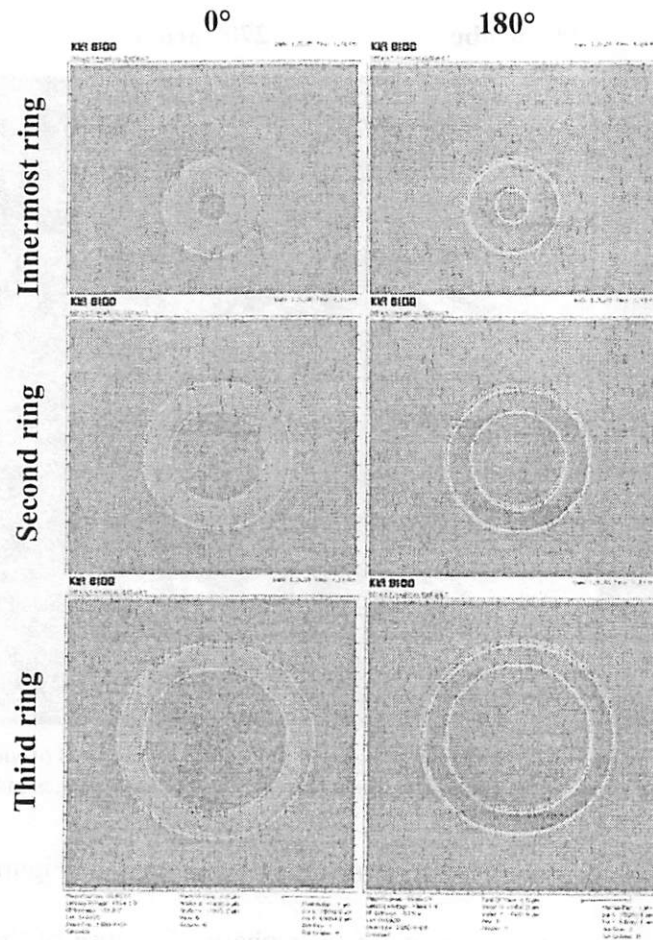


Figure 7-6. SEMs of isolated rings of 0° and 180° phase designed to be the same size.

7.2.2. Phase Etch Depth

While the phase etch depths were not measured for these targets, data on the phases is available from measurements of other features on the photomask. For features similar in dimension to the aberration monitors the 180° region was measured to be 176° in the middle of the mask and it was 172° at the edge of the mask. In larger multi-phase grating structures, the 90°, 180°, and 270° regions were measured to be 91.3°, 179°, and 269.9°, respectively.

7.3. Advanced AIMS Results for the Defocus Target

The AIMS intensity cut-lines for the two-ring defocus target designed for $NA = 0.80$ with $r_{cr} = 0.55$ from Target Set 3, imaged through 21 focal planes, is shown inset in Figure 7-7. For a $4\times$ imaging system with these imaging parameters, and with standard illumination of $\sigma = 0.30$, moving the object plane by $2.4 \mu\text{m}$ corresponds to 1 RU of focus shift at the image plane. The intensity at the central probe position is plotted as a function of the amount of defocus along with the Strehl behavior of a nominally-sized 0° isolated probe and the intensity of the 0° outer target ring in the main part of the figure. The center intensity reaches a minimum value of 53.4% CF, which is significantly brighter than the 34% CF predicted by SPLAT. SPLAT analysis of the design indicates that with $\lambda = 193 \text{ nm}$ and $NA = 0.80$, the lateral shift should be 75 nm. However, as is the case for the two-ring defocus target designed for $\lambda = 248 \text{ nm}$, there is virtually no lateral shift of the parabolic target response from best focus. Thus, the slope of the target response through best focus is nearly zero. Looking to the left of the focal position where the target center becomes brighter than the outer target ring, the target shows a strong 60% CF/RU change, indicating that it can be extremely sensitive to defocus. Finally, it is noted that while thin-mask simulation predicts that the maximum intensity of the nominal-size 0° isolated probe should be 19.2% CF, the AIMS results indicates that it is only 0.71 of this value.

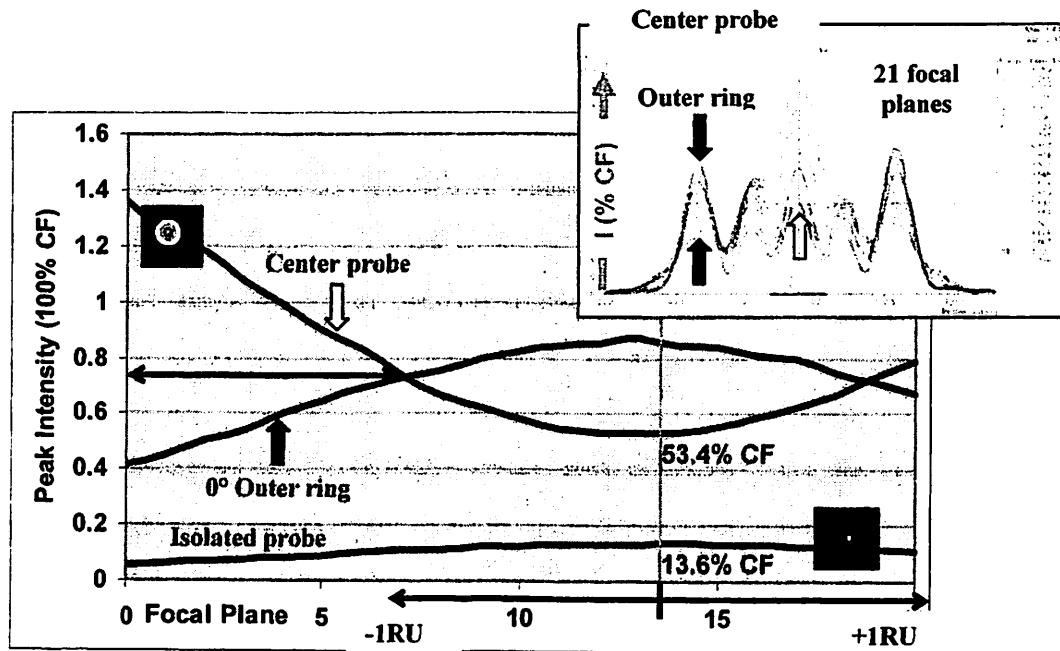


Figure 7-7. AIMS intensity response of isolated probe (bottom curve), the center of the two-ring defocus target (top upward-opening parabola), and the 0° outer ring of the target (large downward-opening parabola) through focus at NA = 0.80, $\sigma = 0.30$. Full AIMS intensity profile for 21 focal planes inset.

7.3.1. Test Target Modifications and Results

The phasor electric-field model established in Section 5.2.2 indicates that if the phase of the probe at the center of the target is changed from 90° to 270° without changing the rings, then the target response parabola will be reflected about the zero-defocus axis. This is because the rings still produce the same spillover and perturbation vectors with defocus, but the direction of E_p is rotated from the positive to the negative imaginary axis. Ideally, according to Figure 5-7, this would have the effect of shifting the minimum of the parabola for the defocus target from about -0.5 RU to +0.5 RU.

Figure 7-8 shows the measured AIMS intensity at the center of the two-ring defocus target with $r_{cr} = 0.55$, with a 90° probe, a 270° probe, and with no probe. It is important to note that the AIMS tool signal saturates above about 140% CF, so any intensity data

greater than this can safely be ignored. The data for the target with the 90° probe is the same as that seen in Figure 7-7. The curves for the targets with a 270° probe and no probe are grouped closely together, with each reaching the same minimum value at approximately the same 1/3 to 1/2 RU lateral shift from best focus. Because these two versions of the target have the same rings and act so similarly, it can be concluded that the 270° probe acts as if there were no probe at all.

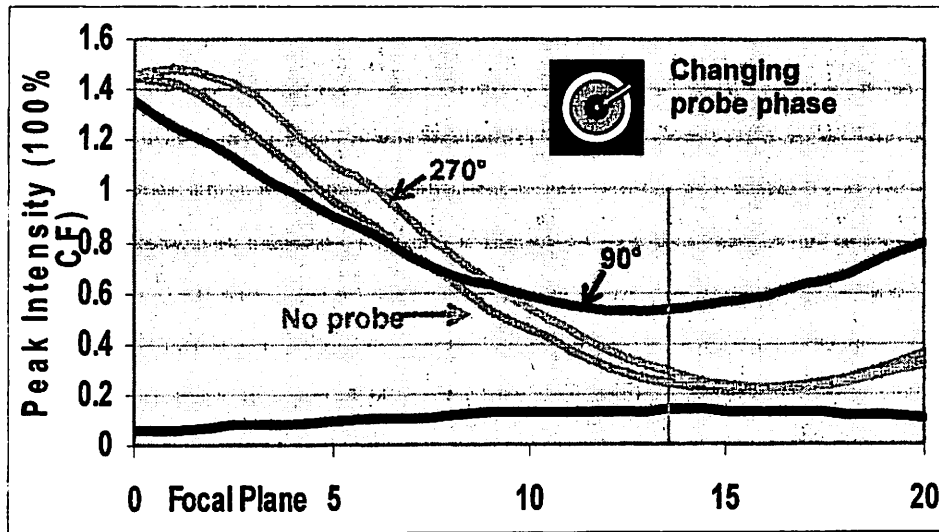


Figure 7-8. AIMS intensity at the center of a two-ring defocus target with a 90° probe, a 270° probe, and with no probe (rings do not change in phase).

One of the goals of this iteration of target design was to make the combined spillover of the rings as small as possible at best focus. When this spillover is zero and defocus is added to the system then the only contributions to the electric-field at the target center comes from the probe and the perturbation to the spillover, both of which are ideally imaginary. Figure 7-9 shows the AIMS intensity at the center of two probeless two-ring defocus targets. The lower curve comes from target A, which has a 180° inner ring and a 0° outer ring and the upper curve comes from target B which has a 0° inner ring and a

180° outer ring. These two targets have their E_{outer_ring} and E_{inner_ring} spillover vectors reflected with respect to one another about the imaginary axis in Figure 5-6.

The center intensity for both of the $r_{cr} = 0.55$, probeless two-ring targets should theoretically respond equivalently through defocus but the data shows some noticeable differences. Both targets do reach their minimum intensity at about the same focal setting, but the minimum of target A is 21.9% CF while that of target B is 29.5% CF. Target A also has a flatter parabolic response than target B. These differences are probably due to encroachment of the 180° phase-shifted region into the 0° region during fabrication. Thick mask electromagnetic effects may also play a part in creating this behavior.

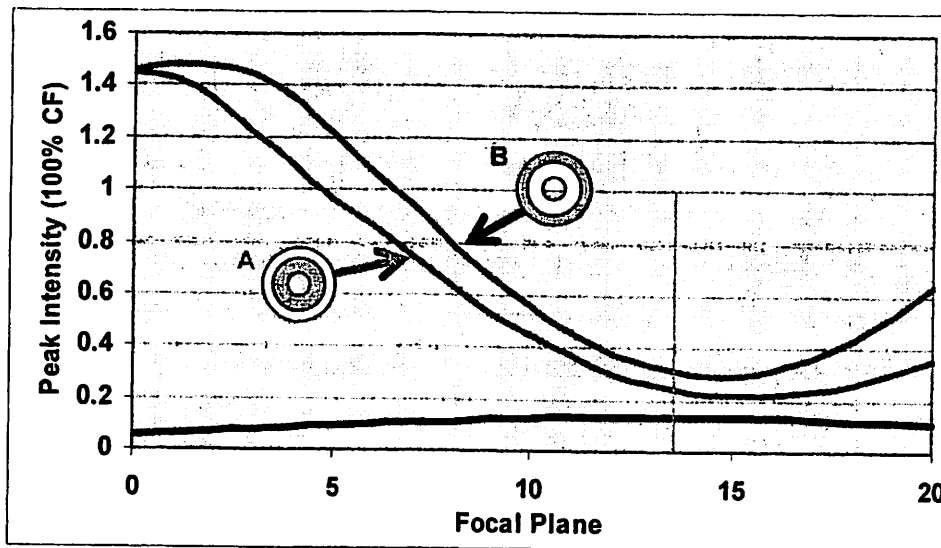


Figure 7-9. AIMS intensity at the center of two two-ring defocus targets with no probe (rings change in phase).

7.4. Experimental Characterization of Target Elements

To understand the initial observations of the full target and the probeless targets, systematic characterization of the components that make them up is necessary. In this

section, isolated dots, lines, and rings, parameterized in size and phase, are studied through both AIMS and simulation. As with the full targets in the previous section, the elements are imaged through a number of focal planes with $NA = 0.80$ and $\sigma = 0.30$.

7.4.1. Imaging Phase-Shifted Dots

A set of probes of 0° , 90° , 180° , and 270° with design diameters of $k_1 = 0.4063$, $k_1 = 0.4514$, $k_1 = 0.4965$, $k_1 = 0.4514$, $k_1 = 0.5417$, and $k_1 = 0.5868$ were fabricated next to each of the sets of aberration targets. The probes shown in Figure 7-3 make up the second and third rows of the probes seen in Figure 7-10. The exact size and phase of the probes is important because of the strong dependence of the peak intensity of small openings upon dimension. The intensity contour measured by AIMS (with the imaging parameters set to $NA = 0.80$ and $\sigma = 0.30$) for all of the probes in the image is given in the upper right hand corner of the figure and shows a sizeable dead zone. That is, while the smallest and the largest probes of 180° and 270° phase produce about the same intensity, the probes of intermediate size at those phases produce very little intensity. The peak intensity at best focus for each of the nominally-sized probes is indicated on the intensity cut-lines in the bottom right hand corner of the figure. The influence of the phase etch topography is evident in that these same-sized 0° , 90° , 180° , and 270° probes, decrease in peak intensity from 13.6%, to 11.0%, to 2.0%, to 1.8% CF.

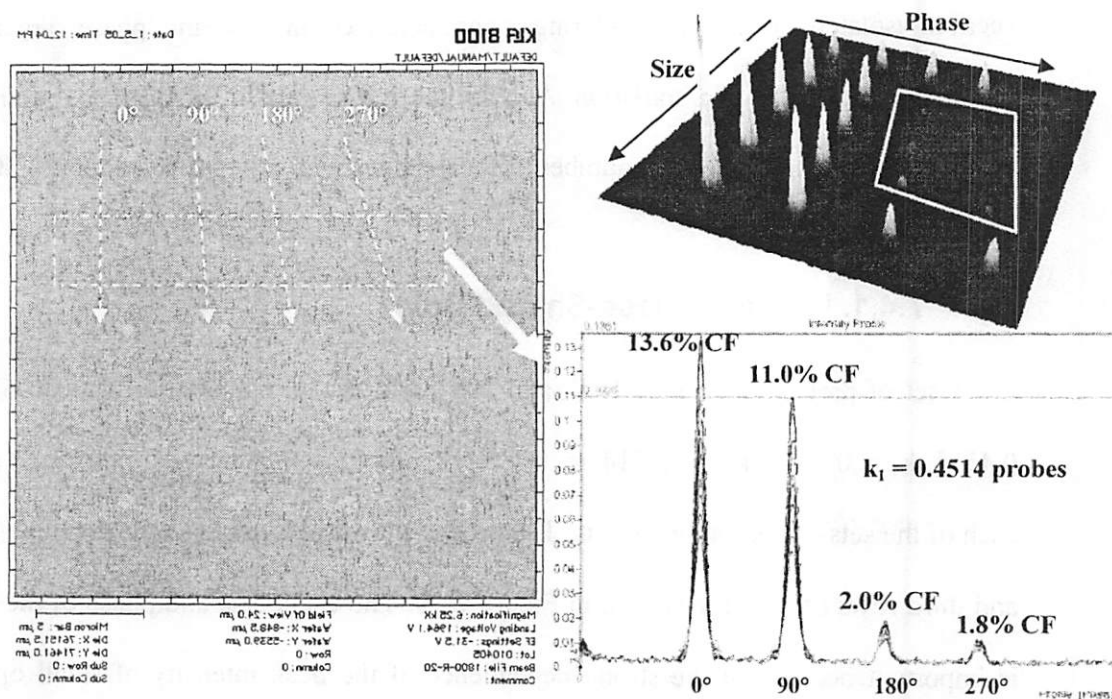


Figure 7-10. (Left) Mask SEM of 0°, 90°, 180°, and 270° isolated probes. (Top right) AIMS intensity profiles of the isolated probes. (Bottom right) AIMS intensity cutlines with peak intensities labeled for probes of nominal size ($k_1 = 0.4514$). Note the significant decrease in intensity with increasing phase etch

Because the probes in Figures 7-3 and 7-10 are not ideal and comparative analysis of them is difficult, a different set of isolated 0°, 90°, 180°, and 270° probes, located at different place on the mask, is used for more painstaking analysis. These probes also range in designed diameter from 50 nm to 250 nm on the mask and SEMs show that the probes of all phases are defined by their chrome edges with no phase steps. Figure 7-11 shows the peak intensity at best focus for the 0° probes as a function of their measured diameters at the mask scaled to wafer dimensions. Also plotted as a solid line are the SPLAT simulated peak intensities for probes of this size. The bias between the design and the fabricated sizes of the features on the mask typically was 5 – 25 nm per edge in wafer dimensions.

Given the discrepancy between the predicted and measured values, the validity of the SPLAT results is checked by comparing them with thin-mask simulations from Panoramic. Panoramic always performs a vector calculation of the image, thereby taking into account the effects of high-NA, so the scalar calculation was emulated by enlarging the probes by a factor of four and reducing the NA by a factor of four (from 0.80 to 0.20). It turns out that the normal thin-mask Panoramic (diamonds), and the emulated “scalar” thin-mask Panoramic (empty boxes) fall virtually on top of one another, indicating both that SPLAT agrees with Panoramic and that, for the thin-mask approximation, the isolated probes are unaffected by vector imaging effects for NAs up to at least 0.80.

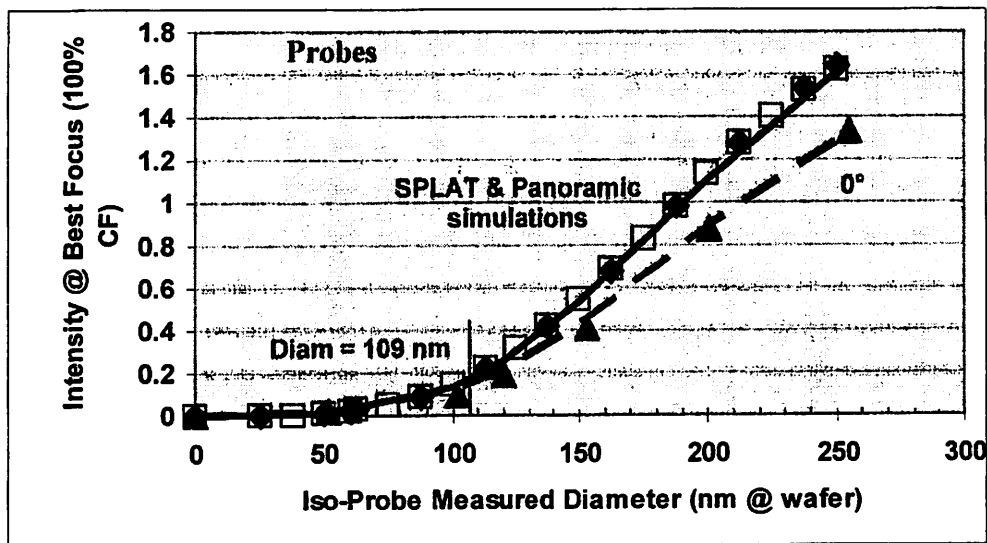


Figure 7-11. Peak AIMS and simulated intensity at best focus for 0° probes vs. measured size.

A dashed line at 80% of the SPLAT values (corresponding to a Strehl ratio of 80%) added to the plot shows excellent agreement to the AIMS data. Full FDTD Panoramic simulations of the nominally-sized probes, including high-NA effects, show that the change with three-dimensional topography for 0°, 90°, 180°, and 270° probes would be a factor of 0.89, 0.64, 0.58, and 0.41 respectively from the ideal probe intensity. (These

numbers are not exact though, as they are dependant upon the simulation domain size.) The difference between the thin-mask simulation and the full electromagnetic simulation accounts for about half of the discrepancy between the ideal and measured peak intensities. The other half of the discrepancy may be attributed to the fact that the AIMS fab 193 may have around 0.05 to 0.07 λ rms of residual aberration [69]. According to Equation 2-17 and Figure 2-7, this much aberration would result in a Strehl ratio around 90%. However, results from a previous experiment at 248 nm show that the AIMS intensity and the peak intensity measured via photoresist exposures agree quite well. Given that the aberrations in the exposure tool are probably significantly less than those in the AIMS tool used, aberrations may not be a significant source of the discrepancy between theory and experiment in the AIMS tool.

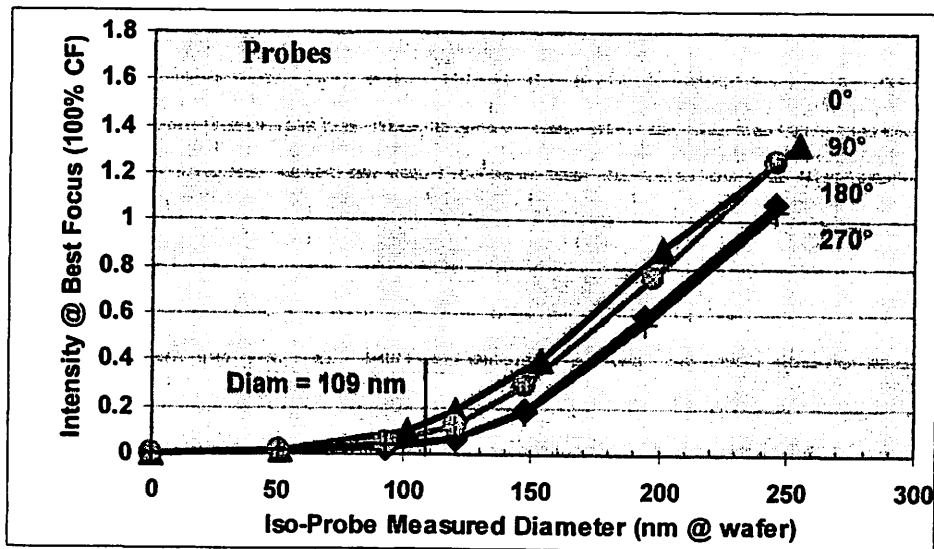


Figure 7-12. Peak AIMS intensity at best focus for 0°, 90°, 180°, and 270° probes vs. measured size.

The AIMS results for all for the phase dot intensities are plotted in Figure 7-12. The intensity curves all follow the same general trend with the 0° probes always the brightest and the 90° probes slightly below. The probes designed to be 180° and 270° have nearly

the same intensity and are noticeably darker than the 0° and 90° probes. At the nominal probe diameter of 109 nm, indicated on the plot, the peak intensities of the 0°, 90°, 180°, and 270° probes are 0.70, 0.49, 0.26, and 0.29 times the ideal 19.2% CF value. In order for a 90° probe to have the same intensity as a 0° probe of the same size, then it would have to be about 80 nm bigger in diameter.

7.4.2. Imaging Phase-Shifted Lines

AIMS measurements and simulation of isolated lines show results consistent with those for the probes. The typical ring thickness for an aberration target is approximately $k_1 = 0.52$, which is equivalent to 125 nm on the wafer. For 0°, 90°, 180°, and 270° lines of 125 nm width, the peak intensities at best focus are 0.86, 0.75, 0.61, and 0.57 of the theoretical thin-mask value of 77% CF, respectively. The peak intensity at best focus of the phase lines is plotted as a function of measured line-width at the wafer in Figure 7-13. As with the probes, the 0° features tend to be the brightest and they tend to decrease in brightness with increasing phase etch depth. SEM inspections of the lines shows that they are well defined for all phases by the chrome on the mask, indicating that the intensity change with etch depth is purely due to electromagnetic edge effects.

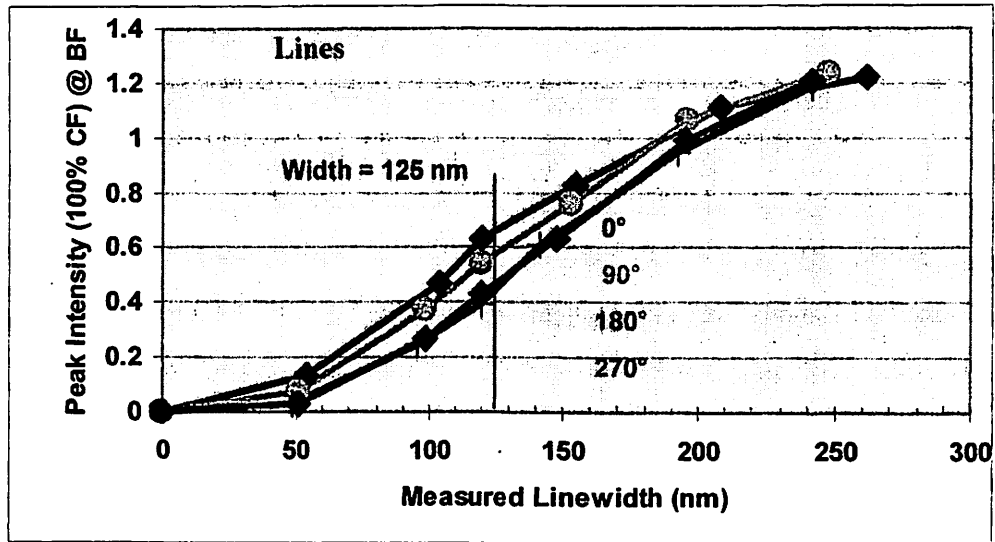


Figure 7-13. Peak AIMS intensity at best focus for 0°, 90°, 180°, and 270° lines vs. measured size.

The SPLAT simulated peak intensity at best focus is plotted along with the AIMS data for the 0° line in Figure 7-14. As with the probes, it is seen that the intensity predicted by simulation is always greater than the measured intensity. In order to confirm that there is not a constant multiplicative factor which results from the way that the AIMS software normalizes to the clear field reference that causes an error, a dashed reference line at 80% of the SPLAT results has been placed on this plot as well. In this case however, the 80% values do not accurately predict the measured intensities for all linewidths. Thus, the suspected causes of the disagreement between the simulated and experimental results remain thick mask effects and aberrations in the AIMS optics.

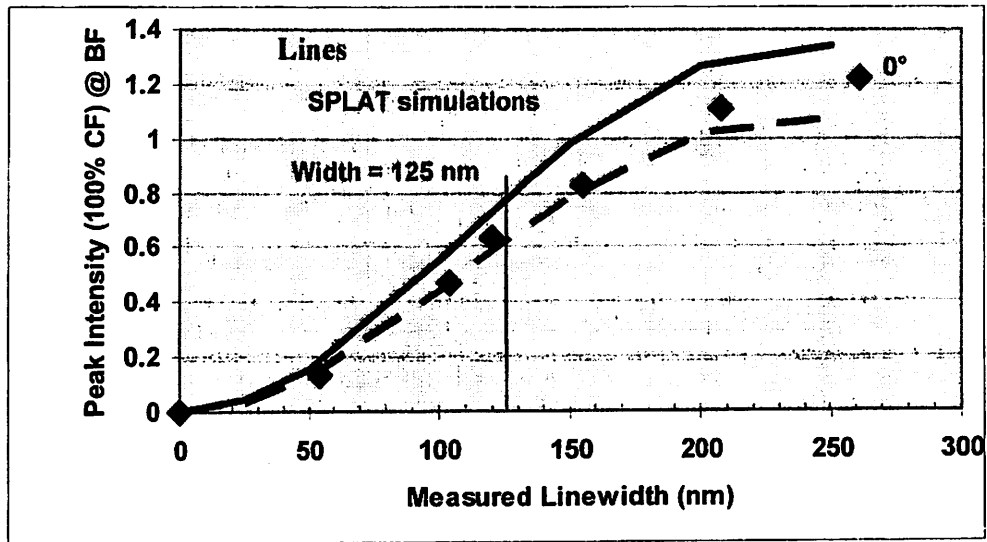


Figure 7-14. Peak AIMS and simulated intensity at best focus for 0° lines vs. measured size.

7.4.3. Imaging Phase-Shifted Rings

Through-focus measurements of isolated versions of the defocus target rings are used to compare the ring image with the proximity spillover to the center. Figure 7-15 shows intensity cut-lines through both 0° and 180° versions of the innermost ring with $r_{cr} = 0.35$, the second ring, and the third ring out from the center. These rings have designed thicknesses of $k_1 = 0.67, 0.53,$ and 0.52 , respectively. In general, the peak intensity at the ring position of the 0° rings are brighter than their 180° counterparts, with the intensity ratio being $0.83, 0.53,$ and 0.53 for the inner, second, and third rings, respectively. This indicates some additional degradation from the case of isolated lines due to the circular shape of the rings.

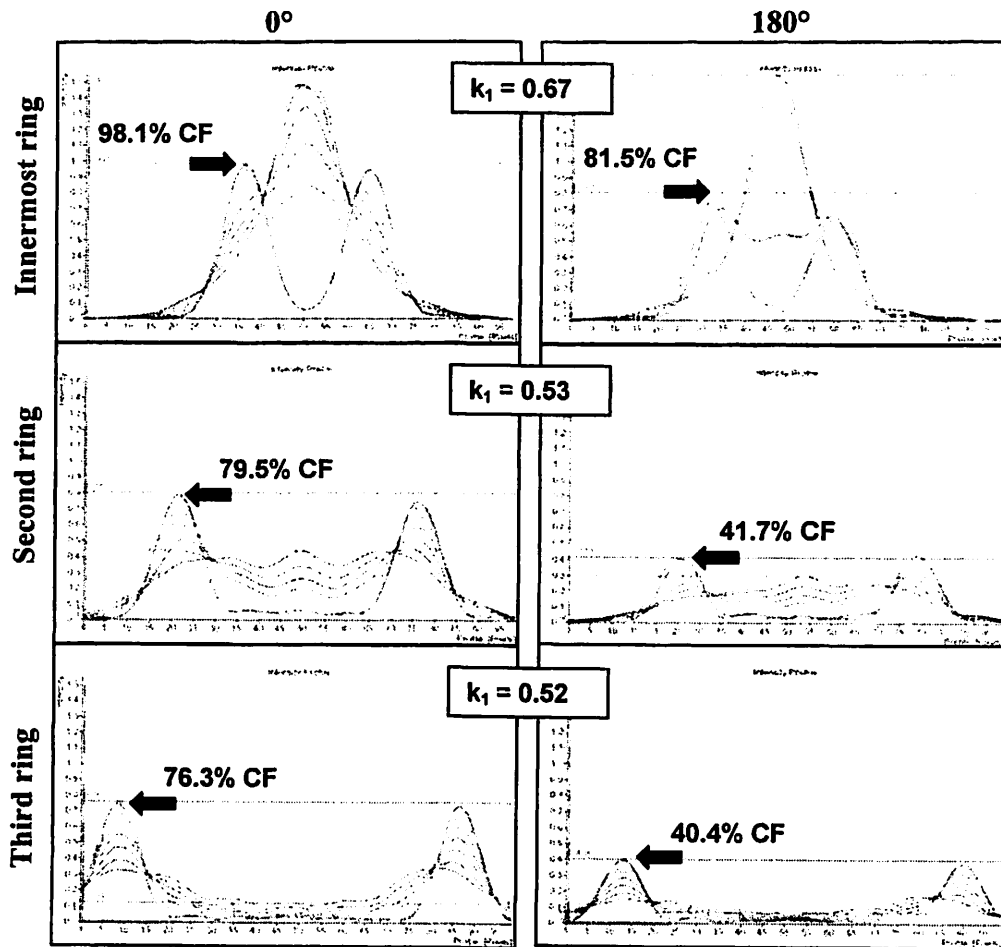


Figure 7-15. Peak AIMS intensity at best focus for both 0° and 180° isolated rings. ($\sigma = 0.30$)

While the intensity at the ring position itself changes, it is the magnitude and phase of the spillover fields which are critical to target operation. In Figure 7-16 the through-focus spillover intensities from both versions of the innermost and second ring are shown. The solid lines represent the data for the 0° rings and the dashed lines represent that for the 180° rings. The spillover influence from the inner ring with focus is larger than anticipated, with a value of 60% CF at best focus, corresponding to a normalized electric-field of 0.77. Ignoring data near the AIMS saturation point, the center intensity response is quite linear near best focus. The spillover from the second ring also responds in a parabolic manner and is lower than anticipated at 8 to 12% CF, corresponding to fields of

0.28 and 0.35. This is most likely because of the decreased mutual coherence factor at the distance of the second ring at this σ . Surprisingly, despite the significant difference in the ring intensities, the center response is nearly identical for both phases of each ring. Unfortunately, this data shows that E_{outer_ring} and E_{inner_ring} are still unbalanced, despite following the prescription set forth in Section 5.3.4 of reducing r_{cr} to 0.35.

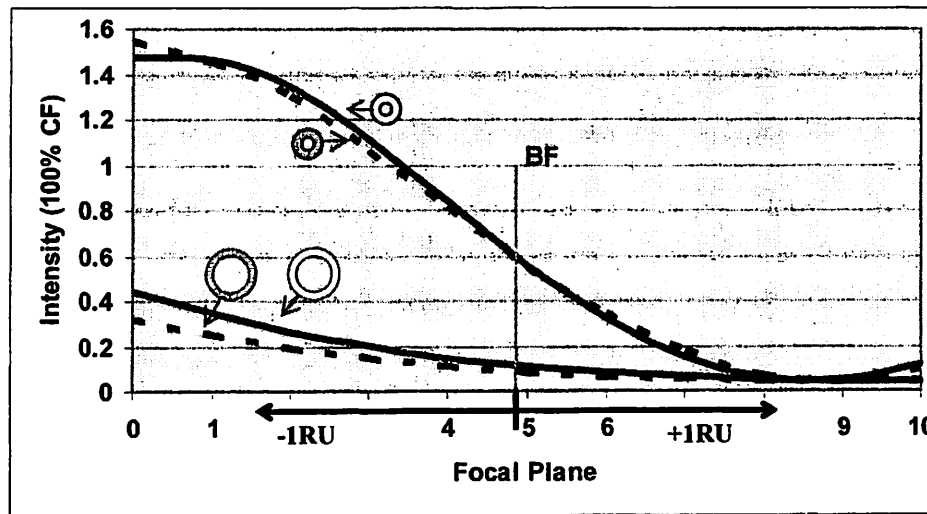


Figure 7-16. Peak AIMS and simulation intensity at best focus for both 0° and 180° lines and probes vs. size.

7.5. Analysis of Full Target Response

In order to make the AIMS results on the full target easier to analyze, intensity values above 130% CF have been eliminated and parabolas have been fit to all of the data. The data points in the plots are the measured intensities and the solid lines are best fit parabolas. Best focus is indicated on the plot at 6.24 focal steps. Each focal step is $0.7 \mu\text{m}$, corresponding to 0.290 RU.

7.5.1. Target Response at $\sigma = 0.30$ and 0.17

Figure 7-17 shows the center intensity as a function of focus for $\sigma = .30$ and 0.17 for the two targets without probes (T_1 and T_4) in Figure 7-4. These structures, just the target rings with no probes, were designed to minimize the total spillover into the center when no aberrations are present by balancing E_{outer_ring} and E_{inner_ring} by making $r_{cr} = 0.35$. Ideally, both of the sets of curves in Figure 7-17 would be identical, with the parabolic response of each reaching zero at best focus and being symmetric about this point. Neither T_1 nor T_4 reach zero however, for three reasons. The first is that biasing and misalignment can cause an imbalance between E_{outer_ring} and E_{inner_ring} . The second is that the relatively large (for these targets) σ value of 0.30 causes E_{inner_ring} to well outweigh E_{outer_ring} . That is, E_{outer_ring} has a significantly larger portion of its spillover which is incoherent than E_{inner_ring} does. Finally, a phase error in the etched ring can rotate its spillover vector (E_{inner_ring} for T_1 and E_{outer_ring} for T_2) so that it is no longer purely real. Furthermore, while the parabolic symmetry about best focus is independent of the biasing and misalignment of the rings (because E_{outer_ring} and E_{inner_ring} are ideally purely real), the minimum of the parabola can be shifted from best focus, and the symmetry broken if a phase etch error induces an imaginary field component. This is because it would then take a certain amount of defocus to provide the imaginary perturbation fields necessary to eliminate this unwanted piece of imaginary field.

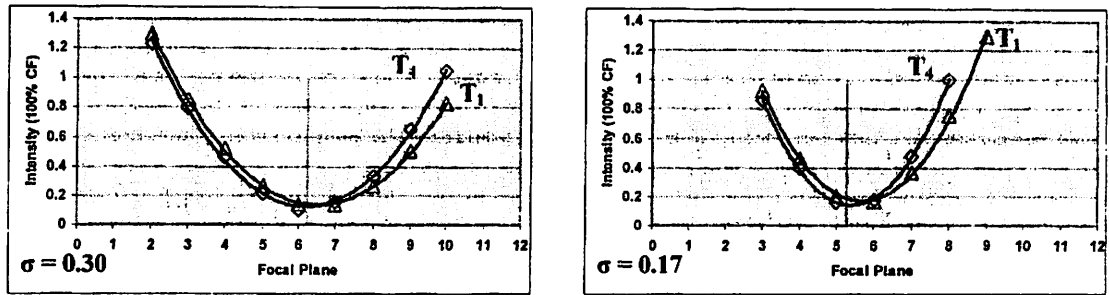


Figure 7-17. AIMS intensity vs. defocus response with best fit parabolas for targets with no probes from Figure 7-4 for $\sigma = 0.30$ on the left and $\sigma = 0.17$ on the right.

For $\sigma = 0.30$ the minima of T_1 and T_4 are 0.078 and -0.015 RU away from best focus, respectively. Combined with the fact that the minimum value of T_1 is 13.9% CF and that of T_4 12.4% CF, it may be that the 4° to 8° phase error in the 180° region is causing a significant rotation of the phase angle of the fields.

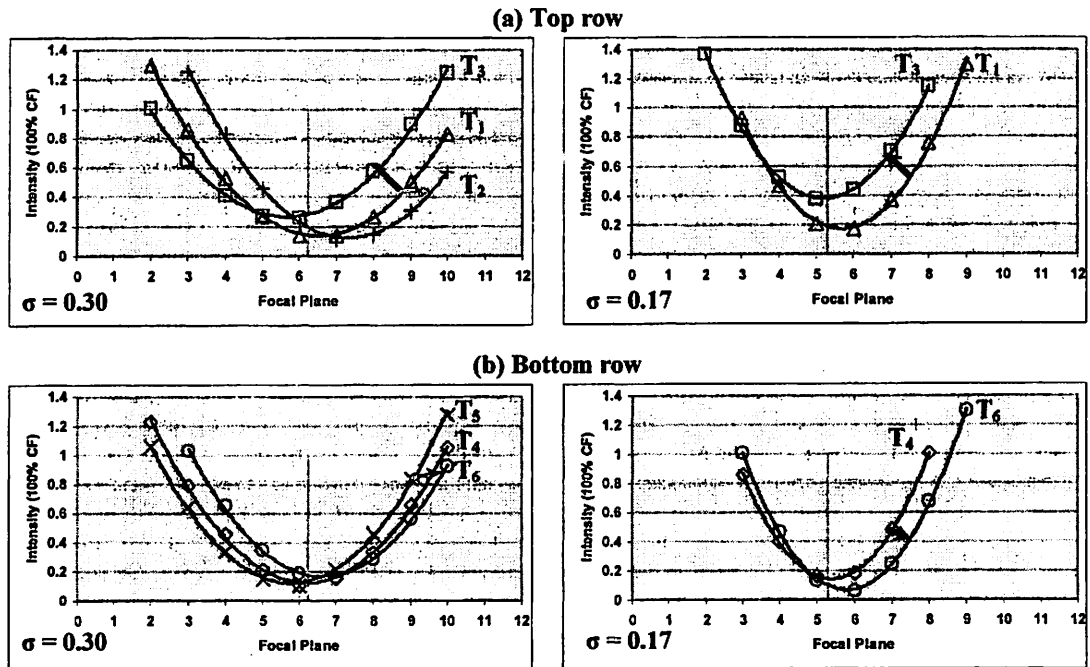


Figure 7-18. AIMS intensity vs. defocus with best fit parabolas for (a) top row of targets with probes and (b) bottom row of targets with probes from Figure 7-4 for $\sigma = 0.30$ on the left and $\sigma = 0.17$ on the right.

7.6. General Trends in the Data

Considering the responses of the different variations of the target in the context of the phasor model of the electric-field illustrated in Figures 5-6 and 5-7, it appears that the targets do respond to some extent as expected since the addition of the probe shifts the parabolic response. The parabola appears to move right and left in a complimentary manner depending upon the phases of the rings and the probe. As discussed earlier though, there are many non-idealities which cause the targets to act differently than anticipated.

7.6.1. Changes with Probes

In theory, the effect of rotating the 90° probe to 270° is the same as leaving the probe alone and interchanging the phases of the rings. The purpose of building targets with 270° probes is to flip its electric-field contribution from the case where it is 90° , which should reflect the parabolic response of the target with the 90° probe about the best focus axis. The through-focus intensity data and parabolic fits for $\sigma = 0.30$ for all of the targets in the top and bottom rows of Figure 7-4 are shown in the left column of Figure 7-18 and the plots for $\sigma = 0.17$ are in the right hand column. In the top row it is seen that adding a 90° probe to the rings causes the parabola to shift up and to the left, while adding a 270° probe in the $\sigma = 0.30$ case causes the parabola to move to the right. In the bottom row, adding a 90° probe causes the parabola to move slightly up and to the right for $\sigma = 0.30$ and down and to the right for $\sigma = 0.17$. Adding a 270° probe in the bottom row for $\sigma = 0.30$ causes the parabola to shift slightly down and to the left.

7.6.2. Changes with σ

Figures 7-17 and 7-18 show that decreasing σ has a significant influence on target behavior. The most obvious change when σ is reduced from 0.30 to 0.17 is that the parabolas become tighter. In fact, the second derivatives of the equations defining the parabolas at $\sigma = 0.17$ are all about a factor of two greater than the second derivatives for each equivalent target at $\sigma = 0.30$. This indicates that the targets give a much stronger response to aberration at lower σ . Also, reducing σ from 0.30 to 0.17 also causes the minimum intensity of the probeless targets to rise from 13.9% CF to 17.4% CF for T_1 and from 12.4% CF to 14.3% CF for T_4 . The positions at which these minima occur move to the right by 0.035 RU for T_1 and by 0.014 RU for T_2 .

7.6.3. Summary

The performance of pattern and probe-based interferometric aberration monitors is highly dependant upon a number of imaging demons. In order of likely importance they are: mask geometry, the partial coherence factor σ , electromagnetic transmission effects, high-NA polarization effects, and resist effects. Initial observations of the two-ring defocus target show discrepancies between the experimental behavior and that which has been predicted by simulation. In general, the results presented in this chapter were as expected from the behavior of probes and lines. The composite targets were more sensitive to focus than any typical layout pattern. However, the theoretical super-sensitivity and linearity through focus was not observed due to the weakness of the probes. Hence larger central probes with isolated intensities of 50% CF or larger may work better. Excellent change in the perturbation to the ring spillover versus focus was

also observed, but at the design size, the spillover from the innermost ring is a factor of five larger than that of the second outer ring, causing it to dominate target behavior. These observations indicate that electromagnetic edge effects impact the probes and to some extent the rings. The lower than expected intensities from the small probes adversely interacted with the low central signal strength from the second ring that is inherent with the partial coherence factor of about 0.3 used as representative of the minimum value on the installed base of exposure tools.

While the issue of intensity imbalance is important in 4× lithography tools, using targets designed for a larger $\frac{\lambda}{NA}$ ratio would significantly reduce the impact of mask topography upon the transmission of phase-shifted regions. For example, if aberration targets were designed for use with the human eye at $\lambda = 650$ nm and $NA = 0.01$, then they would be over 50× larger than the targets shown in this chapter and the aspect ratio of the phase etched regions would be reduced by 20×. Use of such a small NA would also eliminate polarization effects and mask geometry effects such as layer alignment would be negligible given the size of the targets. All of these factors combined would cause these larger targets to act much more like they are predicted to by SPLAT.

8. Quantitative Analysis

This chapter presents quantitative analysis of the different factors which cause the target behavior to deviate from the ideal. The factors of alignment, bias, phase etching, electromagnetic transmission, high-NA imaging, and the partial coherence used in imaging are all investigated. The analysis can be quite complicated because each electric-field contribution has its own magnitude and phase.

8.1. *Estimated Influences of Non-Idealities*

8.1.1. Alignment

Probe magnitude

The theoretical development of these patterns in Chapter 4 indicates that only 0° and 90° probes are needed for implementation of both even and odd aberration targets. The mask fabrication process described in Section 7.1 shows that both types of probes are initially opened with the electron beam tool in the first processing step. Thus, the overall sizes of the probes are quite close to their design, as seen in Figure 7-5. Figure 7-11 shows that the intensities of the 0° probes are 80% of their theoretical values predicted by SPLAT, and about half of this discrepancy can be accounted for by considering aberrations in the AIMS tool. If a probe intensity is 90% of its theoretical value this corresponds to a drop in electric-field of only 5% from its theoretical value.

Probe phase

Under-biasing of the 90° portion of the probe region can cause the electric-field to be split between a 0° contribution and a 90° contribution. The images in Figure 7-5 show the

case where the contributions seem to be split evenly. This results in the phasor electric-field contribution of the probe pointing at a 45° angle, which gives a 30% drop in the amount of imaginary electric-field from its ideal value. This case however is considered catastrophic because this amount of bias is most likely due to considerations that were made for other students' patterns which are on the mask. In the future it should be possible to eliminate such problems. Misaligning the 90° write and etch to the 0° first layer by a more reasonable 50 nm (the Alta tool's 3σ error) would cause the 90° region to be about 80% and the 0° region to be 20% of the total probe area. This would make the electric-field point at 75°, giving a 3% drop in the desired imaginary electric-field.

Ring spillover magnitude

As discussed in Chapter 4, the properties of the targets derive directly from the form of the Zernike aberration term of interest. The targets are each made of electric-field which decrease in magnitude regularly from the center and have a characteristic ripple distance on the order of $\frac{\lambda}{2NA}$, resulting from interference of waves from the edges of the pupil. Looking at the IFT target for the first Zernike term of piston, the lobes of Airy spillover function are relatively flat and wide, as seen in Figure 8-1. For the first side-lobe the minimum in electric-field is -0.134. A 50 nm misalignment on the mask would correspond to a $0.052 \frac{\lambda}{NA}$ misalignment of the spillover from the ring into the center on the wafer, resulting in a 3 to 5% decrease in the spillover electric-field. Measurements on the current mask indicate that the misalignment is actually about twice this, resulting in a 20 to 25% reduction in spillover electric-field. Although the side-lobes become smaller

and smaller with increasing radius, it appears that, per unit electric-field contributed, the impact of misalignment remains constant.

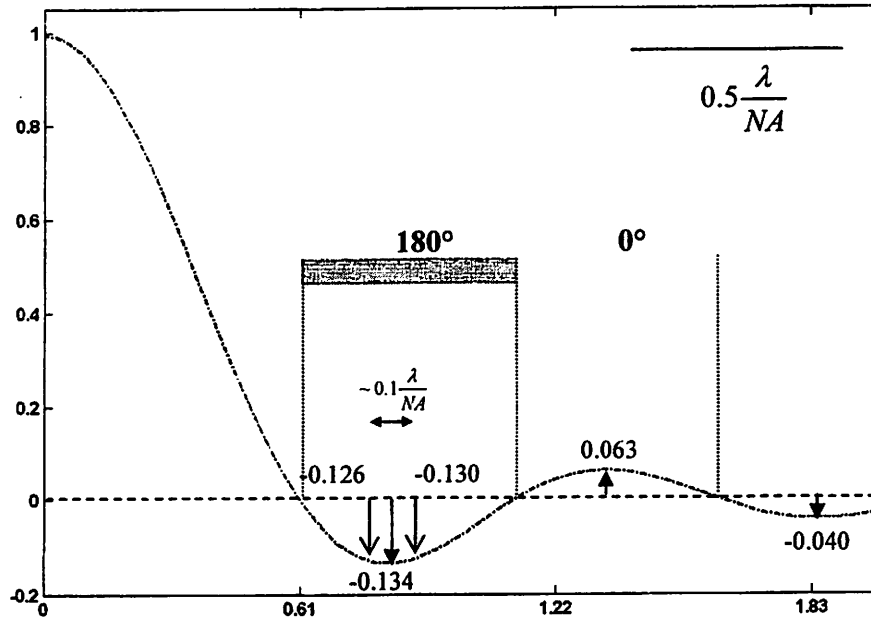


Figure 8-1. The spillover electric-field from a pattern ring onto the center and the effect of misalignment.

8.1.2. Bias

Ring spillover magnitude

The bias used in processing the rings can also have an impact upon their spillover. While biasing is often used to mitigate mask edge electromagnetic transmission effects, it can have an even more complex interaction in the implementation of the aberration monitors. The effective edge biases measured in Section 8.1.1 of + 0.03 μm and -0.035 μm , are approximately equal to the 50 nm = 0.052 $\frac{\lambda}{NA}$ alignment accuracy of the tool. If

the 180° region is biased by + 50 nm on each edge then in the two-dimensional view of the Airy spillover function shows that to first order, there are two extra triangular areas which contribute electric-field. The original fields can be approximated with a triangle as

well. Comparing the sum of the areas of the triangles associated with the extra fields to that associated with the original fields, it is found that this amount of edge bias would likely cause a 4% decrease in the electric-field.

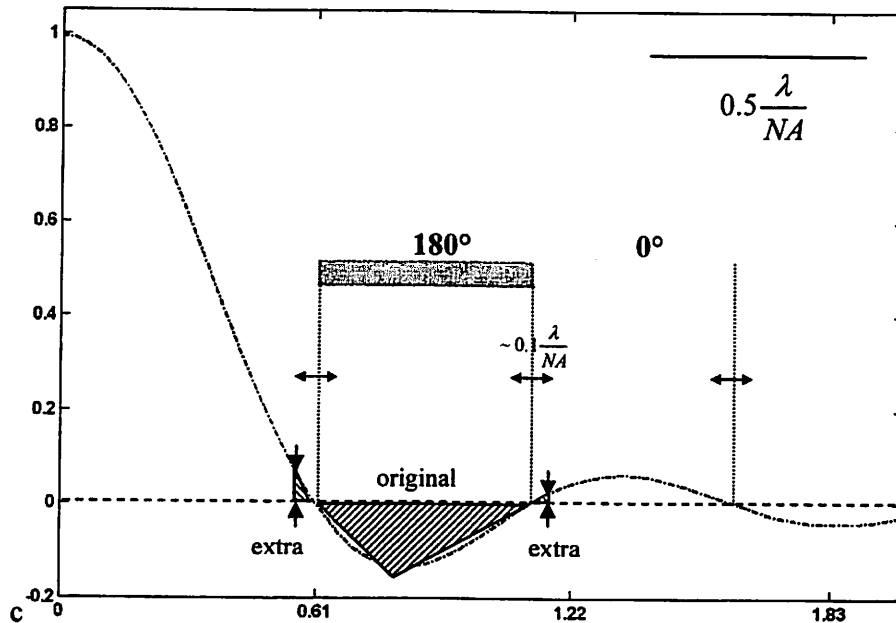


Figure 8-2. The spillover electric-field from a pattern ring onto the center and the effect of ring feature edge bias.

8.1.3. Phase Etch Error

Ring spillover phase

Alignment, bias, and phase etch errors can change the net spillover electric-field from the rings just as they can change the field from the probe. The rings are all either 0° or 180° in phase so phase etch error can only occur in the 180° rings. The phase etch error reported in Section 8.1.2 depends on the exact feature type, but errors from 4° to 8° have been reported for these types of ring structures. A -4° phase error in the spillover from the ring would correspond to a 0.5% decrease in the desired electric-field. An -8° error would only cause a 1% decrease.

8.1.4. Topography Effects

Electromagnetic transmission

At the 193 nm wavelength, the real part of the refractive index for glass is 1.56. Using Equation 2-13, the etch depths for 90°, 180°, and 270° phase shifts are 0.446, 0.893, and 1.339× 193 nm. It is the electromagnetic effects associated with these sidewalls, created by the etching, that act to steal electric-field from the etched openings, giving them less intensity than 0° openings of the same size. For long 180° lines, A. Wong calculated in his PhD thesis [66, ch. 7] that, the bias necessary to compensate for these edge effects is $0.021 \frac{\lambda}{NA}$ per edge. Looking at the data for 180° versus 0° lines and probes in Figures 7-12 and 7-13, the lateral shift is approximately 21 nm. This equates to $0.087 \frac{\lambda}{NA}$ in line-width or probe diameter, which corresponds to a $0.044 \frac{\lambda}{NA}$ bias needed per line edge or in probe radius to make their intensities equal to their 0° counterparts. While the measured results for the required bias agrees with the results obtained via TEMPEST to within a factor of 2, one would expect the holes to reflect a relatively larger “dead zone” along their edges than the lines because they have significantly more sidewall area per lateral. If a nominally $0.45 \frac{\lambda}{NA}$ diameter 180° probe is effectively undersized by $0.087 \frac{\lambda}{NA}$ in diameter, then the amount of electric-field that it generates is 20% less than it’s ideal value.

8.1.5. High-NA

Probe magnitude

In Section 7.4.1 a discussion of simulation and AIMS imaging results on probes is given. Figure 7-11 shows that the thin-mask simulation results obtained through Panoramic are consistent with those from SPLAT. Because Panoramic always performs a vector calculation of the intensity at the image plane and SPLAT performs only a scalar calculation, this indicates that polarization effects due to high-numerical aperture imaging are negligible for the probes. This is supported by the plot in Figure 8-3, where both AIMS and photoresist exposure data are presented for 0° and 90° probes of different sizes at $\lambda = 248$ nm and $NA = 0.80$. In every case the high-NA exposure tool data falls very close to that from the low-NA AIMS tool.

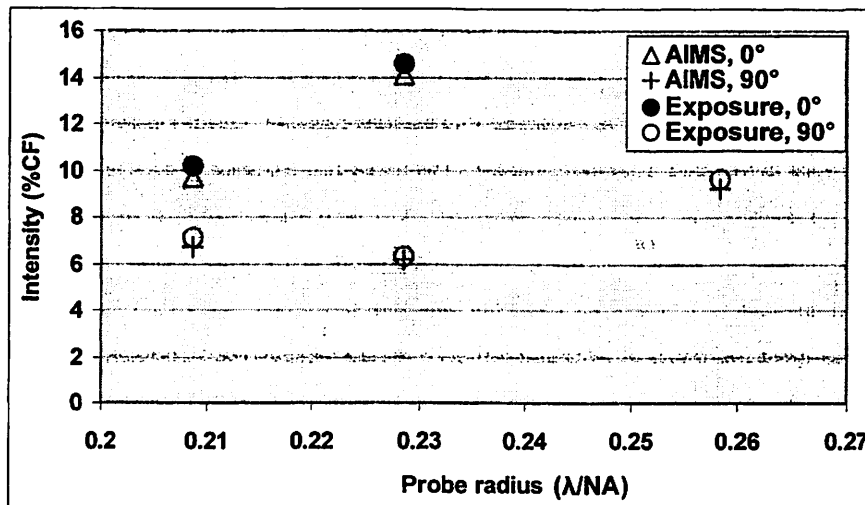


Figure 8-3. Plot showing the measured intensity of probes in a high-NA exposure tool and a low-NA AIMS tool emulating the scanner. $\lambda = 248$ nm, $NA = 0.80$.

Ring magnitude

While the probe intensity is not significantly affected by high-NA imaging, the interaction of the electric-fields from the target rings at the imaging plane can be

significantly impacted by polarization effects. The rings, which are near the tool's resolution limit, are similar to a radial grating, throwing light out towards the edges of the lens. To quantify the potential impact of such effects upon the important electric-field contributions to the target, the worst case scenario of all of the fields scattered from the rings being collected by the edge of the lens is investigated.

For unpolarized illumination the energy arriving at the image plane is split equally between the TE and TM modes of the electric-field, E_{TE} and E_{TM} . Assuming a system with $NA = 0.80$, the maximum ray angle of light arriving at the image plane is 53° and the electric-field in the TM mode is split between a desired in-wafer plane component, $E_{TM,xy}$, and an unwanted out-of wafer plane component, $E_{TM,z}$. Due to the high angles involved, $E_{TM,xy}$, which provides contrast in the image plane, is only 60% of E_{TM} and $E_{TM,z}$ is 80% of E_{TM} . Since half of the energy is contained in the unaffected mode, the total in-plane electric-field arriving at the image plane from the rings is reduced by about 20% from its ideal value. The energy in the $E_{TM,z}$ fields is not lost however. It merely adds a background electric-field which reduces the overall image contrast.

8.2. *Partial Coherence*

8.2.1. Ring Self-Influence

Figure 8-4 shows an inner 0° defocus target ring surrounding a 0° probe. Through a detailed study of the implementation of the defocus target it has become evident that there is a major complication created by σ . The crux of the problem is that, even though the mutual coherence function is smooth over the entire target, the envelope that it provides greatly influences the weighting of the spillover fields from each element of the

rings. That is, contributions from different radii are weighted differently when σ is sufficiently large so that the mutual coherence between the ring element and the probe change with radius. Two ring elements, “A” and “B”, are shown in Figure 8-4 along with their mutual coherence envelopes for $\sigma = 0.30$ (solid lines) and for a much greater σ (dashed lines). The σ value affects how the point spread electric-field from each element adds together with the probe field and with the field of all other elements at the center of the target. The vertical arrows show that the difference between $\mu_{A,P}$ and $\mu_{B,P}$ at the probe position is about 30% of their peak value of 1 for $\sigma = 0.30$. The effect of this is that the sign of the net spillover fields used in the electric-field phasor addition model is σ -dependant.

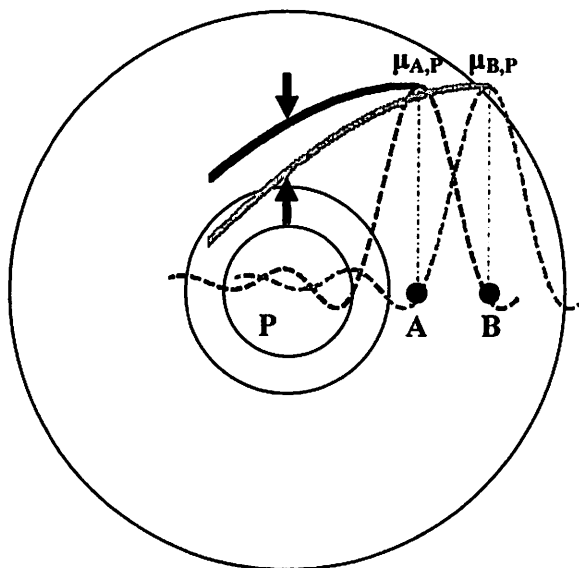


Figure 8-4. Schematic diagram showing (a) the difference between the mutual coherence envelopes of ring elements “A” and “B” and (b) the self-influence of these elements at the target center.

To investigate the impact of σ , the target was simulated using SPLAT. Figure 8-5 shows the intensity of an isolated probe as well as the center intensity of the single 0° ring and 0° probe composite, with no aberration, for varying σ . For $\sigma < 0.22$, the intensity

at the center of the composite target is less than that of the isolated probe, while for $\sigma > 0.22$, it is greater. Since the field from the probe is 0° , this implies that the net spillover field from the ring must be 180° for $\sigma < 0.22$ and 0° for $\sigma > 0.22$. That is, the net spillover field changes sign depending upon the value of sigma. Assuming collinear addition of the probe and spillover fields, the net electric-field spillover from the rings is calculated to be 0.06 at 180° for σ near zero and 0.06 at 0° for $\sigma = 0.30$. Compared to the electric-field of 0.43 generated by the probe, this is a 28% change in the field at the center of the target. Reducing σ from 0.30 to 0.15 lowers this effect to less than 4%.

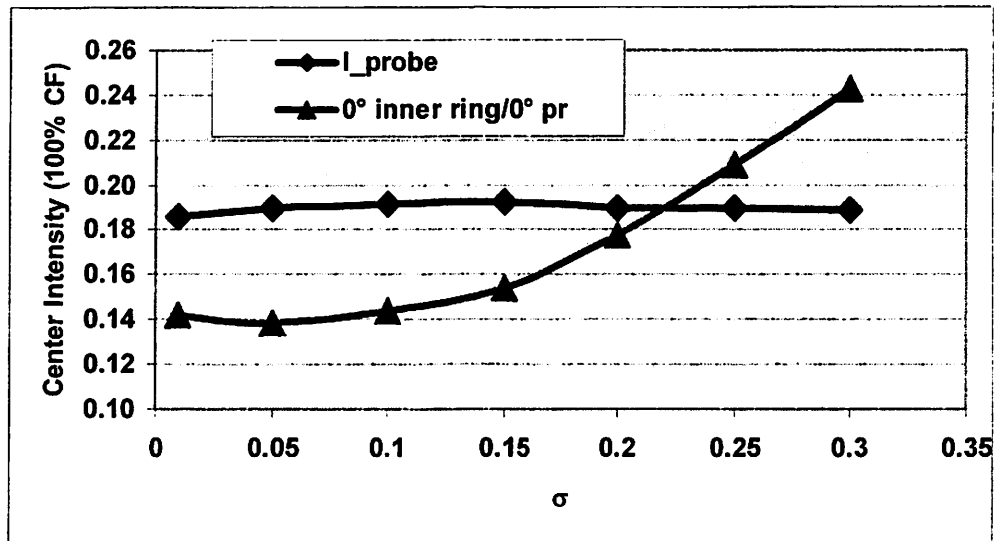


Figure 8-5. SPLAT simulated intensity of an isolated 0° probe and of a 0° inner target ring surrounding a 0° probe vs. σ . This shows where the sign for the collinear addition of electric-field changes.

Finally, the interaction of the elements themselves at the center of the target is explored. Again, the theoretical development of the aberration monitors calls for fully-coherent on-axis illumination, but taking the influence of σ upon the electric-field contributions of each of the target elements into account, the electric-field and resultant central intensity can be given by

$$\begin{aligned}
E_{center} &= E_{A_center} + E_{B_center} + E_P \\
I_{center} &= \langle E_{center} E_{center}^* \rangle \\
I_{center} &= (E_P^2 + E_{A_center}^2 + E_{B_center}^2) + \\
&\quad (E_{A_center} E_P \mu_{A,P} + E_{B_center} E_P \mu_{B,P} + E_{B_center} E_{A_center} \mu_{A_center,B_center})
\end{aligned}$$

Equation 8-1. Equation showing the interaction of the electric-field contributions at the target center.

Here $\mu_{B,P}$ is the normal mutual coherence function defined for two points separated by the distance from B to P and μ_{A_center,B_center} is the mutual coherence of E_{A_center} and E_{B_center} . Reducing σ so that the coherence radius is large compared to length scales of interest for the targets would eliminate this considerable complication.

8.2.2. Searching for an Imaginary Component

One concern is that the change in center intensity of the composite target in Figure 8-5 is due to an imaginary component of electric-field being generated by changing σ rather than the real spillover fields changing as discussed. To study this, the phase of the probe in the target can be rotated to 90° and the center intensity for an isolated probe, an isolated ring, and their composite simulated as a function of σ . Because the ring and probe fields are orthogonal, the sum of their intensities should always equal that at the center of a composite target made up of both components, unless changing σ creates an imaginary electric-field component. The results are plotted in Figure 8-6 and, in what is perhaps a testament to the accuracy of SPLAT, the sum matches the composite out to at least four decimal places over a wide range of σ values. Thus, it is concluded that changing σ does not create any imaginary electric-fields.

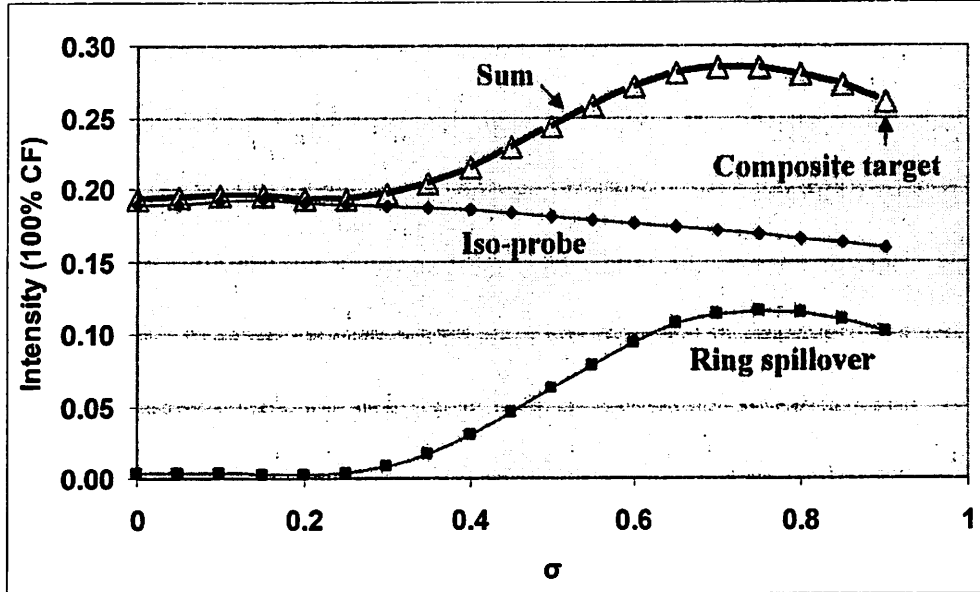


Figure 8-6. SPLAT simulated intensities for target components and a composite target over a wide range of σ .

8.3. Conclusions and Outlook for the Future

The three most important factors that limit the pattern and probe-based aberration monitors in practice are:

- 1) High-NA polarization effects upon the rings (20%)
 - 2) Edge electromagnetic transmission effects on the probes (20%)
- and
- 3) The illumination partial coherence (28%)

The other factors discussed are important, but are significantly less, ranging in impact in electric-field from less than 1% to 5%.

The positions in the lens at which the scattered fields from the target rings land is a fundamental property of the shape and size of the rings. Therefore, rays will always arrive at steep angles in the image plane. While this is important in determining the aerial

image, introducing photoresist greatly mitigates the effect. For resist with a refractive index $n \approx 1.7$, the rays will be bent back towards the normal and an NA of 0.80 will be reduced to an effective NA 0.47. This makes, $E_{TM,xy} = 88\%$ of E_{TM} , and reduces the amount of in-plane electric-field lost from 20% to only 6%.

Electromagnetic edge effects significantly impact the intensity of phase shifted probes. SPLAT simulation shows that the net influence of a reduction in probe intensity is to reduce the lateral shift of the parabolic target response, which is detrimental to target sensitivity at low aberration levels. For a probe which has an intensity which is 10% less than designed, the sensitivity of the defocus target is reduced from 80% CF/RU to 57% CF/RU. This should be relatively simple to alleviate though because Figure 7-12 shows that the probes merely need to be oversized by an amount dependant upon their phase shift in order to yield the desired electric-field magnitude.

Finally, the use of partially coherent light seems to have the biggest impact upon target performance. Partial coherence causes the spillover fields and the perturbations to the spillover fields due to aberrations, to be partially coherent and partially incoherent, thus making the theoretical prediction of target behavior extremely complicated. It is found however, that by reducing σ from 0.30 to 0.15, this effect can be shrunk to less than 4%. While this is not an unreasonably low number for σ , and indeed some tools can achieve it, one proposed solution is to generate a photomask which has chrome on the backside with pinhole openings to provide highly-coherent illumination at the target plane. Unfortunately, there are concerns about contaminating the processing tools used to fabricate such a mask, so this idea has not yet been implemented.

It appears that the major hurdles to implementation which were observed for the defocus target, are surmountable. All of the effects which impact target behavior to 20% or more have reasonable solutions which reduce their influence to a level around 5%. Thus, the rotationally-symmetric targets for defocus and spherical aberration should be able to be redesigned with the proper biases on the phase shifted regions, and imaged using low- σ , so that they yield good results. The targets could be improved even further by eliminating the issue of electromagnetic mask transmission through a small probe hole by making all of the probes 0° and making the ring phases 90° and 270° . One problem though may be that the defocus target and the spherical target have very similar ring structures, so there may be a large amount of crosstalk between the two.

As immersion lithography becomes more common, effectively increasing NA, the target feature sizes on the mask will shrink. Partial coherence, will still affect target performance in the same way, but high-NA polarization effects and electromagnetic transmission effects will become increasingly important. Steeper angles will take more and more electric-field out of the desired in-plane component and it will become more and more difficult to get light through the phase shifted openings on the mask. For immersion lithography at $\lambda = 193$ nm with $n = 1.25$, the target features will be $0.80/1.25$ smaller, bringing a target ring from a thickness of 120 nm down to 77 nm. At this size, Alfred Wong's prescription of $0.021 \frac{\lambda}{NA}$ bias per edge for 180° phase shifted features should continue to work at this reduced size and Figure 7-13 supports this to within a factor of two for the bias. This will not continue indefinitely however.

With this increased understanding of the performance-limiting factors relevant to the defocus target, the coma target can be revisited. The coma target is just as susceptible to

the issues which arise when using partially coherent rather than fully coherent light, as well as high-NA effects and electromagnetic transmission effects, as the defocus target. It is not however, susceptible to the same problem of the zero-aberration reference value as rotationally-symmetric targets. On the other hand it, and indeed all targets with azimuthal variation, has a problem which the rotationally-symmetric targets do not demonstrate. That is the problem of the probe “bleeding” into the portion of the innermost target ring which is of the same phase, making reading the target extremely difficult. This is purely an electromagnetic effect and it seems that the only remedy is to increase the size of the chrome donut isolating the probe from the rings. Finally, Figure 6-14 indicates that the rings in the coma target are potentially twice as sensitive to coma aberration as the probe. This may offer a way to make super-sensitive measurements of coma but the ring response may be highly-sensitive to aberrations other than coma. The only location for which the theory regarding the quantitative interpretation of the amount of coma currently exists is at the probe position.

With the first and second-order effects well characterized, the interferometric pattern and probe-based aberration monitors show great promise for the future.

9. Aberrometry for the Human Eye

One potentially interesting application for pattern and probe-based aberration monitors lies in the field of ophthalmology. This field dates back thousands of years and, as such, many methods for characterizing and improving the performance of the visual system have been well established. Therefore the space for innovation in the clinical environment is somewhat tight. Pattern and probe-based aberration monitors designed for the quantification of residual aberrations in optical lithography exposure tools show promise for measuring aberrations with great precision in human eyes in a robust low-cost apparatus which can be implemented in both subjective and objective measurement modes.

9.1. Background

The field of characterization of human vision is advancing rapidly. The human eye is significantly more aberrated than a lithographic lens and in today's clinical setting, an autorefractor is often used to first get a rough estimate of the patient's prescription, followed by a phoropter, which is essentially a set of trial lenses placed upon dials. These lenses are positioned in front of the subject's eyes in a suspended unit and, using the patient's feedback as a guide, the refraction of the eye can be measured.

A history of aberrometry in human eyes is provided in [70] and [71] and an excellent resource on the subject is available in [72]. Two main types of aberrometers are used to monitor the human eye. The first is a subjective system dating back to Scheiner's disk from the 1600's in which the patient reports image shifts they observe with their retina. The amount of image shift or adjustment needed to cause a shifted image to overlap with

a reference image is directly related to the local wavefront tilt. Such psychophysically detected signals are affected by the somewhat subjective nature of human perception.

The second type of aberrometer, based on the Hartman-Shack wavefront sensor, makes an objective measurement of the aberration by measuring the local wavefront tilt of light exiting the eye. Several hundred small lenslets are used to convert local wavefront tilt from the lens aberrations into a shift among their individual images. This is accomplished by creating a small "point" source on the retina, which then creates a spherical wave incident upon the pupil from inside the eye. The wave passing through the pupil picks up the aberrations in the lens and cornea, resulting in a distorted wavefront which is then incident upon a Hartman-Shack wavefront sensor. An array of microlenses can be used with a CCD sensor in the focal plane of the lenses. Each lenslet forms an image of the same retinal point source on the CCD. The displacement of each spot from the corresponding lenslet axis gives a measure of the local wavefront slope at that lenslet aperture. The local slopes can then be integrated to yield the overall shape and optical path error of the wavefront.

The benefits of this technique are that it does not depend upon the psychophysical response of the patient, that it does not require coherent illumination, and that only the positions of the sub images need to be measured and not their brightness. Furthermore, the measurements can be taken quickly, allowing real time feedback. This is useful in the field of adaptive optics and in wavefront guided laser ablation for refractive surgery. Drawbacks of such a system are that it operates at a single wavelength (the human eye must work over a wide range of wavelengths from about 450 nm to about 750 nm, under varying ambient light conditions and pupil radii) and that the apparatus itself can be quite

expensive. The fact that the tool works at a single wavelength is not terribly important though, as the aberrations tend to scale accordingly.

9.2. *Potential of Pattern and Probe Monitors*

Since the human eye can view the aberration test patterns developed in this thesis in a manner similar to that in which the wafer "views" a photomask through the imaging lens, it is likely that pattern and probe-based aberration monitors might also be used to assess aberrations in the human eye. Thus, a new class of aberrometer is proposed for the human eye, based upon observing the image intensity change at the center of the target change rather than an image shift. Figure 10-1 shows how the aberration targets can be presented to the observer from the object plane under coherent Kohler illumination at a visible wavelength. Light passes through the targets and the scattered light is collected by the eye lens and imaged onto the image plane/retina. The observer then reports the relative brightness among various incremental targets, thus indicating the level of aberration present in the eye associated with a given target.

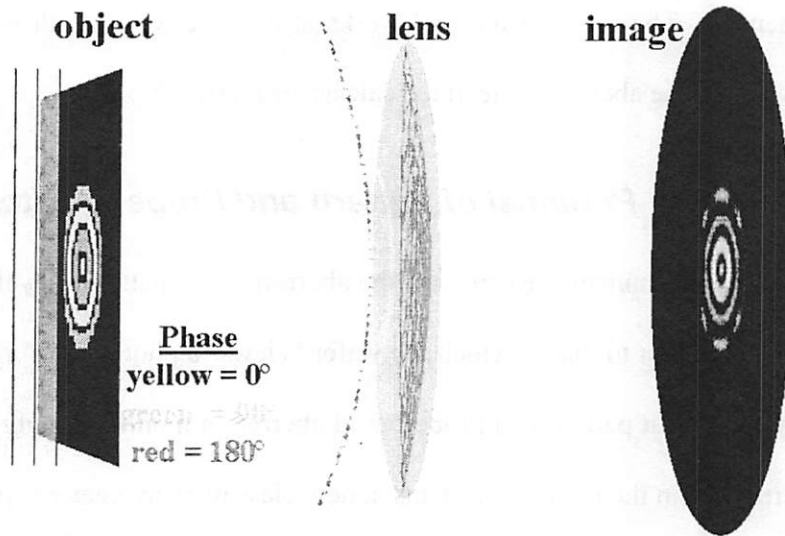


Figure 9-1. Subjective aberrometer in a “camera” setup with the phase shifted target in the object plane and the retina as the image plane.

A typical human eye has a Strehl ratio which is significantly less than 0.6 and is often dominated by the lower order defocus, astigmatism, coma, and tri-foil aberrations [73]. The diameter of the average human pupil ranges from 3 mm in bright light to 8 mm in dark ambient. The eye is filled with fluid which has a refractive index of $n = 1.33$ and the inside focal length is 24.4 mm. For an everyday application such as reading with a 4 mm diameter pupil at a wavelength of 632 nm, the numerical aperture is 0.082 and the Rayleigh resolution is 2.9 μm . For comparison, the letters on the Snellen visual acuity chart are designed to subtend an angle of 5 minutes of arc on the retinal plane. This corresponds to a total letter height of about 25 μm . This means that each stroke in the letter “E” is about $0.86 \frac{\lambda}{NA}$ in width, which is nearly double the size of the $0.45 \frac{\lambda}{NA}$ diameter target probes. The spacing between the rows of cones (one type of photoreceptor) on the retina is about 0.5 minutes of arc, which means that each stroke in

the Snellen letters lands on two to three photoreceptors while the probe will probably illuminate less than two.

The total rms wavefront error present increases with pupil size [74]. The majority of the rms wavefront error in human eyes is contained within the first three radial orders of Zernike polynomials (piston and tilt are ignored), which include defocus and astigmatism (both 2nd order), coma and tri-foil (both 3rd order), and spherical, 2nd order astigmatism, and 4-foil (all three 4th order). After correcting for the second order aberrations (defocus and astigmatism) the typical Strehl ratios for a 3 mm and a 7.3 mm pupil are 0.61 and 0.02, respectively.

The question of immediate interest is: what do these targets look like when viewed? The answer is that it all depends on the aberrations present in the observer's eye. Figure 10-2 shows four different aberration targets under three different lens conditions simulated using SPLAT with $\sigma = 0.3$. These targets, shown at the top, are two-ring versions of the defocus, astigmatism, coma, and tri-foil monitors. The first row of aerial images corresponds to the case where there are no aberrations. The second row contains the target images when some typical visual aberrations are present: 0.07λ rms each of both defocus and astigmatism and 0.03λ rms each of both coma and tri-foil, corresponding to a Strehl ratio of 0.67. Finally, the third row shows the aerial images after defocus is removed from the system, yielding a Strehl ratio of 0.79.

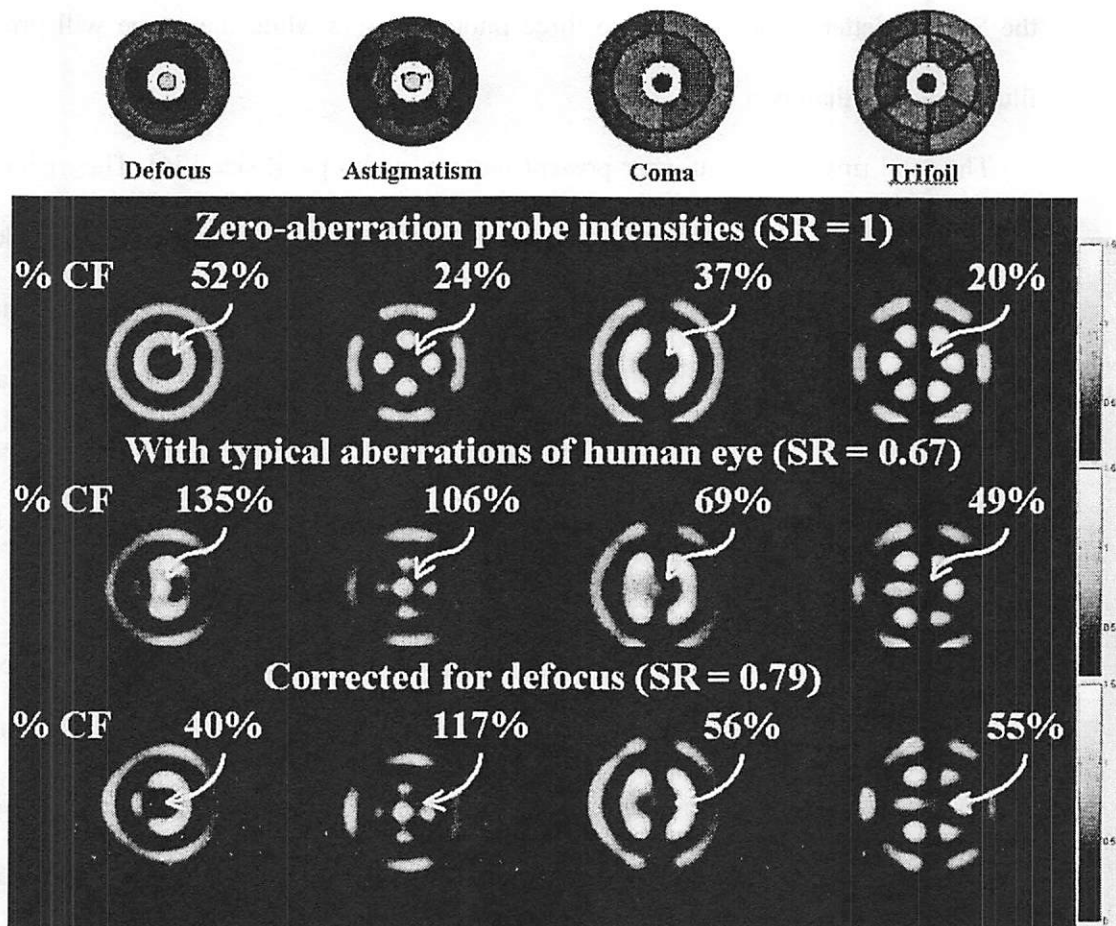


Figure 9-2. Two ring targets for defocus, astigmatism, coma, and tri-foil and their associated images at the retinal plane for three lens conditions: (top row) zero-aberration, (second row) with typical aberrations of human eye, (third row) corrected for defocus only. The scale bar on the side ranges from 0% CF (black) to 150% CF (white).

From the symmetries and ring radii it is easy to tell which image in the top row corresponds to which aberration target. In the zero-aberration case the probe intensity of the defocus, astigmatism, coma, and tri-foil targets are 52%, 24%, 37%, and 20% of the clear field (CF), respectively. When typical visual aberrations are present in the second row these intensities increase by 83%, 82%, 32%, and 29% CF, respectively. Removing defocus from the system in the third row, they change by -95%, 11%, -13%, and 6% CF. The large difference between the first and second rows indicate that each target has good sensitivity for the Zernike aberration term it is designed to detect. In fact the signal is

8.4% of the clear field per 0.01λ rms of any of the aberrations. In going from the second to the third row the major change only in the defocus target shows that there is low crosstalk. It is also noted that in the second and third rows the coma and/or tri-foil present in the system causes extra light to be thrown out to the left of each target.

Observing the brightness at the center of the defocus target, it is seen that the intensity increases significantly (83%) between the first and second rows. This is a very noticeable change for 0.07λ rms of defocus. The same is true for the astigmatism target (82%) for 0.07λ rms. The intensity at the center of the coma target also increases noticeably (32%) for 0.03λ rms between the first and second rows, even though there is significantly less coma than defocus and astigmatism. This is still quite a noticeable change. The tri-foil target shows a similar (29%) increase from the first to the second row. Since the probe is so small and it is surrounded by other bright features, the contrast discrimination of the eye will come into play as a potential limiting factor for this size target.

While lithographers use Rayleigh's quarter wave criterion to define depth of focus, ophthalmologists are most familiar with measuring and reporting the aberrations of defocus and astigmatism in diopters, D , which corresponds to the reciprocal of the focal length in meters. The definition of dioptric defocus is

$$D \equiv \frac{n}{d_1} - \frac{n}{d_2},$$

Equation 9-1. Equation defining diopters.

where d_1 is the original focal length of the eye (24.4 mm) and d_2 is the defocused length eye in meters, respectively. Modifying Equation 10-1, the equation

$$D \equiv \frac{n}{d_1} - \frac{n}{d_1 + 1RU},$$

Equation 9-2. Equation to translate the Rayleigh depth of focus into diopters.

is found. Accounting for the refractive index of the fluid filling the eye, the Rayleigh depth of focus for a 4 mm diameter pupil at $\lambda = 0.632 \mu\text{m}$, is at least $63 \mu\text{m}$ [75] and this much defocus is equal to 0.14 diopters.

While the preceding discussion assumed an eye with a relatively small amount of aberration, resulting in a high Strehl ratio, most eyes are significantly more aberrated. When the Strehl ratio of the eye is less than 0.1 the small aberration assumption allowing for the expansion of the OPD function in the diffraction integral becomes invalid, causing the behavior of the targets to be different from the simple theory presented earlier. With this, the target behavior becomes nonlinear and more confounded. Thus, an alternative approach might be better suited for making these types of measurements.

9.2.1. Benefits and Drawbacks

The use of the pattern and probe-based aberration targets for measuring the quality of the human eye has both benefits and drawbacks when compared to current schemes. One of the greatest benefits when considering the targets themselves is that implementing them at the comparatively low-NA and high λ of the eye eliminates most of the imaging demons discussed in Section 5.1. Because the lateral sizes of the features scale as $\frac{\lambda}{NA}$, and are therefore large compared to their etch depths, the electromagnetic mask edge effect for phase shifted regions becomes negligible. Secondly, polarization effects are virtually eliminated since the numerical aperture of the eye is quite small, resulting in

small ray angles incident upon the retina. Finally, small fabrication errors in making the targets become less important given the large overall sizes of the targets.

Further benefit can be realized when considering the fabrication of these targets. It may be possible to generate them in plastic by stamping them with a mold, similar to how a compact disk is made. The phase shifts needed for operation would be created by stamping different trench depths in the plastic. Once the patterns are made, it should be possible to generate coherent illumination over the target by using a broadband light source with a chromatic and spatial filters. Though the technique is designed for single wavelength measurements of aberrations, multiple versions of the targets could be generated on the same plastic substrate for testing at different colors such as red, blue, and green. The combination of the inexpensive fabrication with the ability to perform multiple wavelength measurements would make this technique appealing for use in non-clinical environments, such as by individuals at home in checking vision and physical health and in third-world countries and rural areas.

While there are many benefits to such an approach of aberrometry of the human eye, there are some significant hurdles which must be overcome. The eye is a complex, decentered optical system with multiple refractive surfaces and a granular detector with graded density. There are many complex processes which go on in the eye, making measurement difficult. They include accommodation of the lens depending upon the perceived distance to the object and dilation of the pupil depending upon the ambient light level, as well as tear film production. Furthermore, humans have evolved to scan their eyes when trying to observe fine detail, so as to have the light focused onto a special

area on the retina known as the fovea. All of these processes together act to dynamically change the aberrations in the eye under test.

While the ambient light level affects the pupil size, thereby changing the NA of the optic under test, an even greater concern is the psychophysical response of the observer when attempting to determine the brightness of a central probe surrounded by rings. That is, humans tend to interpret the size and brightness of a feature based upon the size and brightness of nearby features. Given this limitation, it may be very difficult for the patient to accurately report the brightness of the central probe in comparison with an absolute scale. It may be possible to remedy this however by creating complimentary sets of targets with different phased rings and probes and having the patient report the relative brightness of each of them. Adaptive optic elements capable of controlling both the amplitude and phase of a wavefront, known as liquid crystal spatial light modulators, may prove very useful in the implementation of these targets for human vision. These elements could be placed in front of the eye to optimize the wavefront incident upon the lens given its current aberration condition.

9.2.2. Conclusions

Initial experimental and simulation results indicate that pattern and probe-based aberration monitors, originally developed for characterizing photolithographic exposure tools in the integrated circuit industry, also show great promise in vision science and aberrometry of the human eye. Both subjective and objective aberrometers based on this technology have been proposed. Examples for typical combinations of aberrations in the

human eye show intensity changes of 8.4% of the clear field per 0.01λ rms of a given aberration in the presence of several others.

Appendix A – Zernike Circle Polynomials

Mathematical representation of the first 36 Zernike Polynomials

$z_1 = 1;$	Piston or Bias
$z_2 = \rho \cos[\theta];$	Tilt x
$z_3 = \rho \sin[\theta];$	Tilt y
$z_4 = -1 + 2\rho^2;$	Power
$z_5 = \rho^2 \cos[2\theta];$	Astig x
$z_6 = \rho^2 \sin[2\theta];$	Astig y
$z_7 = \rho(-2 + 3\rho^2) \cos[\theta];$	Coma x
$z_8 = \rho(-2 + 3\rho^2) \sin[\theta];$	Coma y
$z_9 = 1 - 6\rho^2 + 6\rho^4;$	Primary Spherical
$z_{10} = \rho^3 \cos[3\theta];$	Trefoil x
$z_{11} = \rho^3 \sin[3\theta];$	Trefoil y
$z_{12} = \rho^2(-3 + 4\rho^2) \cos[2\theta];$	Secondary Astigmatism x
$z_{13} = \rho^2(-3 + 4\rho^2) \sin[2\theta];$	Secondary Astigmatism y
$z_{14} = \rho(3 - 12\rho^2 + 10\rho^4) \cos[\theta];$	Secondary Coma x
$z_{15} = \rho(3 - 12\rho^2 + 10\rho^4) \sin[\theta];$	Secondary Coma y
$z_{16} = -1 + 12\rho^2 - 30\rho^4 + 20\rho^6;$	Secondary Spherical
$z_{17} = \rho^4 \cos[4\theta];$	Tetrafoil x
$z_{18} = \rho^4 \sin[4\theta];$	Tetrafoil y
$z_{19} = \rho^3(-4 + 5\rho^2) \cos[3\theta];$	Secondary Trefoil x
$z_{20} = \rho^3(-4 + 5\rho^2) \sin[3\theta];$	Secondary Trefoil y
$z_{21} = \rho^2(6 - 20\rho^2 + 15\rho^4) \cos[2\theta];$	Tertiary Astigmatism x
$z_{22} = \rho^2(6 - 20\rho^2 + 15\rho^4) \sin[2\theta];$	Tertiary Astigmatism y
$z_{23} = \rho(-4 + 30\rho^2 - 60\rho^4 + 35\rho^6) \cos[\theta];$	Tertiary Coma x
$z_{24} = \rho(-4 + 30\rho^2 - 60\rho^4 + 35\rho^6) \sin[\theta];$	Tertiary Coma y
$z_{25} = 1 - 20\rho^2 + 90\rho^4 - 140\rho^6 + 70\rho^8;$	Tertiary Spherical
$z_{26} = \rho^5 \cos[5\theta];$	Pentafoil x
$z_{27} = \rho^5 \sin[5\theta];$	Pentafoil y
$z_{28} = \rho^4(-5 + 6\rho^2) \cos[4\theta];$	Secondary Tetrafoil x
$z_{29} = \rho^4(-5 + 6\rho^2) \sin[4\theta];$	Secondary Tetrafoil y
$z_{30} = \rho^3(10 - 30\rho^2 + 21\rho^4) \cos[3\theta];$	Tertiary Trefoil x
$z_{31} = \rho^3(10 - 30\rho^2 + 21\rho^4) \sin[3\theta];$	Tertiary Trefoil y
$z_{32} = \rho^2(-10 + 60\rho^2 - 105\rho^4 + 56\rho^6) \cos[2\theta];$	Quaternary Astigmatism x
$z_{33} = \rho^2(-10 + 60\rho^2 - 105\rho^4 + 56\rho^6) \sin[2\theta];$	Quaternary Astigmatism y
$z_{34} = \rho(5 - 60\rho^2 + 210\rho^4 - 280\rho^6 + 126\rho^8) \cos[\theta];$	Quaternary Coma x
$z_{35} = \rho(5 - 60\rho^2 + 210\rho^4 - 280\rho^6 + 126\rho^8) \sin[\theta];$	Quaternary Coma y
$z_{36} = -1 + 30\rho^2 - 210\rho^4 + 560\rho^6 - 630\rho^8 + 252\rho^{10};$	Quaternary Spherical

From: <http://astron.berkeley.edu/~jrg/Aberrations/node11.html>

Appendix B – The Taylor Expansion

It is important to establish the range of validity of the Taylor expansion of the aberration portion of the electromagnetic diffraction integral. The Taylor series expansion of the exponential function is given by

$$e^x = 1 + \frac{x}{1!} + \frac{x^2}{2!} + \frac{x^3}{3!} + \dots$$

The aberration portion of the diffraction integral is given by

$$e^{jk\Phi_{peak}},$$

where Φ is more explicitly written as Φ_{peak} since the OPD term in the diffraction integral is actually peak waves of aberration. Assuming small aberrations so that only the first two terms in the expansion are retained

$$e^{jk\Phi_{peak}} \approx 1 + jk\Phi_{peak}.$$

The function e^x and its approximation $1+x$ are plotted in Figure A-1, along with the error ratio $\frac{e^x - (1+x)}{e^x}$.

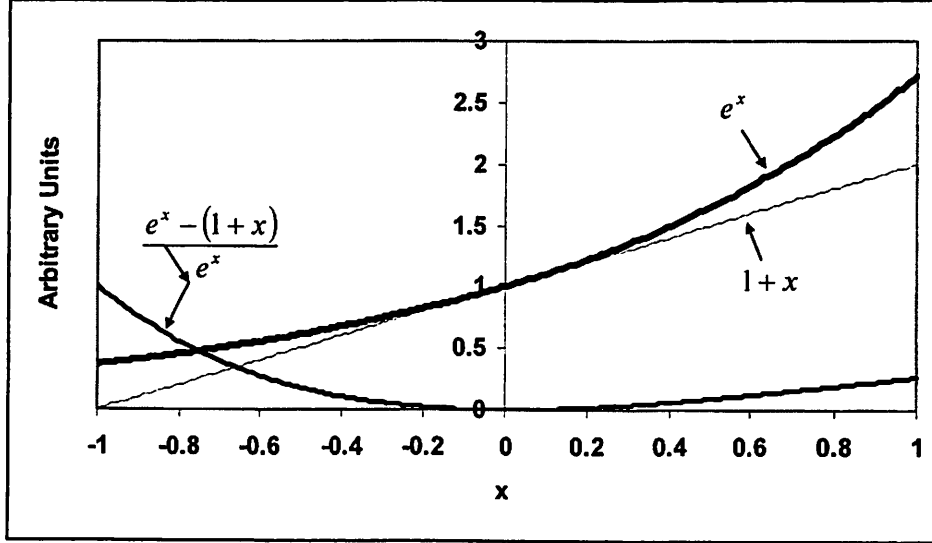


Figure A-0-1. Plot showing the exponential function as well as its approximation with the first two terms of the Taylor series expansion. The ratio of their difference to the original function is also shown.

The plot indicates that the first two terms of the Taylor series expansion is accurate to within 5% of the exponential function for $-0.29 < x < 0.36$. Setting

$$x = k\Phi_{peak} = \frac{2\pi}{\lambda}\Phi_{peak}, \Phi_{peak} \text{ lies in the range } -0.04615 < \frac{\Phi_{peak}}{\lambda} < 0.05730. \text{ It is}$$

important to note however that these limiting values of peak aberration can translate into very different rms values for each aberration. That is, the same amount of peak waves of aberration from two different aberrations can equate to different rms aberration values.

Figure A-2 shows the curves indicating how peak waves of Zernike coma and defocus are converted into rms waves. The minimum and maximum values along the vertical axis correspond to a Strehl ratio of 41%. It is interesting to note that the curve for coma aberration is extremely straight and that the curve for defocus matches it between -0.05 and 0.05 peak waves. This allows for a straightforward conversion of the limits of the range of validity from peak waves to rms waves: $-0.01609 < \frac{\Phi_{rms}}{\lambda} < 0.01998$.

0.01609 rms waves of aberration corresponds to a Strehl ratio of 99%. If the constraint upon the accuracy of the Taylor expansion approximation is relaxed to 10% allowable error then the limits change to $-0.02164 < \frac{\Phi_{rms}}{\lambda} < 0.02941$ and 0.02164 rms waves of aberration corresponds to a Strehl ratio of 98%. Thus, keeping only the first two terms of the Taylor expansion is reasonable for lenses with Strehl ratios above 97.5%.

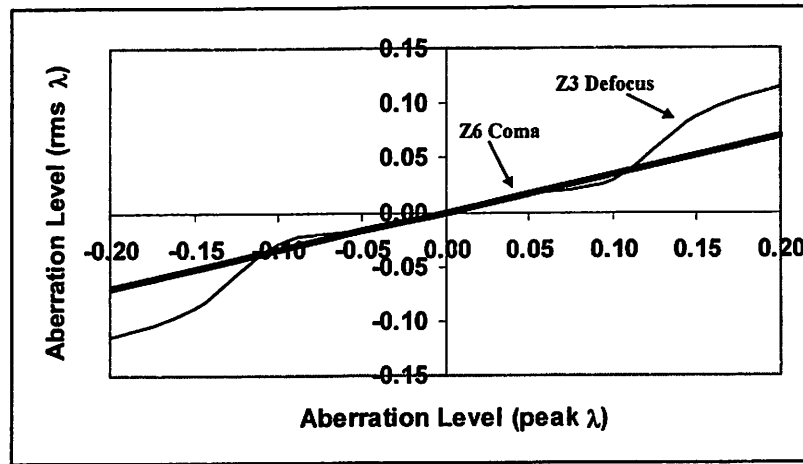


Figure A-0-2. Plot showing how to convert between peak waves and rms waves of aberration for defocus and coma.

Appendix C – Strehl Behavior

SPLAT simulation of square openings 0.3, 0.4, and 0.515 $\frac{\lambda}{NA}$ on a side in a dark field mask. We see that the peak image intensity through focus has a parabolic shape for about 1 Rayleigh unit on either side of best focus, where $1RU = \frac{\lambda}{2NA^2}$. The SPLAT input is normalized with $\lambda = 0.5 \mu\text{m}$ and $NA = 0.5$, giving 1 RU of defocus = $1 \mu\text{m}$. The partial coherence factor of the top hat illumination was set at $\sigma = 0.5$.

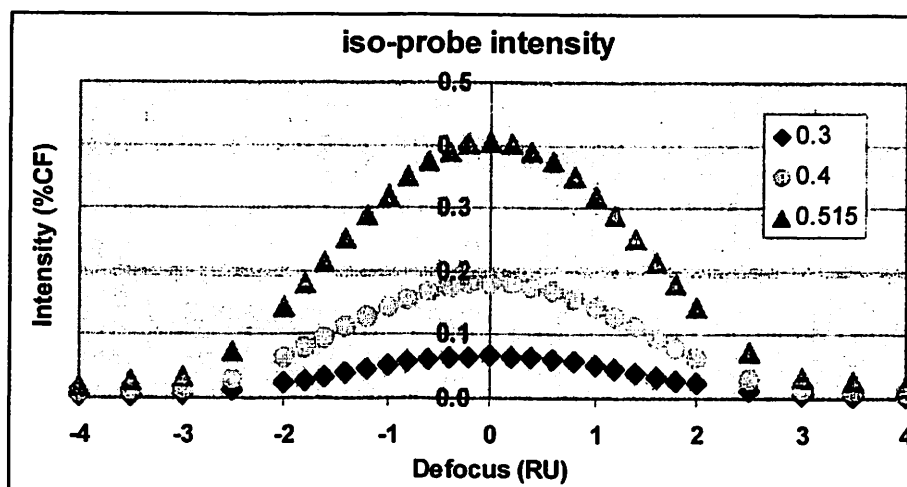


Figure A-0-1. Plot showing intensity through focus for probes of different sizes.

If we divide the peak aberrated intensity by the peak unaberrated intensity for each size opening we calculate the Strehl ratio as a function of defocus. When the focus is perfect and no other aberrations are present in the system, the optics are said to be diffraction-limited and the Strehl ratio (SR) is 100%. For small amounts of aberrations the Strehl ratio is given by

$$SR \approx \exp\left[-4\pi^2 \sum_{j=2} a_j^2\right] \rightarrow SR \approx 1 - 4\pi^2 \sum_{j=2} a_j^2,$$

where a_j is coefficient of the j 'th Zernike polynomial in the decomposition of the aberrated wavefront. Plotting the Strehl ratio through focus for all of the different sized openings we find that all of the data sets fall on top of each other, indicating that the Strehl behavior through focus is independent of feature size, so long as the feature is sub-printable (i.e., $<0.61 \frac{\lambda}{NA}$ on a side). We also see that the parabolic behavior is retained, as indicated by the equation on the right hand side above. By observing where the simulation results deviate appreciably from a parabola fitted to data points within 1 RU of either side of best focus we begin to get an idea of just how small $\sum_{j=2} a_j^2$ has to be properly described by the above equations. It appears that the equivalent defocus above which the equations break down is approximately 1 RU.

A good rule of thumb is that 1 RU of defocus causes the Strehl ratio to decrease to 79% and that 0.74 RU of defocus gives a Strehl ratio of 88%.

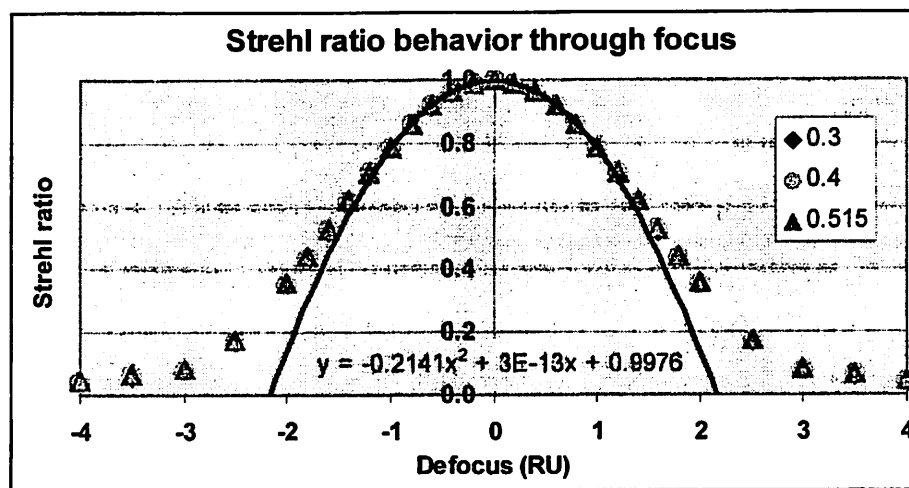
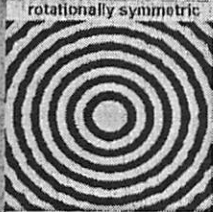
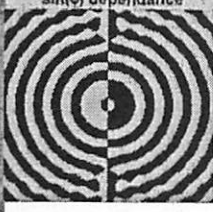
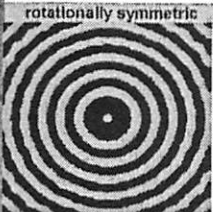



Figure A-0-2. Plot showing Strehl behavior for different sized probes.

Appendix D – IFT Target Layout

Garth C. Robins <garth@eecs.berkeley.edu> 1/16/02

This file gives the radii at which the concentric rings of alternating phase that compose the various aberration targets occur. The aberration that the target is designed to measure is highlighted in yellow. (This is the target name.)
 The angular dependence of the target is given on the far left. A ring with a $\sin(\phi)$ dependence changes phase 2π as it traverses 360 degrees. A ring with a $\sin(2\phi)$ dependence changes phase 4π as it traverses 360 degrees.
 The first circle $0 <x^2+y^2 < 0.2257 \lambda / NA$ represents a probe with area equivalent to that of a $0.4 \lambda / NA \times 0.4 \lambda / NA$ square opening in the mask.
 The probe phase is 0 for even aberrations and 90 degrees for odd aberrations.
 The first column gives the radii in normalized units of λ / NA .
 In all cases $\lambda = 0.248\mu\text{m}$.
 All other columns give ring radii in units of μm .
 The second column gives the radii for $NA = 0.5$.
 The third column gives the radii for $NA = 0.63$.
 The fourth column gives the radii for $NA = 0.7$.
 The fifth column gives the radii for $NA = 0.8$.
 I HAVE NOT included the 5x magnification factor for the $NA = 0.5$ machine or the 4x magnification for the $NA = 0.63, 0.7,$ and 0.8 machines.
 This file DOES include bias for phase etched regions (following Prof. ARN's e-mail of 01/08/02)

Bias amt. per edge in (λ / NA) = 0					Normalized units (λ / NA)				
Z3 (Defocus)					$\lambda / NA = 1$				
original	new	+	-		0 $<x^2+y^2 <$	0.2257 @	90 (probe)		
1.01987875 @	180 1.019879	1.019879	1.019879		0.5 $<x^2+y^2 <$	1.019879 @	180 (Fat ring)		
1.55364 @	0 1.55364	1.55364	1.55364		1.019879 $<x^2+y^2 <$	1.55364 @	0		
2.07394 @	180 2.07394	2.07394	2.07394		1.55364 $<x^2+y^2 <$	2.07394 @	180		
2.5866775 @	0 2.586678	2.586678	2.586678		2.07394 $<x^2+y^2 <$	2.586678 @	0		
3.114419 @	180 3.114419	3.114419	3.114419		2.586678 $<x^2+y^2 <$	3.114419 @	180		
3.61911 @	0 3.61911	3.61911	3.61911		3.114419 $<x^2+y^2 <$	3.61911 @	0		
4.1167225 @	180 4.116723	4.116723	4.116723		3.61911 $<x^2+y^2 <$	4.116723 @	180		
4.66455 @	0 4.66455	4.66455	4.66455		4.116723 $<x^2+y^2 <$	4.66455 @	0		
5.1052925 @	180 5.105293	5.105293	5.105293		4.66455 $<x^2+y^2 <$	5.105293 @	180		
5.6497925 @	0 5.649793	5.649793	5.649793		5.105293 $<x^2+y^2 <$	5.649793 @	0		
6.126835 @	180 6.126835	6.126835	6.126835		5.649793 $<x^2+y^2 <$	6.126835 @	180		
Z7 (Coma)					Z7 (Coma)				
original	new	+	-		0 $<x^2+y^2 <$	0.2257 @	0 (probe)		
1.2096975 @	0 1.209698	1.209698	1.209698		0.5 $<x^2+y^2 <$	1.209698 @	0 (Fat ring)		
1.7632725 @	180 1.763273	1.763273	1.763273		1.209698 $<x^2+y^2 <$	1.763273 @	180		
2.29295 @	0 2.29295	2.29295	2.29295		1.763273 $<x^2+y^2 <$	2.29295 @	0		
2.8183925 @	180 2.818393	2.818393	2.818393		2.29295 $<x^2+y^2 <$	2.818393 @	180		
3.33884375 @	0 3.338844	3.338844	3.338844		2.818393 $<x^2+y^2 <$	3.338844 @	0		
3.84649925 @	180 3.846499	3.846499	3.846499		3.338844 $<x^2+y^2 <$	3.846499 @	180		
4.36447 @	0 4.36447	4.36447	4.36447		3.846499 $<x^2+y^2 <$	4.36447 @	0		
4.867225 @	180 4.867225	4.867225	4.867225		4.36447 $<x^2+y^2 <$	4.867225 @	180		
5.359695 @	0 5.359695	5.359695	5.359695		4.867225 $<x^2+y^2 <$	5.359695 @	0		
5.871525 @	180 5.871525	5.871525	5.871525		5.359695 $<x^2+y^2 <$	5.871525 @	180		
Z8 (Spherical)					Z8 (Spherical)				
original	new	+	-		0 $<x^2+y^2 <$	0.2257 @	90 (probe)		
1.39271 @	0 1.39271	1.39271	1.39271		0.5 $<x^2+y^2 <$	1.39271 @	0 (Fat ring)		
1.9665525 @	180 1.966553	1.966553	1.966553		1.39271 $<x^2+y^2 <$	1.966553 @	180		
2.5068175 @	0 2.506818	2.506818	2.506818		1.966553 $<x^2+y^2 <$	2.506818 @	0		
3.0488975 @	180 3.048898	3.048898	3.048898		2.506818 $<x^2+y^2 <$	3.048898 @	180		
3.56224 @	0 3.56224	3.56224	3.56224		3.048898 $<x^2+y^2 <$	3.56224 @	0		
4.0671125 @	180 4.067113	4.067113	4.067113		3.56224 $<x^2+y^2 <$	4.067113 @	180		
4.6200825 @	0 4.620083	4.620083	4.620083		4.067113 $<x^2+y^2 <$	4.620083 @	0		
5.06143 @	180 5.06143	5.06143	5.06143		4.620083 $<x^2+y^2 <$	5.06143 @	180		
5.60472 @	0 5.60472	5.60472	5.60472		5.06143 $<x^2+y^2 <$	5.60472 @	0		
Z4 (Astigmatism)					Z4 (Astigmatism)				
original	new	+	-		0 $<x^2+y^2 <$	0.2257 @	90 (probe)		
1.01600675 @	0 1.016007	1.016007	1.016007		0.5 $<x^2+y^2 <$	1.016007 @	0 (Fat ring)		
1.5604765 @	180 1.560477	1.560477	1.560477		1.016007 $<x^2+y^2 <$	1.560477 @	180		
2.077691 @	0 2.077691	2.077691	2.077691		1.560477 $<x^2+y^2 <$	2.077691 @	0		
2.59554075 @	180 2.595541	2.595541	2.595541		2.077691 $<x^2+y^2 <$	2.595541 @	180		
3.09654125 @	0 3.096541	3.096541	3.096541		2.595541 $<x^2+y^2 <$	3.096541 @	0		
3.61345325 @	180 3.613453	3.613453	3.613453		3.096541 $<x^2+y^2 <$	3.613453 @	180		
4.1337835 @	0 4.133784	4.133784	4.133784		3.613453 $<x^2+y^2 <$	4.133784 @	0		
4.6043525 @	180 4.604353	4.604353	4.604353		4.133784 $<x^2+y^2 <$	4.604353 @	180		
5.1561125 @	0 5.156113	5.156113	5.156113		4.604353 $<x^2+y^2 <$	5.156113 @	0		

X

		Z10 (Trifol)			
original		new	+	-	
1.2205875	@ 180	1.220588	1.220588	1.220588	
1.77213575	@	1.772136	1.772136	1.772136	
2.30090575	@ 180	2.300906	2.300906	2.300906	
2.8119795	@	2.81198	2.81198	2.81198	
3.31966525	@ 180	3.319665	3.319665	3.319665	
3.849131	@	3.849131	3.849131	3.849131	
4.33830375	@ 180	4.338304	4.338304	4.338304	
4.856335	@	4.856335	4.856335	4.856335	
5.3896425	@ 180	5.389643	5.389643	5.389643	
5.88958425	@	5.889584	5.889584	5.889584	



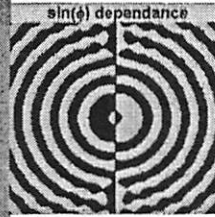
		Z10 (Trifol)			
		<x^2+y^2<	0.2257	@	0 (probe)
0.5	<x^2+y^2<	1.220588	@	180	(Fat ring)
1.220588	<x^2+y^2<	1.772136	@	0	
1.772136	<x^2+y^2<	2.300906	@	180	
2.300906	<x^2+y^2<	2.81198	@	0	
2.81198	<x^2+y^2<	3.319665	@	180	
3.319665	<x^2+y^2<	3.849131	@	0	
3.849131	<x^2+y^2<	4.338304	@	180	
4.338304	<x^2+y^2<	4.856335	@	0	
4.856335	<x^2+y^2<	5.389643	@	180	
5.389643	<x^2+y^2<	5.889584	@	0	

		Z11 (HO Astigmatism)			
original		new	+	-	
1.40108925	@ 180	1.401089	1.401089	1.401089	
1.969275	@	1.969275	1.969275	1.969275	
2.511355	@ 180	2.511355	2.511355	2.511355	
3.02920475	@	3.029205	3.029205	3.029205	
3.55706725	@ 180	3.557067	3.557067	3.557067	
4.0840525	@	4.084053	4.084053	4.084053	
4.55961275	@ 180	4.559613	4.559613	4.559613	
5.11923775	@	5.119238	5.119238	5.119238	
5.590563	@ 180	5.590563	5.590563	5.590563	



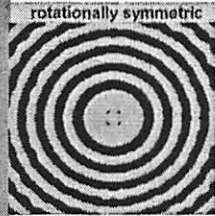
		Z11 (HO Astigmatism)			
		<x^2+y^2<	0.2257	@	90 (probe)
0.5	<x^2+y^2<	1.401089	@	180	(Fat ring)
1.401089	<x^2+y^2<	1.969275	@	0	
1.969275	<x^2+y^2<	2.511355	@	180	
2.511355	<x^2+y^2<	3.029205	@	0	
3.029205	<x^2+y^2<	3.557067	@	180	
3.557067	<x^2+y^2<	4.084053	@	0	
4.084053	<x^2+y^2<	4.559613	@	180	
4.559613	<x^2+y^2<	5.119238	@	0	
5.119238	<x^2+y^2<	5.590563	@	180	

		Z14 (HO Coma)			
original		new	+	-	
1.5793525	@ 180	1.579353	1.579353	1.579353	
2.16786625	@	2.167866	2.167866	2.167866	
2.721532	@ 180	2.721532	2.721532	2.721532	
3.25795525	@	3.257955	3.257955	3.257955	
3.77656125	@ 180	3.776561	3.776561	3.776561	
4.3026995	@	4.3027	4.3027	4.3027	
4.810355	@ 180	4.810355	4.810355	4.810355	
5.30926825	@	5.309268	5.309268	5.309268	
5.82896325	@ 180	5.828963	5.828963	5.828963	



		Z14 (HO Coma)			
		<x^2+y^2<	0.2257	@	0 (probe)
0.5	<x^2+y^2<	1.579353	@	180	(Fat ring)
1.579353	<x^2+y^2<	2.167866	@	0	
2.167866	<x^2+y^2<	2.721532	@	180	
2.721532	<x^2+y^2<	3.257955	@	0	
3.257955	<x^2+y^2<	3.776561	@	180	
3.776561	<x^2+y^2<	4.3027	@	0	
4.3027	<x^2+y^2<	4.810355	@	180	
4.810355	<x^2+y^2<	5.309268	@	0	
5.309268	<x^2+y^2<	5.828963	@	180	

		Z15 (HO Spherical)			
original		new	+	-	
1.76300025	@ 180	1.763	1.763	1.763	
2.366155	@	2.366155	2.366155	2.366155	
2.93494575	@ 180	2.934946	2.934946	2.934946	
3.464593	@	3.464593	3.464593	3.464593	
3.98274525	@ 180	3.982745	3.982745	3.982745	
4.5453045	@	4.545305	4.545305	4.545305	
4.9881645	@ 180	4.988165	4.988165	4.988165	
5.5475475	@	5.547548	5.547548	5.547548	
6.04658175	@ 180	6.046582	6.046582	6.046582	



		Z15 (HO Spherical)			
		<x^2+y^2<	0.2257	@	90 (probe)
0.5	<x^2+y^2<	1.763	@	180	(Fat ring)
1.763	<x^2+y^2<	2.366155	@	0	
2.366155	<x^2+y^2<	2.934946	@	180	
2.934946	<x^2+y^2<	3.464593	@	0	
3.464593	<x^2+y^2<	3.982745	@	180	
3.982745	<x^2+y^2<	4.545305	@	0	
4.545305	<x^2+y^2<	4.988165	@	180	
4.988165	<x^2+y^2<	5.547548	@	0	
5.547548	<x^2+y^2<	6.046582	@	180	

		Z16 (Quadrifol)			
original		new	+	-	
1.400212	@	1.400212	1.400212	1.400212	
1.97783575	@ 180	1.977836	1.977836	1.977836	
2.505305	@	2.505305	2.505305	2.505305	
3.02902325	@ 180	3.029023	3.029023	3.029023	
3.543947825	@	3.543948	3.543948	3.543948	
4.04996075	@ 180	4.049961	4.049961	4.049961	
4.58972965	@	4.58973	4.58973	4.58973	
5.078612	@ 180	5.078612	5.078612	5.078612	
5.6387815	@	5.638782	5.638782	5.638782	



		Z16 (Quadrifol)			
		<x^2+y^2<	0.2257	@	90 (probe)
0.5	<x^2+y^2<	1.400212	@	0	(Fat ring)
1.400212	<x^2+y^2<	1.977836	@	180	
1.977836	<x^2+y^2<	2.505305	@	0	
2.505305	<x^2+y^2<	3.029023	@	180	
3.029023	<x^2+y^2<	3.543948	@	0	
3.543948	<x^2+y^2<	4.049961	@	180	
4.049961	<x^2+y^2<	4.58973	@	0	
4.58973	<x^2+y^2<	5.078612	@	180	
5.078612	<x^2+y^2<	5.638782	@	0	

10. References

-
- [1] C. Garza, W. Conley, B. Roman, and M. Schippers, "Ring test aberration determination & device lithography correlation," *Proc. of SPIE*, vol. 4346, pp. 36 – 43, 2001.
 - [2] T.A Brunner, "Impact of lens aberrations on optical lithography," *IBM J. Res. Develop*, vol. 41, pp. 57 – 67, January/March 1997.
 - [3] F. Gennari and A.R. Neureuther, "Aberrations are a big part of OPC for phase-shifting masks," *Proc. of SPIE*, vol. 4562, pp. 1077 – 1086, March, 2002.
 - [4] F. Gennari, "Linking TCAD and EDA Through Pattern Matching," Ph.D. Dissertation, University of California at Berkeley, 2004.
 - [5] G. McIntyre and A. Neureuther, "Characterizing illumination angular uniformity with phase-shifting masks," *Proc. of SPIE*, vol. 5040, pp. 162 – 170, June 2003.
 - [6] A. Neureuther, G. McIntyre, F. Gennari, M. Lam, J. Cain, G. Robins, E. Huang, J. Choi, L. Wang, L. Yuan, H. Oshima, "Feature level test patterns for characterizing residual process effects," *Proc. of SPIE*, vol. 5379, pp. 76 – 84, May 2004.
 - [7] G. McIntyre and A. Neureuther, "Initial experimental verification: characterizing tool illumination and PSM performance with phase-shifting masks," *Proc. of SPIE*, vol. 5377, pp. 185 – 194, May 2004.
 - [8] S. Hafeman, F. Gennari and A. Neureuther, "Fast algorithm for extraction of worst-case image degradation due to flare," *Proc. of SPIE*, vol. 5377, pp. 1397 – 1404, May 2004.
 - [9] S. Hafeman and A. Neureuther, "Simulation of imaging and stray light effects in immersion lithography," *Proc. of SPIE*, vol. 5040, pp. 700 – 712, June 2003.
 - [10] E. Hecht, *Optics*, 2nd ed. Reading, Massachusetts: Addison-Wesley, 1987.
 - [11] J.R. Sheats and B.W. Smith, *Microlithography Science and Technology*, 1st ed., New York, New York: Marcel Dekker, 1998.
 - [12] J.W. Goodman, *Introduction To Fourier Optics*, 2nd ed., New York, New York: McGraw-Hill, 1996.
 - [13] J.W. Goodman, *Statistical Optics*, New Ed ed., New York, New York: Wiley-Interscience, 2000.

-
- [14] V.N. Mahajan, *Aberration Theory Made Simple*, Bellingham, Washington: SPIE Optical Engineering Press, 1991, ch. 8.
- [15] M. Born and E. Wolf, *Principles of Optics: Electromagnetic Theory of Propagation, Interference and Diffraction of Light*, New York, New York: Cambridge University Press, 7th ed., 1999.
- [16] P. Dirksen, C. Juffermans, R. Pellens, M. Maenhoudt, and P. De Bisschop, "Novel aberration monitor for optical lithography," *Proc. of SPIE*, vol. 3679, pp. 77 – 87, March 1999.
- [17] C. Mack, *Inside Prolith: A Comprehensive Guide to Optical Lithography Simulation*, Austin, Texas: Finle Technologies, Inc., 1997.
- [18] H. Levinson, *Principles of Lithography*, 2nd ed., Bellingham, WA: SPIE Press, 2005.
- [19] H. Ito, C.G. Willson and J.M.J. Grechet, "New UV Resists With Negative or Positive Tone," *Digest of Technical Papers of 1982 Symposium on VLSI Technology*, pp. 86 – 87, 1982.
- [20] H. Ito, "Chemically amplification resists: History and development within IBM," *IBM J. Res. Develop.*, vol. 41, No.1-2, pp. 69 – 80, 1997.
- [21] L. Yuan and A. Neureuther, "Improving chemically-amplified resist modeling for 2D layout patterns," *Proc. of SPIE*, vol. 5039, pp. 1041 – 1051, 2003.
- [22] H. Fukuda, K. Hattori and T. Hagiwara, "Impact of acid/quencher diffusion behavior on lithography performance," *Proc. of SPIE*, vol. 4346, pp. 319 – 330, 2001.
- [23] K.H. Toh and A.R. Neureuther, "Identifying and Monitoring Effects of Lens Aberrations in Projection Printing," *Proc. of SPIE*, vol. 772, pp. 202-209, 1987.
- [24] C. Pierrat, A. Wong and S. Vaidya, "Phase-shifting mask topography effects on lithographic image quality," *IEDM Tech. Digest*, pp. 53 – 56, December 1992.
- [25] F. Zernike, "Beugungstheorie des Schneidverfahrens und seiner verbesserten Form, der Phasenkontrastmethode," *Physica*, vol. 1, pp. 689 – 704, 1934.
- [26] E.W. Weisstein, "Zernike Polynomial," *From MathWorld – A Wolfram Web Resource*. <http://mathworld.wolfram.com/ZernikePolynomial.html>
- [27] E.W. Weisstein. "Jinc Function," *From MathWorld – A Wolfram Web Resource*. <http://mathworld.wolfram.com/JincFunction.html>

-
- [28] K.K.H. Toh, C.C. Fu, K.L. Zollinger, A.R. Neureuther and R.F.W. Pease, "Characterization of Voting Suppression of Optical Defects Through Simulation," *Proc. of SPIE*, March 1998.
- [29] H. Fukuda, K. Hayano and S. Shirai, "Determination of high-order lens aberrations using phase/amplitude linear algebra," *J. Vac Sci. Technol. B*, vol. 17, no. 6, pp. 3318 – 3321, November/December 1999.
- [30] J. Kirk, "Review of photoresist-based lens evaluation methods," *Proc. of SPIE*, vol. 4000, pp. 2 – 8, July 2000.
- [31] J. Liang, B. Grimm, S. Goelz and J.F. Bille, "Objective measurement of wave aberrations of the human eye with use of a Hartmann-Shack wave-front sensor," *J. Opt. Soc. Am. A*, vol. 11, pp. 1949 – 1957, 1994.
- [32] J. Liang and D.R. Williams, "Aberrations and retinal image quality of the normal human eye," *J. Opt. Soc. Am. A*, vol. 14, pp. 2873 – 2883, 1997.
- [33] J. Liang, D.R. Williams and D. Miller, "Supernormal vision and high-resolution retinal imaging through adaptive optics," *J. Opt. Soc. Am. A*, vol. 14, pp. 2884 – 2892, 1997.
- [34] D. Miller, D.R. Williams, G.M. Morris and J. Liang, "Images of cone photoreceptors in the living human eye," *Vision Res.*, vol. 36, pp. 1067 – 1079, 1996.
- [35] T.A. Brunner, A.L. Martin, R.M. Martino, C.P. Ausschnitt and T.H. Newman, "Quantitative stepper metrology using the focus monitor test mask," *Proc. of SPIE*, vol. 2197, pp. 541 – 549, 1994.
- [36] T.A. Brunner, "New Focus Metrology Technique Using Special Test Mask," *Microlith. World*, pp. 5 – 13, Winter 1994.
- [37] E.R. Sherman, "Characterization and monitoring of variable NA and variable coherence capable photo steppers utilizing the phase shift focus monitor," *Proc. of SPIE*, vol. 2439, pp. 61 – 69, 1995.
- [38] R.D. Mih, A. Martin, T. Brunner, D. Long and D. Brown, "Using the focus monitor test mask to characterize lithographic performance," *Proc. of SPIE*, vol. 2440, pp. 657 – 666, 1995.
- [39] G.M. Pugh, "Detailed study of a phase-shift focus monitor," *Proc. of SPIE*, vol. 2440, pp. 690 – 700, 1995.

-
- [40] D. Wheeler, E. Solecky, T. Dinh and R. Mih, "Phase shift focus monitor applications to lithography tool control," *Proc. of SPIE*, vol. 3051, pp. 225 – 233, 1997.
- [41] R. Edwards, P. Ackerman, C. Fischer, M. Desrocher and M. Puzerewski, "Characterization of autofocus uniformity and precision of ASML steppers using the phase shift focus monitor reticle," *Proc. of SPIE*, vol. 3051, pp. 448 – 455, 1997.
- [42] B. La Fontaine, M. Dusa, J. Krist, A. Acheta, J. Kye, H. Levinson, C. Luijten, E. Rodriguez, C. Sager, J. Thomas and J. Van Praagh, "Analysis of focus errors in lithography using phase-shift monitors," *Proc. of SPIE*, vol. 4691, pp. 315 – 324, 2002.
- [43] B. Roberts, J. Guerrero, C. Gould, K. Rebitz and A. Smith, "Quantifying the Capability of a New In-situ Interferometer," *IEEE/SEMI Advanced Semicon. Mfg. Conf.*, pp. 407 – 412, 2000.
- [44] N.R. Farrar, A.L. Smith, D. Busath and D. Taitano, "In-situ measurement of lens aberrations," *Proc. of SPIE*, vol. 4000, pp. 18 – 29, March 2000.
- [45] P. Dirksen, C. Juffermans, A. Engelen, P. De Bisschop and H. Muellerke, "Impact of high-order aberrations on the performance of the aberration monitor," *Proc. of SPIE*, vol. 4000, pp. 9 – 17, 2000.
- [46] J.P. Kirk, S. Schank and C.Y. Lin, "Detection of focus and spherical aberration by use of a phase grating," *Proc. of SPIE*, vol. 4346, pp. 1355 – 1361, 2001.
- [47] W. Hinsberg, F.A. Houle, J. Hoffnagle, M. Sanchez, G. Wallraff, M. Morrison and S. Frank, "Deep-ultraviolet interferometric lithography as a tool for assessment of chemically amplified photoresist performance," *J. Vac. Sci. Technol. B*, vol. 16, no. 6, pp. 3689, Nov/Dec 1998.
- [48] Meddecki, E. Tejnil, K.A. Goldberg and J. Bokor, "Phase-shifting point diffraction interferometer," *Optics Letters*, vol. 21, no. 19, pp. 1526 – 1528, October 1996.
- [49] F. Zach, C.Y. Lin and J. Kirk, "Aberration analysis using reconstructed aerial images of isolated contacts on attenuated phase shift masks," *Proc. of SPIE*, vol. 4346, pp. 1362 – 1368, 2001.
- [50] P. Leroux, D. Ziger and N. Juig, "Focus characterization using end of line metrology," *IEEE Transactions on Semicon. Mfg.*, vol. 13, no. 3, pp. 322 - 330, August 2000.
- [51] K. Hayano, *et al*, *Proc. of IEICE Technical Report*, SDM98-163, 1998.

-
- [52] A. Imai, K. Hayano, H. Fukuda, N. Asai and N. Hasegawa, "Lens aberration measurement technique using attenuated phase-shifting mask," *Proc. of SPIE*, vol. 4000, pp. 1260 – 1268, 2000.
- [53] K. Adam, S. Hotta and A.R. Neureuther, "Characterization of phase defects in phase shift masks," *J. Vac. Sci. Technol. B*, vol. 18, no. 6, pp. 3227-3231, November/December 2000.
- [54] A.R. Neureuther, P. Flanner III and S. Shen, "Coherence of Defect Interactions with Features in Optical Imaging," *Jour. Vac. Sci. Tech. B*, vol. 5, no. 1, pp. 308-312, January/February 1987.
- [55] V. Mastromarco, K.H. Toh and A.R. Neureuther, "Printability of defects in optical lithography: Polarity and critical location effects," *J. Vac. Sci. Technol. B*, pp. 224 – 229, 1987.
- [56] A.R. Neureuther, "Modelling phase-shifting masks," *Proc. of SPIE*, vol. 1496, pp. 80 – 88, 1991.
- [57] R. Socha, D. Van Den Broeke, S. Hsu, J. Fung Chen, T. Laidig, N. Corcoran, U. Hollerbach, K.E. Wampler, X. Shi and W. Conley, "Contact Hole Reticule Optimization by Using Interference Mapping Lithography (IML™)," *Proc. of SPIE*, vol. 5377, pp. 222 – 240, 2004.
- [58] F. Schellenberg, D. Levenson and P. Brock, "Optimization of real phase-mask performance," *Proc. of SPIE*, vol. 1604, pp. 274 – 296, 1992.
- [59] A.E. Rosenbluth, S. Bukofsky, M. Hibbs, K. Lai, A. Molless, R.N. Singh and A. Wong, "Optimum Mask and Source Patterns to Print a Given Shape," *Proc. of SPIE*, vol. 4346, pp. 486 – 502, September 2001.
- [60] A.R. Neureuther, S. Hotta and K. Adam: "Modeling defect-feature interactions in the presence of aberrations," *Proc. of SPIE*, vol. 4186, pp. 405 – 414, 2001.
- [61] S. Lee, K. Ng, T. Orimoto, J. Pittenger, T. Horie, K. Adam, M. Cheng, E. Croffie, Y. Deng, F. Gennari, T. Pistor, G. Robins, M. Williamson, B. Wu, L. Yuan, A. Neureuther, "LAVA web-based remote simulation: enhancements for education and technology innovation," *Proc. of SPIE*, vol. 4346, pp. 1500 – 1506, September 2001.
- [62] Bracewell, R. *The Fourier Transform and Its Applications*, New York, New York: McGraw-Hill, 3rd ed., 1999.

-
- [63] R.J. Sasiela, *Electromagnetic Wave Propagation in Turbulence*, Berlin: Springer-Verlag, Ch. 3, 1994.
- [64] T.A. Brunner, N. Seong, W.D. Hinsberg, J.A. Hoffnagle, F.A. Houle and M.I. Sanchez, "High NA lithographic imagery at Brewster's angle," *Proc. of SPIE*, vol. 4691, pp. 1 – 10, March 2002.
- [65] B. Stegemann, "10 Years of Aerial Image Measurement Systems – AIMS™," *Future Fab International*, vol. 16, ch. 4, February 2004.
- [66] A. Wong, "Rigorous Three-Dimensional Time-Domain Finite-Difference Electromagnetic Simulation," Ph.D. Dissertation, University of California at Berkeley 1994.
- [67] V. N. Mahajan, *Aberration Theory Made Simple*, Bellingham, WA: SPIE Press, 1991.
- [68] D. Van Den Broeke, R. Socha, S. Hsu, J. Fung Chen, T. Laidig, N. Corcoran, U. Hollerbach, K. Wampler, and X. Shi, "Near-0.3 λ full pitch range contact hole patterning using chromeless phase lithography (CPL)," *Proc. of SPIE*, vol. 5256, pp. 297 – 308, December 2003.
- [69] Dr. Axel Zibold, Zeiss Corporation, Personal communication, February/March 2005.
- [70] L. Thibos, R. Applegate, and S. Marcos, "Aberrometry: The Past, Present, and Future of Optometry," *Optometry and Vision Science*, vol. 80, no. 1, pp. 1 – 2, January 2003.
- [71] L. Thibos, "Principles of Hartmann-Shack aberrometry," *J. Refract. Surg.*, vol. 16, pp. S563-565, September/October 2000.
- [72] R. Krueger, R. Applegate and S. MacRae, *Wavefront Customized Visual Correction*, Thorofare, New Jersey: SLACK Inc., 2004.
- [73] J. Liang and D. R. Williams, "Aberrations and retinal image quality of the normal human eye," *J. Opt. Soc. Am. A*, vol. 14, no. 11, pp. 2873-2883, November 1997.
- [74] J. Castejón-Mochón, N. López-Gil, A. Benito, and P. Artal, "Ocular wave-front statistics in a normal young population," *Vision Research*, vol. 42, no. 1, pp. 1611-1617, 2002.
- [75] C. Mack, "The Rayleigh Depth of Focus," *Microlith. World*, vol. 13, no. 1, pp. 14 – 15, February 2004.